

UNIVERSITY OF CALIFORNIA,  
IRVINE

**Composition and Photochemistry of Anthropogenic and Biogenic Organic Aerosols**

DISSERTATION

submitted in partial satisfaction of the requirements  
for the degree of

DOCTOR OF PHILOSOPHY

in Chemical and Materials Physics-Chemistry

by

Sandra Louise Blair

Dissertation Committee:  
Professor Sergey Nizkorodov, Chair  
Professor Barbara Finlayson-Pitts  
Assistant Professor Craig Murray

2016

Portions of Chapter 1 © Taylor & Francis  
Portions of Chapter 2 © Taylor & Francis  
Portions of Chapter 3 and Chapter 5 © American Chemical Society  
Figure 1.1 (cig). Copyright © Wiley-VCH Verlag GmbH & Co. KGaA, Weinheim.  
Figure 1.2 (ecig) Copyright © 1937-2016 Tax Foundation.  
All other material © 2016 Sandra Louise Blair

*“The task is, not so much to see what no one has yet seen; but to think what nobody has yet thought, about that which everybody sees.”*

*— Erwin Schrödinger*

# Table of Contents

<b>List of Acronyms</b> .....	<b>viii</b>
<b>List of Figures</b> .....	<b>xi</b>
<b>List of Schemes</b> .....	<b>ix</b>
<b>List of Tables</b> .....	<b>x</b>
<b>Acknowledgements</b> .....	<b>xiii</b>
<b>Curriculum Vitae</b> .....	<b>xv</b>
<b>Abstract of the Dissertation</b> .....	<b>xviii</b>
<b>Chapter 1: Introduction</b> .....	<b>1</b>
1.1. Background .....	2
1.1.1. Atmospheric Organic Aerosols (OA) .....	2
1.1.2. Primary Emissions of Combustion and Electronic Cigarettes .....	3
1.1.3. Aqueous Iron Chemistry .....	6
1.1.4. Photooxidation of Fuel SOA .....	6
1.1.5. $\alpha$ -Pinene Ozonolysis SOA .....	11
1.1.6. Photochemical Aging .....	11
1.2. Goals .....	13
1.3. General Methods .....	15
1.3.1. Chamber Generation of SOA .....	15



1.3.2. Dual Flow Tube Photolysis .....	17
1.3.3. HRMS Analysis with LTQ-Orbitrap and 21T FTICR .....	18
References .....	19
<b>Chapter 2: Particle and VOC Content of Electronic and Combustion Cigarettes.....</b>	<b>29</b>
2.1. Abstract .....	30
2.2. Introduction .....	31
2.3. Experimental .....	34
2.3.1. Chamber Experiments .....	34
2.3.2. Fast Flow Tube .....	35
2.3.3. Sampling .....	37
2.3.4. Emissions .....	39
2.4. Results and Discussion .....	41
2.4.1. Chamber Experiments .....	41
2.4.2. Real-Time Fast-Flow Tube Data .....	45
2.4.3. E-cigarette Emissions in Continuous Mode .....	56
2.5. Conclusion .....	59
2.6. Impact and Influence in the Field .....	59
References .....	61
<b>Chapter 3: SOA Mediated by Fe (III) Chemistry .....</b>	<b>69</b>
3.1. Abstract .....	70
3.2. Introduction .....	70
3.3. Experimental .....	73

3.3.1. Chemicals .....	73
3.3.2. UV–Vis Spectroscopy and HPLC Experiments .....	74
3.3.3. Mass Spectrometry Experiments .....	75
3.3.4. Particles Characterization .....	76
3.3.5. Acid-Dissolution of Hematite Followed by Reaction with Organic .....	77
3.4. Results and Discussion .....	79
3.4.1. Optical Properties and Time Profile of Reactants and Products .....	79
3.4.2. Product Identification Using LC-ESI-MS/MS .....	91
3.4.3. Formation of Polymeric Catechol and Guaiacol Particles .....	99
References .....	107

**Chapter 4: Molecular Characterization and the Effects of SO<sub>2</sub> on Biodiesel and Diesel Fuel Secondary Organic Aerosol ..... 114**

4.1. Abstract .....	115
4.2. Introduction .....	115
4.3. Experimental .....	119
4.3.1. Fuel Precursor Analysis .....	119
4.3.2. Chamber Generation of SOA .....	120
4.3.3. Filter Collection and Analysis of SOA Particles .....	120
4.4. Results and Discussion .....	122
4.4.1. Fuel Precursors and SOA Generation .....	122
4.4.2. Average Molecular Composition.....	125
4.4.3. Photooxidation of BDSL/DSL Mixture .....	129
4.4.4. Formation of Organosulfur Species with the Addition of SO <sub>2</sub> .....	131

4.4.5. Unique Subset of Organosulfur Species .....	137
4.4.6. Comparison of CHOS Species to Previous Literature .....	141
4.5. Atmospheric Implications .....	143
References .....	145
<b>Chapter 5: Direct Photolysis of <math>\alpha</math>-Pinene Ozonolysis SOA .....</b>	<b>152</b>
5.1. Abstract .....	153
5.2. Introduction .....	153
5.3. Experimental .....	156
5.3.1. Case Studies A–C: Effect of Irradiation on Particle Composition and Size with and without High-Volatility Vapors and Oxidants .....	156
5.3.2. Case Study D: Measurements of Aerosol Size as a Function of Irradiation Time .....	160
5.3.3. Case Study E: Measurements of Aerosol Peroxide Content as a Function of Irradiation Time .....	161
5.4. Results and Discussion .....	164
5.4.1. Studies A–C: Effect of Irradiation on Particle Composition and Size with and without High-Volatility Vapors and Oxidants .....	164
5.4.2. Case Studies D and E: Dual-Flow Cell Experiments .....	168
5.5. Broader Implications .....	173
5.6. Literature Update on the Photolysis of Organic Peroxides in APIN SOA .....	175
References .....	176
<b>Appendices .....</b>	<b>181</b>
<b>Appendix A: SOA Quantification of UV-light Intensity in the Flow Cell .....</b>	<b>181</b>

<b>Appendix B: Negligible Overheating of Aerosol Particles in Flow Cell .....</b>	<b>187</b>
<b>Appendix References .....</b>	<b>191</b>

## List of Acronyms

- **21T-FTICR/uHRMS:** Ultra-high resolution 21 Tesla Fourier transform ion cyclotron resonance mass spectrometry
- **AI:** Aromaticity index
- **AI\*:** Modified aromaticity index;  $AI^* = (1 + C - O^* - 0.5H)/(C - O^*)$
- **APIN:**  $\alpha$ -Pinene ozonolysis SOA
- **AMS:** Aerosol mass spectrometer
- **ATR-FTIR:** Attenuated total reflectance-Fourier transform infrared spectroscopy
- **BDSL:** Biodiesel photooxidized SOA
- **BVOC:** Biogenic VOC
- **CHO:** Species of the general chemical formula  $C_cH_hO_o$  where both  $N = 0$  and  $S = 0$
- **CHON:** Species of the general chemical formula  $C_cH_hO_oN_n$  where  $S = 0$
- **CHONS:** Species of the general chemical formula  $C_cH_hO_oN_nS_s$
- **CHOS:** Species of the general chemical formula  $C_cH_hO_oS_s$  where  $N = 0$
- **CS:** Cigarette smoke
- **DBE:** Double bond equivalency;  $DBE = 1 + C - (H/2) + (N/2)$ ; Where only the organic portion is accounted for; the double bonds due to organosulfate or organosulfonate groups are not included
- **DF:** Dilution factor
- **DLS:** Dynamic light scattering
- **DSL:** Diesel photooxidized SOA

- **E-cigarette:** Electronic cigarette
- **FAMEs:** Fatty acid methyl esters
- **GC:** Gas chromatography
- **GCMS:** Gas chromatography mass spectrometry
- **GC/VUV/MS:** Gas chromatography vacuum ultraviolet high resolution time-of-flight mass spectrometry
- **HPLC:** High performance liquid chromatography
- **HRMS:** High resolution mass spectrometry
- **ICP-MS:** Inductively coupled plasma-mass spectrometry
- **IPN:** Isopropyl nitrite
- **LC-ESI-MS:** Liquid chromatography-electrospray ionization-mass spectrometry
- **LMCT:** Ligand-to-metal-charge transfer
- **Nano-DESI/HRMS:** High-resolution nanospray desorption electrospray ionization
- **NMHCs:** Non-methane hydrocarbons
- **NO<sub>x</sub>:** Nitrogen oxides where ( $\text{NO}_x = \text{NO} + \text{NO}_2$ )
- **NO<sub>y</sub>:** The sum of NO<sub>x</sub> and all the nitrogen compounds produced from NO<sub>x</sub>
- **OA:** Organic aerosols
- **OH:** Hydroxyl radical
- **OS:** Organosulfate
- **PAH:** Polyaromatic hydrocarbon
- **Pb:** Lead
- **PM:** Particulate matter

- **PM<sub>2.5</sub>**: Particulate matter of diameters below 2.5 μm
- **PM<sub>10</sub>**: Particulate matter of diameters below 10 μm
- **POA**: Primary organic aerosols
- **PTR-ToF-MS**: Proton transfer reaction time-of-flight mass spectrometry
- **RH**: Relative humidity
- **SAR**: Structure-activity relationship
- **SEM-EDS**: Scanning electron microscopy-energy dispersive X-ray spectroscopy
- **SMPS**: Scanning Mobility Particle Sizer
- **SOA**: Secondary organic aerosols
- **TME**: 2,3-dimethyl-2-butene
- **ToF-AMS**: Time-of-flight aerosol mass spectrometer
- **UV**: Ultraviolet
- **UV-vis**: Ultra violet-visible
- **VOC**: Volatile organic compound

## List of Figures

†Denotes data that was recorded by our collaborators at Wilfrid Laurier University, Waterloo, Ontario N2L 3C5, Canada.

<b>Figure 1.1</b>	Diagram of a typical combustion cigarette .....	4
<b>Figure 1.2</b>	Diagram of two common designs of e-cigarettes .....	5
<b>Figure 1.3</b>	Rate constants of OH reactivity with several different types of compounds that contain six carbons, along with toluene and naphthalene. The rate constants are in units of $\text{cm}^3 \text{ molecule}^{-1} \text{ s}^{-1}$ .....	10
<b>Figure 1.4</b>	Diagram of the primary ozonide and Criegee intermediates formed in the ozonolysis of $\alpha$ -pinene .....	12
<b>Figure 1.5</b>	Organic peroxides of $\alpha$ -pinene ozonolysis SOA .....	13
<b>Figure 1.6</b>	Diagram of the smog chamber at UCI. SOA is generated by a VOC precursor and reactive gases of interest. In aging experiments, SOA can be sent to the dual flow cell for direct photolysis .....	16
<b>Figure 1.7</b>	Diagram of the dual flow cell. SOA generated from chamber experiments is sent either through a bypass or a denuder train and then photolyzed .....	17
<b>Figure 2.1</b>	Diagram of the fast-flow tube setup, where $F_A$ was the flow rate of either zero air or a puff of smoke delivered at 1.30 L/min; $f_A$ , $f_B$ , and $f_C$ were the volume fractions of a VOC in each region; $R_m$ was the rate ( $\mu\text{g/s}$ ) of a VOC entering the	



flow tube;  $C_x$  was the initial concentration (molecules/cm<sup>3</sup>) of a VOC in the flow tube;  $F_1=F_2$  were dilution flows of zero air (e-cigarette: 5 L/min, cigarette: 10 L/min); and  $\Delta P$  (e-cigarette: 52 torr, cigarette: 2.8 torr) was the pressure difference between sections B and C separated by a 1.25 mm orifice; the pressure difference was precisely set with a valve in section B ..... 36

**Figure 2.2** PTR-ToF-MS mass spectra of well resolved  $[M+H]^+$  peaks for the fifth puff of a 3R4F cigarette: a) CO<sub>2</sub> ( $m/z$  44.998) was not detected, but acetaldehyde ( $m/z$  45.034) was clearly observed; b) both the acrolein ( $m/z$  57.034) and butenes ( $m/z$  57.070) are well resolved ..... 40

**Figure 2.3** Particle size distribution observed after injecting a single puff (from E-cigarette-1, 1R5F, or a 3R4F cigarette) in a Teflon™ chamber filled with zero air. This data set was normalized to the total particle number concentrations data measured directly with the CPC and was then multiplied by the dilution factor ..... 42

**Figure 2.4** Particle size distribution (a), particle concentration, and particle diameter (b), of e-cigarette-1 observed after injecting 4 successive puffs in a Teflon™ chamber filled with zero air. The data were corrected for dilution to reflect the concentrations in the puff volume ..... 44

**Figure 2.5** PTR-ToF-MS time profile of 1R5F at a frequency of 1 puff/min for fast flow tube experiments. The contributions from the individual puffs are clearly resolved with the present time resolution. The first spike near  $t = 0$  corresponds to the 1st puff and there are 9 puffs total ..... 46

**Figure 2.6** CPC time profile of 1R5F at a frequency of 1 puff/min for fast flow tube experiments. The first spike near  $t = 0$  corresponds to the 1st puff and there are 9 puffs total ..... 46

**Figure 2.7** PTR-ToF-MS time profile of e-cigarette-2 at a frequency of 4 puff/min for fast flow tube experiments. As this figure shows, the contributions from different puffs would overlap at higher puff frequencies complicating the quantitative analysis of the PTR-ToF-MS data. Therefore, most PTR-ToF-MS measurements reported in the paper were done at 1 puff/min puffing rate ..... 47

**Figure 2.8** CPC time profile of e-cigarette-2 at a frequency of 4 puff/min for fast flow tube experiments. The first spike near  $t=0$  corresponds to the 1st puff and there are 9 puffs total. Unlike the convoluted PTR-TOF-MS signal shown in Figure 2.7, the CPC signal for each puff was clearly resolved even at the highest puff frequency probed here (4 puff/min) ..... 47

**Figure 2.9** Amount of acrolein (a) and particles (b) per puff for a puff frequency of 1 puff/min measured in fast flow tube experiments ..... 48

**Figure 2.10** Puff frequency dependence of selected VOC emitted by 1R5F in fast flow tube experiments. There is no quantifiable difference in the VOCs in the cigarettes for different puff frequencies ..... 48

**Figure 2.11** Puff frequency dependence of the number of particles emitted in fast flow tube experiments. The particle concentration similarly has no puff frequency dependence except for menthol light-5 and original-5 where the 1 puff/min

frequency had somewhat larger particle emissions than the other frequencies ..... 49

**Figure 2.12** Amount of selected VOCs in an e-cigarette and conventional cigarettes for a puff frequency of 1 puff/min in fast flow tube experiments. The values were based on assuming a cigarette lifetime of 9 puffs ..... 50

**Figure 2.13** Amount of selected VOCs in conventional cigarettes for a puff frequency of 2 puffs/min in fast flow tube experiments ..... 51

**Figure 2.14** Amount of selected VOCs in conventional cigarettes for a puff frequency of 3 puffs/min in fast flow tube experiments ..... 52

**Figure 2.15** Amount of selected VOCs in conventional cigarettes for a puff frequency of 4 puffs/min in fast flow tube experiments ..... 53

**Figure 2.16** The total number of particles emitted per puff by e-cigarettes and conventional cigarettes for 1 puff/min frequency. The values were based on assuming a cigarette lifetime of 9 puffs ..... 57

**Figure 2.17** Gravimetrically determined particle size distributions of e-cigarette-2 at two different dilutions: 1) dilution by 13 and 2) dilution by 190. The latter was close to the dilution used in the fast flow tube experiments ..... 57

**Figure 2.18** VOC and particle content of e-cigarette-2 as a function of puff number during continuous use with a single cartridge (the battery was fully recharged at the beginning of vaping and at each interval (indicated by a vertical line) ..... 58

- Figure 3.1<sup>†</sup>** (a) Representative UV-vis absorbance spectra of the complexes between standard solutions of  $(\text{NH}_4)_2\text{Fe}(\text{SO}_4)_2 \cdot 6\text{H}_2\text{O}$  and 1,10-phenanthroline. (b) Calibration curve constructed from the absorbance at 510 nm from spectra shown in panel (a) .. 79
- Figure 3.2** UV-vis spectra of unfiltered solutions after dark reaction of catechol (0.98 mM) with  $\text{FeCl}_3$  (1:2 organic reactant/Fe molar ratio) at pH 3 as a function of mixing time. Scans were recorded every 3 min. The dark green trace is due to absorbance from primary products and residual catechol. The formation of secondary products appeared as mixing time increased, as well as an unresolved background due to the formation of a colloid ..... 80
- Figure 3.3<sup>†</sup>** Dark reaction of catechol and guaiacol with  $\text{FeCl}_3$  at pH 3: (a and b) digital images of 1:2 organic reactant/Fe molar ratio of unfiltered solutions as a function of time; (c and d) particles on filter after 30 min; (e and f) the corresponding UV-vis spectra after filtration ..... 81
- Figure 3.4<sup>†</sup>** UV-vis spectra of unfiltered solutions after dark reaction and filtration of catechol (0.98 mM) with  $\text{FeCl}_3$  at pH 3 at different ratios a function of time. Digital images of the corresponding unfiltered solutions and particles on filter after 30 min are shown on the right ..... 82
- Figure 3.5<sup>†</sup>** HPLC chromatograms collected at (a) 271 nm and (b) 388 nm for the initial catechol solutions (0.98 mM) and after reaction with  $\text{FeCl}_3$  at pH 3 as a function of reaction time. (c and d). Resulting kinetic curves from the integrated areas of the peaks at 7 min and 17 min. The solution mixture contains 1:2 molar ratio of catechol/Fe ..... 85

**Figure 3.6**<sup>†</sup> (a) and (b) HPLC chromatograms collected for initial catechol solutions (0.98 mM) and after reaction with FeCl<sub>3</sub> at pH 3 as a function of reaction time with a final molar ratio of 1:1. (c) and (d). The resultant kinetic curves from the integrated areas of the peaks at 7 and 17 min for solution mixtures containing 1:1 and 2:1 molar ratio of catechol:Fe ..... 86

**Figure 3.7**<sup>†</sup> (a) HPLC chromatograms collected for initial catechol solutions (0.98 mM) and after reaction with FeCl<sub>3</sub> at pH 3 as a function of reaction time with a final molar ratio of 1:2, and (b) kinetic curves for the product peak at 7 min as a function of detector wavelength. The phrase “detector artifact” refers to the signal at 700 nm for the 17 min peak that does not originate from the catechol standard solution in the absence of iron ..... 87

**Figure 3.8** (a) and (b) HPLC chromatograms using a gradient method collected for initial catechol solutions (0.98 mM) and after reaction with FeCl<sub>3</sub> at pH 3 as a function of reaction time with a final molar ratio of 1:2, and (b) kinetic curves for the catechol peak at 18 min and product peaks at 16 and 22 min as a function of detector wavelength ..... 89

**Figure 3.9** Absorption spectra for unfiltered UV-vis spectra of catechol + FeCl<sub>3</sub> reaction (1:2) for 3 and 40 min mixing times and absorption of catechol and 2 products observed in gradient HPLC experiments..... 90

**Figure 3.10**<sup>†</sup> Total ion and *m/z* 123 LC-ESI-MS/MS negative ion mode chromatograms for the reaction of catechol with FeCl<sub>3</sub>(aq) under acidic conditions after 3 min dark reaction in (a and b) normal water (H<sub>2</sub><sup>16</sup>O) and (c and d) <sup>18</sup>O-labeled water

(H<sub>2</sub><sup>18</sup>O). (a and c, insets) Mass spectra for the major peaks; (b and d, insets) MS/MS spectra for the *m/z* 123 ion ..... 92

**Figure 3.11**<sup>†</sup> Total ion and *m/z* 123 LC-ESI-MS/MS negative ion mode chromatograms for catechol standard solutions under acidic conditions in normal water (H<sub>2</sub><sup>16</sup>O, (a)-(b)) and in water-<sup>18</sup>O (H<sub>2</sub><sup>18</sup>O, (c)-(d)). The insets in (a) and (c) show the mass spectra for the major peaks, and those in (b) and (d) show the MS/MS spectra for the *m/z* 123 ion ..... 93

**Figure 3.12**<sup>†</sup> Chromatograms for *m/z* 123 of reference compounds 1,2,4-benzotriol and pyrogallol under acidic conditions in normal water (H<sub>2</sub><sup>16</sup>O). The insets show the MS/MS spectra for the *m/z* 123 fragment ..... 96

**Figure 3.13**<sup>†</sup> HPLC chromatogram collected for 1 mM standard solution of 1,2,4-benzotriol at pH 3 ..... 96

**Figure 3.14** SEM images for (a) polycatechol and (b) polyguaiacol collected on copper grids after a 90 min dark reaction of catechol with FeCl<sub>3</sub> at pH 3 in a 1:2 molar ratio ..... 99

**Figure 3.15** DLS measurements of the average particle size of polycatechol and polyguaiacol as a function of reaction time during the dark reaction of catechol with FeCl<sub>3</sub> at pH 3 in a 1:2 molar ratio ..... 99

**Figure 3.16**<sup>†</sup> ATR-FTIR absorbance spectra of (a) solid polycatechol (bottom) and polyguaiacol (top) deposited on a ZnSe ATR crystal from a water/ethanol slurry followed by drying overnight, and (b) 0.1 M aqueous solution ..... 102

<b>Figure 3.17<sup>†</sup></b>	Formation of polycatechol and polyguaiacol from reaction with dissolved iron from acid-promoted hematite dissolution .....	104
<b>Figure 3.18</b>	Mass-normalized absorption coefficient (MAC) plot for the reaction of 1 mM catechol with FeCl <sub>3</sub> after 3 min dark reaction at pH 3 (unfiltered solution). The final reaction mixture contained 1:2 molar ratio catechol:Fe. The MAC values were calculated from Eq. (1) and it was not corrected for the contribution from scattering by particles in solution .....	105
<b>Figure 4.1</b>	Mass fraction of species in diesel fuel from GC/VUV/MS analysis as a function of the carbon number of detected molecules. Species are stacked in the bar graph such that the height of the combined bars for a specific C <sub>n</sub> represents the mass fraction.....	122
<b>Figure 4.2</b>	Time profile of SOA formation from sample 1, DSL/NO <sub>x</sub> . Time zero corresponds to turning on the UV lamps. The AMS sampled throughout the entire experiment; particle sampling for high-resolution analysis started after 200 minutes of photooxidation when the particle mass concentration reached the maximum ..	124
<b>Figure 4.3</b>	a) Uncorrected yield and b) particle number-weighted geometric mean particle diameter of the SOA generated in the chamber. The index corresponds to the sample number in Table 1 (samples 6 and 7 are from BDSL, samples 8 and 9 are from the DSL/BDSL mixture, and the rest of the samples are from DSL). The samples are colored by the presence of SO <sub>2</sub> and NH <sub>3</sub> .....	124

<b>Figure 4.4</b>	Comparison of aromatic species in diesel fuel and DSL SOA. Mass fraction of aromatics and PAHs of diesel fuel a) and mass spectral relative intensities of the dry b) and humid c) DSL SOA samples are overlaid in bar plots. Relative intensities of SOA samples are normalized to fractions such that the sum of relative intensities of all of the peaks in an individual sample is 1; the relative intensities of mass spectral peaks of the same Cn were added ..... 128
<b>Figure 4.5</b>	21T-FTICR/uHRMS spectra of observed peaks and new peaks in MIX/NO <sub>x</sub> /SO <sub>2</sub> and a calculated spectrum of a linear combination of DSL/NO <sub>x</sub> /SO <sub>2</sub> and BDSL/NO <sub>x</sub> /SO <sub>2</sub> fit to overlapping peaks with the MIX/NO <sub>x</sub> /SO <sub>2</sub> sample ..... 130
<b>Figure 4.6</b>	The difference 21T-FTICR/uHRMS spectra between observed and calculated MIX/NO <sub>x</sub> /SO <sub>2</sub> . New and lost peaks of individual samples relative to the observed sample are also plotted. Note the change in scale relative to Figure 4.4. .... 130
<b>Figure 4.7</b>	Venn diagrams of the overlap of peaks between DSL/NO <sub>x</sub> /SO <sub>2</sub> (A), BDSL/NO <sub>x</sub> /SO <sub>2</sub> (B), and MIX/NO <sub>x</sub> /SO <sub>2</sub> (C) weighted by a) the <i>number</i> of peaks and b) the <i>intensity</i> of peaks ..... 131
<b>Figure 4.8</b>	The effect of SO <sub>2</sub> addition on the nano-DESI/HRMS spectra of diesel fuel SOA (longer denuder samples 10 (a), 11 (b), and 12 (c)). The peaks are colored by elemental composition. Pie charts are intensity-weighted elemental composition of the peaks ..... 133
<b>Figure 4.9</b>	nano-DESI/HRMS spectra of diesel fuel SOA a) sample 1 (DSL/NO <sub>x</sub> ) and b) sample 2 (DSL/NO <sub>x</sub> /SO <sub>2</sub> ) colored by composition. Pie charts are intensity weighted percent CHONS composition of peaks ..... 134



- Figure 4.10** nano-DESI/HRMS spectra of diesel fuel SOA high humidity a) sample 4 (DSL/NO<sub>x</sub>/RH) and b) sample 5 (DSL/NO<sub>x</sub>/SO<sub>2</sub>/RH) colored by composition. Pie charts are intensity weighted percent CHONS composition of peaks ..... 134
- Figure 4.11** nano-DESI/HRMS spectra of mixed fuel SOA a) sample 8 (MIX/NO<sub>x</sub>) and b) sample 9 (MIX/NO<sub>x</sub>/SO<sub>2</sub>) colored by composition. Pie charts are intensity weighted percent CHONS composition of peaks..... 134
- Figure 4.12** nano-DESI/HRMS spectra of biodiesel SOA samples a) 6 (BDSL/NO<sub>x</sub>) and b) 7 (BDSL/NO<sub>x</sub>/SO<sub>2</sub>) colored by composition. Pie charts are intensity weighted percent CHONS composition of peaks ..... 134
- Figure 4.13** Bar plot of AMS sulfate to organics data for SO<sub>2</sub> containing fuel SOA samples..... 135
- Figure 4.14** Double bond equivalent (DBE) as a function of carbon number (C<sub>n</sub>) for diesel fuel SOA samples a) 10, b) 11, and c) 12. The intensities of peaks with a specific C<sub>n</sub> and DBE were summed and then the marker size was weighted by this. Trend lines for specific types of species with increasing C<sub>n</sub> are plotted in color. The chemical formulas and DBE equations for these are as follows: graphene, C<sub>n</sub>, DBE = 1 + C; cata-PAHs, C<sub>2n-6</sub>H<sub>(c+6)/2</sub>, DBE = 0.75·C<sub>n</sub>; polyenes, C<sub>n</sub>H<sub>n+2</sub>, DBE = 0.5·C<sub>n</sub>; terpenes, C<sub>5n</sub>H<sub>8n</sub>, DBE = 0.2·C<sub>n</sub> + 1; saturated compounds, C<sub>n</sub>H<sub>2n+2</sub>, DBE = 0. .... 136
- Figure 4.15** Van Krevelen diagrams of CHOS species (CHO and CHONS not shown) for a) sample 11 (DSL/NO<sub>x</sub>/SO<sub>2</sub>, long denuder) and b) sample 12 (DSL/NO<sub>x</sub>/SO<sub>2</sub>-high,

long denuder).  $O^*$  is the number of oxygen atoms minus 3 to emphasize the degree of oxidation that is not due to the sulfate group addition. Unique aliphatic CHOS species, distinguished by  $O^* < 4$  and  $DBE < 3$ , are shown in red ..... 139

**Figure 4.16** Kendrick mass defect  $CH_2$  plot for CHOS species of DSL/ $NO_x$ / $SO_2^a$ , sample 11. The mass spectral peaks are colored by DBE and shaped by the total number,  $x$ , of oxygen atoms (as  $SO_x$ ). Prominent families are labeled with general chemical formulas ..... 140

**Figure 4.17** Carbon number distribution for CHOS species observed by Tao et al. (2014), Riva et al. (2015), and Riva et al. (2016) where points are colored by source. The data from this study for the diesel SOA sample 2 ( $\times$ 's) are only included in the plot when the formula overlaps with one of the formulas previously reported in the literature. The size of the  $\times$  is weighted by  $\text{Log}(\text{Intensity} \cdot 10)$  ..... 142

**Figure 5.1** Ozone signal as measured before and after the denuder train. The monitor was moved between 16 and 30 minutes. The charcoal denuders remove ozone such that resulting concentrations are below detection limits. The denuder efficiency for ozone is greater than 400 ppb ..... 157

**Figure 5.2** PTR-ToF-MS data showing the removal of VOCs after passing through the denuder and the generation of methanol upon photolysis of  $\alpha$ -pinene ozonolysis SOA. The decay of  $\alpha$ -pinene upon reaction with ozone is also evident. Pinonaldehyde is slow to respond due to its propensity to absorb to PTR-ToF-MS transfer line tubing ..... 157

- Figure 5.3** Wavelength dependence of the UV-light used to photolyze the aerosol. The intensities are scaled by using the isopropyl nitrite actinometer to quantify the power of the lamps. The majority of the intensity is carried by the 312 nm line. The amount of radiation from wavelengths below 300 nm is negligible (note the logarithmic scale). Radiation above 350 nm does not significantly contribute to photolysis because of the low absorption cross sections of SOA at these wavelengths ..... 158
- Figure 5.4** The required reaction time (5 hours) for an upper limit concentration of a 44.0  $\mu\text{M}$   $\text{H}_2\text{O}_2$  standard (black) and an  $\alpha$ -pinene SOA (APIN SOA) sample concentration of 8.50  $\mu\text{g/ml}$  (blue) to finish reacting with the KI solution..... 163
- Figure 5.5** Calibration of  $\text{H}_2\text{O}_2$  solutions to the absorption of  $\text{I}_3^-$  at 351 nm. The extracted molar extinction coefficient is 26,710  $\text{M}^{-1} \text{cm}^{-1}$  ..... 163
- Figure 5.6** Number concentration, median mobility-equivalent diameter, and mass concentration estimated from the mobility measurements in the flow cell. The black line at time = 0 indicates when the lights were turned on. The points denoted with solid markers were acquired when the lights were on. Empty markers indicate that the lights were off during that point in the experiment. Lights were turned off after a different period in each of the three case studies ..... 164
- Figure 5.7** Fraction of signal attributed to purely hydrocarbon fragments and oxygenated hydrocarbon fragments during aerosol irradiation in case study A (the fractions do not add to 1; the remainder corresponds to fragments that do not contain carbon

atoms). Average O/C corresponding to the left axis and average H/C corresponding to the right axis are also shown for the same experiment. The initial black line represents the time where the lights were turned on. The second black line indicates the time that the lights were turned off ..... 166

**Figure 5.8** Average oxygen to carbon ratio (O:C) of the SOA from the ToF-AMS before and after photolysis for all three case studies. The change in the O:C ratio is approximately the same in all cases. This observation implies that photochemistry of gas-phase compounds (which are present in case B and reduced substantially in case A) has an insignificant effect on particle composition compared to the condensed-phase photochemical processes occurring in the particles..... 167

**Figure 5.9** Change in median mobility-equivalent diameter as a function of aerosol residence time inside the flow cell (left y-axis). The percent change in the geometric standard deviation-between the dark and light flow cell-normalized by the median mobility-equivalent diameter is shown on the right y-axis. The red x-axis,  $\tau_{\text{atm}}$ , shows the corresponding atmospheric irradiation time at a solar zenith angle of  $65^\circ$ . The gray line is a linear-least-squares fit of the data. Dash gray lines indicate the bounds of the fit considering the uncertainty in the fitting constants ..... 169

**Figure 5.10** Fraction of peroxide remaining on a molar basis [moles remaining after UV exposure/mol present before UV exposure] in SOA after exposure to UV light. Exposure to laboratory UV light is shown on the black x-axis. The red x-axis

shows the corresponding atmospheric irradiation time at a solar zenith angle of 65° ..... 171

**Figure 5.11** Aerosol peroxide lifetime in the atmosphere in Los Angeles, CA (34° latitude) as a function of month. The increase in the lifetime in winter months is due to the drastic reduction in the 24-hour average solar zenith angle ..... 174

**Figure A.1** Change in relative concentration of isopropyl nitrite after the UV-lamps were turned on measured with the PTR-ToF-MS. For this experiment, the residence time in the flow cell was one hour. The flux is determined from comparison of the steady-state values of IPN before and after photolysis, as described below ..... 182

**Figure A.2** Absorption cross section of IPN and the molar extinction coefficient of  $\alpha$ -pinene ozonolysis SOA ..... 185

**Figure A.3** Action spectrum for IPN light absorption from the UV-lamp ..... 186

**Figure A.4** Action spectrum for SOA light absorption from the UV-lamp ..... 186

**Figure A.5** Action spectrum for SOA light absorption from sunlight at a solar zenith angle of 65° ..... 186

**Figure B.1** The normalized change in signal for seven key unit-masses as measured by the ToF-AMS. The upper pane details changes in these key masses when the SOA is photolyzed (time = 0) and the lamps are turned off (indicated by the second vertical black line). The lower pane details changes when the SOA is heated by

4.4°C inside the flow cell. The second vertical black line indicates when the heat source was removed ..... 188

## List of Schemes

- Scheme 3.1** Chemical structures of (I) catechol, (II) guaiacol, (III) catechol-Fe complex, (IV) o-quinone, (V) 3,3'-dimethoxy-4,4'-biphenyldiol, (VIa) 3,3'-dimethoxy-4,4'-biphenoquinone, (VIb) 3,5'-dimethoxy-4,4'-biphenoquinone, (VII) 1,2,4-benzenetriol, and (VIII) pyrogallol ..... 73
- Scheme 3.2** Suggested mechanism for catechol oxidation and polycatechol formation in the presence of excess Fe(III) in the dark under acidic conditions ..... 90
- Scheme 3.3** Suggested mechanism for the oxidation of (a) catechol and (b) 1,2,4-benzenetriol induced in the ESI chamber by O<sub>2</sub>(aq) explaining the origin of the *m/z* 123 with the same fragmentation pattern for both chemicals ..... 95

## List of Tables

<b>Table 2.1</b>	Tar and nicotine content of e-cigarettes and conventional cigarettes. Cigarettes were numbered to differentiate between brands. E-cigarette-1 contained propylene glycol with a voltage of 3.6 V and e-cigarette-2 contained vegetable glycerin with a voltage of 3.7 V. Charcoal-3 and charcoal-4 cigarettes have a charcoal mass loading of 37 mg and 50 mg. All cigarettes were contained in hard pack boxes except for the unfiltered-6 cigarette ..... 38
<b>Table 2.2</b>	Emitted masses of acrolein measured in chamber experiments ..... 44
<b>Table 2.3</b>	Amount ( $\mu\text{g}$ in 9 puffs) of selected VOCs emitted by an e-cigarette and conventional cigarettes for a puff frequency of 1 puff/min in fast flow tube experiments. Numbers in parentheses represent standard deviations for n=3 samples ..... 50
<b>Table 2.4</b>	Amount ( $\mu\text{g}$ in 9 puffs) of selected VOCs emitted by conventional cigarettes for n=3 samples and (standard deviation) for a puff frequency of 2 puffs/min in fast flow tube experiments ..... 51
<b>Table 2.5</b>	Amount ( $\mu\text{g}$ in 9 puffs) of selected VOCs emitted by conventional cigarettes for n=3 samples and (standard deviation) for a puff frequency of 3 puffs/min in fast flow tube experiments ..... 52



<b>Table 2.6</b>	Amount ( $\mu\text{g}$ in 9 puffs) of selected VOCs emitted by conventional cigarettes for $n=3$ samples and (standard deviation) for a puff frequency of 4 puffs/min in fast flow tube experiments .....	53
<b>Table 3.1</b>	Intensity ratios of major peaks observed in the mass spectra of catechol and iron chloride solution with different ratios at pH 3 at a given different retention times .....	97
<b>Table 4.1</b>	Experimental conditions for chamber generated fuel SOA. Sample number, sample code name, reactant concentrations, relative humidity (RH), and SOA mass concentration are listed. The SOA mass concentrations are reported as maxima reached at the end of photooxidation (3 hr) .....	121
<b>Table 4.2</b>	Average molecular formulas and ratios of SOA samples from nano-DESI/HRMS spectra. Data for samples that were also recorded with 21T-FTICR/uHRMS are provided in parentheses .....	126
<b>Table 4.3</b>	Composition of species in SOA samples from nano-DESI/HRMS spectra. Data for samples that were also recorded with 21T-FTICR/uHRMS are provided in parentheses .....	133
<b>Table 4.4</b>	Percent CHOS species and percent subsets of CHOS species for each sample. Percent CHOS for each sample are weighted by the sum of the intensity of <i>all</i> peaks within that sample. The subsets of CHOS species are weighted by the sum of the intensity of <i>only CHOS</i> peaks for each sample: aliphatic (A), $\text{C}_c\text{H}_h\text{SO}_3$ (B),	

$C_cH_hSO_4$  (C), and aromatic (D) with an average aromatic index (AI\*). An “x” denotes that peaks of that specific type were not observed ..... 138

**Table 5.1** Summary of Experimental Conditions ..... 160

## Acknowledgements

I would like to acknowledge a variety of influential people that have provided me with invaluable support during the journey of an important chapter of my life.

I am extremely grateful to my adviser, Professor Sergey Nizkorodov, for guidance in my graduate career, supporting my “Rosie the Riveter” approach to research, patience in listening to my exponentially increasing line of thinking, and whose excitement for chemistry and teaching is very contagious. Sergey allowed me to take advantage of the instrumentation resources offered within our research group, at the University of California, Irvine facilities, and with collaborators at the Pacific Northwestern National Laboratory. I was also able to share my research at multiple conferences each year with his support. Without his mentorship, this dissertation would not be possible. I would also like to thank my committee members, Professor Barbara Finlayson-Pitts and Assistant Professor Craig Murray, for their support and suggestions throughout the research and writing of this thesis.

In addition, a thank you to Dr. Alexander Laskin, Dr. Julia Laskin, and Dr. Peng Lin for their collaboration at the Pacific Northwestern National Laboratory and for generously allowing me instrument time.

I would like to thank colleagues that I have collaborated with during my graduate career. I had a great time working with a previous post doctoral fellow, Dr. Scott Epstein, on projects including the direct photolysis of  $\alpha$ -pinene ozonolysis SOA and the composition of cigarettes. We were able to combine our diverse ways of thinking, from a chemist’s and a chemical engineer’s line of reasoning, to approach a scientific problem, to design and carryout experiments, and to publish the results. I am thankful to Amanda MacMillan for collaboration in

the fuel SOA project and, more personally, for her continued encouragement and support as a fellow female scientist. I would also like to thank Professor Hind Al-Abadleh from the Wilfrid Laurier University for allowing me to collaborate with her on the iron mediated SOA project. Hind's high energy and drive for atmospheric chemistry was refreshing and motivational.

Financial support was provided by the University of California, Irvine Chemistry Department, the University of California, Irvine Chancellor's Club for Excellence Fellowship, the University of California, Irvine Dissertation Fellowship, the University of California, Irvine Associated Graduate Students' Travel Grant, the American Association of Aerosol Research Travel Grant, NSF Grant CHE-0909227, NSF Grant AGS-1227579, and NCI of NIH Grant R21CA164540.

I would like to thank the Chemistry Department at the California State University, Chico for becoming a home away from home during my undergraduate career. I was provided with many job and research opportunities to financially support myself and to grow as a chemist. Professors within the Chemistry Department were very understanding of and accommodating to my busy schedule of juggling classes, part-time jobs, and laboratory work. With their help, I was able to access resources even on weekends and holidays. Professor David Ball offered me my first research opportunity in his organic chemistry laboratory and was very supportive during my beginning stages as a growing chemist. I later worked with Professor Randy Miller who introduced me to Physical Chemistry and had an enthusiasm for teaching with a lasting effect. My studies at the California State University, Chico greatly prepared me for my graduate career.

I especially thank my mom, Donna Blair, for believing in me.

# Curriculum Vitae

Sandra Blair

## Education and Research:

- 2016**                    **Ph.D. in Chemistry**, University of California – Irvine
- 2014-2015**            **Visiting Scholar** at the Environmental Molecular Sciences Laboratory,  
Pacific Northwestern National Laboratory
- 2014**                    **M.S. in Chemistry**, University of California – Irvine
- 2010-2016**            **Graduate Research Assistant** in the Sergey Nizkorodov Research Group,  
University of California – Irvine
- 2010**                    **B.S. in Chemistry** *with honors*, California State University-Chico
- 2009-2010**            **Undergraduate Research Assistant**, in the Randy Miller Group,  
California State University-Chico
- 2009**                    **Undergraduate Research Assistant**, in the Microbial Biochemistry  
Laboratory, California State University-Chico
- 2007**                    **Undergraduate Research Assistant**, in the David Ball Group, California  
State University-Chico

## Awards and Honors:

- 2015**                    **Chancellor's Club Fund for Excellence Fellowship**, UC Irvine Graduate  
Division
- 2015**                    **Regent's Dissertation Fellowship**, UC Irvine Department of Chemistry
- 2014**                    **Michael E. Gebel Award**, UC Irvine Department of Chemistry
- 2009**                    **Chemistry Summer Research Institute Fellowship**, CSU - Chico  
Department of Chemistry
- 2009**                    **Physical Chemistry Award**, CSU - Chico Department of Chemistry
- 2009**                    **Physical Chemistry Grover Willis Award**, CSU - Chico Department of  
Chemistry
- 2009**                    **Integrated Laboratory Award**, CSU - Chico Department of Chemistry

- 2009** “**Best in Category**” **Poster Award** at the 13<sup>th</sup> Annual Student Research Poster Symposium, CSU - Chico Department of Biological Sciences
- 2006** **Chemistry Summer Research Institute Fellowship**, CSU - Chico Department of Chemistry
- 2006** **General Chemistry Award**, CSU - Chico Department of Chemistry
- 2006** **Golden Member of the Student Affiliates of the American Chemical Society Club Award**, CSU - Chico Department of Chemistry

### **Publications:**

- 6.** **Blair, S. L.**; MacMillan, A. C.; Drozd, G. T.; Goldstein, A. H.; Lin, P.; Laskin, A.; Laskin, J.; Nizkorodov, S. A. Molecular Characterization of High NO<sub>x</sub> Biodiesel and Diesel Fuel SOA and the Effects of SO<sub>2</sub>. (2016) [*Submitted to Environ. Sci. Technol.*].
- 5.** **Blair, S. L.**; Epstein, S. A.; Nizkorodov, S. A.; Staimer, N. A Real-Time Fast-Flow Tube Study of VOC and Particulate Emissions from Electronic, Reduced-Harm, Conventional, and Reference Cigarettes. *Aerosol Sci. Technol.* 2015, 49 (9), 816-827.
- 4.** Slikboer, S.; Grandy, L.<sup>‡</sup>; **Blair, S. L.**<sup>‡</sup>; Nizkorodov, S. A.; Smith, R.; and Al-Abadleh, H. A. Formation of Light Absorbing Soluble Secondary Organics and Insoluble Polymeric Particles from the Dark Mixing of Catechol and Guaiacol with Fe(III). *Environ. Sci. Technol.* 2015, 49 (13) 7793-7801. <sup>‡</sup> *These authors contributed equally*
- 3.** Shrestha, M.; Zhang, Y.; Upshur, M. A.; Liu, P.; **Blair, S. L.**; Wang, H.; Nizkorodov, S. A.; Thomson, R. J.; Martin, S.T.; Geiger, F. M. On surface order and disorder of  $\alpha$ -pinene secondary organic material. *J. Phys. Chem. A.* 2014, 119 (19), 4609-4617.
- 2.** Shemesh, D.; **Blair, S. L.**; Nizkorodov, S. A.; Gerber, R. B. Photochemistry of aldehyde clusters: cross-molecular versus unimolecular reaction dynamics. *Phys. Chem. Chem. Phys.* 2014, 16 (43), 23861-23868.
- 1.** Epstein, S. A.; **Blair, S. L.**; Nizkorodov, S. A. Direct photolysis of  $\alpha$ -pinene ozonolysis secondary organic aerosol: Effect on particle mass and peroxide content. *Environ. Sci. Technol.* 2014, 48 (19), 11251-11258.

### **Publications in Preparation:**

2. **Blair, S. L.**; Lawrence, C; Washton, N.; Nizkorodov, S. A. 2D NMR Spectroscopy as a probe to alpha-Pinene SOA Photochemistry. *In Prep for Environ. Sci. Technol. (2016)*
  
1. **Blair, S. L.**; MacMillan, A. C.; Lin, P.; Laskin, A.; Laskin, J.; Nizkorodov, S. A. Photochemistry of High NO<sub>x</sub> Biodiesel and Diesel Fuel SOA. *In Prep for Environ. Sci. Technol., **Submission, draft complete, final edits stage (2016)***

## **Abstract of the Thesis**

Composition and Photochemistry of Anthropogenic and Biogenic Organic Aerosols

By

Sandra Louise Blair

Doctor of Philosophy in Chemical and Materials Physics-Chemistry

University of California, Irvine, 2016

Professor Sergey Nizkorodov, Chair

Aerosols can substantially impact human health, atmospheric chemistry, and climate. The composition and photochemistry of a variety of anthropogenic and biogenic primary and secondary organic aerosols (POA and SOA) have yet to be fully characterized. The composition of organic aerosols is extremely complex - they contain a variety of highly oxidized, multifunctional, low vapor pressure organic compounds. The primary focus of this thesis is on the molecular characterization of organic aerosols that are not well understood or have not been studied before, such as primary emissions from electronic cigarettes, iron (III) mediated SOA, and photooxidized biodiesel and diesel fuel SOA. Another focus of this dissertation is the effect of direct photochemical aging on the composition of organic aerosol. Direct photolysis experiments were first applied to a system that is known to have a photolabile composition, alpha-pinene ozonolysis SOA, such that characterization of a photochemical effect would be possible to quantify. Photolysis of more complex SOA that have not been studied before, photooxidized biodiesel and diesel fuel SOA, were also investigated in this thesis. Advanced high resolution mass spectrometry techniques were used in the molecular characterization of organic aerosols, including nano-Desorption Electrospray Ionization Mass Spectrometry (nano-



DESI) and Fourier Transform Ion Cyclotron Resonance Mass Spectrometry (FTICR). An additional suite of online instrumentation was used to measure gas-phase composition, particle-phase composition, particle size and concentration, and absorption properties: Proton Transfer Reaction Time-of-Flight Mass Spectrometry (PTR-ToF-MS), Aerosol Mass Spectrometry (ToF-AMS), Scanning Mobility Particle Sizing (SMPS), and UV-vis spectroscopy. The molecular analysis of these aerosols provides valuable insight to the formation and photochemical behavior of unexpected, polymeric, light absorbing, and unique organosulfur species.

## Chapter 1: Introduction

Portions of this chapter were reproduced in part by permission from:

Blair, S. L.; Epstein, S. A.; Nizkorodov, S. A.; Staimer, N., A Real-Time Fast-Flow Tube Study of VOC and Particulate Emissions from Electronic, Potentially Reduced-Harm, Conventional, and Reference Cigarettes. *Aerosol Science and Technology* **2015**, *49* (9), 816-827. Copyright © 2015 Taylor & Francis.

Figure 1.1 was reproduced by permission from:

Streller, S.; Roth, K. *ChemViews Mag.* **2015**. DOI: 10.1002/chemv.201400135. Copyright © Wiley-VCH Verlag GmbH & Co. KGaA, Weinheim.

Figure 1.2 was reproduced by permission from:

Drenkard, Scott, Vapor Products and Tax Policy. *Tax Foundation Publications* March 22<sup>nd</sup> **2016**. Retrieved from: <http://taxfoundation.org/article/vapor-products-and-tax-policy>. Copyright © 1937-2016 Tax Foundation.

Chemical equations in this chapter were adapted from:

Finlayson-Pitts, B. J.; Pitts Jr, J. N., CHAPTER 6 - Rates and Mechanisms of Gas-Phase Reactions in Irradiated Organic - NO<sub>x</sub> - Air Mixtures. In *Chemistry of the Upper and Lower Atmosphere*, Academic Press: San Diego, **2000**; pp 179-263.

## 1.1. Background

### 1.1.1. Atmospheric Organic Aerosols (OA)

Air pollutants, such as particulate matter (PM) and toxic gases, have harmful effects on human health, atmospheric chemistry, and climate.<sup>1</sup> The regulated criteria pollutants are PM<sub>2.5</sub> (particles with diameter below 2.5 μm) and PM<sub>10</sub> (particles with diameter below 10 μm), ozone (O<sub>3</sub>), carbon monoxide (CO), sulfur dioxide (SO<sub>2</sub>), and lead (Pb). PM is known to have negative cardiovascular, respiratory, morbidity, and mortality effects and is suggested to also cause reproductive and developmental problems, impaired cognitive abilities, and cancer.<sup>2-4</sup> There is no “golden standard” solution that will predict the health outcome of multi-pollutant exposures or, alternatively, predict the multiple source emissions responsible for a particular state of health; some metrics are additive while others may behave in a synergistic or antagonistic manner.<sup>5</sup> The World Health Organization estimated that 3.7 million deaths globally were attributed to PM<sub>10</sub> from ambient air pollution of 2012.<sup>6</sup> In addition to health effects, particles can affect the climate directly by absorbing or scattering solar radiation and indirectly by acting as cloud condensation nuclei, and can dramatically reduce visibility.<sup>7</sup>

PM contains many different types of compounds including sulfates, nitrates, organics, ammonium, and chlorides.<sup>8</sup> Organic aerosols (OA) represent a significant and sometimes the major component of PM<sub>2.5</sub> and PM<sub>10</sub>,<sup>9-11</sup> providing up to 90% of the submicron particle mass.<sup>12-15</sup> The composition of OA is extremely complex - they contain a variety of highly oxidized, multifunctional, low vapor pressure organic compounds. OAs that are directly emitted into the atmosphere, such as those emitted by cigarettes and vehicles, are defined as primary organic aerosols (POA). Oxidation of volatile organic compounds (VOCs) in the atmosphere form low vapor pressure multifunctional organics that condense into secondary organic aerosols (SOA),

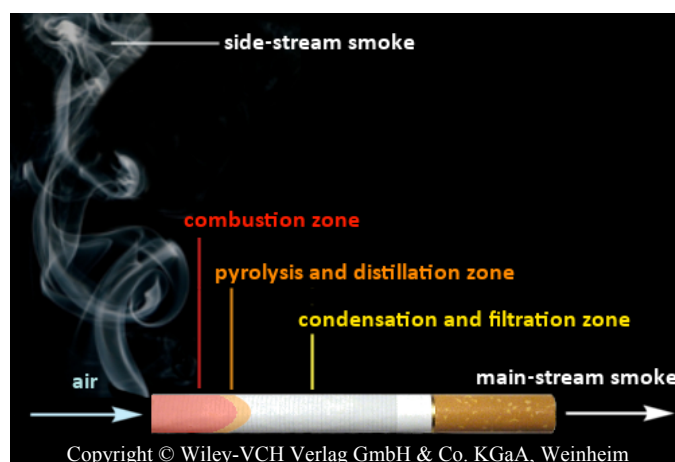
which often dominate the overall contribution to OA. POA and SOA can be aged further in heterogeneous processes such as oxidation by atmospheric free radicals ( $\text{OH}^{16}$  and  $\text{NO}_3^{17}$ ) and  $\text{O}_3$ ,<sup>18</sup> acid-catalyzed oligomer formation<sup>19</sup> and cyclization,<sup>20</sup> and photochemical processes.<sup>21</sup> The complexity of OA generally increases as it ages, which makes its characterization a challenging task. Measurement challenges in the composition of OA are primarily speciation and time resolution.<sup>1</sup> Therefore, it is important to understand the abilities and limitations of various forms of aerosol instrumentation in the determination of the chemical composition of OA, and to apply the best analytical tool to a specific system of interest.

### **1.1.2. Primary Emissions of Combustion and Electronic Cigarettes**

Cigarette smoke causes both indoor and outdoor air pollution.<sup>22</sup> The smokers get exposed to exceedingly high concentrations of PM and VOC ( $> 1 \text{ mg m}^{-3}$ ),<sup>23, 24</sup> which are orders of magnitude higher than concentrations of comparable air pollutants in a typical urban environment. People living in the immediate proximity to the smokers get exposed to so-called “second-hand smoke” that is emitted by the burning cigarettes or exhaled by the smoker. Finally, people who enter the environments previously exposed to tobacco smoke are subjected to “third-hand smoke” that slowly desorbs from the indoor surfaces.<sup>25, 26</sup>

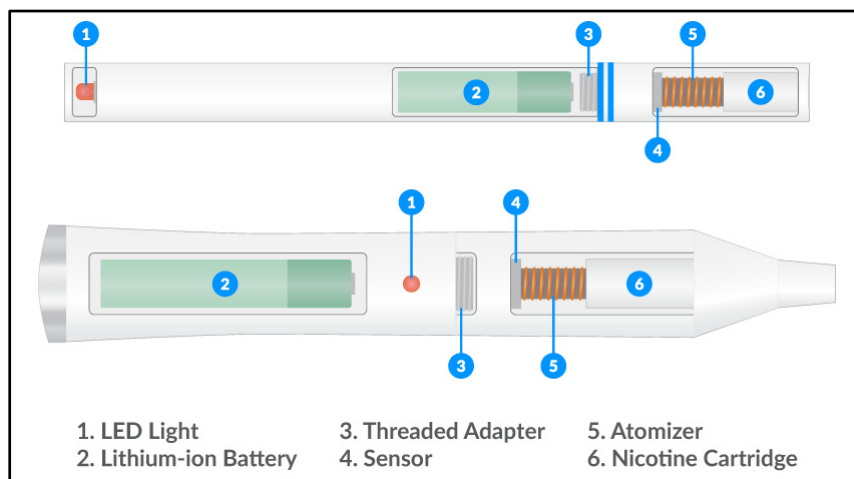
Mainstream smoke (the one the smoker would inhale directly) of combustion cigarettes has been well studied and characterized over the past several decades.<sup>27</sup> A diagram of a typical combustion cigarette is seen in Figure 1.1. Some of the processes that result from lighting a cigarette include combustion, pyrolysis, distillation, condensation, and filtration. Tobacco smoke has been found to contain ~4800 substances.<sup>28</sup> The gaseous components of cigarette smoke include carbon monoxide, acetaldehyde, methane, hydrogen cyanide, nitric acid, acetone, acrolein, ammonia, methanol, hydrogen sulfide, hydrocarbons, gas phase nitrosamines, and

carbonyl compounds.<sup>29</sup> Particulate phase constituents contain carboxylic acids, phenols, water, humectants, nicotine, terpenoids, paraffin waxes, tobacco-specific nitrosamines, PAHs, and catechols.<sup>29</sup> The complex composition of tobacco smoke has been known to cause or contribute to the development of lung, liver, colorectal, prostate, and breast cancer, diseases of nearly all of the organs in the body, and other outcomes such as inflammation, impaired immune system, congenital malformations, and erectile dysfunction, etc.<sup>30, 31</sup> Cigarettes mainly vary by tobacco blend, the presence or absence of filter, filter type, ventilation, flavor additives, and sometimes by diameter and length. Some cigarettes even have a combination of several filters that are of different types. Commonly used filters for the removal of particles and VOCs are cellulose acetate filters and charcoal filters. Cigarettes containing filters have been referred to as “reduced harm” cigarettes because the filters remove some particles and VOCs. This claim is generally misleading to consumers because filters do not have a 100% efficiency in the removal of particles and VOCs.<sup>32</sup>



**Figure 1.1.** Diagram of a typical combustion cigarette.<sup>33</sup>

As a more recent development in 2003, an electronic cigarette (e-cigarette) was invented and for years was advertised as “safe” smoking.<sup>34</sup> Its design (Figure 1.2) differs greatly from any previous cigarette in that it does not contain tobacco; puffing on the device leads to volatilization of nicotine at elevated temperatures, but in the absence of any combustion. This mode of cigarette use is often referred to as “vaping” instead of “smoking”. Tobacco of the conventional cigarette was replaced by a liquid cartridge that contained water, propylene glycol and/or vegetable glycerin, flavoring additives, and nicotine in the e-cigarette; combustion was replaced by vaporization.<sup>35</sup> Although e-cigarettes were advertised as only a physical process of vaporizing liquid solutions, it was found to be more complex. Oxidized versions of components of the liquid cartridges were found in the emissions of e-cigarettes and explained by electrochemistry from the battery voltage.<sup>36, 37</sup> Some of these oxidized species include harmful reactive carbonyls such as acrolein, acetaldehyde, and formaldehyde.<sup>37</sup> Therefore it is important to compare the emissions from combustion cigarettes and e-cigarettes and investigate their behavior under different smoking conditions.



**Figure 1.2.** Diagram of two common designs of e-cigarettes.<sup>38</sup>

### **1.1.3. Aqueous Iron Chemistry**

Iron is a key element in biology needed for building a number of essential proteins. The biological activity in remote ocean waters is often iron-limited. Transport of mineral dust from the continents is an important mechanism of delivery of bioavailable iron to the remote oceans; other contributions may include anthropogenic sources, biomass burning, hydrothermal vents, and release from ocean sediment.<sup>39</sup> Once dissolved on the ocean surface, iron may be removed by biological uptake and through abiotic particle scavenging.<sup>40</sup> The chemical reactivity of iron depends on several factors: solubility, redox conditions, UV light, pH, and temperature.<sup>39</sup> Aside from the well known Fenton chemistry where hydrogen peroxide reacts with Fe(II) to produce Fe(III) and radicals that can degrade soluble organic matter, dissolved iron can form complexes with organic ligands.<sup>41</sup> This chemistry has been observed to behave differently between bulk and surface reactions. Tofan-Lazar et al.<sup>42</sup> found that under humid heterogeneous surface reactions of catechol vapor and a Fe(III) salt that stable metal-ligand complexes were formed, but that in bulk aqueous reactions of these reactants complexation lead to the oxidation of catechol. Therefore, soluble Fe(III) ions can also be an efficient pathway to degrade soluble organic matter.

### **1.1.4. Photooxidation of Fuel SOA**

The hydroxyl radical (OH) is the most reactive oxidant in the atmosphere and is a major sink for organic species. The largest source of OH formation is via photolytic processes. In remote regions, OH is mainly produced from the photolysis of O<sub>3</sub> in the presence of water vapor (1.1a,b). This may occur in more polluted regions, but additional sources exist such as nitrous acid (1.2), hydrogen peroxide (1.3), hydroperoxy radicals (1.4), and alkene ozonolysis during

night. In the presence of nitrous oxides ( $\text{NO}_x = \text{NO} + \text{NO}_2$ ) and a third body, M, ozone can also be formed (1.5a,b).<sup>43</sup>



The generation of reactive oxidant radicals upon photolysis of precursors, followed by reaction with VOCs is known as photooxidation. Atmospheric chemistry of the photooxidation of VOCs can be modeled and studied in the laboratory using smog chambers and flow reactors (experimental details are described in section 1.3). Experiments must first generate hydroxyl radicals which can be formed by the ozonolysis of alkenes or by photolysis of precursor species such as hydrogen peroxide ( $\text{H}_2\text{O}_2$ ), nitrous acid, or small organonitrates.<sup>44</sup> Hydrogen peroxide is a commonly used OH precursor and produces two hydroxyl radicals when photolyzed (1.3). For a recent review of atmospheric organic chemistry and laboratory studies, see Glasius and Goldstein (2016)<sup>1</sup> and references therein.

Previous VOC photooxidation studies have focused on single component biogenic and anthropogenic sources.<sup>45</sup> More complex systems that have been investigated include motor oil particles,<sup>46</sup> diesel exhaust,<sup>47</sup> and biogenic VOC (BVOC) mixtures.<sup>48</sup> Interestingly, emissions of diesel vehicle exhaust can contain a large contribution from unburned fuel.<sup>49</sup> Similarly, unburned fuel was also found in biodiesel exhaust.<sup>50</sup> Such products of incomplete combustion



and incomplete catalytic converter oxidation may be efficient SOA precursors.<sup>51</sup> Other sources of fugitive oil and natural gas emissions of non-methane hydrocarbons (NMHCs) exist such as oil spills, refinery processing, and hydraulic fracturing.<sup>52-54</sup> Diesel fuel composition is dominated by aliphatics and contains some aromatic and polyaromatic hydrocarbons (PAHs) whereas biodiesel fuel contains fatty acid methyl esters (FAMES). The reactivity of hydroxyl radicals with species in these fuels is described next.

Diesel fuel contains an abundance of different types of aliphatics.<sup>55</sup> The hydroxyl radical reacts via hydrogen abstraction with aliphatics (1.6) to form water and an alkyl radical (R•). The reactivity of the hydroxyl radical to hydrogen-abtract from an alkyl carbon increases in the following order: methane (H-CH<sub>3</sub>) << primary (H-CH<sub>2</sub>-R) < secondary (H-CH-R) < tertiary (H-C-(R)R) bonds.<sup>56</sup> The rate constant for the overall reaction of OH with a species can be treated as a sum of the contributions from each abstractable hydrogen using a structure-activity relationship (SAR) which includes corrections for the effects of adjacent groups that were secondary or tertiary.<sup>57</sup> Further corrections and also other methods for estimating these rate constants are described by Ziemann and Atkinson (2012)<sup>45</sup> and references therein. In general, the OH reactivity of alkanes increases with chain length and cyclization, and stays the same or increases with branching.



The presence of a double bond in alkenes creates an additional reaction pathway where hydroxyl radicals react via addition (1.7a). Hydrogen abstraction (1.7b) may occur at allylic or alkyl side chain hydrogens, but, in general, addition is the dominant path in the overall

contribution to OH reactivity. It should be noted that abstraction may become significant for alkenes that have large side chains.<sup>56</sup> In the addition of hydroxyl radicals to asymmetric double bonds, the addition favors formation of a more stable alkyl radical. The radical stability increases in the following order: primary < secondary < tertiary < allylic (R-CH<sub>2</sub>-CH=CH-R').<sup>58</sup> Reactivity of alkenes increase with the number of double bonds, chain length, and with cyclization; it stays the same or increases with branching. Biodiesel fuel contains some methyl esters with one, two, and three double bonds, where the latter would be the most reactive towards hydroxyl radicals.


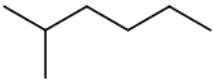
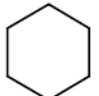
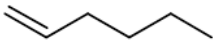
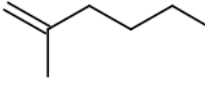
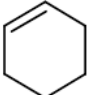
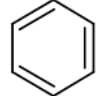
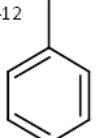
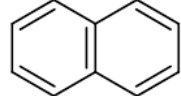
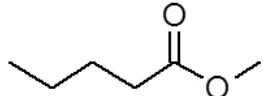


Esters are similar in reactivity with OH to alkanes. In the case of a methyl ester, C<sup>1</sup> in 1.8 is slightly more reactive than that of an alkane.<sup>45</sup> The alkyl end of the ester is similar in reactivity as an alkane except that the carbon site closest to the ester, C<sup>3</sup>, is about half as reactive.<sup>45</sup> Including these small effects from an ester group to the reactivity of alkenes, FAMES with double bonds are more reactive than the alkanes in diesel fuel.



Simple aromatic and PAH species may also react with hydroxyl radicals via addition to aromatic double bonds or hydrogen abstraction of alkyl chains. Benzene is an exception and reacts almost exclusively by OH addition and is the least reactive of all the aromatics in general as it is the smallest aromatic and lacks alkyl chains. Reactions of hydroxyl radicals with aromatics at room temperature are dominated by OH addition, where abstraction accounts for

less than 10%.<sup>43</sup> While OH rate constants of some PAHs have been measured and observed to increase with molecular size, the reason is not currently known.<sup>59</sup> Therefore PAHs in the diesel fuel will react faster than the simple aromatics. Rate constants of OH reactivity with several different types of compounds that contain six carbons, along with toluene and naphthalene are presented in Figure 1.3)

 $5.45 \cdot 10^{-12}$ n-hexane	$\alpha$  $5.3 \cdot 10^{-12}$ 2-methyl-pentane	$\alpha$  $7.21 \cdot 10^{-12}$ cyclohexane
$\alpha$  $37 \cdot 10^{-12}$ 1-hexene	$\alpha$  $63 \cdot 10^{-12}$ 2-methyl-1-pentene	$\alpha$  $67.7 \cdot 10^{-12}$ cyclohexene
$\beta$  $1.22 \cdot 10^{-12}$ benzene	$5.63 \cdot 10^{-12}$ $\beta$  toluene	$\beta$  $23.9 \cdot 10^{-12}$ naphthalene
$\gamma$  $5.41 \cdot 10^{-11}$ methyl-pentanoate	$\alpha$ Atkinson et al. <sup>56</sup> (1997) $\beta$ Atkinson et al. <sup>60</sup> (2007) $\gamma$ Schütze et al. <sup>61</sup> (2010)	

**Figure 1.3.** Rate constants for OH with several different types of compounds that contain six carbons, along with toluene and naphthalene. The rate constants are in units of  $\text{cm}^3 \text{ molecule}^{-1} \text{ s}^{-1}$ .

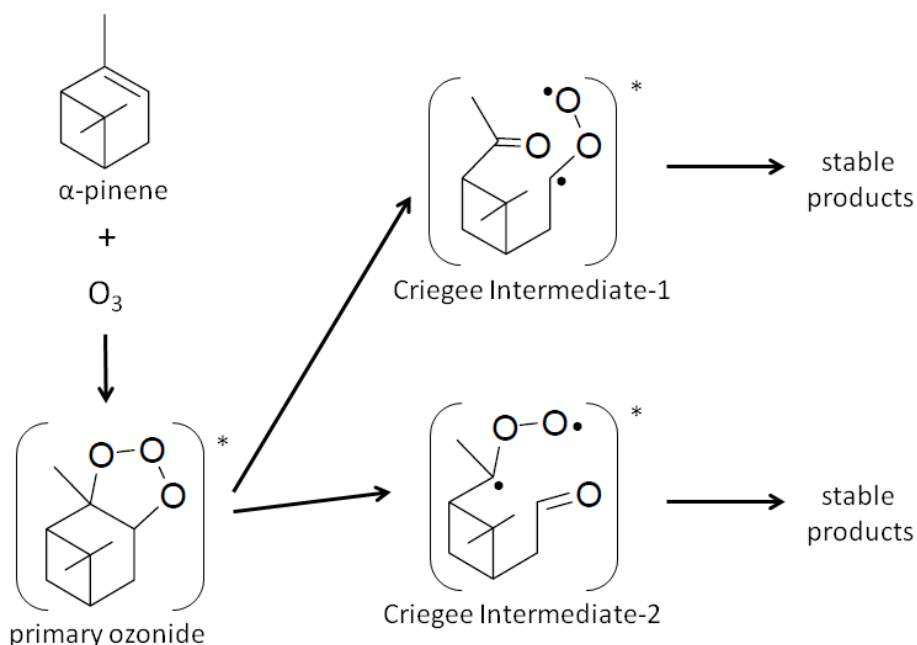
### 1.1.5. $\alpha$ -Pinene Ozonolysis SOA

Another important pathway of SOA formation is the ozonolysis of alkenes, which are common amongst BVOC. The most dominant global BVOC emissions are from isoprene, which contains two double bonds, but its ozonolysis does not make a major contribution to SOA.<sup>9</sup> Other BVOC terpenes that are emitted in the atmosphere include monoterpenes (C<sub>10</sub>), sesquiterpenes (C<sub>15</sub>), and larger compounds. The most important species in the monoterpene group are  $\alpha$ -pinene,  $\beta$ -pinene, sabinene, and limonene.<sup>9</sup> Ozonolysis of  $\alpha$ -pinene is a sink for about 80% of  $\alpha$ -pinene emissions and a major source of SOA.<sup>60</sup> The first step in the reaction of ozone with  $\alpha$ -pinene is the addition of ozone to the double bond forming a primary ozonide (Figure 1.4). It is highly unstable and decomposes to form two different Criegee intermediates that each contain a biradical carbonyl oxide and a carbonyl functional group. The Criegee intermediates are formed with a lot of internal energy and they quickly decompose via two pathways, ring closure to a dioxirane or hydrogen migration to a hydroperoxide intermediate.<sup>61</sup> The latter can undergo isomerization or decomposition to form OH, carbonyls, and a variety of other products.<sup>62</sup> Criegee intermediates can also be collisionally stabilized and survive long enough to react with products of  $\alpha$ -pinene ozonolysis (especially under smog chamber conditions) to form larger dimeric species or form an intramolecular secondary ozonide.<sup>63</sup>

### 1.1.6. Photochemical Aging

The majority of past OA aging studies have focused on photooxidation driven by gas-phase and heterogeneous reactions of gas-phase oxidants with OA constituents and gas-phase photochemistry.<sup>1, 64</sup> However, UV radiation from the sun can induce photolysis and other photochemical reactions of oxygenated organic compounds directly in the condensed organic

aerosol phase.<sup>65</sup> Photochemistry can be a dominant driving force behind most chemical processes occurring in the atmosphere.<sup>66</sup> Photochemical studies can reveal if an aerosol is a temporary

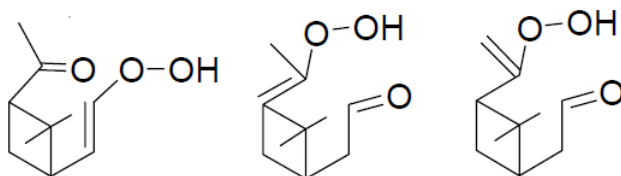
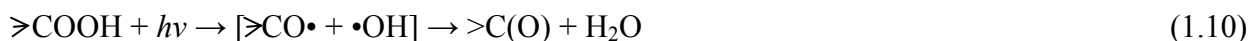
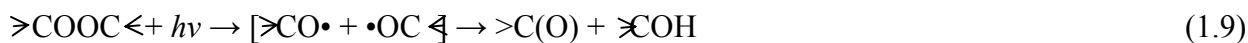


**Figure 1.4.** Diagram of the primary ozonide and Criegee intermediates formed in the ozonolysis of  $\alpha$ -pinene. The intermediates decompose giving rise to a great number of secondary products, some of which end up in SOA.

or permanent sink of  $NO_x$ ,<sup>67</sup> and can cause physical and chemical changes in properties such as hygroscopicity, particle mass, absorption, oxidation, and volatility.<sup>68-70</sup> Gas-phase photolysis of VOC is well studied and is accounted for in atmospheric models. On the contrary, changes in OA composition and concentration arising from condensed-phase photolysis of low volatility organic compounds have not been thoroughly quantified.

The importance of condensed-phase photochemistry in the atmosphere has not been recognized until recently.<sup>66, 71</sup> SOA contains photolabile species at actinic wavelengths such as carbonyls, peroxides, and nitrates.<sup>72</sup> In particular, the SOA of  $\alpha$ -pinene ozonolysis is rich in

photolabile species such as ketones, aldehydes, and peroxides. Organic peroxides are significant in  $\alpha$ -pinene ozonolysis SOA and were previously found to attribute up to 50% by weight of this SOA mass.<sup>73, 74</sup> The photolysis of organic peroxides leads to two radicals (reactions 1.9 and 1.10) that may either recombine or disproportionate.<sup>75</sup> More complex reactions are also possible that involve isomerization, hydrogen abstraction, etc.<sup>43</sup> The main organic peroxides initially formed from  $\alpha$ -pinene ozonolysis are shown in Figure 1.5.<sup>76</sup> Other peroxides, such as hydrogen peroxide, hydromethyl hydroperoxide, peroxyformic acid, peroxyacetic acid, and larger organic peroxides, can be formed from multi-generation products.<sup>74, 77-79</sup> Due to their dominant mass contribution and photolability, peroxide species within  $\alpha$ -pinene ozonolysis SOA can be used to estimate the photolysis lifetime of this SOA.



**Figure 1.5.** Organic peroxides of  $\alpha$ -pinene ozonolysis SOA.<sup>76</sup>

## 1.2. Goals

The principal goal of this thesis is to comprehensively describe molecular formulas, compare absorption properties, characterize various environmental effects on the composition, and to investigate the photochemistry of biogenic and anthropogenic organic aerosols. Systems

investigated in this thesis include: cigarette and e-cigarette POA, iron (III) mediated SOA, photooxidized fuel SOA, and  $\alpha$ -pinene ozonolysis SOA. POA of cigarettes and e-cigarettes were produced by smoking and “vaping”, respectively, with a puff pump and control board. Iron (III) mediated SOA were formed in reaction mixtures of aqueous solutions. Photooxidized fuel SOA and  $\alpha$ -pinene ozonolysis SOA were generated in a Teflon<sup>TM</sup> chamber constructed at UCI (further described in the following section).

Chapter 2 presents the first study of the real-time analysis of e-cigarettes. This study demonstrated the application of PTR-ToF-MS to the characterization the VOCs in e-cigarettes which has since gained increasing popularity. The advantages of utilizing a fast dilution flow tube in characterizing cigarette and e-cigarette emissions were presented. Additionally, this work supported recent observations of carbonyl emissions in e-cigarettes and their battery dependency.

Chapter 3 shifts the focus of this thesis to more atmospherically relevant SOA. The importance of aqueous iron (III) chemistry in the atmosphere is described. Dark reactions of iron (III) and select models for the aromatic fraction of humic like substances in aerosols formed light absorbing secondary organics and colloidal organic particles. Results showed that these reaction products significantly changed the absorption properties if the initial aqueous media. This study provided possible evidence for new pathways for SOA and polymer formation.

Chapter 4 describes the first study of the effect of SO<sub>2</sub> on the formation of photooxidized unburned diesel and biodiesel fuel. Furthermore, this was the first study to characterize unburned diesel fuel and biodiesel fuel SOA with state-of-the-art high-resolution mass spectrometry (HRMS) techniques that offer higher resolving power than the commonly used mass analyzers. This chapter highlights the importance of diesel and biodiesel fuel as contributors to SOA in urban areas, and argues that certain SOA compounds previously assigned to biogenic sources

may have originated from the fuel. Also, this work supports additional pathways for the formation of organosulfur species in the presence of SO<sub>2</sub> that are not possible in sulfate seed studies.

Chapter 5 outlines the first direct photolysis study of SOA in its aerosol phase with separation from oxidant recycling and the interaction of particles with more volatile species. The importance (and possible dominance) of condensed-phase processes in the photochemical aging of SOA was emphasized for a key biogenic SOA system,  $\alpha$ -pinene ozonolysis SOA. The results demonstrate the significant changes in both the physical and chemical properties of the SOA undergoing photolysis. For example, particulate peroxides are shown to degrade as a result of photolysis on an atmospherically relevant time scale of days.

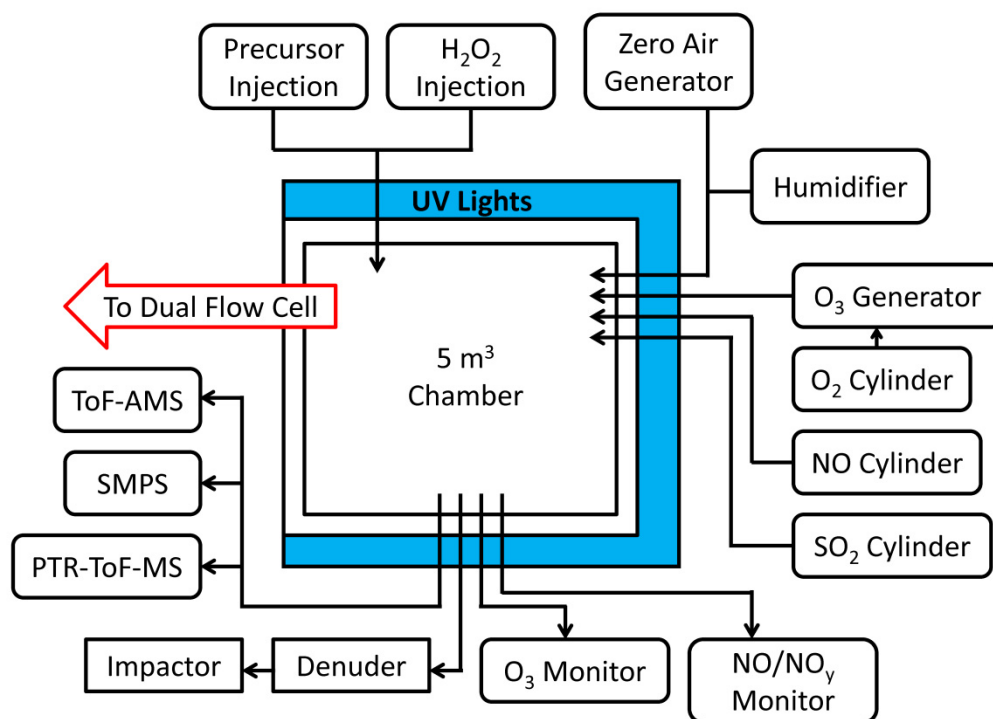
## **1.3. General Methods**

### **1.3.1. Chamber Generation of SOA**

The Nizkorodov lab smog chamber (Figure 1.6) consisted of an enclosed 5 m<sup>3</sup> Teflon<sup>TM</sup> chamber that was surrounded by ultra-violet broadband (UV) lamps (FS40T12/UVB, Solarc Systems Inc.) with an emission centered at 310 nm. Reactive gases were introduced to the chamber through stainless steel tubing and a Teflon<sup>TM</sup> manifold. These include O<sub>3</sub>, NO, and sulfur dioxide (SO<sub>2</sub>). In photooxidation experiments, hydrogen peroxide (Aldrich; 30% by volume in water) was used to form hydroxyl radicals when the UV lamps are turned on. A VOC precursor of interest was added to the chamber through an injection port with evaporation from a flow of zero air. Ozone and nitrogen monoxide were recorded by a Thermo Scientific model 49i ozone analyzer and a Thermo Scientific model 42i-Y NO<sub>y</sub> analyzer. VOCs that had a proton affinity greater than water were able to be chemically ionized by hydronium ions with a Proton



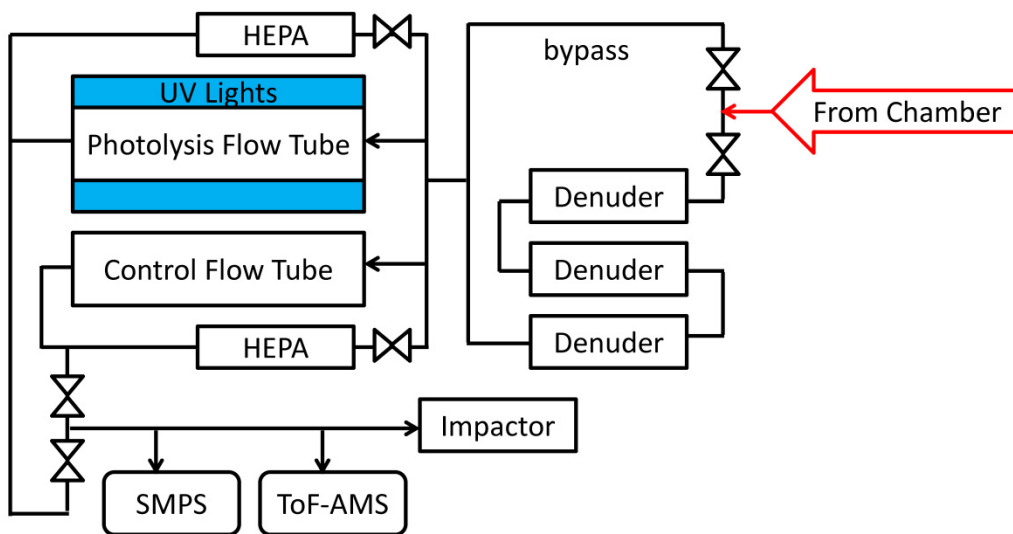
Transfer Reaction Time of Flight Mass Spectrometer (PTR-ToF-MS). Particle size, concentration, and composition were monitored with a scanning mobility particle sizer (SMPS, TSI 3080 Electrostatic Classifier and TSI 3775 Condensation Particle Counter) and an Aerodyne Time-of-Flight Aerosol Mass Spectrometer (ToF-AMS). SOA generated in the chamber was collected on filters for offline analysis or sent to a dual flow cell for direct photolysis experiments.



**Figure 1.6.** Diagram of the smog chamber at UCI. SOA is generated by a VOC precursor and reactive gases of interest. In aging experiments, SOA can be sent to the dual flow cell for direct photolysis.

### 1.3.2. Dual Flow Cell Photolysis

A diagram of the dual flow tube apparatus for direct photolysis experiments is shown in Figure 1.7. SOA that was generated by chamber experiments is pulled via vacuum pressure difference to the dual flow tube setup for photolysis experiments. The SOA flow was next split between a photolysis flow tube and a control flow tube. The denuder train removed unreacted oxidants and the majority of volatile gas-phase species. The SOA was next simultaneously sent through a photolysis flow tube and a control flow tube. The photolysis flow tube was a 24 L quartz flow tube (7" outer diameter) surrounded by 16 UV lamps (Phillips 20W Ultraviolet B TL 20W/01 RS) in a vented protective enclosure. The residence time of the SOA in the photolysis flow tube was set by the sample flow rate of the instruments and the collection flow rate of impaction for filter sample collection. The control flow tube was a dark borosilicate flow tube covered with UV-protective aluminum foil. Both photolyzed and control samples may be analyzed in real-time with SMPS, and/or a ToF-AMS or may be collected on filters for offline analysis.



**Figure 1.7.** Diagram of the dual flow cell. SOA generated from chamber experiments is sent either through a bypass or a denuder train and then photolyzed.

### 1.3.3. HRMS Analysis with LTQ-Orbitrap and 21T FTICR

Mass spectral features with a minimum signal-to-noise ratio of 3 were extracted from averaged mass spectra of both solvent background and sample using Decon 2LS software developed at PNNL (<http://omics.pnl.gov/software/decontools-decon2ls>). Background and sample peaks were aligned by a mass accuracy of 0.001  $m/z$  and 0.0005  $m/z$  for Orbitrap and FTICR data, respectively. Sample peaks that were less than 3 times larger than the background were removed. Formula assignments with constraints of C = 1-40, H = 2-80, O = 0-35, N = 0-1, S = 0-1, H/C = 0.3-2.25, and O/C = 0-1.2 were performed using the Molecular Formula Calculator (<https://nationalmaglab.org/user-facilities/icr/icr-software>) for ions of the type [M - H].

## References

1. Glasius, M.; Goldstein, A. H., Recent Discoveries and Future Challenges in Atmospheric Organic Chemistry. *Environ. Sci. & Technol.* **2016**, *50* (6), 2754-2764.
2. U.S. EPA. Provisional Assessment of Recent Studies on Health Effects of Particulate Matter Exposure. U.S. Environmental Protection Agency, W., DC, EPA/600/R-12/056, **2012**.
3. Mayoralas-Alises, S.; Diaz-Lobato, S., Air pollution and lung cancer. *Curr. Respir. Med. Rev.* **2012**, *8* (6), 418-429.
4. Kurt, O. K.; Zhang, J.; Pinkerton, K. E., Pulmonary health effects of air pollution. *Curr. Opin. Pulm. Med.* **2016**, *22* (2), 138-143.
5. Oakes, M.; Baxter, L.; Long, T. C., Evaluating the application of multipollutant exposure metrics in air pollution health studies. *Environ. Int.* **2014**, *69*, 90-99.
6. Suda, S. R.; Petters, M. D.; Yeh, G. K.; Strollo, C.; Matsunaga, A.; Faulhaber, A.; Ziemann, P. J.; Prenni, A. J.; Carrico, C. M.; Sullivan, R. C.; Kreidenweis, S. M., Influence of functional groups on organic aerosol cloud condensation nucleus activity. *Environ. Sci. Technol.* **2014**, *48* (17), 10182-10190.
7. Russell, L. M.; Bahadur, R.; Hawkins, L. N.; Allan, J.; Baumgardner, D.; Quinn, P. K.; Bates, T. S., Organic aerosol characterization by complementary measurements of chemical bonds and molecular fragments. *Atmos. Environ.* **2009**, *43* (38), 6100-6105.
8. Zhang, Q.; Jimenez, J. L.; Canagaratna, M. R.; Allan, J. D.; Coe, H.; Ulbrich, I.; Alfarra, M. R.; Takami, A.; Middlebrook, A. M.; Sun, Y. L.; Dzepina, K.; Dunlea, E.; Docherty, K.; DeCarlo, P. F.; Salcedo, D.; Onasch, T.; Jayne, J. T.; Miyoshi, T.; Shimono, A.; Hatakeyama, S.; Takegawa, N.; Kondo, Y.; Schneider, J.; Drewnick, F.; Borrmann, S.; Weimer, S.; Demerjian, K.; Williams, P.; Bower, K.; Bahreini, R.; Cottrell, L.; Griffin, R. J.; Rautiainen, J.; Sun, J. Y.; Zhang, Y. M.; Worsnop, D. R. C. L., Ubiquity and dominance of oxygenated species in organic aerosols in anthropogenically-influenced Northern Hemisphere midlatitudes. *Geophys. Res. Lett.* **2007**, *34* (13). DOI:10.1029/2007GL029979.
9. Kanakidou, M.; Seinfeld, J. H.; Pandis, S. N.; Barnes, I.; Dentener, F. J.; Facchini, M. C.; Van Dingenen, R.; Ervens, B.; Nenes, A.; Nielsen, C. J.; Swietlicki, E.; Putaud, J. P.;

- Balkanski, Y.; Fuzzi, S.; Horth, J.; Moortgat, G. K.; Winterhalter, R.; Myhre, C. E. L.; Tsigaridis, K.; Vignati, E.; Stephanou, E. G.; Wilson, J., Organic aerosol and global climate modelling: a review. *Atmos. Chem. Phys.* **2005**, *5* (4), 1053-1123.
10. Putaud, J. P.; Van Dingenen, R.; Alastuey, A.; Bauer, H.; Birmili, W.; Cyrys, J.; Flentje, H.; Fuzzi, S.; Gehrig, R.; Hansson, H. C.; Harrison, R. M.; Herrmann, H.; Hitzenberger, R.; Hüglin, C.; Jones, A. M.; Kasper-Giebl, A.; Kiss, G.; Koussa, A.; Kuhlbusch, T. A. J.; Löschau, G.; Maenhaut, W.; Molnar, A.; Moreno, T.; Pekkanen, J.; Perrino, C.; Pitz, M.; Puxbaum, H.; Querol, X.; Rodriguez, S.; Salma, I.; Schwarz, J.; Smolik, J.; Schneider, J.; Spindler, G.; ten Brink, H.; Tursic, J.; Viana, M.; Wiedensohler, A.; Raes, F., A European aerosol phenomenology - 3: Physical and chemical characteristics of particulate matter from 60 rural, urban, and kerbside sites across Europe. *Atmos. Environ.* **2010**, *44* (10), 1308-1320.
11. Minguillón, M. C.; Querol, X.; Baltensperger, U.; Prévôt, A. S. H., Fine and coarse PM composition and sources in rural and urban sites in Switzerland: Local or regional pollution? *Sci. Total Environ.* **2012**, *427-428*, 191-202.
12. Donahue, N. M.; Henry, K. M.; Mentel, T. F.; Kiendler-Scharr, A.; Spindler, C.; Bohn, B.; Brauers, T.; Dorn, H. P.; Fuchs, H.; Tillmann, R.; Wahner, A.; Saathoff, H.; Naumann, K.-H.; Möhler, O.; Leisner, T.; Müller, L.; Reinnig, M.-C.; Hoffmann, T.; Salo, K.; Hallquist, M.; Frosch, M.; Bilde, M.; Tritscher, T.; Barmet, P.; Praplan, A. P.; DeCarlo, P. F.; Dommen, J.; Prévôt, A. S. H.; Baltensperger, U., Aging of biogenic secondary organic aerosol via gas-phase OH radical reactions. *Proc. Natl. Acad. Sci. U.S.A.* **2012**, *109* (34), 13503-13508.
13. Qi, L.; Nakao, S.; Cocker, D. R., Aging of secondary organic aerosol from  $\alpha$ -pinene ozonolysis: Roles of hydroxyl and nitrate radicals. *J. Air Waste Manag. Assoc.* **2012**, *62* (12), 1359-1369.
14. Amin, H. S.; Hatfield, M. L.; Huff Hartz, K. E., Characterization of secondary organic aerosol generated from ozonolysis of  $\alpha$ -pinene mixtures. *Atmos. Environ.* **2013**, *67*, 323-330.
15. Kalberer, M.; Paulsen, D.; Sax, M.; Steinbacher, M.; Dommen, J.; Prévôt, A. S. H.; Fisseha, R.; Weingartner, E.; Frankevich, V.; Zenobi, R.; Baltensperger, U., Identification of

- Polymers as Major Components of Atmospheric Organic Aerosols. *Science* **2004**, *303* (5664), 1659-1662.
16. Jiang, H.; Jang, M.; Sabo-Attwood, T.; Robinson, S. E., Oxidative potential of secondary organic aerosols produced from photooxidation of different hydrocarbons using outdoor chamber under ambient sunlight. *Atmos. Environ.* **2016**, *131*, 382-389.
  17. Nah, T.; Sanchez, J.; Boyd, C. M.; Ng, N. L., Photochemical aging of  $\alpha$ -pinene and  $\alpha$ -pinene secondary organic aerosol formed from nitrate radical oxidation. *Environ. Sci. Technol.* **2016**, *50* (1), 222-231.
  18. Sato, K.; Jia, T.; Tanabe, K.; Morino, Y.; Kajii, Y.; Imamura, T., Terpenylic acid and nine-carbon multifunctional compounds formed during the aging of  $\alpha$ -pinene ozonolysis secondary organic aerosol. *Atmos. Environ.* **2016**, *130*, 127-135.
  19. Strollo, C. M.; Ziemann, P. J., Products and mechanism of secondary organic aerosol formation from the reaction of 3-methylfuran with OH radicals in the presence of NO<sub>x</sub>. *Atmos. Environ.* **2013**, *77*, 534-543.
  20. Zhang, Z.; Lin, Y. H.; Zhang, H.; Surratt, J. D.; Ball, L. M.; Gold, A., Technical Note: Synthesis of isoprene atmospheric oxidation products: isomeric epoxydiols and the rearrangement products *cis*- and *trans*-3-methyl-3,4-dihydroxytetrahydrofuran. *Atmos. Chem. Phys.* **2012**, *12* (18), 8529-8535.
  21. Epstein, S. A.; Blair, S. L.; Nizkorodov, S. A., Direct Photolysis of  $\alpha$ -Pinene Ozonolysis Secondary Organic Aerosol: Effect on Particle Mass and Peroxide Content. *Environ. Sci. Technol.* **2014**, *48* (19), 11251-11258.
  22. Farmer, S. A.; Nelin, T. D.; Falvo, M. J.; Wold, L. E., Ambient and household air pollution: complex triggers of disease. *Am. J. Physiol.* **2014**, *307* (2, Pt. 2), H467-H476.
  23. Pichelstorfer, L.; Winkler-Heil, R.; Hofmann, W., Lagrangian/Eulerian model of coagulation and deposition of inhaled particles in the human lung. *J. Aerosol Sci.* **2013**, *64*, 125-142.
  24. Zhang, Z.; Kleinstreuer, C.; Feng, Y., Vapor deposition during cigarette smoke inhalation in a subject-specific human airway model. *J. Aerosol Sci.* **2012**, *53*, 40-60.

25. Sleiman, M.; Logue, J. M.; Luo, W.; Pankow, J. F.; Gundel, L. A.; Destailats, H., Inhalable Constituents of Thirdhand Tobacco Smoke: Chemical Characterization and Health Impact Considerations. *Environ. Sci. Technol.* **2014**, *48* (22), 13093-13101.
26. Petrick, L. M.; Svidovsky, A.; Dubowski, Y., Thirdhand Smoke: Heterogeneous Oxidation of Nicotine and Secondary Aerosol Formation in the Indoor Environment. *Environ. Sci. Technol.* **2011**, *45* (1), 328-333.
27. Piade, J. J.; Wajrock, S.; Jaccard, G.; Janeke, G., Formation of mainstream cigarette smoke constituents prioritized by the World Health Organization - Yield patterns observed in market surveys, clustering and inverse correlations. *Food Chem. Toxicol.* **2013**, *55*, 329-347.
28. Baker, R. R., Smoke generation inside a burning cigarette: modifying combustion to develop cigarettes that may be less hazardous to health. *Prog. Energy Combust. Sci.* **2006**, *32* (4), 373-385.
29. U.S. Department of Health and Human Services. *How Tobacco Smoke Causes Disease: The Biology and Behavioral Basis for Smoking-Attributable Disease: A Report of the Surgeon General*. Atlanta, GA: U.S. Department of Health and Human Services, Centers for Disease Control and Prevention, National Center for Chronic Disease Prevention and Health Promotion, Office on Smoking and Health, 2010.
30. U.S. Department of Health and Human Services. *The Health Consequences of Smoking—50 Years of Progress: A Report of the Surgeon General*. Office on Smoking and Health, National Center for Chronic Disease Prevention and Health Promotion, Centers for Disease Control and Prevention, U.S. Department of Health and Human Services, Atlanta, GA. **2014**.
31. Kim, K. E.; Cho, D.; Park, H. J., Air pollution and skin diseases: Adverse effects of airborne particulate matter on various skin diseases. *Life Sci.* **2016**, *152*, 126-134.
32. Harris, B., The intractable cigarette ‘filter problem’. *Tobacco Control* **2011**, *20* (Suppl 1), i10-i16.
33. Streller, S.; Roth, K. *ChemViews Mag.* **2015**. DOI: 10.1002/chemv.201400135.
34. Grana, R. P. M. P. H.; Benowitz, N. M. D.; Glantz, S. A. P., Background Paper on E-cigarettes (Electronic Nicotine Delivery Systems). 2013.

35. Brown, C. J.; Cheng, J. M., Electronic cigarettes: product characterisation and design considerations. *Tobacco Control* **2014**, *23* (suppl 2), ii4-ii10.
36. Kosmider, L.; Sobczak, A.; Fik, M.; Knysak, J.; Zaciera, M.; Kurek, J.; Goniewicz, M. L., Carbonyl compounds in electronic cigarette vapors: effects of nicotine solvent and battery output voltage. *Nicotine Tob. Res.* **2014**, *16* (10), 1319-26.
37. Ohta, K.; Uchiyama, S.; Inaba, Y.; Nakagome, H.; Kunugita, N., Determination of Carbonyl Compounds Generated from the Electronic Cigarette Using Coupled Silica Cartridges Impregnated with Hydroquinone and 2,4-Dinitrophenylhydrazine. *Bunseki Kagaku* **2011**, *60* (10), 791-797.
38. Drenkard, Scott, Vapor Products and Tax Policy. *Tax Foundation Publications* March 22<sup>nd</sup> 2016. Retrieved from: <http://taxfoundation.org/article/vapor-products-and-tax-policy>.
39. Al-Abadleh, H. A., Review of the bulk and surface chemistry of iron in atmospherically relevant systems containing humic-like substances. *RSC Adv.* **2015**, *5* (57), 45785-45811.
40. Moore, J. K.; Braucher, O., Sedimentary and mineral dust sources of dissolved iron to the world ocean. *Biogeosciences* **2008**, *5* (3), 631-656.
41. Perron, N. R.; Brumaghim, J. L., A Review of the Antioxidant Mechanisms of Polyphenol Compounds Related to Iron Binding. *Cell Biochem. Biophys.* **2009**, *53* (2), 75-100.
42. Tofan-Lazar, J.; Situm, A.; Al-Abadleh, H. A., DRIFTS Studies on the Role of Surface Water in Stabilizing Catechol-Iron(III) Complexes at the Gas/Solid Interface. *J. Phys. Chem. A* **2013**, *117* (40), 10368-10380.
43. Finlayson-Pitts, B. J.; Pitts Jr, J. N., CHAPTER 6 - Rates and Mechanisms of Gas-Phase Reactions in Irradiated Organic - NO<sub>x</sub> - Air Mixtures. In *Chemistry of the Upper and Lower Atmosphere*, Academic Press: San Diego, **2000**; pp 179-263.
44. Eddingsaas, N. C.; Loza, C. L.; Yee, L. D.; Seinfeld, J. H.; Wennberg, P. O.,  $\alpha$ -pinene photooxidation under controlled chemical conditions -Part 1: Gas-phase composition in low- and high-NO<sub>x</sub> environments. *Atmos. Chem. Phys.* **2012**, *12* (14), 6489-6504.
45. Ziemann, P. J.; Atkinson, R., Kinetics, products, and mechanisms of secondary organic aerosol formation. *Chem. Soc. Rev.* **2012**, *41* (19), 6582-6605.



46. Isaacman, G.; Chan, A. W. H.; Nah, T.; Worton, D. R.; Ruehl, C. R.; Wilson, K. R.; Goldstein, A. H., Heterogeneous OH Oxidation of Motor Oil Particles Causes Selective Depletion of Branched and Less Cyclic Hydrocarbons. *Environ. Sci. Technol.* **2012**, *46* (19), 10632-10640.
47. Lambe, A. T.; Miracolo, M. A.; Hennigan, C. J.; Robinson, A. L.; Donahue, N. M., Effective rate constants and uptake coefficients for the reactions of organic molecular markers (n-alkanes, hopanes, and steranes) in motor oil and diesel primary organic aerosols with hydroxyl radicals. *Environ. Sci. Technol.* **2009**, *43* (23), 8794-800.
48. Kourtchev, I.; Doussin, J. F.; Giorio, C.; Mahon, B.; Wilson, E. M.; Maurin, N.; Pangu, E.; Venables, D. S.; Wenger, J. C.; Kalberer, M., Molecular composition of fresh and aged secondary organic aerosol from a mixture of biogenic volatile compounds: a high-resolution mass spectrometry study. *Atmos. Chem. Phys.* **2015**, *15* (10), 5683-5695.
49. Gentner, D. R.; Isaacman, G.; Worton, D. R.; Chan, A. W. H.; Dallmann, T. R.; Davis, L.; Liu, S.; Day, D. A.; Russell, L. M.; Wilson, K. R.; Weber, R.; Guha, A.; Harley, R. A.; Goldstein, A. H., Elucidating secondary organic aerosol from diesel and gasoline vehicles through detailed characterization of organic carbon emissions. *Proc. Natl. Acad. Sci. U. S. A.* **2012**, *109* (45), 18318-18323.
50. Fukagawa, N. K.; Li, M.; Poynter, M. E.; Palmer, B. C.; Parker, E.; Kasumba, J.; Holmen, B. A., Soy Biodiesel and Petrodiesel Emissions Differ in Size, Chemical Composition and Stimulation of Inflammatory Responses in Cells and Animals. *Environ. Sci. Technol.* **2013**, *47* (21), 12496-12504.
51. Gordon, T. D.; Presto, A. A.; May, A. A.; Nguyen, N. T.; Lipsky, E. M.; Donahue, N. M.; Gutierrez, A.; Zhang, M.; Maddox, C.; Rieger, P.; Chattopadhyay, S.; Maldonado, H.; Maricq, M. M.; Robinson, A. L., Secondary organic aerosol formation exceeds primary particulate matter emissions for light-duty gasoline vehicles. *Atmos. Chem. Phys.* **2014**, *14* (9), 4661-4678.
52. Drozd, G. T.; Worton, D. R.; Aeppli, C.; Reddy, C. M.; Zhang, H.; Variano, E.; Goldstein, A. H., Modeling comprehensive chemical composition of weathered oil following a marine spill

- to predict ozone and potential secondary aerosol formation and constrain transport pathways. *J. Geophys. Res.: Oceans* **2015**, *120* (11), 7300-7315.
53. Field, R. A.; Soltis, J.; McCarthy, M. C.; Murphy, S.; Montague, D. C., Influence of oil and gas field operations on spatial and temporal distributions of atmospheric non-methane hydrocarbons and their effect on ozone formation in winter. *Atmos. Chem. Phys.* **2015**, *15* (6), 3527-3542.
54. Altieri, K. E.; Stone, A., Prospective air pollutant emissions inventory for the development and production of unconventional natural gas in the Karoo basin, South Africa. *Atmos. Environ.* **2016**, *129*, 34-42.
55. Isaacman, G.; Wilson, K. R.; Chan, A. W. H.; Worton, D. R.; Kimmel, J. R.; Nah, T.; Hohaus, T.; Gonin, M.; Kroll, J. H.; Worsnop, D. R.; Goldstein, A. H., Improved Resolution of Hydrocarbon Structures and Constitutional Isomers in Complex Mixtures Using Gas Chromatography-Vacuum Ultraviolet-Mass Spectrometry. *Anal. Chem.* **2012**, *84* (5), 2335-2342.
56. Atkinson, R., Gas-Phase Tropospheric Chemistry of Volatile Organic Compounds: 1. Alkanes and Alkenes. *J. Phys. Chem. Ref. Data* **1997**, *26* (2), 215-290.
57. Atkinson, R.; Baulch, D. L.; Cox, R. A.; Hampson, R. F.; Kerr, J. A.; Rossi, M. J.; Troe, J., Evaluated Kinetic, Photochemical and Heterogeneous Data for Atmospheric Chemistry: Supplement V. IUPAC Subcommittee on Gas Kinetic Data Evaluation for Atmospheric Chemistry. *J. Phys. Chem. Ref. Data* **1997**, *26* (3), 521-1011.
58. Brown, W. H.; Iverson, B. L.; Anslyn, E.; Foote, C. S., CHAPTER 8: Haloalkanes, Halogenation, and Radical Reactions. In *Org. Chem.*, Cengage Learning: 2014; pp 305-340.
59. Keyte, I. J.; Harrison, R. M.; Lammel, G., Chemical reactivity and long-range transport potential of polycyclic aromatic hydrocarbons - a review. *Chem. Soc. Rev.* **2013**, *42* (24), 9333-9391.
60. Griffin, R. J.; Cocker, D. R.; Flagan, R. C.; Seinfeld, J. H., Organic aerosol formation from the oxidation of biogenic hydrocarbons. *J. Geophys. Res.: Atmospheres* **1999**, *104* (D3), 3555-3567.

61. Zhang, D.; Zhang, R., Ozonolysis of  $\alpha$ -pinene and  $\beta$ -pinene: Kinetics and mechanism. *The J. Chem. Phys.* **2005**, *122* (11), 114308.
62. Calogirou, A.; Larsen, B. R.; Kotzias, D., Gas-phase terpene oxidation products: a review. *Atmos. Environ.* **1999**, *33* (9), 1423-1439.
63. Lee, S.; Kamens, R. M., Particle nucleation from the reaction of  $\alpha$ -pinene and O<sub>3</sub>. *Atmos. Environ.* **2005**, *39* (36), 6822-6832.
64. Hallquist, M.; Wenger, J. C.; Baltensperger, U.; Rudich, Y.; Simpson, D.; Claeys, M.; Dommen, J.; Donahue, N. M.; George, C.; Goldstein, A. H.; Hamilton, J. F.; Herrmann, H.; Hoffmann, T.; Iinuma, Y.; Jang, M.; Jenkin, M. E.; Jimenez, J. L.; Kiendler-Scharr, A.; Maenhaut, W.; McFiggans, G.; Mentel, T. F.; Monod, A.; Prévôt, A. S. H.; Seinfeld, J. H.; Surratt, J. D.; Szmigielski, R.; Wildt, J., The formation, properties and impact of secondary organic aerosol: current and emerging issues. *Atmos. Chem. Phys.* **2009**, *9* (14), 5155-5236.
65. Kroll, J. H.; Seinfeld, J. H., Chemistry of secondary organic aerosol: Formation and evolution of low-volatility organics in the atmosphere. *Atmos. Environ.* **2008**, *42* (16), 3593-3624.
66. George, C.; Ammann, M.; D'Anna, B.; Donaldson, D. J.; Nizkorodov, S. A., Heterogeneous Photochemistry in the Atmosphere. *Chem. Rev. (Washington, DC, U. S.)* **2015**, *115* (10), 4218-4258.
67. Boyd, C. M.; Sanchez, J.; Xu, L.; Eugene, A. J.; Nah, T.; Tuet, W. Y.; Guzman, M. I.; Ng, N. L., Secondary organic aerosol formation from the  $\alpha$ -pinene + NO<sub>3</sub> system: effect of humidity and peroxy radical fate. *Atmos. Chem. Phys.* **2015**, *15* (13), 7497-7522.
68. Wong, J. P. S.; Zhou, S.; Abbatt, J. P. D., Changes in Secondary Organic Aerosol Composition and Mass due to Photolysis: Relative Humidity Dependence. *J. Phys. Chem. A* **2015**, *119* (19), 4309-4316.
69. Romonosky, D. E.; Laskin, A.; Laskin, J.; Nizkorodov, S. A., High-Resolution Mass Spectrometry and Molecular Characterization of Aqueous Photochemistry Products of Common Types of Secondary Organic Aerosols. *The Journal of Physical Chemistry A* **2015**, *119* (11), 2594-2606.

70. Romonosky, D. E.; Ali, N. N.; Saiduddin, M. N.; Wu, M.; Lee, H. J.; Aiona, P. K.; Nizkorodov, S. A., Effective absorption cross sections and photolysis rates of anthropogenic and biogenic secondary organic aerosols. *Atmos. Environ.* **2016**, *130*, 172-179.
71. Hodzic, A.; Madronich, S.; Kasibhatla, P. S.; Tyndall, G.; Aumont, B.; Jimenez, J. L.; Lee-Taylor, J.; Orlando, J., Organic photolysis reactions in tropospheric aerosols: effect on secondary organic aerosol formation and lifetime. *Atmos. Chem. Phys.* **2015**, *15* (16), 9253-9269.
72. Suda, S. R.; Petters, M. D.; Yeh, G. K.; Strollo, C.; Matsunaga, A.; Faulhaber, A.; Ziemann, P. J.; Prenni, A. J.; Carrico, C. M.; Sullivan, R. C.; Kreidenweis, S. M., Influence of Functional Groups on Organic Aerosol Cloud Condensation Nucleus Activity. *Environ. Sci. Technol.* **2014**, *48* (17), 10182-10190.
73. Docherty, K. S.; Wu, W.; Lim, Y. B.; Ziemann, P. J., Contributions of Organic Peroxides to Secondary Aerosol Formed from Reactions of Monoterpenes with O<sub>3</sub>. *Environ. Sci. Technol.* **2005**, *39* (11), 4049-4059.
74. Li, H.; Chen, Z.; Huang, L.; Huang, D., Organic peroxides' gas-particle partitioning and rapid heterogeneous decomposition on secondary organic aerosol. *Atmos. Chem. Phys.* **2016**, *16* (3), 1837-1848.
75. Kamboures, M. A.; Nizkorodov, S. A.; Gerber, R. B., Ultrafast photochemistry of methyl hydroperoxide on ice particles. *Proc. Natl. Acad. Sci. U. S. A.* **2010**, *107* (15), 6600-6604.
76. Winterhalter, R.; Van Dingenen, R.; Larsen, B. R.; Jensen, N. R.; Hjorth, J., LC-MS analysis of aerosol particles from the oxidation of  $\alpha$ -pinene by ozone and OH-radicals. *Atmos. Chem. Phys.* **2003**, *2005*, *5*, 1053-1123.
77. Venkatachari, P.; Hopke, P. K., Characterization of products formed in the reaction of ozone with  $\alpha$ -pinene: case for organic peroxides. *J. Environ. Monit.* **2008**, *10* (8), 966-974.
78. Mentel, T. F.; Springer, M.; Ehn, M.; Kleist, E.; Pullinen, I.; Kurtén, T.; Rissanen, M.; Wahner, A.; Wildt, J., Formation of highly oxidized multifunctional compounds: autoxidation of peroxy radicals formed in the ozonolysis of alkenes - deduced from structure-product relationships. *Atmos. Chem. Phys.* **2015**, *15* (12), 6745-6765.

79. Ehn, M.; Thornton, J. A.; Kleist, E.; Sipila, M.; Junninen, H.; Pullinen, I.; Springer, M.; Rubach, F.; Tillmann, R.; Lee, B.; Lopez-Hilfiker, F.; Andres, S.; Acir, I.-H.; Rissanen, M.; Jokinen, T.; Schobesberger, S.; Kangasluoma, J.; Kontkanen, J.; Nieminen, T.; Kurten, T.; Nielsen, L. B.; Jorgensen, S.; Kjaergaard, H. G.; Canagaratna, M.; Maso, M. D.; Berndt, T.; Petaja, T.; Wahner, A.; Kerminen, V.-M.; Kulmala, M.; Worsnop, D. R.; Wildt, J.; Mentel, T. F., A large source of low-volatility secondary organic aerosol. *Nature* **2014**, *506* (7489), 476-479.

## Chapter 2: Particle and VOC Content of Electronic and Combustion Cigarettes

Portions of this chapter were reproduced in part by permission from:

Blair, S. L.; Epstein, S. A.; Nizkorodov, S. A.; Staimer, N., A Real-Time Fast-Flow Tube Study of VOC and Particulate Emissions from Electronic, Potentially Reduced-Harm, Conventional, and Reference Cigarettes. *Aerosol Sci. and Tech.* **2015**, *49* (9), 816-827. Copyright © 2015 Taylor & Francis.

\* Note that the statements made in sections 2.1-2.5 were based on available literature at the time of the publication submission (May 2015). Section 2.6 includes current literature available up to the submission date of this thesis (May 2016).

## 2.1. Abstract

Tobacco-free electronic cigarettes (e-cigarettes), which are currently not regulated by the FDA, have become widespread as a “safe” form of smoking. One approach to evaluate the potential toxicity of e-cigarettes and other types of potentially “reduced-harm” cigarettes is to compare their emissions of volatile organic compounds (VOCs), including reactive organic electrophilic compounds such as acrolein, and particulate matter to those of conventional and reference cigarettes. Our newly designed fast-flow tube system enabled us to analyze VOC composition and particle number concentration in real-time by promptly diluting puffs of mainstream smoke obtained from different brands of combustion cigarettes and e-cigarettes. A proton transfer reaction time-of-flight mass spectrometer (PTR-ToF-MS) was used to analyze real-time cigarette VOC emissions with a 1 s time resolution. Particles were detected with a condensation particle counter (CPC). This technique offers real-time analysis of VOCs and particles in each puff without sample aging and does not require any sample pretreatment or extra handling. Several important determining factors in VOC and particle concentration were investigated: (1) puff frequency; (2) puff number; (3) tar content; (4) filter type. Results indicate that electronic cigarettes are not free from acrolein and acetaldehyde emissions and produce comparable particle number concentrations to those of combustion cigarettes, more specifically to the 1R5F reference cigarette. Unlike conventional cigarettes, which emit different amounts of particles and VOCs each puff, there was no significant puff dependence in the e-cigarette emissions. Charcoal filter cigarettes did not fully prevent the emission of acrolein and other VOCs.

## 2.2. Introduction

Mainstream smoke of conventional cigarettes has been well studied<sup>1</sup> and characterized over the past several decades. It is known to cause or contribute to the development of lung, liver, colorectal, prostate, and breast cancer, diseases of nearly all of the organs in the body, and other outcomes such as inflammation, impaired immune system, congenital malformations, and erectile dysfunction, etc.<sup>2</sup> As for morbidity, more than 20 million premature deaths in the U.S. can be attributed to smoking over a time span of 50 years, 1964-2014.<sup>2</sup> Since the first Surgeon General report in 1964, conventional cigarettes have been modified in several different ways to design potentially “reduced-harm cigarettes”, in efforts to lessen the harmful health effects.<sup>3</sup> For example, the modifications have included the use of porous paper, processed cellulose-acetate filters, charcoal filters, and ventilation holes in filters.<sup>4</sup> The most recent development in the search for a potentially reduced harm cigarette has been the electronic cigarette (e-cigarette). Its design differs greatly from any previous cigarette in that it does not contain tobacco; puffing on the device leads to volatilization of nicotine at elevated temperatures, but in the absence of any combustion. This mode of cigarette use is often referred to as “vaping” instead of “smoking”. In general, there are two types of e-cigarettes: type A that uses an atomizer and type B that uses a cartomizer.<sup>5</sup> Type A consists of three parts: the refill liquid reservoir, an atomizer, and a battery. E-cigarettes of type B have a liquid cartridge with a heating element and a battery as second piece.<sup>6</sup> The liquid cartridge consists of a mixture of water, propylene glycol and/or vegetable glycerin, and differing amounts of dissolved nicotine and flavoring additives. E-cigarettes are still a new emerging product and they have an impressively large variety of available flavored cartridges.<sup>7</sup> A recent review by Chapman and Wu<sup>8</sup> found that in 2011, adolescents aged 11-19 in



grades 6-12 attributed to up to 3.3% of e-cigarette ever-use (meaning tried at least once) in the U.S., and their number increased to 6.8% in 2012.

In most studies, VOC measurements of mainstream smoke or vapor were limited to multi-step chemical analysis and low time resolution. High performance liquid chromatography (HPLC) and gas chromatography mass spectrometry (GCMS) analysis of VOC and tar composition commonly require sample pretreatment such as extraction and/or derivatization.<sup>5, 9-15</sup> A recent puff-by-puff cigarette study by Sampson et al.<sup>16</sup> used solid-phase microextraction-GCMS, which required less sample handling. Several other studies have analyzed cigarette smoke on a puff-per-puff basis using a variety of techniques such as two-dimensional characterization with fast GC combined with single-photon ionization mass spectrometry,<sup>17</sup> GC ultraviolet-diode array detection,<sup>18</sup> and thermal desorption multidimensional GC-MS.<sup>19</sup> Cigarette VOCs have also been analyzed in high resolution real-time studies including vacuum ultraviolet single-photon ionization ToF-MS,<sup>20</sup> ion-molecule reaction MS,<sup>21</sup> and tunable diode laser absorption spectroscopy.<sup>22, 23</sup> To the authors' best of knowledge, there are currently no real-time VOC e-cigarette studies.

Mainstream smoke particles emitted by numerous types of cigarettes have been analyzed using various techniques such as a differential mobility analyzer and a centrifugal particle mass analyzer,<sup>24</sup> an optical aerosol spectrometer,<sup>25</sup> a differential mobility spectrometer,<sup>26, 27</sup> and an electrical low-pressure impactor (ELPI).<sup>28</sup> Although e-cigarette particles have been studied in the last several years, using methods such as spectral transmission and an electrical mobility analyzer,<sup>29</sup> ELPI,<sup>30</sup> a scanning mobility particle sizer (SMPS),<sup>31, 32</sup> a fast mobility particle sizer (FMPS),<sup>11, 33, 34</sup> and an aerosol spectrometer and ultrafine particle counter,<sup>5</sup> online particle concentration data represent an interesting complement to VOC data.

Tobacco smoke has been found to contain ~4800 substances.<sup>35</sup> As indicated above, these include highly electrophilic compounds such as acrolein. In contrast to other carcinogens (polyaromatic hydrocarbons, N-nitrosamines, and dioxins) reactive organic electrophilic compounds detected in cigarette smoke (CS) do not require metabolic activation, but can react readily with proteins or bind covalently to nucleic acids.<sup>36, 37</sup> Moreover, mainstream cigarette smoke contains high concentrations of small particles. These particles are efficiently deposited in the smallest airways of the lung and the condensed organic material (such as nicotine) can diffuse deep into the respiratory tract.<sup>38</sup> While e-cigarettes have not been fully studied, their vapor has also been found to contain several reactive carbonyls such as formaldehyde, acetaldehyde, and acrolein, and to also contain acetone.<sup>39</sup> There are still many important questions left unanswered about the impact of e-cigarettes: (1) What are the potential risks? (2) Are there potentially harmful chemicals emitted? (3) Are there benefits associated with use?<sup>1, 39</sup> This thesis investigated question (2), more broadly, with a comparative study of the VOCs and particles in electronic, potentially reduced-harm, conventional, and Kentucky reference (University of Kentucky, Lexington, KY) cigarette smoke using a real-time fast flow tube setup. Kentucky reference cigarettes are made to be sufficiently homogeneous and to have well established measurement values such that they can be used for calibration as internal lab controls and can be easily compared between laboratories.<sup>40</sup> To answer this question, we carried out chamber experiments to find the optimal dilution of cigarette smoke, and did measurements on a number of different cigarette types.

## 2.3. Experimental

### 2.3.1. Mini-Chamber Experiments

Although this study focused on real-time analysis of cigarette and e-cigarette emissions using a fast-flow tube, initial measurements were conducted in inflatable Teflon™ FEP coated bags, made in house, in order to optimize the experimental conditions. A large dilution ( $\sim 10^3$ ) of the initial cigarette mainstream smoke was necessary to analyze the VOC and particle content with an Ionicon Analytik Proton Transfer Reaction Time-of-Flight Mass Spectrometer (PTR-ToF-MS) and a Scanning Mobility Particle Sizer (SMPS, TSI 3080 Electrostatic Classifier and TSI 3775 Condensation Particle Counter, CPC). The PTR-ToF-MS settings for the drift voltage, temperature, and pressure were 600 V, 60 °C, and 2.26 mbar, respectively; the time resolution was 18 s. Two reference cigarettes, 1R5F and 3R4F, and one e-cigarette, e-cigarette-1, (18 mg nicotine/cartridge, propylene glycol, 3.6 V) were analyzed. Reference cigarettes 1R5F and 3R4F have filter ventilations of 70% and 29%.<sup>16</sup> To the author's best of knowledge, filter ventilation data were not available for the conventional name brand cigarettes. Before use, each conventional cigarette was conditioned to a relative humidity of  $60 \pm 3\%$  with exposure to headspace air above a  $\sim 75$  wt% aqueous glycerol solution for 48 hrs in a closed container. A puff pump (Brailsford & Co. Inc. TD-2NA(7)), operated at a flow of 1.10 L/min, was connected to a solenoid air control valve (Ingersoll Rand, P251SS-012-D) that was timed by a control board (Teague Enterprises, TE-2) to provide a 2 s puff for a total mainstream smoke puff volume of  $\sim 37$  ml at a frequency of 4 puffs/min. The 5<sup>th</sup> puff was sent into a Teflon™ bag prefilled with 150 L of zero air supplied with an FTIR purge gas generator (Parker model 75-62). The bag content was allowed to mix for 15 min before analysis. An additional experiment of a collection of 4 successive puffs under the conditions previously described looked at the particle behavior

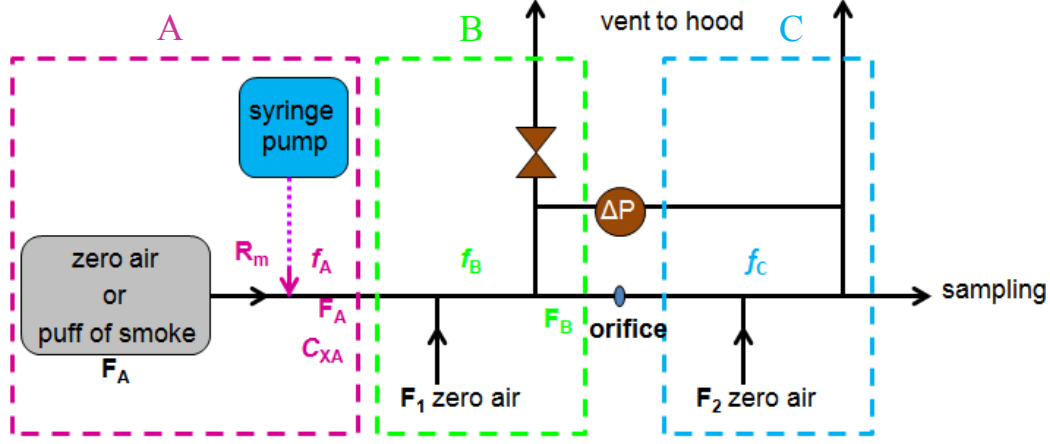
over time. A single experiment took more than an hour due to bag cleaning via flushing with zero air several times and preparation between samples.

### 2.3.2. Fast-Flow Tube

To allow many cigarette samples to be analyzed in triplicate with minimal cleaning demands, we designed a stainless steel flow tube as shown in Figure 2.1. This flow tube was capable of a fast dilution of the cigarette smoke to levels that the PTR-ToF-MS and CPC instruments can comfortably measure. In short, a puff of mainstream smoke entered the flow tube and was diluted by (1) an addition of zero air flow (labeled  $F_1$  in Fig. 2.1), (2) a passage of a small fraction of the flow through an orifice, and (3) a second addition of zero air flow (labeled  $F_2$  in Fig. 2.1). The diluted mainstream smoke was sampled at the end of the flow tube with the PTR-ToF-MS and CPC instruments; any excess smoke was vented to a hood. The conventional cigarettes were conditioned before the measurements as described in the previous section. The PTR-ToF-MS settings differed from the previous by a higher time resolution (1 s) that allowed nearly real-time measurements for a range of puff frequencies. The flow tube was typically operated under standard temperature and pressure conditions with Reynolds numbers ranging from ~200 to ~500 suggesting a laminar flow regime inside the flow tube.

Equations 2.1-2.6 were used for the calculations that described the concentrations of injected VOCs and particles in different sections of the flow tube setup. Note that these equations served as a guideline to the data analysis; the actual measurements relied on explicit calibration measurements described in the text. The parameters used in these equations include:  $R_m$  = mass delivery rate of injection of a specific chemical standard (by a cigarette or a calibration syringe pump);  $C_{XA}$  = concentration of chemical at stage “A”;  $F_A$  and  $F_B$  = flow of chemical at stage “A”

or “B”;  $f_A$ ,  $f_B$ , and  $f_C$  = fraction of flow of chemical in stage “A”, “B”, or “C”; and  $DF$  = dilution factor between stage “B” and stage “C”.



**Figure 2.1.** Diagram of the fast-flow tube setup, where  $F_A$  was the flow rate of either zero air or a puff of smoke delivered at 1.30 L/min;  $f_A$ ,  $f_B$ , and  $f_C$  were the volume fractions of a VOC in each region;  $R_m$  was the rate ( $\mu\text{g/s}$ ) of a VOC entering the flow tube;  $C_x$  was the initial concentration (molecules/ $\text{cm}^3$ ) of a VOC in the flow tube;  $F_1 = F_2$  were dilution flows of zero air (e-cigarette: 5 L/min, cigarette: 10 L/min); and  $\Delta P$  (e-cigarette: 52 torr, cigarette: 2.8 torr) was the pressure difference between sections B and C separated by a 1.25 mm orifice; the pressure difference was precisely set with a valve in section B.

$$R_m \left( \frac{\mu\text{g}}{\text{s}} \right) = R_v \left( \frac{\mu\text{L}}{\text{hr}} \right) \cdot \frac{10^{-3} \text{cm}^3}{\mu\text{L}} \cdot \frac{1 \text{hr}}{3600 \text{s}} \cdot \rho \left( \frac{\text{g}}{\text{cm}^3} \right) \cdot \frac{10^6 \mu\text{g}}{\text{g}} \quad (\text{Eq. 2.1})$$

$$R_N \left( \frac{\text{molec}}{\text{s}} \right) = R_m \left( \frac{\text{g}}{\text{s}} \right) \cdot \frac{N_A}{MW \left( \frac{\text{g}}{\text{mol}} \right)} \quad (\text{Eq. 2.2})$$

$$C_{XA} \left( \frac{\text{molec}}{\text{cm}^3} \right) = \frac{R_N \left( \frac{\text{molec}}{\text{s}} \right)}{F_A \left( \frac{\text{cm}^3}{\text{s}} \right)}, \text{ assuming STP inside flowtube} \quad (\text{Eq. 2.3})$$

$$f_A = \frac{C_{XA} \left( \frac{\text{molec}}{\text{cm}^3} \right)}{C_0 \left( \frac{\text{molec}}{\text{cm}^3} \right)}, \text{ assuming STP inside flowtube} \quad (\text{Eq. 2.4})$$

$$f_B = f_A \cdot \frac{F_A \left( \frac{cm^3}{s} \right)}{F_A \left( \frac{cm^3}{s} \right) + F_1 \left( \frac{cm^3}{s} \right)}, \text{ assuming STP inside flowtube} \quad (\text{Eq. 2.5})$$

$$f_C = f_B \cdot \frac{F_B \left( \frac{cm^3}{s} \right)}{F_B \left( \frac{cm^3}{s} \right) + F_2 \left( \frac{cm^3}{s} \right)} \Rightarrow f_B \cdot DF \quad (\text{Eq. 2.6})$$

### 2.3.3. Sampling

Various cigarette types listed in Table 2.1 were chosen to study the tar and filter type dependence of the VOC and particle emissions. Experiments for each cigarette were done in triplicate at each puff frequency of 1, 2, 3, or 4 puffs/min. The unfiltered-6 cigarette typically extinguished at 1 puff/min and we only provide data for this cigarette at frequencies of 2, 3, and 4 puffs/min. The puff pump operated at a flow of 1.30 L/min with a 2s puff duration to provide for a total mainstream smoke puff volume of ~43 ml. The flow was set at this level in order to overcome any back pressure from the dilution flow. Although this study was not intended to mimic human smoking behavior, the smoking conditions used in these experiments can be considered to be similar to that of a more intense tobacco cigarette smoker and/or a hybrid e-cigarette smoker with a flow rate used by slow average e-cigarette users, but with half the volume being vaped.<sup>41</sup> Larger flows may be required for e-cigarette puffing than conventional cigarettes and is variable between brands.<sup>42, 43</sup> The conventional cigarettes and e-cigarette, e-cigarette-2 (16 mg nicotine/cartridge, propylene glycol, 3.7 V), had different dilution flows of zero air ( $F_1=F_2$ ) and pressure drops ( $\Delta P$ ) in the flow tube to make the measured signal consistent with dynamic ranges of the PTR-ToF-MS and CPC instruments. The conventional cigarettes and e-cigarette were diluted by a factor of ( $\sim 10^3$ ) and ( $\sim 10^2$ ), respectively, with the exact dilution factor determined from a calibration. The conventional cigarettes ( $F_1=10$  L/min,  $\Delta P=2.8$  torr)

**Table 2.1.** Tar and nicotine content of e-cigarettes and conventional cigarettes. Cigarettes were numbered to differentiate between brands. E-cigarette-1 contained propylene glycol with a voltage of 3.6 V and e-cigarette-2 contained vegetable glycerin with a voltage of 3.7 V. Charcoal-3 and charcoal-4 cigarettes have a charcoal mass loading<sup>ε</sup> of 37 mg and 50 mg. All cigarettes were contained in hard pack boxes except for the unfiltered-6 cigarette.

Cigarette Type	Tar (mg/cig)	Nicotine (mg/cig)	Length (mm)	Circumference (mm)
e-cigarette-1	0	0.58	115 <sup>ε</sup>	29 <sup>ε</sup>
e-cigarette-2	0	0.54	87 <sup>ε</sup>	27 <sup>ε</sup>
1R5F <sup>*α</sup>	1.67	0.16	84	25
3R4F <sup>*α</sup>	9.40	0.73	84	25
charcoal-3 <sup>*γ</sup>	8.00	0.70	84	25
charcoal-4 <sup>*β</sup>	10.0	0.90	84	25
menthol light-5 <sup>*β</sup>	6.00	0.50	84	25
light-6 <sup>*δ</sup>	10.0	0.80	84	25
original-5 <sup>*β</sup>	12.0	0.80	84	25
original-6 <sup>*δ</sup>	16.0	1.20	84	25
unfiltered-6 <sup>δ</sup>	25.0	1.70	84	25

\*Denotes the presence of a cellulose acetate filter.

<sup>α</sup> Obtained from the University of Kentucky (2015); tar and nicotine content was measured by FTC method.

<sup>β</sup> Tar and nicotine content obtained from advertisements.

<sup>γ</sup> International Organization for Standards (ISO) tar and nicotine yields from the Government of the Hong Kong Special Administrative Region (2014).

<sup>δ</sup> Federal Trade Commission (FTC) yields from the Federal Trade Commission (1998).

<sup>ε</sup> Measured in this study.

were calculated to be diluted 24 times more than the e-cigarette ( $F_1=5$  L/min and  $\Delta P=52$  torr) by comparing the PTR-ToF-MS signals between the two flow settings (with the linearity of PTR-ToF-MS verified in a separate experiment). A conventional cigarette was lit upon the first puff whereas the e-cigarette would generate smoke only during the puffing mechanism. The battery of the e-cigarette was fully charged before each puff frequency experiment. A new cartridge was used for each different set (1, 2, 3, or 4 puffs/min) of puff frequency experiments. A separate experiment that looked at the puff number dependence of VOC and particle emissions in an e-cigarette was performed. The battery was recharged 4 times throughout the experiment. The

variation in the VOC and particle emissions in the e-cigarette from sampling at different puff numbers of the cartridge lifetime were included in the values' uncertainties as the triplicate experiments were performed in both increasing and decreasing order of puff frequency.

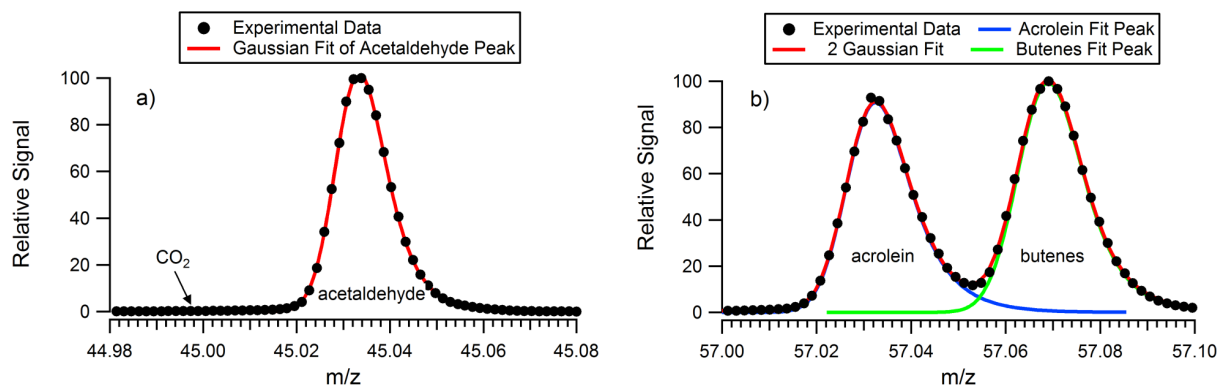
In a separate set of experiments, particles of e-cigarette-2 were gravimetrically analyzed by collection on clean foil substrates using a multi-orifice uniform-deposit impactor (MOUDI, MSP model 110-R) sampling at 30 SLM under two different dilution settings: (1) dilution by a factor of 13 with all the smoke being sent in the MOUDI; (2) dilution by a factor of 190 similar to the fast flow tube, but with a fraction of the smoke being sent in the MOUDI.

#### **2.3.4. Emissions**

The PTR-ToF-MS data were analyzed for the largest changes in the  $m/z$  peak intensities that represented a protonated parent species,  $[M+H]^+$ , between a puff of mainstream smoke and background. From there, select  $m/z$  peaks that were considered reasonably free from any influence of possible fragmentation of larger VOCs<sup>44</sup> were chosen for calibration experiments. In order to calibrate the PTR-ToF-MS, a syringe pump was loaded with a 50  $\mu$ L syringe filled with acetaldehyde (> 95 %), acetone, acetonitrile, acrolein (> 95 %), or methanol and delivered at varying rates on a  $\mu$ L/hr scale. All chemicals were purchased from Sigma-Aldrich. Calibration plots were created for PTR-ToF-MS parent  $m/z$  signals as a function of the mass delivery rate (see Equations 2.1-2.6),  $R_m(\mu\text{g/s})$ , for methanol ( $m/z$  33), acetonitrile ( $m/z$  42), acetaldehyde ( $m/z$  45), acrolein ( $m/z$  57), and acetone ( $m/z$  59). As the PTR-ToF-MS cannot distinguish structural isomers, the  $m/z$  59 peak represents the combined acetone and propanal signal, where the former has the larger contribution in conventional cigarettes.<sup>45-47</sup> An example of mass spectra near  $m/z$  45 and  $m/z$  57 is shown in Figure 2.2. The PTR-ToF-MS signal for the protonated carbon dioxide peak ( $[\text{CO}_2 + \text{H}]^+$ ,  $m/z$  44.998) was not detected in this study, as its proton affinity is too



low relative to that of water and major VOCs of the cigarette smoke. However, if this peak was present, it would still be well separated from the acetaldehyde peak ( $m/z$  45.034). Similarly, the acrolein peak ( $m/z$  57.034) was well separated from that of the butenes peak ( $m/z$  57.070). The flow that passed through the orifice (labeled  $F_B$  in the equations in Equation 2.6) was unknown and following the equations that describe the flow tube the dilution factor,  $DF$ , was necessary to determine the particle concentration before dilution. A separate acetone calibration was performed in a Teflon™ bag which involved flowing zero air past an injection port where acetone was added. This calibration was applied to an acetone syringe pump experiment to get the diluted fraction of acetone at the end of the flow tube,  $f_c$ , to calculate  $DF$ , in equation 2.6, where the initial fraction,  $f_A$ , of acetone was calculated using equations 2.1-2.4.



**Figure 2.2.** PTR-ToF-MS mass spectra of well resolved  $[M+H]^+$  peaks for the fifth puff of a 3R4F cigarette: a)  $CO_2$  ( $m/z$  44.998) was not detected, but acetaldehyde ( $m/z$  45.034) was clearly observed; b) both the acrolein ( $m/z$  57.034) and butenes ( $m/z$  57.070) are well resolved.

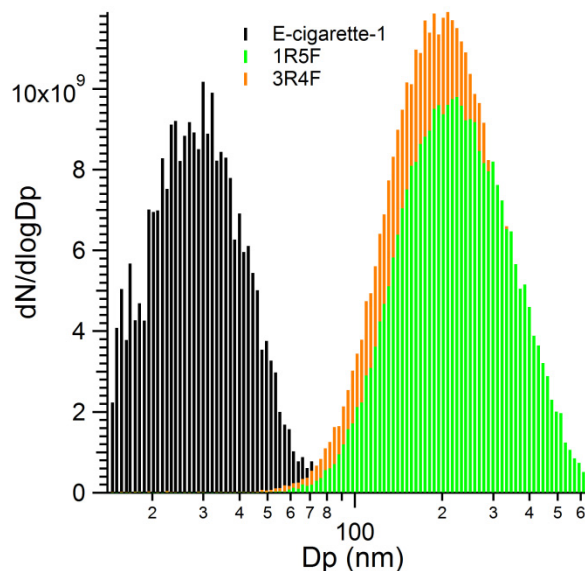
The e-cigarette data were compared to the conventional cigarette data by taking into account the difference in dilutions in order to express all measurements in easily interpretable units of “overall amount emitted per puff”. The PTR-ToF-MS raw data were converted to a mass delivery rate, summed over the 2 s puff, and dilution-corrected to give the amount ( $\mu g$ ) of each

VOC of interest per puff. The CPC data were dilution-corrected to give particle concentration,  $\#/cm^3$  in the puff and that was further multiplied by the puff volume to give the total amount of particles per puff. The lifetime of the conventional cigarettes was assumed to be 9 puffs in order to compare total VOC and particle emissions between each type of cigarette. We wrote a MATLAB code that would take in extracted PTR-ToF-MS VOC signal files and calculate areas of individual puffs for each sample.

## 2.4. Results and Discussion

### 2.4.1. Chamber Experiments

A representative plot of the particle size distributions of the diluted 5<sup>th</sup> puff of cigarettes e-cigarette-1, 1R5F, and 3R4F is shown in Figure 2.3. The dilution corrected particle number concentrations (also normalized by the total particle number concentrations measured through the CPC) in the puffs for the e-cigarette-1, 1R5F, and 3R4F samples were  $4.0 \cdot 10^9$ ,  $4.8 \cdot 10^9$ , and  $5.7 \cdot 10^9 \#/cm^3$ , respectively. Conventional cigarettes have particle diameters ranging from 140-340 nm and number concentrations on the order of  $10^9 \#/cm^3$ .<sup>24, 26-28, 48</sup> E-cigarette particle number concentrations have been found to be of the same order of magnitude.<sup>5, 29, 33, 34</sup> The small particle diameter, 30 nm, of e-cigarette-1 was most likely due to the high dilution of the smoke where most of the water and volatile components have evaporated before sampling.<sup>5, 11</sup> Ingebrethsen et al.<sup>29</sup> found particle diameters with an electrical mobility analyzer of 2 s puffs of two cartomizer electronic cigarettes to be of diameters 14 nm and 21 nm, but the same samples characterized with a spectral extinction approach were found to have diameters of 300 nm and 240 nm, respectively. Therefore, it was reasonable to expect that the e-cigarette particle



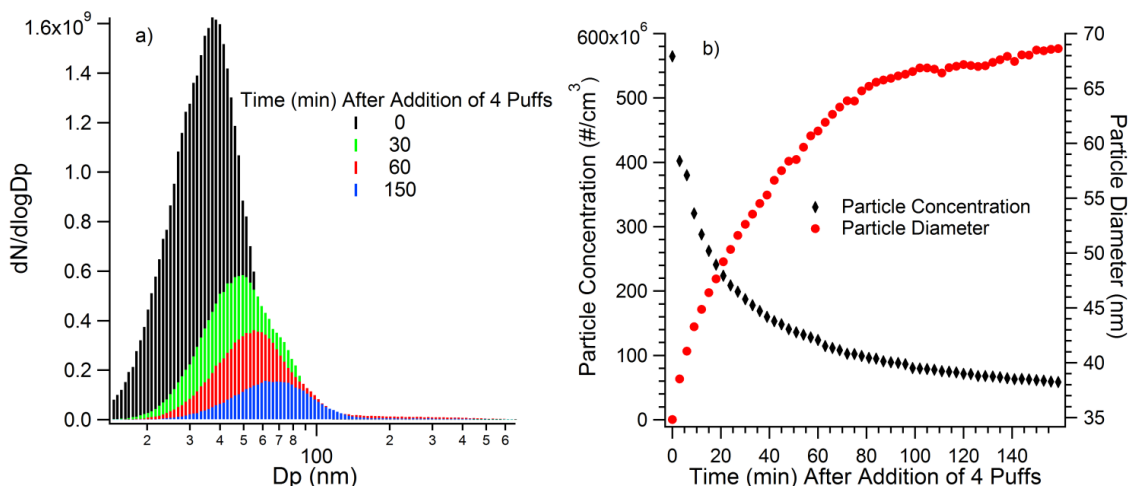
**Figure 2.3.** Particle size distribution observed after injecting a single puff (from E-cigarette-1, 1R5F, or a 3R4F cigarette) in a Teflon™ chamber filled with zero air. This data set was normalized to the total particle number concentrations data measured directly with the CPC and was then multiplied by the dilution factor.

diameters should have significantly decreased upon dilution. The e-cigarette-1 particles of this study that were diluted by a factor of  $10^3$  and measured with the SMPS instrument had similar particle size diameters as the e-cigarette particles in the study by Ingebrethsen et al.<sup>29</sup> that relied on an electrical mobility analyzer and also diluted the puffs by a factor of  $10^3$ .

A bimodal distribution of e-cigarette particles from a single 4.3 s puff centered around 50 nm and 250 nm (estimated from their Figure 2.4B) was observed by Williams et al.<sup>31</sup> using an SMPS. Schripp et al.<sup>11</sup> also saw a bimodal distribution at particle diameters of 30 nm and 100 nm for a 3 s puff of a tank system e-cigarette. Much larger particle diameters, 600 nm from a cartridge without nicotine and 650 nm from a cartridge with nicotine, were found by Bertholon et al.<sup>30</sup> using an ELPI that analyzed ten 2 s *successive* puffs of a cartomizer e-cigarette. A study by Zhang et al.<sup>32</sup> on a cartomizer e-cigarette found that for a single puff the particle diameters were 117 nm and 180 nm for cartridges with propylene glycol and vegetable glycerin. When the e-

cigarette was sampled at a steady state such that the concentrated aerosol aged via condensation of vapors and coagulation, the particle size distribution was found to be bimodal; a small peak with a diameter near that of a single puff, and a larger peak more than twice the diameter of the smaller one was observed. This steady state aging may also explain the larger diameter particles observed by Bertholon et al.<sup>30</sup> since 10 puffs were combined. Fuoco et al.<sup>33</sup> found that the aerosol from a 2 s puff of a tank system e-cigarette with varying nicotine and flavoring content had particle diameter of 120-165 nm; a smaller mode of 10 nm was only seen with an FMPS and was considered to be an artifact. Particle diameters of 107-165 nm for a variety of e-cigarette cartridges of differing nicotine levels and flavorings was found by Manigrasso et al.<sup>34</sup> The absence of a larger mean particle diameter in the present e-cigarette-1 measurements may either be from evaporation or wall loss as the aerosol aged with time for 15 min before analysis. Geiss et al.<sup>5</sup> found that particles larger than 300 nm would immediately drop in number concentration after puffing, owing to their higher vapor pressure. The particle size distribution and concentration for the combined 4 puff experiment is shown in Figure 2.4. The particle diameter was twice as large as the single puff diameter as the smoke reached a steady state, a behavior similar as that seen by Zhang et al.,<sup>32</sup> although the particles were not as large and were not bimodal.

The acrolein data from the PTR-ToF-MS chamber experiments are listed in Table 2.2. Thweatt et al.<sup>23</sup> analyzed 1R5F cigarettes and found that the 5<sup>th</sup> puff contained 1.90  $\mu\text{g}$  of acrolein (estimated from their Figure 2.6) and that of the 1R5F cigarette was 15  $\mu\text{g}$  (also observed by Uchiyama et al.<sup>46</sup>) where the lifetime of the cigarette was 9 puffs (this was used to scale the 5<sup>th</sup> puff data in this study to per cigarette quantities). The values in our chamber study agree within uncertainty with previous literature values. Both studies by Roemer et al.<sup>12</sup> and



**Figure 2.4.** Particle size distribution (a), particle concentration, and particle diameter (b), of e-cigarette-1 observed after injecting 4 successive puffs in a Teflon™ chamber filled with zero air. The data were corrected for dilution to reflect the concentrations in the puff volume.

**Table 2.2.** Emitted masses of acrolein measured in mini-chamber experiments.

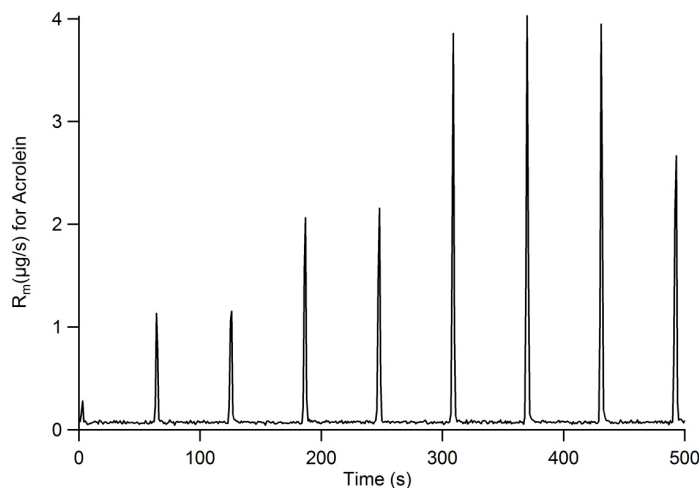
Cigarette Type	Acrolein ( $\mu\text{g}/5^{\text{th}}$ puff)	*acrolein ( $\mu\text{g}/\text{cigarette}$ )
1R5F	$2.43 \pm 0.56$	$21.9 \pm 5.0$
3R4F	$2.99 \pm 1.13$	$26.9 \pm 10.2$
e-cigarette-1	$0.290 \pm 0.018$	$2.61 \pm 0.16$

\*values based on assuming a cigarette lifetime of 9 puffs

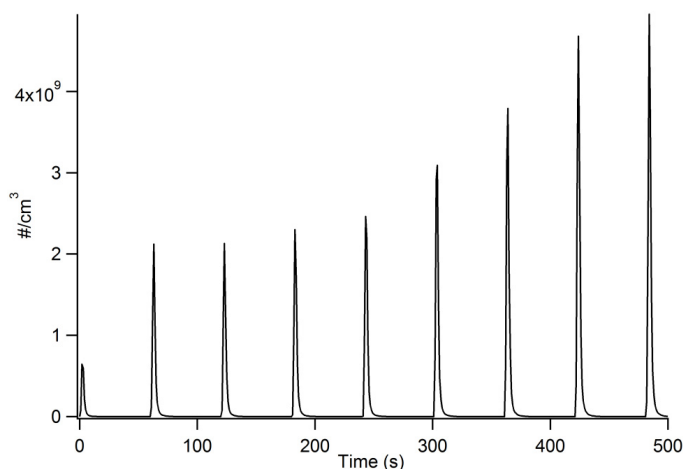
Uchiyama et al.<sup>46</sup> found acrolein values for a 3R4F puff to be 56  $\mu\text{g}/\text{cigarette}$ , whereas the acrolein content found in the chamber study was about half that amount (27  $\mu\text{g}/\text{cigarette}$ ), but the flow tube experiment result was similar (66  $\mu\text{g}/\text{cigarette}$ ). Although acrolein was not detected in e-cigarettes by Kosmider et al.,<sup>49</sup> it was mentioned that it may be a lower bound due to experimental limitations. Both Goniewicz et al.<sup>50</sup> (upper limit value scaled down from the amount/150 puffs) and Tayyarah and Long<sup>51</sup> found  $\sim 0.2$   $\mu\text{g}/\text{puff}$  of acrolein in e-cigarettes studied similar to that observed in our chamber study, but Geiss et al.<sup>5</sup> found smaller amounts ranging from 0.5-13.5 ng/puff.

#### **2.4. 2. Real-Time Fast-Flow Tube Data**

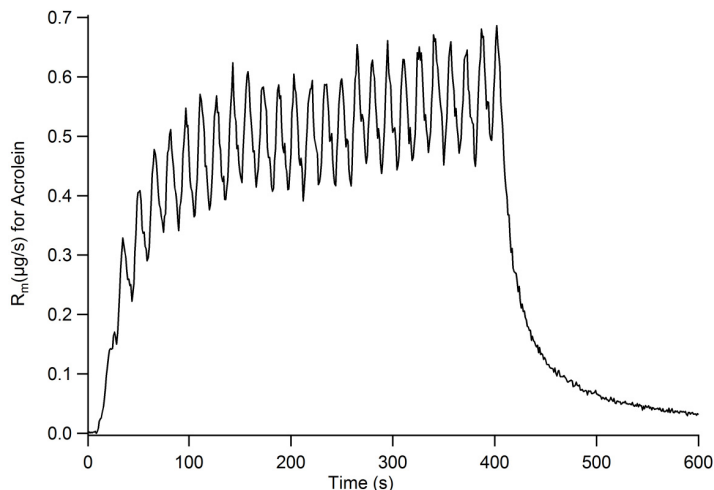
An example PTR-ToF-MS acrolein time profile for 1R5F puffing at 1 puff/min frequency is shown in Figure 2.5 and a corresponding time profile of particle concentration is shown in Figure 2.6. Frequencies other than 1 puff/min for e-cigarette-2 did not allow enough time for the PTR-ToF-MS signals to reach baseline before the next puff; an example of this convolution of peaks for acrolein is seen in Figure 2.7 (the particle time profile did not exhibit this problem as can be seen in Figure 2.8). The amount of VOC and particle concentration increases with puff number for conventional cigarettes tested here, but not for the e-cigarette, e-cigarette-2, which had no puff number dependence. Kane et al.<sup>28</sup> also observed an increase in particle concentration with puff number in several Kentucky reference cigarettes. A time profile of acrolein and particle concentration for all samples is seen in Figure 2.9. There was no quantifiable difference in the total amount of VOCs in the cigarettes for different puff frequencies as can be seen in Figure 2.10. The main contributing factor to the uncertainties in this study was from the variability between cigarettes of the same brand and type. The particle counts of the cigarettes have no significant puff frequency dependence, except for menthol light-5 and original-5 where the 1 puff/min frequency had somewhat larger particle emissions than the other frequencies as seen in Figure 2.11.



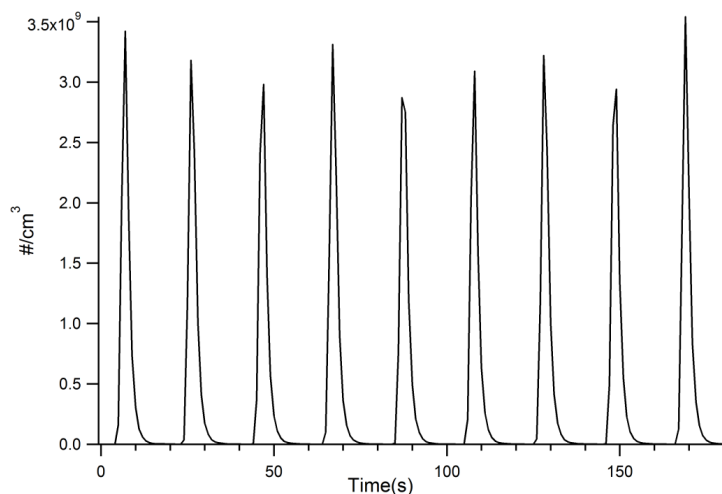
**Figure 2.5.** PTR-ToF-MS time profile of 1R5F at a frequency of 1 puff/min for fast flow tube experiments. The contributions from the individual puffs are clearly resolved with the present time resolution. The first spike near  $t = 0$  corresponds to the 1st puff and there are 9 puffs total.



**Figure 2.6.** CPC time profile of 1R5F at a frequency of 1 puff/min for fast flow tube experiments. The first spike near  $t = 0$  corresponds to the 1st puff and there are 9 puffs total.

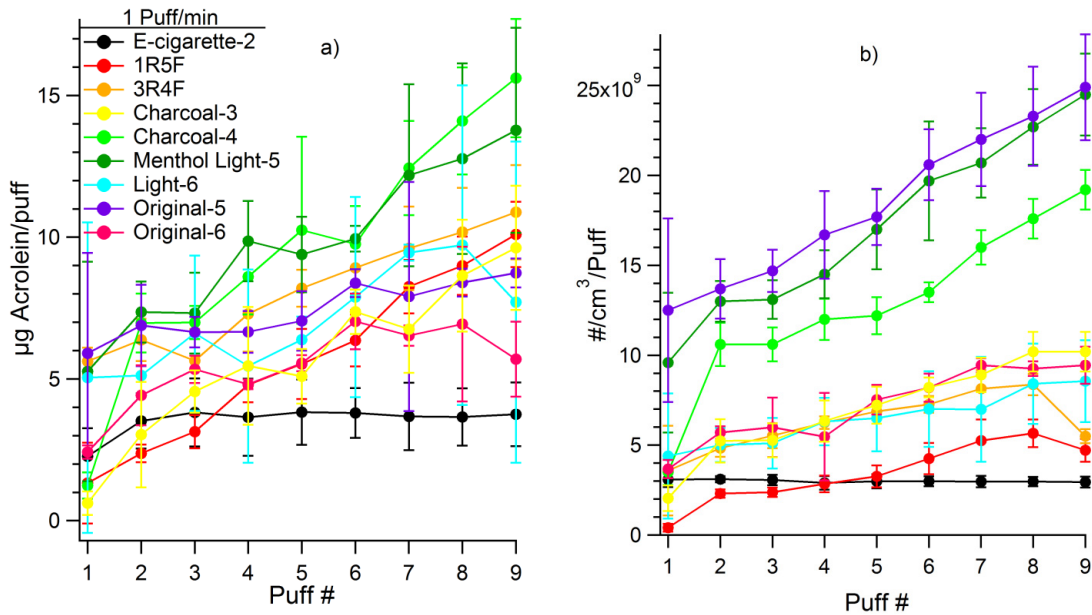


**Figure 2.7.** PTR-ToF-MS time profile of e-cigarette-2 at a frequency of 4 puff/min for fast flow tube experiments. As this figure shows, the contributions from different puffs would overlap at higher puff frequencies complicating the quantitative analysis of the PTR-ToF-MS data. Therefore, most PTR-ToF-MS measurements reported in this thesis were done at 1 puff/min puffing rate.

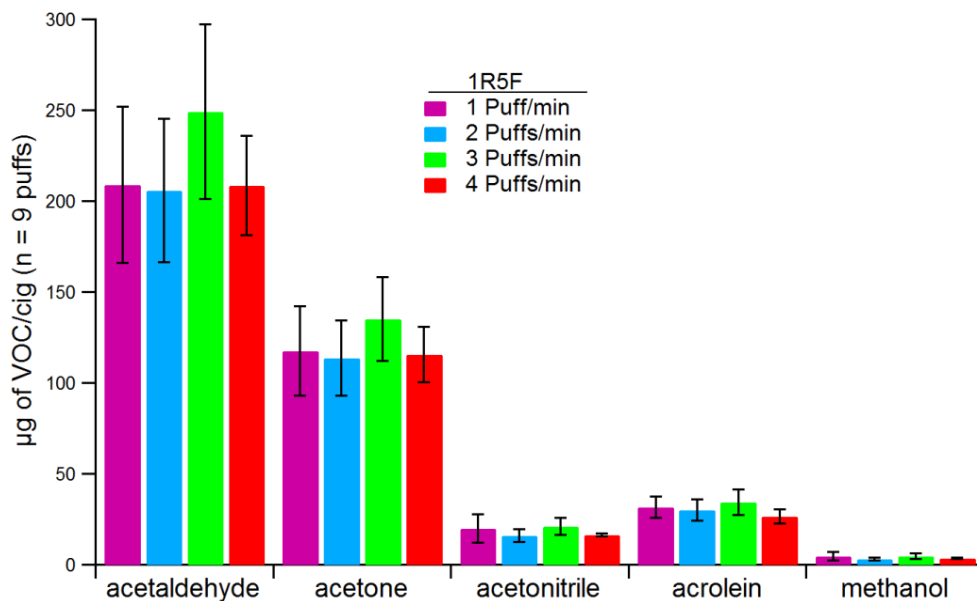


**Figure 2.8.** CPC time profile of e-cigarette-2 at a frequency of 4 puff/min for fast flow tube experiments. The first spike near  $t=0$  corresponds to the 1st puff and there are 9 puffs total. Unlike the convoluted PTR-ToF-MS signal shown in Figure 2.7, the CPC signal for each puff was clearly resolved even at the highest puff frequency probed here (4 puff/min).

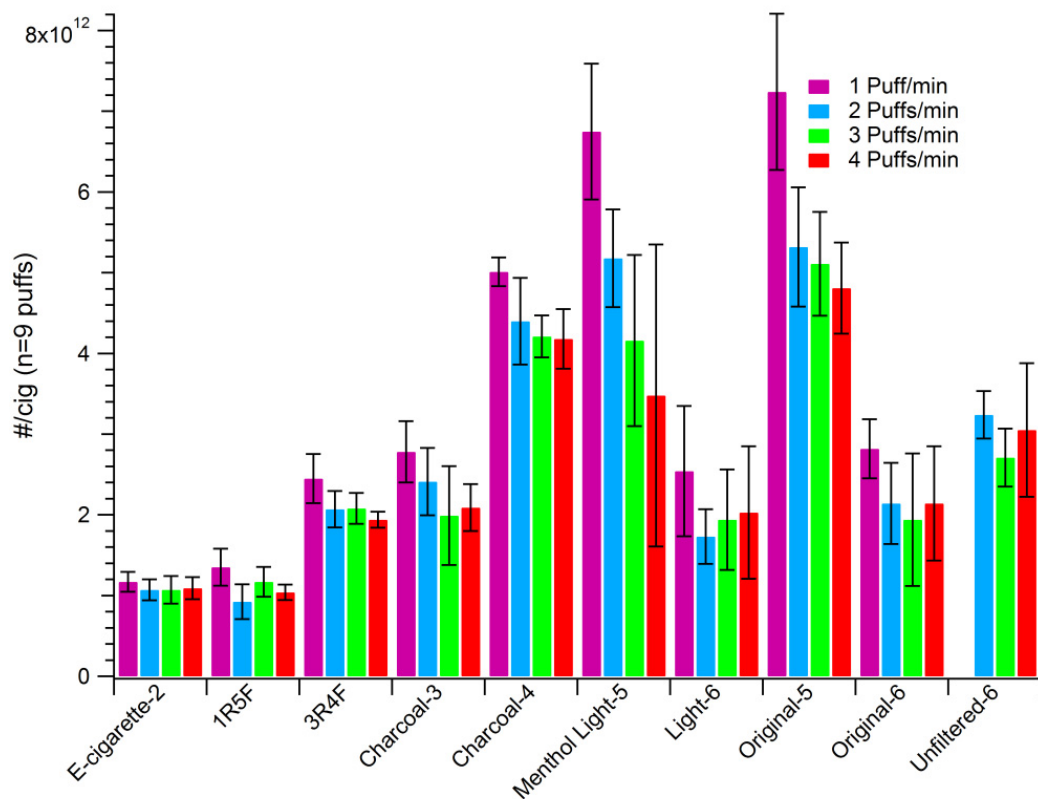




**Figure 2.9.** Amount of acrolein (a) and particles (b) per puff for a puff frequency of 1 puff/min measured in fast flow tube experiments.

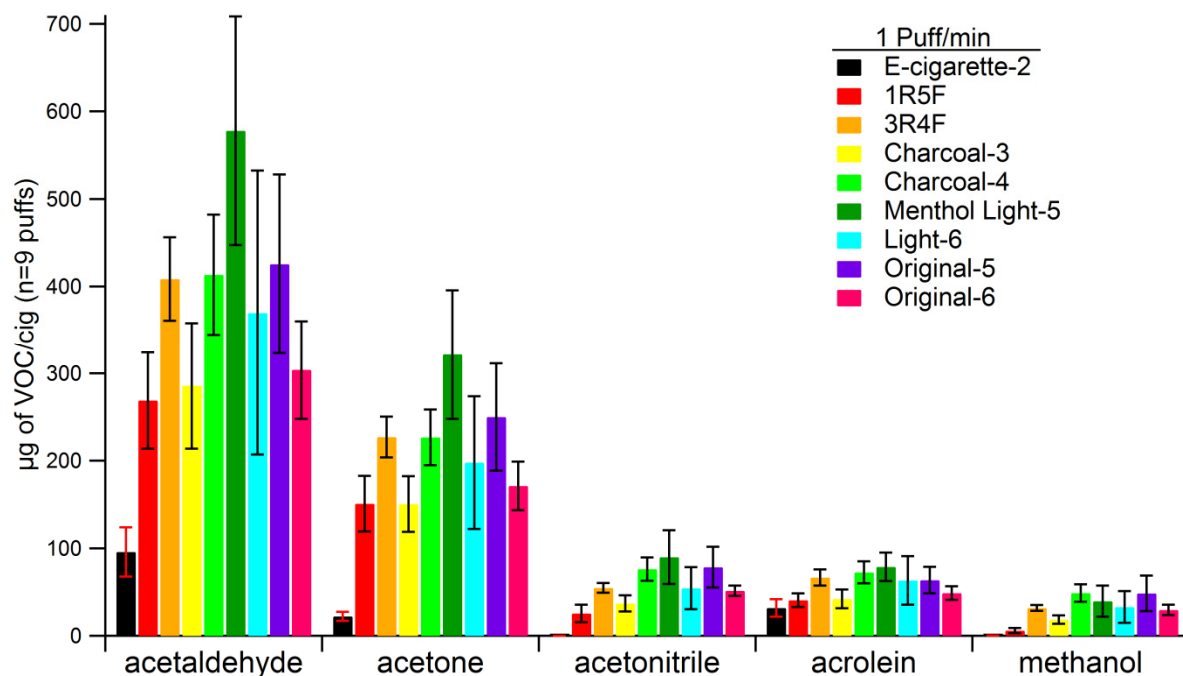


**Figure 2.10.** Puff frequency dependence of selected VOCs emitted by 1R5F in fast flow tube experiments. There is no quantifiable difference in the VOCs in the cigarettes for different puff frequencies.



**Figure 2.11.** Puff frequency dependence of the number of particles emitted in fast flow tube experiments. The particle concentration similarly has no puff frequency dependence except for menthol light-5 and original-5 where the 1 puff/min frequency had somewhat larger particle emissions than the other frequencies.

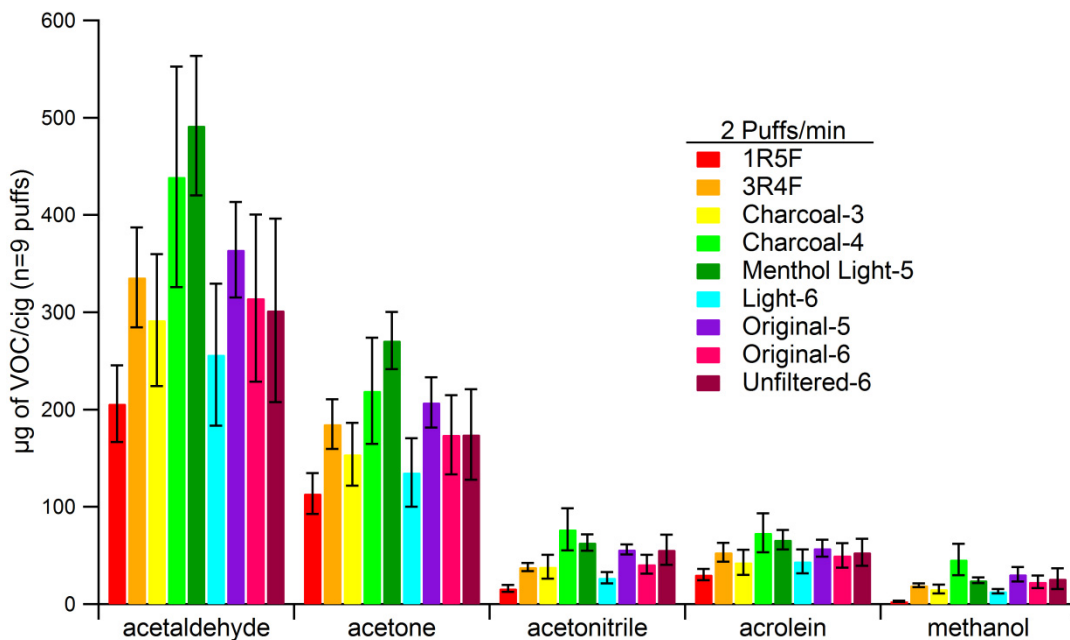
Acetaldehyde, acetone, and acrolein can form from thermal decomposition of sugars, cellulose, pectin, triglycerides, and glycerol.<sup>1, 52</sup> Acetonitrile may be formed by nitrogen sources that form ammonia as an intermediate, such as tobacco pigments and proteins. Tobacco leaves can produce methanol from cell signaling, but it can also be formed from other pyrolysis processes of pectin during smoking. The amounts of acetaldehyde, acetone, acetonitrile, acrolein, and methanol for samples are shown in Figure 2.12 (values listed in Table 2.3) for the puff frequency of 1 puff/min. Similar data for puff frequencies of 2, 3, and 4 puffs/min are seen in Figures 2.13-2.15 and Tables 2.4-2.6. Of the selected VOCs in the cigarettes, acetaldehyde and



**Figure 2.12.** Amount of selected VOCs in an e-cigarette and conventional cigarettes for a puff frequency of 1 puff/min in fast flow tube experiments. The values were based on assuming a cigarette lifetime of 9 puffs.

**Table 2.3.** Amount ( $\mu\text{g}$  in 9 puffs) of selected VOCs emitted by an e-cigarette and conventional cigarettes for a puff frequency of 1 puff/min in fast flow tube experiments. Numbers in parentheses represent standard deviations for  $n=3$  samples.

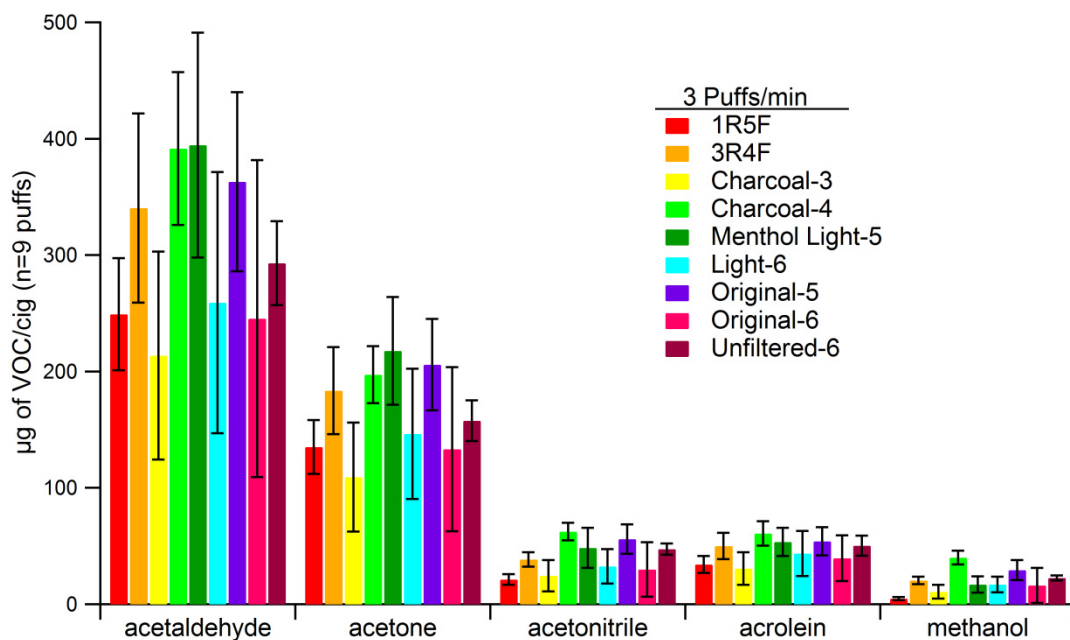
Cigarette Type	Acetaldehyde	Acetone	Acetonitrile	Acrolein	Methanol
e-cigarette-2	95.9 (28.3)	22.0 (5.0)	$8.85 (2.14) \cdot 10^{-2}$	32.0 (9.9)	0.292 (0.025)
1R5F	269 (55)	151 (32)	25.7 (10.1)	40.9 (7.8)	5.80 (2.84)
3R4F	409 (48)	227 (23)	54.6 (5.5)	66.4 (9.4)	31.7 (3.3)
charcoal-3	413 (69)	227 (32)	76.2 (13.4)	72.3 (12.5)	48.9 (10.0)
charcoal-4	286 (72)	150 (32)	37.2 (9.3)	42.3 (10.8)	18.4 (4.7)
menthol light-5	578 (130)	322 (74)	90.0 (30.6)	78.9 (16.4)	39.6 (17.7)
light-6	370 (163)	198 (76)	54.5 (24.0)	63.4 (27.6)	32.8 (18.1)
original-5	426 (103)	250 (61)	78.3 (23.5)	63.6 (15.2)	48.5 (20.2)
original-6	304 (56)	171 (28)	51.6 (5.9)	48.8 (7.6)	29.6 (6.2)



**Figure 2.13.** Amount of selected VOCs in conventional cigarettes for a puff frequency of 2 puffs/min in fast flow tube experiments.

**Table 2.4.** Amount ( $\mu\text{g}$  in 9 puffs) of selected VOCs emitted by conventional cigarettes for  $n=3$  samples and (standard deviation) for a puff frequency of 2 puffs/min in fast flow tube experiments.

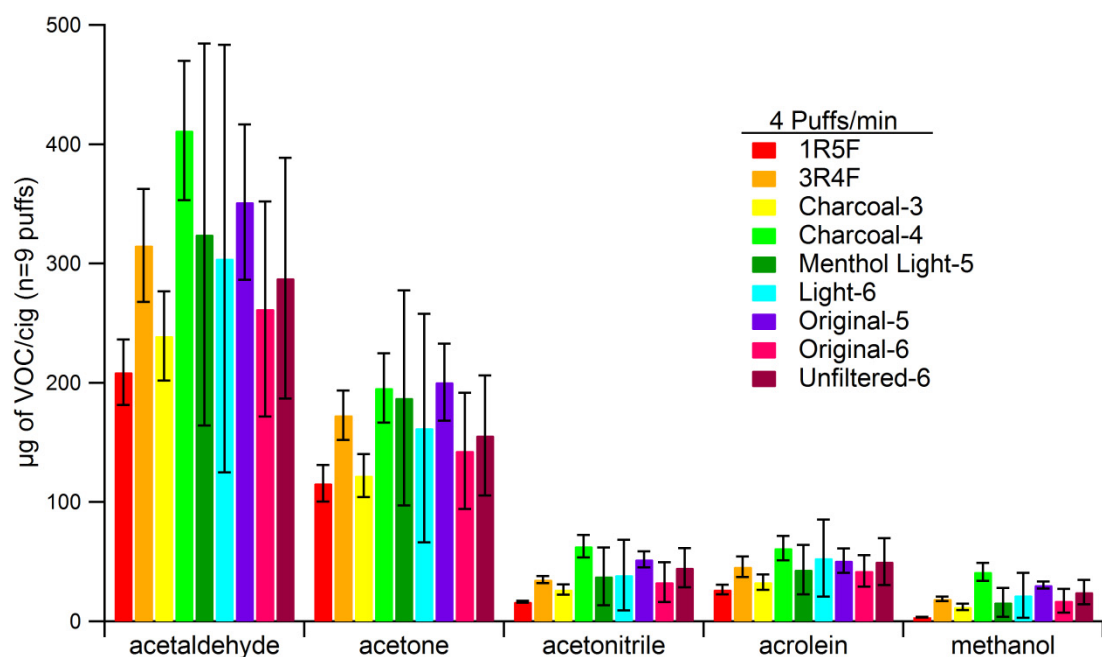
Cigarette Type	Acetaldehyde	Acetone	Acetonitrile	Acrolein	Methanol
1R5F	206 (40)	114 (21)	16.1 (3.7)	30.2 (5.8)	2.96 (0.69)
3R4F	336 (52)	185 (25)	38.3 (4.2)	53.2 (9.7)	19.5 (2.0)
charcoal-3	292 (68)	154 (32)	38.4 (12.3)	43.1 (12.9)	15.4 (4.5)
charcoal-4	439 (113)	219 (55)	76.8 (21.8)	73.4 (20.0)	45.9 (16.3)
menthol light-5	492 (72)	271 (29)	63.3 (8.3)	66.4 (10.2)	24.6 (3.0)
light-6	256 (73)	135 (35)	27.2 (5.8)	43.9 (12.3)	13.4 (2.2)
original-5	364 (49)	207 (26)	56.1 (5.1)	57.4 (8.6)	30.8 (7.3)
original-6	315 (86)	174 (41)	40.9 (9.8)	50.1 (12.6)	22.8 (6.6)
unfiltered-6	302 (94)	175 (46)	56.0 (15.6)	53.4 (13.9)	26.2 (10.8)



**Figure 2.14.** Amount of selected VOCs in conventional cigarettes for a puff frequency of 3 puffs/min in fast flow tube experiments.

**Table 2.5.** Amount ( $\mu\text{g}$  in 9 puffs) of selected VOCs emitted by conventional cigarettes for  $n=3$  samples and (standard deviation) for a puff frequency of 3 puffs/min in fast flow tube experiments.

Cigarette Type	Acetaldehyde	Acetone	Acetonitrile	Acrolein	Methanol
1R5F	249 (48)	135 (23)	21.2 (4.7)	34.3 (7.2)	4.76 (1.37)
3R4F	341 (81)	184 (38)	38.6 (6.2)	50.0 (11.3)	20.6 (3.3)
charcoal-3	214 (89)	109 (47)	24.5 (13.5)	30.6 (14.0)	10.7 (5.9)
charcoal-4	392 (66)	197 (24)	62.4 (7.7)	60.9 (5.9)	40.0 (5.9)
menthol light-5	395 (97)	218 (46)	48.3 (17.2)	53.7 (12.2)	17.0 (6.9)
light-6	259 (112)	147 (56)	32.5 (14.8)	43.6 (19.3)	16.8 (6.8)
original-5	363 (77)	206 (39)	55.8 (12.6)	54.0 (12.0)	29.4 (8.5)
original-6	245 (136)	133 (70)	29.8 (23.4)	39.6 (19.8)	16.1 (15.2)
unfiltered-6	293 (36)	158 (18)	47.3 (4.8)	50.4 (8.7)	22.5 (2.2)



**Figure 2.15.** Amount of selected VOCs in conventional cigarettes for a puff frequency of 4 puffs/min in fast flow tube experiments.

**Table 2.6.** Amount ( $\mu\text{g}$  in 9 puffs) of selected VOCs emitted by conventional cigarettes for  $n=3$  samples and (standard deviation) for a puff frequency of 4 puffs/min in fast flow tube experiments.

Cigarette Type	Acetaldehyde	Acetone	Acetonitrile	Acrolein	Methanol
1R5F	208.7 (27.4)	115 (15)	16.3 (0.8)	26.7 (4.1)	3.40 (0.27)
3R4F	315 (47)	173 (21)	35.1 (2.9)	45.6 (8.6)	19.0 (2.0)
charcoal-3	239 (37)	122 (18)	26.7 (4.2)	32.8 (6.5)	12.2 (2.7)
charcoal-4	411 (58)	196 (29)	62.9 (9.3)	61.4 (10.2)	41.3 (7.5)
menthol light-5	324 (160)	187 (90)	37.6 (24.2)	43.3 (20.7)	15.9 (12.0)
light-6	304 (179)	162 (96)	38.8 (29.6)	52.9 (32.4)	21.8 (18.8)
original-5	351 (65)	200 (32)	51.9 (6.7)	50.8 (10.4)	30.4 (3.0)
original-6	262 (90)	142.9 (48.7)	33.0 (16.6)	42.2 (13.3)	17.2 (10.0)
unfiltered-6	288 (101)	156 (50)	44.8 (16.5)	50.1 (19.6)	24.4 (10.2)

acetone were the most abundant. The reference cigarettes had ~3 times more acrolein in the flow tube experiments than in the chamber experiments and they agreed with previous literature<sup>12, 13, 23, 46</sup> for acetaldehyde, but the 1R5F values for acetone and acrolein were higher, whereas the corresponding 3R4F values were similar. E-cigarette-2 in the flow tube experiments had ~10 times more acrolein than e-cigarette-1 measured in the chamber experiments. E-cigarette-1 and e-cigarette-2 and their cartridges were from different brands which might have contributed to this difference. Another possible contributor to this difference may include acrolein loss to the Teflon™ walls in the chamber experiments as carbonyl groups and double bonds increase a compound's affinity to Teflon™ walls.<sup>53</sup>

Previous studies have found that almost all constituents in cigarette smoke have a positive correlation to tar content.<sup>54</sup> In this study e-cigarette-2, 1R5F, 3R4F, and original-5 follow the trend of increasing VOC emissions with increasing tar content. The charcoal cigarettes do not align with this trend, as the addition of a charcoal filter can decrease the amount of VOCs in smoke.<sup>55</sup> The charcoal-3 cigarette appeared to filter VOCs more efficiently than charcoal-4, which had 30% less charcoal loading. This can be seen by comparing VOC emissions of charcoal-3 and the 1R5F cigarette which has less than 25% the tar content of charcoal-3; VOC emissions were similar even though the tar content was different. The acetonitrile values also agreed with literature.<sup>56, 57</sup> There was no significant difference in the VOC emissions of charcoal-4 and the 3R4F cigarette which had similar tar content. The VOC content for brand 5 (menthol light-5 and original-5) and brand 6 (light-6 and original-6) cigarettes were more variable, but on average showed the opposite trend in that the lowest tar containing cigarette, menthol light-5, had the largest VOC emissions. Greg et al.<sup>54</sup> observed that filter ventilation had a greater correlation to tar content than filter type. The cigarettes that

deviated from the positive tar/VOC correlation other than the previously explained charcoal cigarettes were those that all had cellulose acetate filters. The variability in the VOC correlation to tar content was most likely due to filter ventilation which can have a larger degree in the reduction of VOCs than particles,<sup>58</sup> although we point out again that filter ventilation data was not available for the conventional cigarettes in this study, to the best of the authors' knowledge.

Although it was not possible to run particle size distributions and mass concentration measurements of cigarette smoke with the SMPS under experimental conditions of the flow tube, particle number concentrations were analyzed. For the 1 puff/min data, e-cigarette-2 was more similar to particle counts than VOC emissions of conventional cigarettes, especially the 1R5F cigarette. After these, in increasing order of particle count, were 3R4F, light-6, charcoal-3, original-6, charcoal-4, menthol light-5, and then original-5 cigarettes. The relative ratios of VOCs between cigarettes that changed for particle counts between cigarettes include e-cigarette-2, charcoal-3, charcoal-4, original-5, light-6 which have all appeared to increase except for that of the latter which decreased relative to the other cigarettes. One cannot expect the relative ratios of charcoal cigarette VOCs to other cigarettes to be the same for particle counts, as charcoal filters mainly reduce VOC levels. It was surprising to see that the largest tar containing cigarettes, unfiltered-6 and original-6, did not have the largest particle counts. One cannot further evaluate particle count results with the tar content in mind without further mass information of particles of cigarettes in this study.

In conventional cigarettes, the pyrolytic generation of acrolein from glycerol would contribute 30% more by weight than just bulk tobacco which contributes 5% to the total acrolein.<sup>1</sup> Although e-cigarettes don't involve combustion, cartridge solutions containing mainly vegetable glycerin or propylene glycol may be oxidized electrochemically. Ohta et al.<sup>14</sup> found

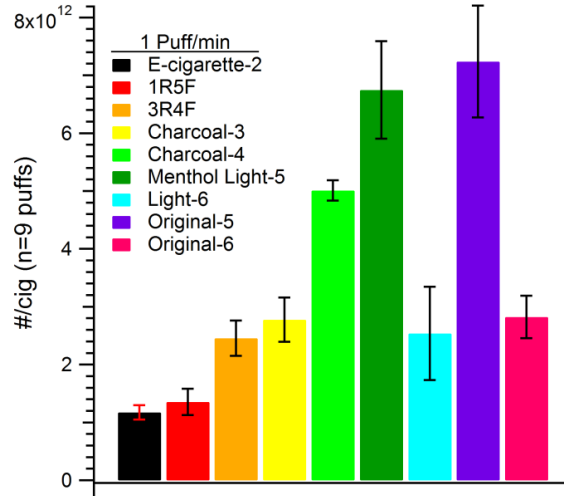


that carbonyls increased at a battery output over 3V and Kosmider et al.<sup>49</sup> saw an increase in carbonyls as the voltage increased from 3.2-4.8 V. These products of vegetable glycerin are seen from e-cigarette-2 in Figure 2.12.

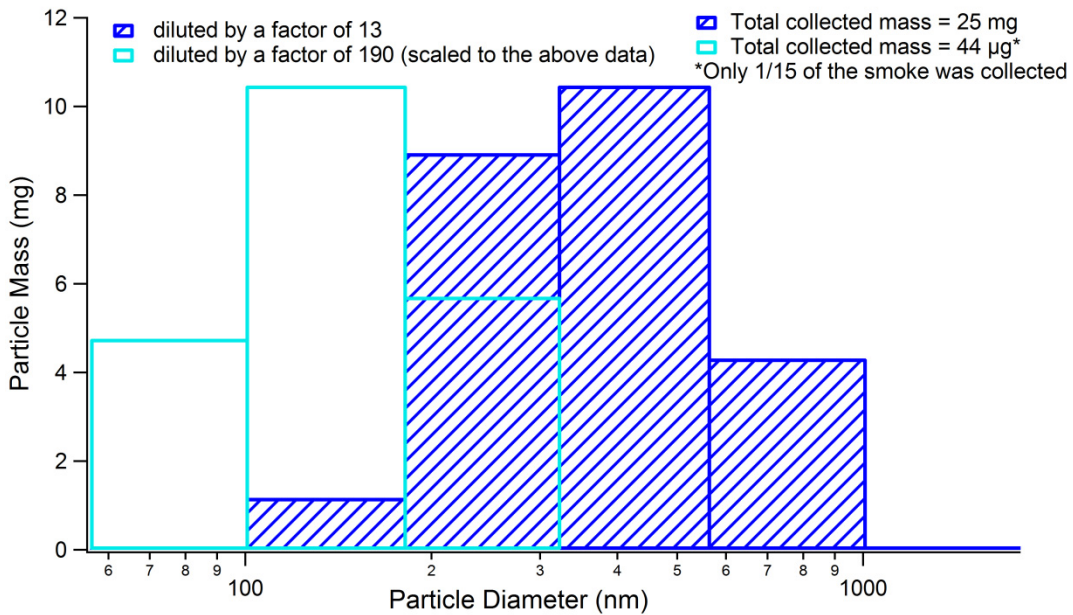
The particle count observed at 1 puff/min rate is seen in Figure 2.16. The particle emissions were on the same order of magnitude for all samples, with the least particle emitting samples being 1R5F and e-cigarette-2. We note that CPC data just provided total particle counts with no size information. To understand the extent of particle evaporation and resulting size perturbations of e-cigarette-2 under settings close to those of the fast flow tube, gravimetric analysis via MOUDI impaction at two different dilutions were compared (see Figure 2.17). The least diluted and aged e-cigarette-2 particles were centered at about ~350 nm, but when diluted to the same extent as the fast flow tube experiments, the center diameter shifted to ~150 nm. Although the particle sizes decreased, they were still larger than those observed in the chamber experiments (Figures 2.3-2.4). This particle shrinkage may be due to evaporation of water and other volatile components with dilution of the e-cigarette emission, as mentioned previously. To reflect this particle evaporation and size change of e-cigarette-2 particles upon dilution, the VOC content measured in this study should be taken as the total amount of VOC for this specific dilution.

#### **2.4.3. E-cigarette Emissions in Continuous Mode**

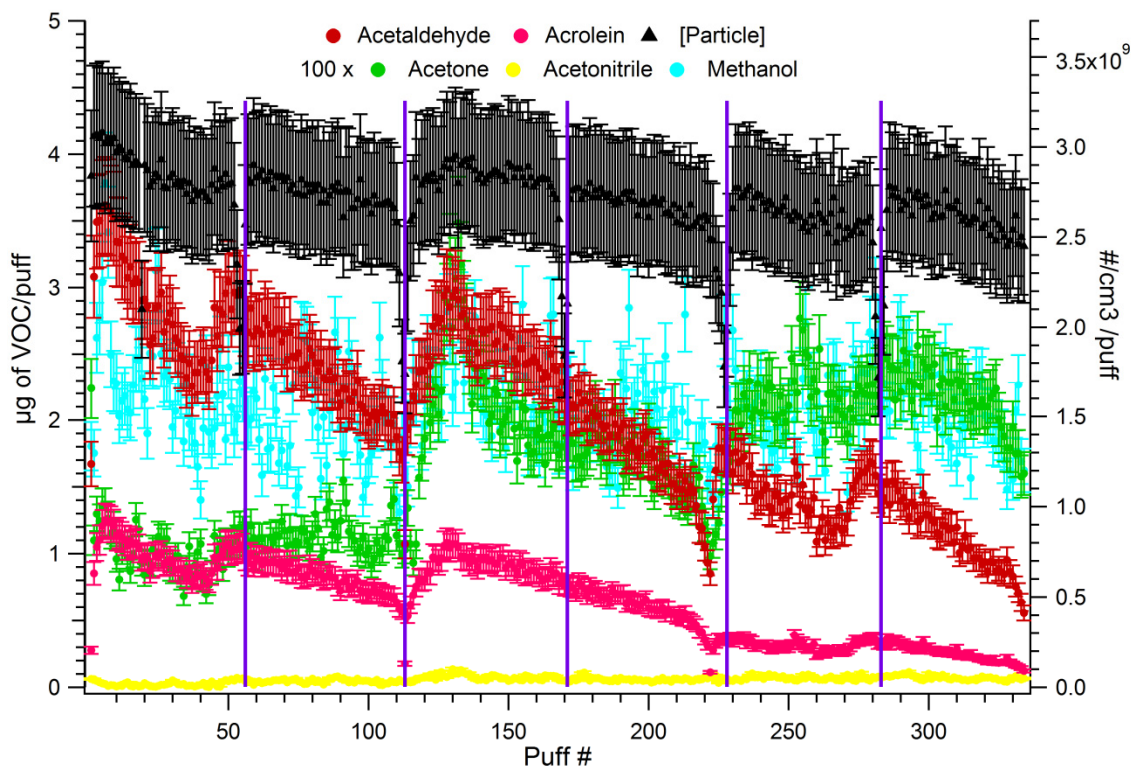
An e-cigarette was operated until the entire cartridge was consumed, with VOC and particle concentration being recorded as a function of puff number. The measurement taken during consumption (about 250 puffs) of a single e-cigarette-2 cartridge showed that volatiles were not emitted with a consistent delivery rate as seen in Figure 2.18. The battery depleted faster than the cartridge was consumed, and had to be recharged several times during the experiment (at points indicated by lines in Figure 2.18). The VOC emissions seemed to



**Figure 2.16.** The total number of particles emitted per puff by e-cigarettes and conventional cigarettes for 1 puff/min frequency. The values were based on assuming a cigarette lifetime of 9 puffs.



**Figure 2.17.** Gravimetrically determined particle size distributions of e-cigarette-2 at two different dilutions: 1) dilution by 13 and 2) dilution by 190. The latter was close to the dilution used in the fast flow tube experiments.



**Figure 2.18.** VOC and particle content of e-cigarette-2 as a function of puff number during continuous use with a single cartridge (the battery was fully recharged at the beginning of vaping and at each interval (indicated by a vertical line)).

generally decrease as either the battery or the cartridge got depleted, but in some instances, after initially decreasing, an increase occurred near the battery depletion. Acetaldehyde and acrolein had the largest decrease in delivery over battery depletion and the cartridge lifetime. Acetone delivery was quite variable and reached its highest concentration near the 130<sup>th</sup> puff. Methanol did not show a trend with the puff number and acetonitrile was not present. The particle concentration did not decrease within the measurement uncertainty.

## 2.5. Conclusion

We developed a fast-flow diluter for real-time observations of cigarette puffs. A cigarette injected the puff into the diluter and real-time sampling instruments were attached to the setup to perform smoke analysis without requiring pretreatment or extra sample handling. The e-cigarette particle emissions were similar to the low tar 1R5F reference cigarette and on the same order of magnitude as the rest of the conventional cigarettes. Acetaldehyde, acrolein, and acetone were found in the e-cigarette studied, supporting the evidence of oxidation of vegetable glycerin during vaping. Between different brands, flavoring, nicotine content, and battery voltage, e-cigarette emissions were highly variable which made it difficult to generalize their possible health effects. The difference in the increased particle volatility of e-cigarettes from cigarettes required similar dilution and analysis methods between different laboratory studies to allow faithful comparison. Although a limited number of substances were measured, this study suggests that e-cigarettes generate potentially harmful VOCs and sufficiently high particle number concentrations. Hence further studies are warranted to evaluate the toxicological effects of e-cigarette emissions in comparison to conventional combustion cigarettes.

## 2.6. Impact and Influence in the Field

Post-publication, the company of the PTR-ToF-MS used in our work, Ionicon Analytik, has published papers<sup>59, 60</sup> emphasizing the full range of applicability of the PTR-ToF-MS to electronic cigarettes, applying a similar double dilution method as was previously presented in our work. The implementation of a fast dilution system allows many sampling environments, such as mainstream aerosol and human exhaled aerosol after either inhaling or “holding” mainstream aerosol, to be investigated much faster than previous methods.<sup>59</sup> Other than toxic

carbonyls, recent PTR-ToF-MS studies have investigated the content of nicotine, propylene glycol, and vegetable glycerin in e-cigarettes by using increased heating inlet temperatures.<sup>59, 60</sup>

Studies of the emissions from e-cigarettes are still popularized as only e-cigarettes that are marketed for therapeutic purposes are currently regulated by the FDA. In 2014, the FDA proposed to extend its authority to cover additional products including e-cigarettes under the proposed rule “Tobacco Products Deemed To Be Subject to the Food, Drug & Cosmetic Act” which was finalized in May 2016 and will go into effect in August 8, 2016.<sup>61</sup> In the meantime, a growing number of state and municipality laws have been enacted that prohibit e-cigarettes in 100% smokefree venues.<sup>62</sup>

## References

1. Piade, J. J.; Wajrock, S.; Jaccard, G.; Janeke, G., Formation of mainstream cigarette smoke constituents prioritized by the World Health Organization - Yield patterns observed in market surveys, clustering and inverse correlations. *Food Chem. Toxicol.* **2013**, *55*, 329-347.
2. U. S. Department of Health and Human Services. *The Health Consequences of Smoking—50 Years of Progress: A Report of the Surgeon General*. Office on Smoking and Health, National Center for Chronic Disease Prevention and Health Promotion, Centers for Disease Control and Prevention, U.S. Department of Health and Human Services, Atlanta, GA. **2014**.
3. Pankow, J. F.; Watanabe, K. H.; Toccalino, P. L.; Luo, W.; Austin, D. F., Calculated cancer risks for conventional and "potentially reduced exposure product" cigarettes. *Cancer Epidemiol., Biomarkers Prev.* **2007**, *16* (3), 584-592.
4. Pauly, J. L.; O'Connor, R. J.; Paszkiewicz, G. M.; Cummings, K. M.; Djordjevic, M. V.; Shields, P. G., Cigarette Filter-based Assays as Proxies for Toxicant Exposure and Smoking Behavior - A Literature Review. *Cancer Epidemiol., Biomarkers Prev.* **2009**, *18* (12), 3321-3333.
5. Geiss, O.; Bianchi, I.; Barahona, F.; Barrero-Moreno, J., Characterisation of mainstream and passive vapours emitted by selected electronic cigarettes. *Int. J. Hyg. Environ. Health* **2015**, *218* (1), 169-180.
6. Brown, C. J.; Cheng, J. M., Electronic cigarettes: product characterisation and design considerations. *Tobacco Control* **2014**, *23* (suppl 2), ii4-ii10.
7. Tierney, P. A.; Karpinski, C. D.; Brown, J. E.; Luo, W.; Pankow, J. F., Flavour chemicals in electronic cigarette fluids. *Tobacco Control* **2015**.
8. Carroll Chapman, S. L.; Wu, L.-T., E-cigarette prevalence and correlates of use among adolescents versus adults: A review and comparison. *J. of Psych. Res.* **2014**, *54*, 43-54.

9. Papousek, R.; Pataj, Z.; Novakova, P.; Lemr, K.; Bartak, P., Determination of Acrylamide and Acrolein in Smoke from Tobacco and E-Cigarettes. *Chromatographia* **2014**, *77* (17-18), 1145-1151.
10. Goniewicz, M. L.; Knysak, J.; Gawron, M.; Kosmider, L.; Sobczak, A.; Kurek, J.; Prokopowicz, A.; Jablonska-Czapla, M.; Rosik-Dulewska, C.; Havel, C.; Jacob, P.; Benowitz, N., Levels of selected carcinogens and toxicants in vapour from electronic cigarettes. *Tobacco Control* **2013**, *0*, 1-7.
11. Schripp, T.; Markewitz, D.; Uhde, E.; Salthammer, T., Does e-cigarette consumption cause passive vaping? *Indoor Air* **2013**, *23* (1), 25-31.
12. Roemer, E.; Schramke, H.; Weiler, H.; Buettner, A.; Kausche, S.; Weber, S.; Berges, A.; Stueber, M.; Muench, M.; Trelles-Sticken, E.; Pype, J.; Kohlgrueber, K.; Voelkel, H.; Wittke, S., Mainstream smoke chemistry and in vitro and in vivo toxicity of the reference cigarettes 3R4F and 2R4F. *Beitr. Tabakforsch. Int.* **2012**, *25* (1), 316-335.
13. Intorp, M.; Purkis, S.; Wagstaff, W., Determination of carbonyl compounds in cigarette mainstream smoke. The CORESTA 2010 collaborative study and recommended method. *Beitr. Tabakforsch. Int.* **2012**, *25* (2), 361-374.
14. Ohta, K.; Uchiyama, S.; Inaba, Y.; Nakagome, H.; Kunugita, N., Determination of carbonyl compounds generated from the electronic cigarette using coupled silica cartridges impregnated with hydroquinone and 2,4-dinitrophenylhydrazine. *Bunseki Kagaku* **2011**, *60* (10), 791-797.
15. Uchiyama, S.; Inaba, Y.; Kunugita, N., Determination of acrolein and other carbonyls in cigarette smoke using coupled silica cartridges impregnated with hydroquinone and 2,4-dinitrophenylhydrazine. *J. Chromatogr. A* **2010**, *1217* (26), 4383-4388.
16. Sampson, M. M.; Chambers, D. M.; Pazo, D. Y.; Moliere, F.; Blount, B. C.; Watson, C. H., Simultaneous Analysis of 22 Volatile Organic Compounds in Cigarette Smoke Using Gas Sampling Bags for High-Throughput Solid-Phase Microextraction. *Anal. Chem.* **2014**, *86* (14), 7088-7095.

17. Eschner, M. S.; Selmani, I.; Groger, T. M.; Zimmermann, R., Online Comprehensive Two-Dimensional Characterization of Puff-by-Puff Resolved Cigarette Smoke by Hyphenation of Fast Gas Chromatography to Single-Photon Ionization Time-of-Flight Mass Spectrometry: Quantification of Hazardous Volatile Organic Compounds. *Anal. Chem.* **2011**, *83* (17), 6619-6627.
18. Hatzinikolaou, D. G.; Lagesson, V.; Stavridou, A. J.; Pouli, A. E.; Lagesson-Andrasko, L.; Stavrides, J. C., Analysis of the Gas Phase of Cigarette Smoke by Gas Chromatography Coupled with UV-Diode Array Detection. *Anal. Chem.* **2006**, *78* (13), 4509-4516.
19. Takanami, Y.; Chida, M.; Hasebe, H.; Sone, Y.; Suhara, S., Analysis of cigarette smoke by an online thermal desorption system and multidimensional GC-MS. *J. Chromatogr. Sci.* **2003**, *41* (6), 317-322.
20. Tan, G.-B.; Gao, W.; Huang, Z.-X.; Hong, Y.; Fu, Z.; Dong, J.-G.; Cheng, P.; Zhou, Z., Vacuum ultraviolet single photon ionization time-of-flight mass spectrometer. *Fenxi Huaxue* **2011**, *39* (10), 1470-1475.
21. Liu, C.; Feng, S.; van Heemst, J.; McAdam, K. G., New insights into the formation of volatile compounds in mainstream cigarette smoke. *Anal. Bioanal. Chem.* **2010**, *396* (5), 1817-1830.
22. Harward, C. N.; Thweatt, W. D.; Baren, R. E.; Parrish, M. E., Determination of molecular line parameters for acrolein (C<sub>3</sub>H<sub>4</sub>O) using infrared tunable diode laser absorption spectroscopy. *Spectrochim. Acta, Part A* **2006**, *63A* (5), 970-980.
23. Thweatt, W. D.; Harward, C. N.; Parrish, M. E., Measurement of acrolein and 1,3-butadiene in a single puff of cigarette smoke using lead-salt tunable diode laser infrared spectroscopy. *Spectrochim. Acta, Part A* **2007**, *67A* (1), 16-24.
24. Johnson, T. J.; Olfert, J. S.; Cabot, R.; Treacy, C.; Yurteri, C. U.; Dickens, C.; McAughey, J.; Symonds, J. P. R., Steady-state measurement of the effective particle density of cigarette smoke. *J. Aerosol Sci.* **2014**, *75*, 9-16.



25. van Dijk, W. D.; Cremers, R.; Klerx, W.; Schermer, T. R. J.; Scheepers, P. T. J., Application of cigarette smoke characterisation based on optical aerosol spectrometry. Dynamics and comparisons with tar values. *Curr. Anal. Chem.* **2012**, *8* (3), 344-350.
26. Adam, T.; McAughey, J.; McGrath, C.; Mocker, C.; Zimmermann, R., Simultaneous on-line size and chemical analysis of gas phase and particulate phase of cigarette mainstream smoke. *Anal. Bioanal. Chem.* **2009**, *394* (4), 1193-1203.
27. Alderman, S. L.; Ingebrethsen, B. J., Characterization of Mainstream Cigarette Smoke Particle Size Distributions from Commercial Cigarettes Using a DMS500 Fast Particulate Spectrometer and Smoking Cycle Simulator. *Aerosol Sci. Technol.* **2011**, *45* (12), 1409-1421.
28. Kane, D. B.; Asgharian, B.; Price, O. T.; Rostami, A.; Oldham, M. J., Effect of smoking parameters on the particle size distribution and predicted airway deposition of mainstream cigarette smoke. *Inhalation Toxicol.* **2010**, *22* (3), 199-209.
29. Ingebrethsen, B. J.; Cole, S. K.; Alderman, S. L., Electronic cigarette aerosol particle size distribution measurements. *Inhalation Toxicol.* **2012**, *24* (14), 976-984.
30. Bertholon, J. F.; Becquemin, M. H.; Roy, M.; Roy, F.; Ledur, D.; Annesi, M. I.; Dautzenberg, B., Comparison of the aerosol produced by electronic cigarettes with conventional cigarettes and the shisha. *Rev. Mal. Respir.* **2013**, *30* (9), 752-7.
31. Williams, M.; Villarreal, A.; Bozhilov, K.; Lin, S.; Talbot, P., Metal and silicate particles including nanoparticles are present in electronic cigarette cartomizer fluid and aerosol. *PLoS One* **2013**, *8* (3), e57987.
32. Zhang, Y.; Sumner, W.; Chen, D.-R., In Vitro Particle Size Distributions in Electronic and Conventional Cigarette Aerosols Suggest Comparable Deposition Patterns. *Nicotine Tob. Res.* **2013**, *15* (2), 501-508.
33. Fuoco, F. C.; Buonanno, G.; Stabile, L.; Vigo, P., Influential parameters on particle concentration and size distribution in the mainstream of e-cigarettes. *Environ. Pollut.* **2014**, *184*, 523-529.

34. Manigrasso, M.; Buonanno, G.; Fuoco, F. C.; Stabile, L.; Avino, P., Aerosol deposition doses in the human respiratory tree of electronic cigarette smokers. *Environ. Pollut.* **2015**, *196*, 257-267.
35. Baker, R. R., Smoke generation inside a burning cigarette: modifying combustion to develop cigarettes that may be less hazardous to health. *Prog. Energy Combust. Sci.* **2006**, *32* (4), 373-385.
36. Fujioka, K.; Shibamoto, T., Determination of toxic carbonyl compounds in cigarette smoke. *Environ. Toxicol.* **2006**, *21* (1), 47-54.
37. Staimer, N.; Nguyen, T. B.; Nizkorodov, S. A.; Delfino, R. J., Glutathione peroxidase inhibitory assay for electrophilic pollutants in diesel exhaust and tobacco smoke. *Anal. Bioanal. Chem.* **2012**, *403* (2), 431-441.
38. Fuoco, F. C.; Buonanno, G.; Stabile, L.; Vigo, P., Influential parameters on particle concentration and size distribution in the mainstream of e-cigarettes. *Environ. Pollut.* **2014**, *184*, 523-529.
39. Grana, R.; Benowitz, N.; Glantz, S. A., E-cigarettes: a scientific review. *Circulation* **2014**, *129* (19), 1972-86.
40. TJI Report. (2013). Reference Products Used in Tobacco and Smoke Analysis. *Health Sci. Aff.: Tob. J. Int.*, 2:150-154. Retrieved from: <http://www2.ca.uky.edu/refcig/Reference%20and%20monitor%20products.pdf>.
41. Talih, S.; Balhas, Z.; El, H. A.; Baalbaki, R.; Saliba, N.; Shihadeh, A.; Eissenberg, T.; Salman, R.; Karaoghlanian, N., Effects of user puff topography, device voltage, and liquid nicotine concentration on electronic cigarette nicotine yield: measurements and model predictions. *Nicotine Tob. Res.* **2015**, *17* (2), 150-7.
42. Evans, S. E.; Hoffman, A. C., Electronic cigarettes: abuse liability, topography and subjective effects. *Tob. Control* **2014**, *23 Suppl 2*, ii23-9.
43. Behar, R. Z.; Hua, M.; Talbot, P., Puffing topography and nicotine intake of electronic cigarette users. *PLoS One* **2015**, *10* (2), e0117222.

44. Buhr, K.; van Ruth, S.; Delahunty, C., Analysis of volatile flavor compounds by Proton Transfer Reaction-Mass Spectrometry: fragmentation patterns and discrimination between isobaric and isomeric compounds. *Int. J. Mass Spectrom.* **2002**, *221* (1), 1-7.
45. Chen, P. X.; Moldoveanu, S. C., Mainstream smoke chemical analyses for 2R4F Kentucky reference cigarette. *Beitr. Tabakforsch. Int.* **2003**, *20* (7), 448-458.
46. Uchiyama, S.; Tomizawa, T.; Inaba, Y.; Kunugita, N., Simultaneous determination of volatile organic compounds and carbonyls in mainstream cigarette smoke using a sorbent cartridge followed by two-step elution. *J. Chromatogr. A* **2013**, *1314*, 31-37.
47. de Gouw, J.; Warneke, C.; Karl, T.; Eerdekens, G.; van der Veen, C.; Fall, R., Sensitivity and specificity of atmospheric trace gas detection by proton-transfer-reaction mass spectrometry. *Int. J. Mass Spectrom.* **2003**, *223-224* (1-3), 365-382.
48. Bernstein, D. M., A review of the influence of particle size, puff volume, and inhalation pattern on the deposition of cigarette smoke particles in the respiratory tract. *Inhalation Toxicol.* **2004**, *16* (10), 675-689.
49. Kosmider, L.; Sobczak, A.; Fik, M.; Knysak, J.; Zaciera, M.; Kurek, J.; Goniewicz, M. L., Carbonyl compounds in electronic cigarette vapors: effects of nicotine solvent and battery output voltage. *Nicotine Tob. Res.* **2014**, *16* (10), 1319-26.
50. Goniewicz, M. L.; Knysak, J.; Gawron, M.; Kosmider, L.; Sobczak, A.; Kurek, J.; Prokopowicz, A.; Jablonska-Czapla, M.; Rosik-Dulewska, C.; Havel, C.; Jacob, P., 3rd; Benowitz, N., Levels of selected carcinogens and toxicants in vapour from electronic cigarettes. *Tob. Control* **2014**, *23* (2), 133-9.
51. Tayyarah, R.; Long, G. A., Comparison of select analytes in aerosol from e-cigarettes with smoke from conventional cigarettes and with ambient air. *Regul. Toxicol. Pharmacol.* **2014**, *70* (3), 704-710.
52. Rodgman, A.; Perfetti, T. A., *The chemical components of tobacco and tobacco smoke*. CRC Press: Boca Raton, **2009**.

53. Matsunaga, A.; Ziemann, P. J., Gas-Wall Partitioning of Organic Compounds in a Teflon Film Chamber and Potential Effects on Reaction Product and Aerosol Yield Measurements. *Aerosol Sci. Technol.* **2010**, *44* (10), 881-892.
54. Gregg, E.; Hill, C.; Hollywood, M.; Kearney, M.; McAdam, K.; McLaughlin, D.; Purkis, S.; Williams, M., The UK smoke constituents testing study. Summary of results and comparison with other studies. *Beitr. Tabakforsch. Int.* **2004**, *21* (2), 117-138.
55. Petraru, C.; Balalau, D.; Ilie, M.; Balalau, C., Evaluation of different kind of cigarette filters ability of to retain the toxic compounds of the vapor phase. A comparative graphical study. *Farmacia (Bucharest, Rom.)* **2013**, *61* (4), 736-741.
56. Purkis, W.; Mueller, C.; Intorp, M.; Seidel, H., The Influence of Cigarette Designs and Smoking Regimes on Vapour Phase Yields. In *Beiträge zur Tabakforschung / Contributions to Tobacco Research*, 2014; Vol. 24, p 34.
57. Hoffmann, D.; Hoffmann, I.; El-Bayoumy, K., The Less Harmful Cigarette: A Controversial Issue. A Tribute to Ernst L. Wynder. *Chem. Res. Toxicol.* **2001**, *14* (7), 767-790.
58. Adam, T.; McAughey, J.; Mocker, C.; McGrath, C.; Zimmermann, R., Influence of filter ventilation on the chemical composition of cigarette mainstream smoke. *Anal. Chim. Acta* **2010**, *657* (1), 36-44.
59. Breiev, K.; Burseg, K. M. M.; O'Connell, G.; Hartungen, E.; Biel, S. S.; Cahours, X.; Colard, S.; Maerk, T. D.; Sulzer, P., An online method for the analysis of volatile organic compounds in electronic cigarette aerosol based on proton transfer reaction mass spectrometry. *Rapid Commun. Mass Spectrom.* **2016**, *30* (6), 691-697.
60. O'Connell, G.; Colard, S.; Breiev, K.; Sulzer, P.; Biel, S. S.; Cahours, X.; Pritchard, J. D.; Burseg, K. M. M., An Experimental Method to Determine the Concentration of Nicotine in Exhaled Breath and its Retention Rate Following Use of an Electronic Cigarette. *J. Environ. Anal. Chem.* **2016**, *2* (5).

61. U. S. Department of Health and Human Services. *Extending Authorities to All Tobacco Products, Including E-Cigarettes, Cigars, and Hookah*. Retrieved May 17, **2016**, from <http://www.fda.gov/TobaccoProducts/Labeling/ucm388395.htm>.
62. State and Minicipalities with Laws Regulating Use of Electronic Cigarettes. *American Nonsmokers' Rights Foundation*. Retrieved April 18, **2016** from <http://www.no-smoke.org/pdf/ecigslaws.pdf>

## Chapter 3: SOA Mediated by Fe(III) Chemistry

Portions of this chapter were reproduced in part by permission from:

Slikboer, S.; Grandy, L.; Blair, S. L.; Nizkorodov, S. A.; Smith, R. W.; Al-Abadleh, H. A., Formation of Light Absorbing Soluble Secondary Organics and Insoluble Polymeric Particles from the Dark Reaction of Catechol and Guaiacol with Fe(III). *Environmental Science & Technology* 2015, 49 (13), 7793-7801. Copyright © American Chemical Society.

Experiments conducted by Sandra Blair at the University of California, Irvine, CA:

- Unfiltered UV-vis time dependent studies of catechol reactions and MAC values
- Initial LC-ESI-MS catechol reaction experiments at the UCI Mass Spectrometry Facility
- Isocratic HPLC duplicate experiments and investigative gradient HPLC experiments
- DLS experiments of catechol and guaiacol reactions at the UCI Laser Spectroscopy Facility
- SEM/EDS of catechol and guaiacol reaction particles at the UCI Laboratory for Electron and X-ray Instrumentation

Data recorded by our collaborators at Wilfrid Laurier University, Waterloo, Ontario N2L 3C5, Canada is noted by a “†”.

### 3.1. Abstract

Transition metals such as iron are reactive components of environmentally relevant surfaces. Here, a dark reaction of Fe(III) with catechol and guaiacol was investigated in an aqueous solution at pH 3 under experimental conditions that mimic reactions in the adsorbed phase of water. Using UV-vis spectroscopy, liquid chromatography, mass spectrometry, elemental analysis, dynamic light scattering, and electron microscopy techniques, we characterized the reactants, intermediates, and products as a function of reaction time. The reactions of Fe(III) with catechol and guaiacol produced significant changes in the optical spectra of the solutions due to the formation of light absorbing secondary organics and colloidal organic particles. The primary steps in the reaction mechanism were shown to include oxidation of catechol and guaiacol to hydroxy- and methoxy-quinones. The particles formed within a few minutes of reaction and grew to micron-size aggregates after half an hour reaction. The mass-normalized absorption coefficients of the particles were comparable to those of strongly absorbing brown carbon compounds produced by biomass burning. These results could account for new pathways that lead to atmospheric secondary organic aerosol formation and abiotic polymer formation on environmental surfaces mediated by transition metals.

### 3.2. Introduction

Despite decades of progress in research on atmospheric aerosols, secondary pathways for their formation,<sup>1, 2</sup> their role in absorbing and scattering radiation (direct effect on climate), acting as cloud and ice condensation nuclei (indirect effect on the climate),<sup>3</sup> and contributing to heterogeneous chemistry of air pollutants remain active areas of investigation.<sup>4</sup> Given their ubiquitous presence in field-collected aerosols from different origins,<sup>5, 6</sup> organic compounds are involved in a number of reactions and processes that transform chemical composition,

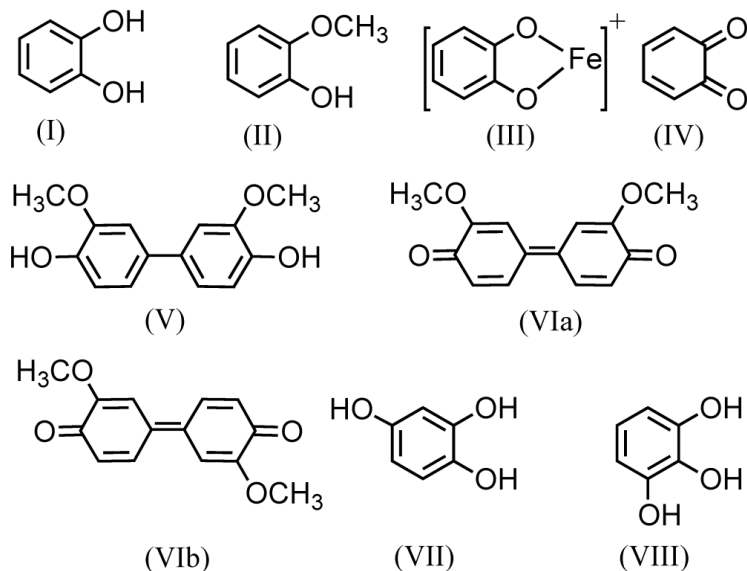
hygroscopicity, phase, and optical properties of atmospheric aerosols.<sup>7, 8</sup> For example, single particle analysis of sea spray particles generated from “ocean-in-a-lab” experiments revealed that under acidic conditions, organic material concentrates at the surface,<sup>9</sup> and that these particles contain transition metals such as iron (Fe).<sup>10</sup> The role of transition metals in the aging and transformation of the organic content on atmospherically relevant surfaces that include aerosols, buildings, and surface water is still unclear and warrants further investigation.<sup>5, 11, 12</sup>

The aging of organics in aerosols due to heterogeneous chemistry with gas phase oxidants such as ozone (O<sub>3</sub>), the hydroxyl radical (OH), and the nitrate radical (NO<sub>3</sub>) has been extensively studied.<sup>2</sup> Dark and photochemical processes driven by dissolved redox active species such as Fe, OH, hydrogen peroxide (H<sub>2</sub>O<sub>2</sub>), and excited triplet states of certain organics were also investigated in detail with respect to their chemistry in large cloud/fog droplets.<sup>13-15</sup> However, our understanding of oxidation processes relevant to multi-component atmospheric systems containing sparse amounts of water, such as environmental films and wet aerosols, is still limited. For example, fluctuations in the water content and acidity of aerosols due to changes in ambient temperature, relative humidity, and reactions with acidic/basic gases affect the solvent-solute ratios and the relative importance of bulk versus surface reactions.<sup>5</sup> Moreover, for some aerosol systems such as mineral dust particles and other atmospherically important surfaces such as buildings, water exists in small pockets of aqueous phase or “adsorbed phase” in the form of islands or films, depending on the underlying substrate and environmental conditions.<sup>12</sup> The high concentrations of solutes in these systems result in reactions that are uniquely different from the corresponding reactions in more dilute bulk aqueous solutions.<sup>16</sup>

The redox chemistry and strong chelating abilities of Fe in the bulk aqueous phase are well established at the fundamental level<sup>11</sup> and recently were utilized in functionalizing surfaces



and nanoparticles for applications in green chemistry<sup>17</sup> and in the development of biomedical and sensing devices.<sup>18-20</sup> In contrast, the role of transition metals such as Fe in driving secondary organic aerosols (SOA) formation from aliphatic and aromatic precursors in heterogeneous/multiphase reactions is not well understood.<sup>1, 2, 11</sup> This study demonstrates that dark reactions of Fe with catechol and guaiacol under high solute-solvent ratios that mimic reactions in the adsorbed phase of water leads to efficient redox reactions, resulting in complex polymeric products that strongly absorb visible radiation. Catechol and guaiacol (the structures of all compounds discussed in this chapter are shown in Scheme 3.1), are semivolatile phenolic compounds emitted from biomass burning. They are moderately soluble in water with Henry's law constants of  $4 \cdot 10^3$  and  $900 \text{ M atm}^{-1}$ , respectively.<sup>21</sup> These compounds are well-known aromatic SOA precursors<sup>22</sup> and are simple models for the aromatic fraction of humic like substances (HULIS) in aerosols.<sup>22</sup> Catechol, guaiacol, and other catecholates are capable of chelating  $\text{Fe}^{20, 23}$  (Scheme 3.1), and they easily oxidize to the corresponding quinones (e.g., o-quinone in Scheme 3.1). Our observation of the formation of polymeric products, in addition to the expected quinones, could account for new pathways that lead to SOA formation mediated by transition metals, and explain observations from single particle analysis of field collected "aged" mineral dust aerosol,<sup>12</sup> sea spray from coastal regions impacted by Fe,<sup>10</sup> and abiotic polymer formation on surfaces<sup>24</sup> such as those imaged in sea spray aerosols.<sup>9</sup> Furthermore, this reaction may serve as a source of atmospheric brown carbon-organic aerosol capable of strongly absorbing near-UV and visible radiation translating into a direct effect on climate.<sup>25, 26</sup>



**Scheme 3.1.** Chemical structures of (I) catechol, (II) guaiacol, (III) catechol-Fe complex, (IV) o-quinone, (V) 3,3'-dimethoxy-4,4'-biphenyldiol, (VIa) 3,3'-dimethoxy-4,4'-biphenoquinone, (VIb) 3,5'-dimethoxy-4,4'-biphenoquinone, (VII) 1,2,4-benzentriol, and (VIII) pyrogallol.

### 3.3. Experimental

#### 3.3.1. Chemicals

All chemicals were used as received without further purification: catechol (1,2-benzenediol, > 99%, CAS 120-80-9, Sigma-Aldrich), guaiacol (2-methoxyphenol,  $\geq$  98%, CAS 90-05-1, Sigma-Aldrich), and iron(III) chloride hexahydrate ( $\text{FeCl}_3 \cdot 6\text{H}_2\text{O}$ , CAS 10025-77-1, Sigma-Aldrich). Pyrogallol (1,2,3-trihydroxybenzene,  $\geq$  99%, CAS 87-66-1, Sigma-Aldrich) and 1,2,4-benzentriol (99%, CAS 533-73-3, Sigma-Aldrich) were used as reference compounds in the mass spectrometry experiments. The following chemicals were used in the hematite dissolution experiments: hematite nanoparticles ( $\alpha\text{-Fe}_2\text{O}_3$ , >99.9%, Nanostructured and Amorphous Materials, 19  $\text{m}^2/\text{g}$  surface area, 67 nm average diameter, 8.6 isoelectric point), sodium chloride (NaCl powder, 99%, ACS grade, BDH), acetic acid ( $\text{CH}_3\text{COOH}$ , 99.7%, ACS grade, glacial, Macron), ammonium acetate ( $\text{CH}_3\text{CO}_2\text{NH}_4$ , BioXtra,  $\geq$  98%, Sigma-Aldrich),

hydroxylamine hydrochloride ( $\text{NH}_2\text{OH}\cdot\text{HCl}$ , 99%, Sigma-Aldrich), 1,10-phenanthroline ( $\text{C}_{12}\text{H}_8\text{N}_2$ ,  $\geq 99\%$ , Sigma-Aldrich), and ammonium iron(II) sulfate hexahydrate ( $(\text{NH}_4)_2\text{Fe}(\text{SO}_4)_2\cdot 6\text{H}_2\text{O}$ , 99% ACS reagent, Sigma-Aldrich). Aqueous phase solutions were prepared by dissolving the chemicals in Milli-Q water (18.5  $\text{M}\Omega\text{ cm}$ ) or  $^{18}\text{O}$ -labeled water (97 atom %  $^{18}\text{O}$ , Sigma-Aldrich) with an ionic strength adjusted to 0.01 M by adding potassium chloride (KCl powder, 99.5%, EM Science) to stabilize the pH reading. The pH was adjusted using solutions of hydrochloric acid (HCl 6 N, Ricca Chemical Company) and sodium hydroxide (NaOH pellets, 99-100%, EMD).

### 3.3.2. UV-Vis Spectroscopy and HPLC Experiments

UV-vis spectra were collected using either a fiber optic UV-vis spectrometer (Ocean Optics USB 4000) or a Shimadzu UV 1800 spectrophotometer with a 1 cm quartz cuvette. Chromatograms were collected using a Waters Delta 600 instrument equipped with a Waters 2487 dual wavelength absorbance detector. An in-line degasser was used for sparging at 20 mL/min throughout the experiment to avoid air bubbles. The  $4.6 \times 250$  mm column had Hypersil GOLD C8 stationary phase, with 5  $\mu\text{m}$  particle size, and 175  $\text{\AA}$  pore size. The mobile phase was flown isocratically using 95% water, with 0.05% TFA and 5% acetonitrile at a flow rate of 1 mL/min. The injection volume of the sample was 30  $\mu\text{L}$ . The following solvents were used in the preparation of mobile phase in the HPLC experiments: acetonitrile (HPLC grade, 99.9%, BDH), water (HPLC grade) and trifluoroacetic acid (TFA, HPLC grade, 99.9%, EMD). In a typical UV-vis experiment, 20 mL of either catechol (1 mM) or guaiacol (0.5 mM) were mixed with 0.4 mL  $\text{FeCl}_3$  at a concentration that would yield the desired organic reactant:Fe molar ratio. The vial was wrapped with aluminum foil to avoid photochemical reactions. After a given reaction time, a 3 mL aliquot was taken using a syringe, and the solution was filtered before collecting the UV-

vis spectrum. In a typical HPLC experiment, 10 mL of a 1 mM catechol solution was placed in a vial wrapped in aluminum foil and placed on a stir plate. Then, 0.2 mL of either 25, 50, or 102 mM FeCl<sub>3</sub> solution was added to the catechol solution with continuous reaction to obtain a 2:1, 1:1 or 1:2 organic reactant:Fe molar ratio. The timer was started as soon as the FeCl<sub>3</sub> was added. Solutions were injected into the HPLC after a given reaction time as described in figures.

### 3.3.3. Mass Spectrometry Experiments

Negative ion mode electrospray ionization coupled to liquid chromatography separation (LC-ESI-MS) experiments were performed with a Thermo Fisher Scientific Q-Exactive hybrid Orbitrap mass spectrometer. Typical operating conditions were: spray voltage 2.8 kV, mass resolving power 70,000 at  $m/z$  200, capillary temperature 275°C, heater temperature 300°C, sheath gas 25 arbitrary units and auxiliary gas 4 arbitrary units. The operating conditions for the MS/MS part of the experiments were: N<sub>2</sub> collision partner and normalized collision energy (NCE = 120 arbitrary units). The sample injection volume was 10 µL. Accurate mass determinations were made with internal lock mass  $m/z$  91.00368 and typical errors were better than 1 mmu. A Dionex Ultimate 3000 UHPLC was employed with a C18, 2.1x150 mm column (Waters, X-Bridge) operated at 0.2 mL/min. Xcalibur software was used for data collection, processing, and analysis. Isocratic elution was achieved with 5/95 v/v mixture of acetonitrile/H<sub>2</sub>O + 0.1% formic acid. TFA was not used in these experiments because it causes ion suppression in ESI and must be avoided, not just for these studies, but also for all subsequent LC/MS analyses. The reaction of chemicals prior to injection was done in a manner similar to that described above for the HPLC experiments.

### 3.3.4. Particles Characterization

Particles that formed in the solution as a result of  $\text{FeCl}_3$  + catechol/guaiacol reactions were collected on nylon membrane filters (0.2  $\mu\text{m}$  pore size, 25 mm dia., EMD) and images of the filters were taken using a digital camera. Mass yield experiments were performed after 2 hr reaction using 1:2 molar ratio organic reactant/Fe by weighing the filters before and after filtration followed by overnight drying. For these experiments, the reaction volumes were considerably scaled up (70 mL for catechol/Fe, and 140 mL for guaiacol/Fe) in order to achieve measurable mass yields of particles, keeping the starting concentrations the same in all experiments. The particles were washed with Milli-Q water several times prior to drying. Also, collected filtrates were subjected to filtration four times to ensure a minimum loss of particles.

The iron content in the particles was analyzed using inductively coupled plasma mass spectrometry (ICP-MS) using method EPA 3050, ALS Global Laboratories. Particle imaging and elemental composition were recorded with scanning electron microscopy-energy dispersive X-ray spectroscopy (SEM-EDS) at the University of California Irvine (UCI) Laboratory for Electron and X-ray Instrumentation (LEXI). Particles from reaction of  $\text{FeCl}_3$  with either catechol or guaiacol solutions were collected on nylon membrane filters after 1.5 hrs, washed multiple times with water, and re-suspended in water, aerosolized with a nebulizer (Salter Labs #8900-7), sent through a diffusion dryer, and collected on carbon type-B 400 mesh copper grids (Ted Pella, Inc. #01814-F) with an SKC Sioutas Cascade Impactor. Particles collected on stage “D” (> 0.25  $\mu\text{m}$ ) of the impactor were analyzed with an FEI Magellan XHR SEM. Images of particles were taken at 10 kV and 25 pA and EDS analysis was done at 20 kV and 0.8 nA.

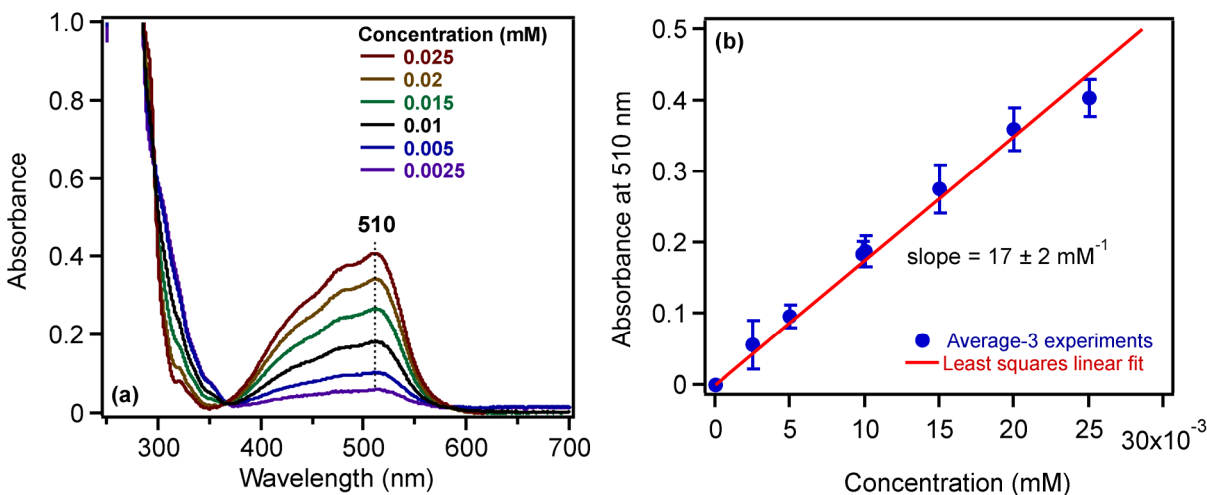
Dynamic light scattering (DLS) experiments were performed on  $\text{FeCl}_3$  with either catechol or guaiacol reaction solutions in a 1 cm Teflon<sup>TM</sup> capped-quartz cuvette with a Malvern

Zetasizer Nano (ZEN3600) with settings for each measurement to average 10 runs with a duration of 10 s at the UCI Laser Spectroscopy Facility. For FTIR measurements, the particles were deposited on a ZnSe attenuated total internal reflectance (ATR-FTIR) cell from a water/ethanol slurry followed by drying overnight. Absorbance spectra of these particles were obtained by referencing to the clean and dry ZnSe crystal.

### **3.3.5. Acid-Dissolution of Hematite Followed by Reaction with Organics**

Hematite nanoparticles were used as a model for iron (oxyhydr)oxides in mineral dust aerosols. A slurry of hematite nanoparticles was prepared in 0.01 M KCl adjusted to pH 1 using HCl, and allowed to mix for 10 days at medium speed in a vortex mixer followed by filtration and determination of total dissolved iron concentration. Five vials containing 0.008 g of hematite were mixed with 1.75 mL of 0.01 M KCl at pH 1 (BKG 1). For determining total iron concentration according to the procedure described by Lanzl et al.,<sup>27</sup> another 1 vial containing 0.008 g of hematite were mixed with 1.75 mL background solutions prepared by mixing 5 mL NaCl (25 mM) and 1 mL buffer (1 mL acetic acid + 0.1 g ammonium acetate) at pH 1 (BKG 2). The slurries were allowed to mix for 10 days on a medium speed vortex in the dark. Then, all vials were filtered using a 0.2  $\mu\text{m}$  nylon membrane filters. The pH of the filtrate was about 0.2 higher from the initial value of 1. All filtrates were wrapped with aluminum foil. To determine the total dissolved iron concentration in these filtrates using UV-vis spectroscopy, a linear calibration was constructed from the absorbance at 510 nm of the complexes of standard solutions of  $(\text{NH}_4)_2\text{Fe}(\text{SO}_4)_2 \cdot 6\text{H}_2\text{O}$  and 1,10-phenanthroline according to a modified procedure described by Stucki and Anderson.<sup>28, 29</sup> Briefly, the concentrations of the standard solutions were in the range 2.5-25  $\mu\text{M}$  using a background solution from a 100 mL NaCl (25 mM), 0.04 mL  $\text{NH}_2\text{OH} \cdot \text{HCl}$  (1.3 mM) and 0.4 mL buffer (0.5 g  $\text{CH}_3\text{CO}_2\text{NH}_4$  (s) + 5 mL  $\text{CH}_3\text{COOH}$ ). The

purpose of the addition of  $\text{NH}_2\text{OH}\cdot\text{HCl}$  was to reduce  $\text{Fe(III)}$  to  $\text{Fe(II)}$ . A 10 mL aliquot from each standard solution was mixed with 0.2 mL 1,10-phenanthroline (1 g/L) and allowed to sit in the dark for 30 min. All of the above was done under red light illumination in the lab to minimize the possible effects of photochemistry. A UV-vis spectrum was then recorded for each standard solution after zeroing the spectrometer with 3 mL of a background solution from a 10 mL  $\text{NaCl}$  (25 mM), 0.01 mL  $\text{NH}_2\text{OH}\cdot\text{HCl}$  (1.3 mM), 0.04 mL buffer, and 0.04 mL 1,10-phenanthroline. Figure 3.1<sup>†</sup> shows the UV-vis spectra of the complexes and calibration curve, respectively. In order to use this calibration curve, the filtrates from hematite dissolution had to be diluted. To do that, 0.05 mL of filtrate with BKG 2 was diluted by the addition of 27 mL BKG 2. Then, 2 mL of this diluted solution was mixed with 0.2 mL  $\text{NH}_2\text{OH}\cdot\text{HCl}$  (1.3 mM) and 2 mL 1,10-phenanthroline (1 g/L) followed by sitting for 30 min. A UV-vis spectrum taken for this solution showed a peak similar to the one in Figure 3.1<sup>†a</sup>, with an absorbance of 0.17 at 510 nm. From the calibration curve in Figure 3.1<sup>†b</sup>, the dissolved  $[\text{Fe}]_{\text{tot}} = 9.94 \mu\text{M}$  in the diluted solution. After taking into account the dilution factor, the  $[\text{Fe}]_{\text{tot}}$  in the original 1 mL filtrate is calculated to be 5.4 mM. For the experiments with standard solutions of catechol and guaiacol, the pH of the filtrates prepared in BKG 1 was raised to 3 by adding  $\text{NaOH}$  solution. After accounting for dilution by the base, the concentration of the organic solutions was calculated such that a 1:2 organic reactant:Fe molar ratio would be obtained in the final solution after reaction. Digital images of solution mixture were taken after 3 min and 1 hr of reaction, and then filtered. After adjusting the pH of the filtrate to 3, catechol or guaiacol was added at half the total iron concentration determined by UV-vis spectroscopy. Samples were allowed to mix in the dark for 60 min prior to filtration and photographing.



**Figure 3.1**<sup>†</sup>. (a) Representative UV-vis absorbance spectra of the complexes between standard solutions of  $(\text{NH}_4)_2\text{Fe}(\text{SO}_4)_2 \cdot 6\text{H}_2\text{O}$  and 1,10-phenanthroline. (b) Calibration curve constructed from the absorbance at 510 nm from spectra shown in panel (a).

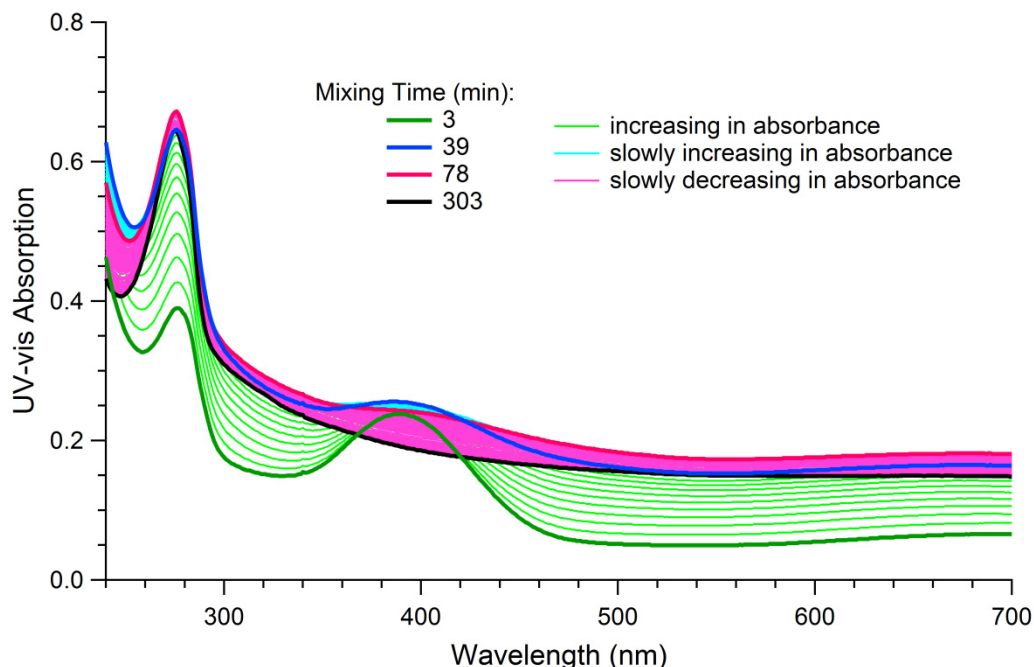
<sup>†</sup>These data were recorded by our collaborators at Wilfrid Laurier University, Waterloo, Ontario N2L 3C5, Canada.

### 3.4. Results and Discussion

#### 3.4.1. Optical Properties and Time Profile of Reactants and Products

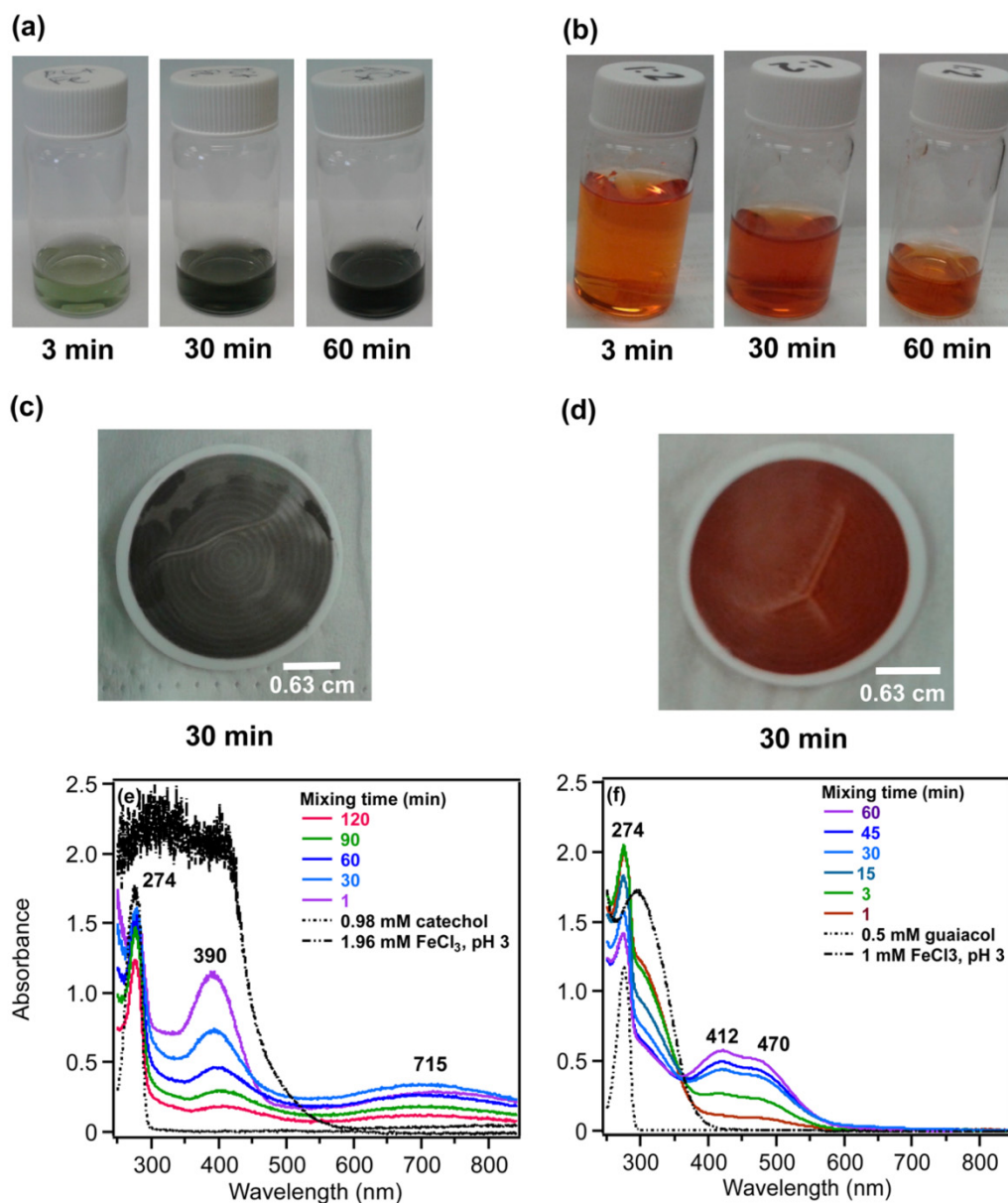
Upon reaction of  $\text{FeCl}_3$  with organics, color development and colloid formation was observed over time. Initial UV-vis experiments (Figure 3.2) showed evidence of colloid formation with a broad absorption at around 700 nm. Since the Shimadzu UV 1800 spectrophotometer did not go above 700 nm, further UV-vis measurements were, from then on, recorded on another instrument capable of providing wavelengths of light up to 850 nm. Figure 3.3<sup>†</sup>a-d and Figure 3.4<sup>†</sup> show time dependent images of solutions and filters resulting from the dark reactions of catechol and guaiacol with  $\text{FeCl}_3$  at pH 3 in the absence of added oxidants, such as  $\text{H}_2\text{O}_2$ . It is important to emphasize here that aqueous solutions are exposed to air, and hence, dissolved  $\text{O}_2$  is the oxidant and Fe(III) plays a role as a catalyst. The corresponding UV-vis





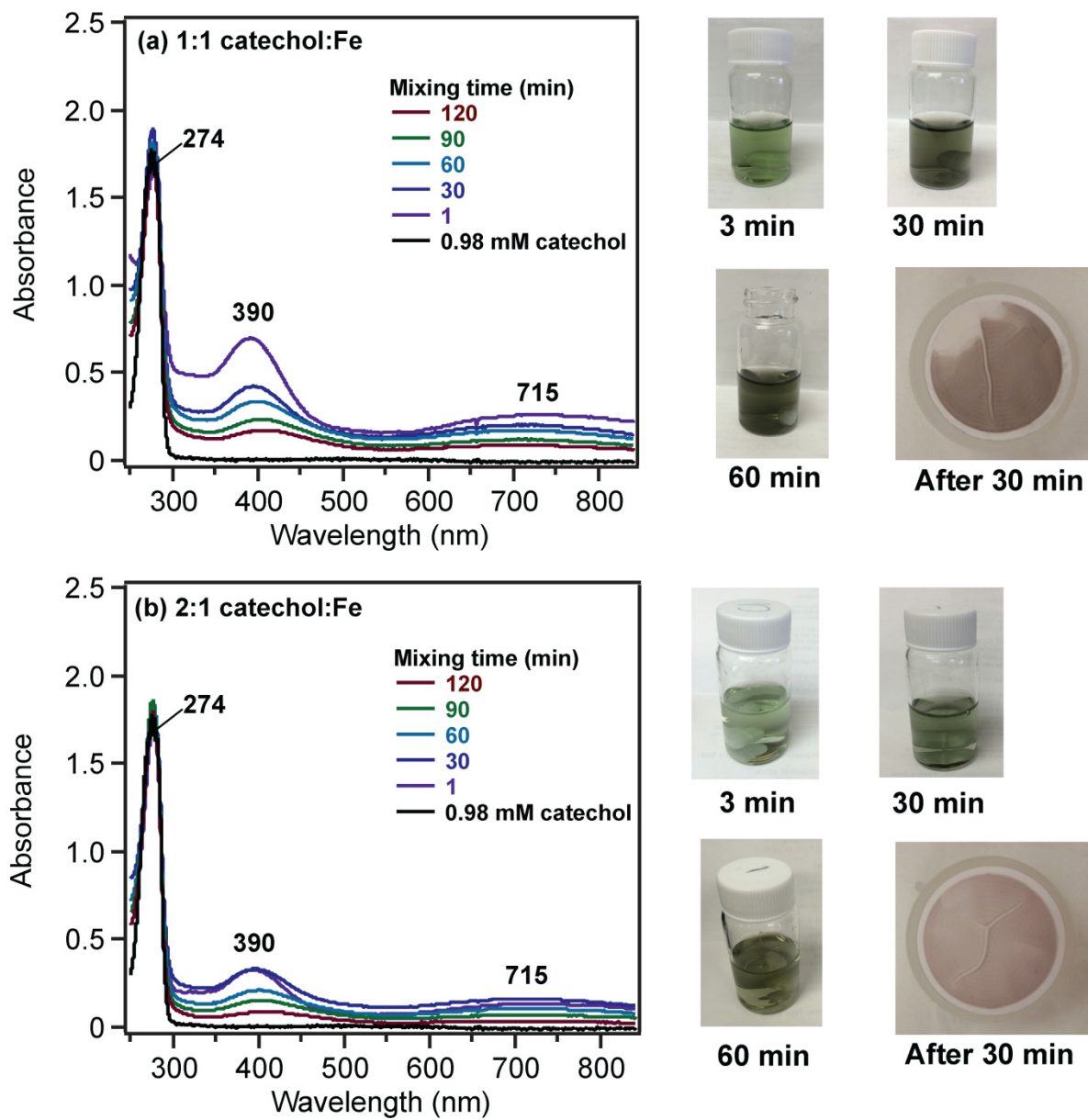
**Figure 3.2.** UV-vis spectra of unfiltered solutions after dark reaction of catechol (0.98 mM) with  $\text{FeCl}_3$  (1:2 organic reactant/Fe molar ratio) at pH 3 as a function of mixing time. Scans were recorded every 3 min. The dark green trace is due to absorbance from primary products and residual catechol. The formation of secondary products appeared as mixing time increased, as well as an unresolved background due to the formation of a colloid.

spectra after filtration (i.e., with particles taken out of the solution) are also shown (Figure 3.3<sup>†</sup>e,f) and compared to those of the initial spectra of catechol/ guaiacol prior to adding  $\text{FeCl}_3$ . While the concentrations are relatively high, they mimic interfacial regions on surfaces where aromatic compounds are enriched at the interface.<sup>30</sup> Both catechol and guaiacol solutions are transparent in the visible range and show a UV band around 274 nm due to  $\pi \rightarrow \pi^*$  transitions. The UV-vis absorbance spectrum of  $\text{FeCl}_3$  solution (pale yellow) shows a band around 295 nm from the ligand-to-metal-charge transfer (LMCT) of the prevailing species in solution,  $[\text{Fe}(\text{H}_2\text{O})_5\text{OH}]^{2+}$ .<sup>31</sup> Spectra collected at pH = 1-5 exhibit a shift in this peak because the iron speciation is strongly pH-dependent.<sup>32</sup> The pH used in our studies was chosen because a



**Figure 3.3.**<sup>†</sup> Dark reaction of catechol and guaiacol with  $\text{FeCl}_3$  at pH 3: (a and b) digital images of 1:2 organic reactant/Fe molar ratio of unfiltered solutions as a function of time; (c and d) particles on filter after 30 min; (e and f) the corresponding UV-vis spectra after filtration.

<sup>†</sup>These data were recorded by our collaborators at Wilfrid Laurier University, Waterloo, Ontario N2L 3C5, Canada.



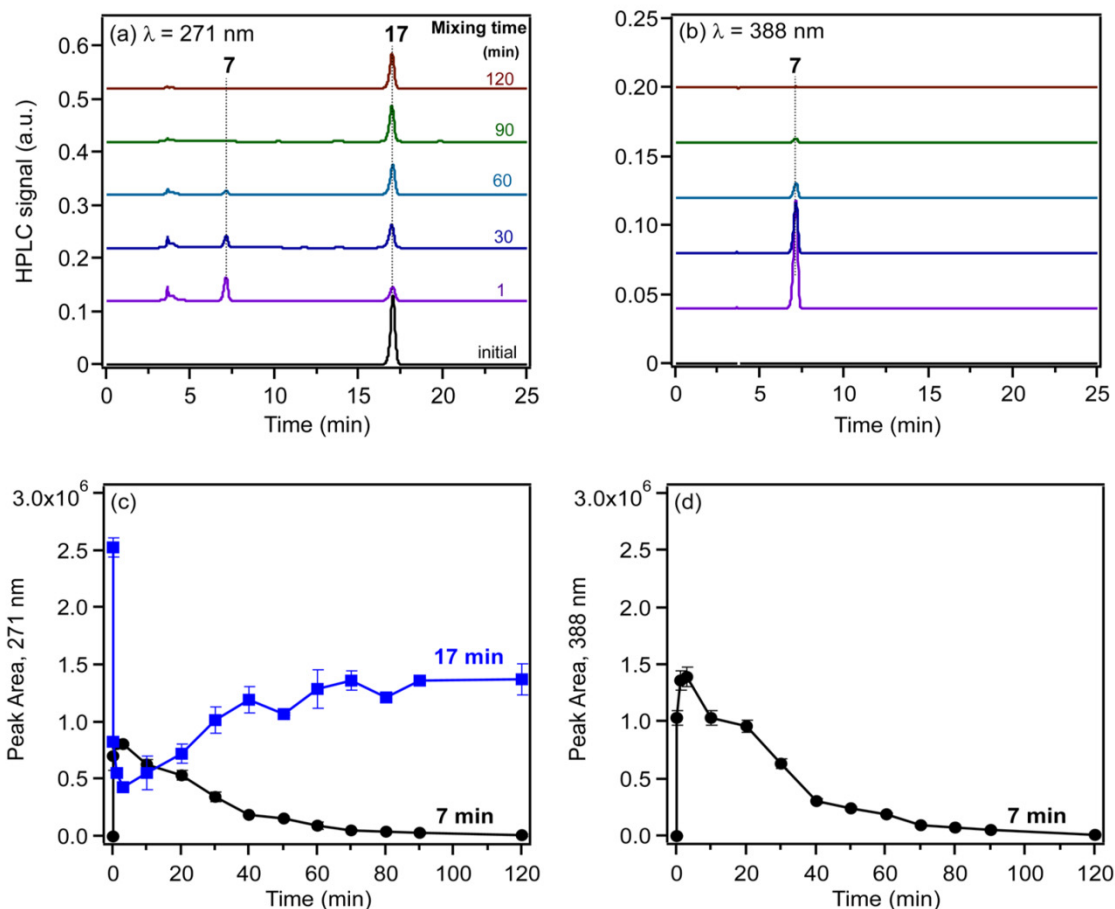
**Figure 3.4.**<sup>†</sup> UV-vis spectra of unfiltered solutions after dark reaction and filtration of catechol (0.98 mM) with  $\text{FeCl}_3$  at pH 3 at different ratios a function of time. Digital images of the corresponding unfiltered solutions and particles on filter after 30 min are shown on the right.

<sup>†</sup>These data were recorded by our collaborators at Wilfrid Laurier University, Waterloo, Ontario N2L 3C5, Canada.

number of studies<sup>32</sup> reported maximum photoreactivity of iron species toward organic degradation at pH 3. This pH is also environmentally relevant since aerosols are generally acidic (e.g., pH 3 is possible for fog droplets in highly polluted areas).<sup>13</sup> In the case of catechol, the initial green color was observed for 1:2, 1:1, and 2:1 organic reactant/Fe molar ratios, attributed to the formation of a bidentate mononuclear catechol-Fe complex (Scheme 3.1) with a LMCT band around 700 nm.<sup>33</sup> The intensity of this feature varies with the amount of Fe in the solution mixture, being the least intense for organic reactant/Fe 2:1 solution mixtures. The Fe(III)/Fe(II) cycling can be followed by flow injection analysis and also online by a continuous flow analysis<sup>34, 35</sup> where the concentration of Fe(II) and total Fe after the reduction of Fe(III) can be determined on the basis of the color of the reaction. The intense spectral feature at 390 nm is attributed to  $n \rightarrow \pi^*$  transitions of o-quinone species formed from oxidation of catechol-Fe complexes.<sup>36</sup> We observed this peak at lower concentrations of catechol and iron under acidic conditions and for other catecholates such as gallic acid.<sup>31</sup> The intensity of this feature decreases with less Fe in the solution mixture (Figure 3.3<sup>†</sup>e vs. Figure 3.4<sup>†</sup>a,b). The presence of -OCH<sub>3</sub> group in the case of guaiacol inhibits the formation of the iron complex evident by the absence of the characteristic LMCT band in Figure 3.3<sup>†</sup>f. Instead, spectra in Figure 3.3<sup>†</sup>f suggest the formation of soluble amber-colored oxidation products (compounds V–VIb; Scheme 3.1) due to iron redox chemistry. These spectra are identical to those observed by Hwang et al.<sup>37</sup> who identified products from the biochemical oxidation of guaiacol by manganese peroxidase (MnP) in the presence of H<sub>2</sub>O<sub>2</sub> by a suite of analytical techniques. In our study, in situ reduction of Fe(III) to Fe(II) leads to the formation of phenoxy radicals, which proceeds through C-C radical coupling to form compound V. Compounds VIa and VIb (Scheme 3.1) give rise to the spectral features at 412 and 470 nm (Figure 3.3<sup>†</sup>f), which were observed to decrease in intensity upon

overnight storage of solutions.<sup>37, 38</sup> Schmalzl et al.<sup>39</sup> assigned the 470 nm peak to an unstable 4,4'-diphenoquinone intermediate.<sup>39</sup> Further characterization of guaiacol oxidation products was not carried out herein given the similarities between our data in Figure 3.3<sup>†f</sup> and published product identification studies.<sup>37, 38</sup> Since studies on the oxidation of catechol by Fe(III) are limited under our experimental conditions, the following paragraphs describe in detail the time profile of reactants and products from HPLC studies.

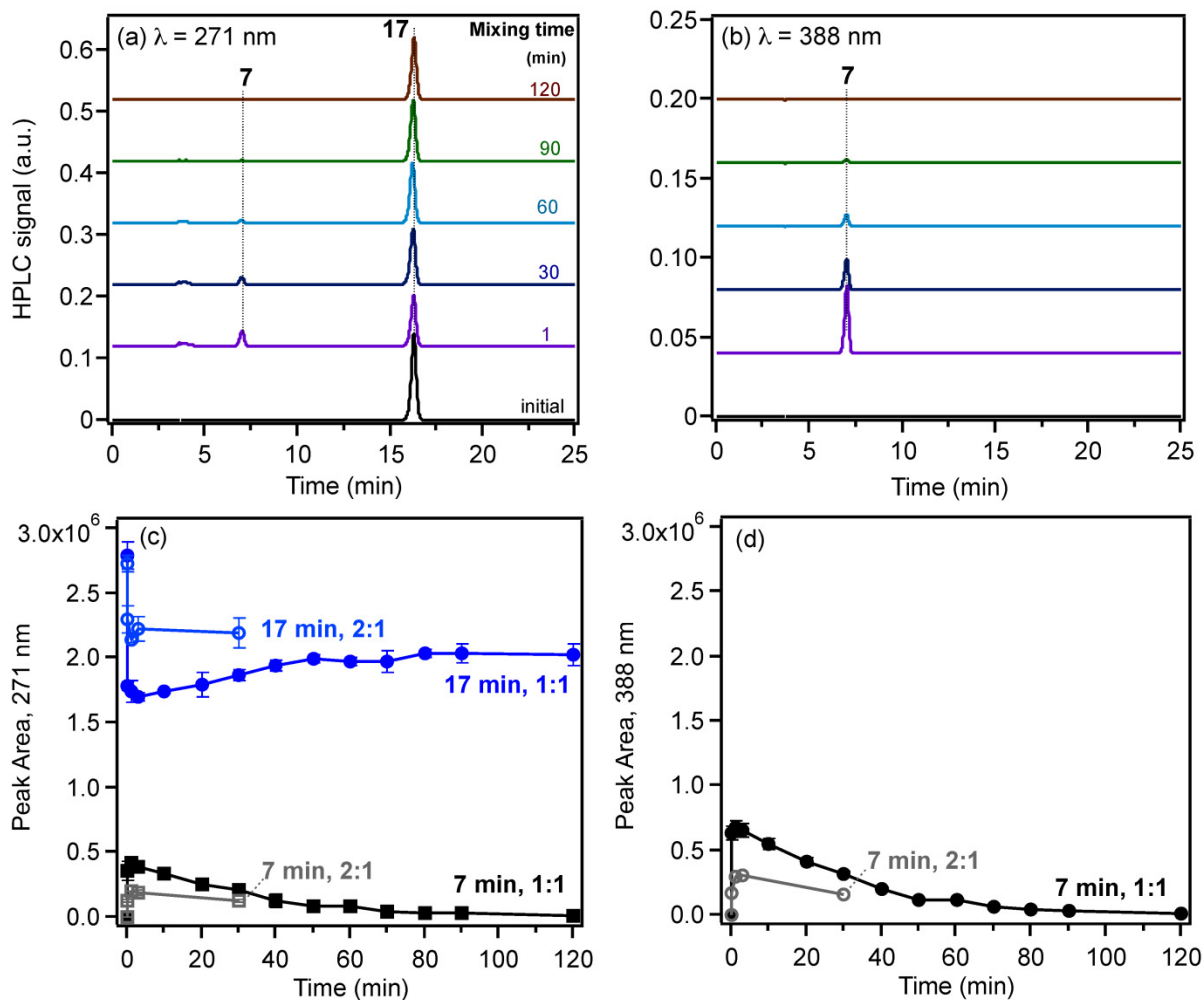
Figure 3.5<sup>†</sup> shows HPLC chromatograms collected before and after the addition of FeCl<sub>3</sub> to a catechol solution at pH 3, which were recorded at  $\lambda = 271$  nm and 388 nm. These wavelengths were chosen based on UV-vis spectra shown in Figures 3.2 and 3.3<sup>†e</sup> to separate compounds contributing to the reactant and product peaks. The chromatograms at  $\lambda = 271$  nm show two major peaks at 7 min and 17 min retention time (RT), whereas only one major peak is present in the chromatograms at  $\lambda = 388$  nm (RT = 7 min). The 7 min and 17 min peaks are assigned to a product and catechol (reactant), respectively, from the comparison with the chromatogram of catechol standard solution. The integrated areas of these peaks are plotted as a function of time in Figure 3.5<sup>†c,d</sup> for solution mixtures with 1:2 molar ratio of catechol/Fe. Similar experiments were conducted by varying the molar ratios, and the data are presented in Figure 3.6<sup>†</sup> for 1:1 and 2:1 molar ratios of catechol/Fe. Despite the drop in the performance of the detector at 700 nm, where the catechol-Fe complex absorbs, experiments were conducted to examine the kinetic behavior of the product peak at this wavelength. Figure 3.7<sup>†</sup> shows results from collecting chromatograms at  $\lambda = 700$  nm and the resulting kinetic curves for the product peak at 7 min compared with data generated from the chromatograms collected at 271 nm. These kinetic curves track well with each other supporting the assignment of the peak at 7 min to a catechol-Fe complex.



**Figure 3.5.**<sup>†</sup> HPLC chromatograms collected at (a) 271 nm and (b) 388 nm for the initial catechol solutions (0.98 mM) and after reaction with  $\text{FeCl}_3$  at pH 3 as a function of reaction time. (c and d). Resulting kinetic curves from the integrated areas of the peaks at 7 min and 17 min. The solution mixture contains 1:2 molar ratio of catechol/Fe.

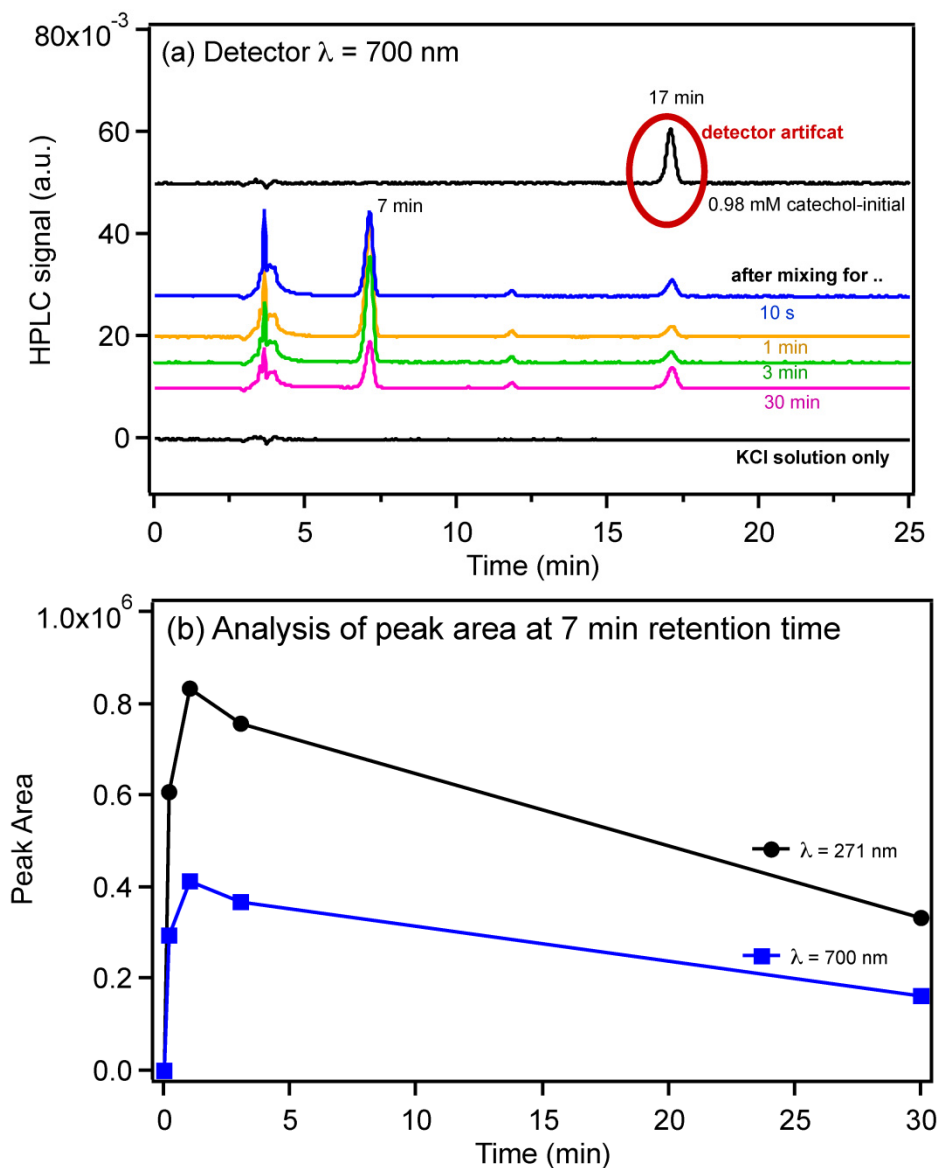
<sup>†</sup>These data were recorded by our collaborators at Wilfrid Laurier University, Waterloo, Ontario N2L 3C5, Canada.

The time profiles of the peak at RT = 7 min clearly show that it is an intermediate species that reaches its maximum concentration at 3 min. Because this product peak has absorptions at 271 nm, 388 nm, and 700 nm, it is consistent with the formation of the catechol-Fe complex and



**Figure 3.6.** † (a) and (b) HPLC chromatograms collected for initial catechol solutions (0.98 mM) and after reaction with  $\text{FeCl}_3$  at pH 3 as a function of reaction time with a final molar ratio of 1:1. (c) and (d) The resultant kinetic curves from the integrated areas of the peaks at 7 and 17 min for solution mixtures containing 1:1 and 2:1 molar ratio of catechol:Fe.

†These data were recorded by our collaborators at Wilfrid Laurier University, Waterloo, Ontario N2L 3C5, Canada.



**Figure 3.7.**<sup>†</sup> (a) HPLC chromatograms collected for initial catechol solutions (0.98 mM) and after reaction with  $\text{FeCl}_3$  at pH 3 as a function of reaction time with a final molar ratio of 1:2, and (b) kinetic curves for the product peak at 7 min as a function of detector wavelength. The phrase “detector artifact” refers to the signal at 700 nm for the 17 min peak that does not originate from the catechol standard solution in the absence of iron.

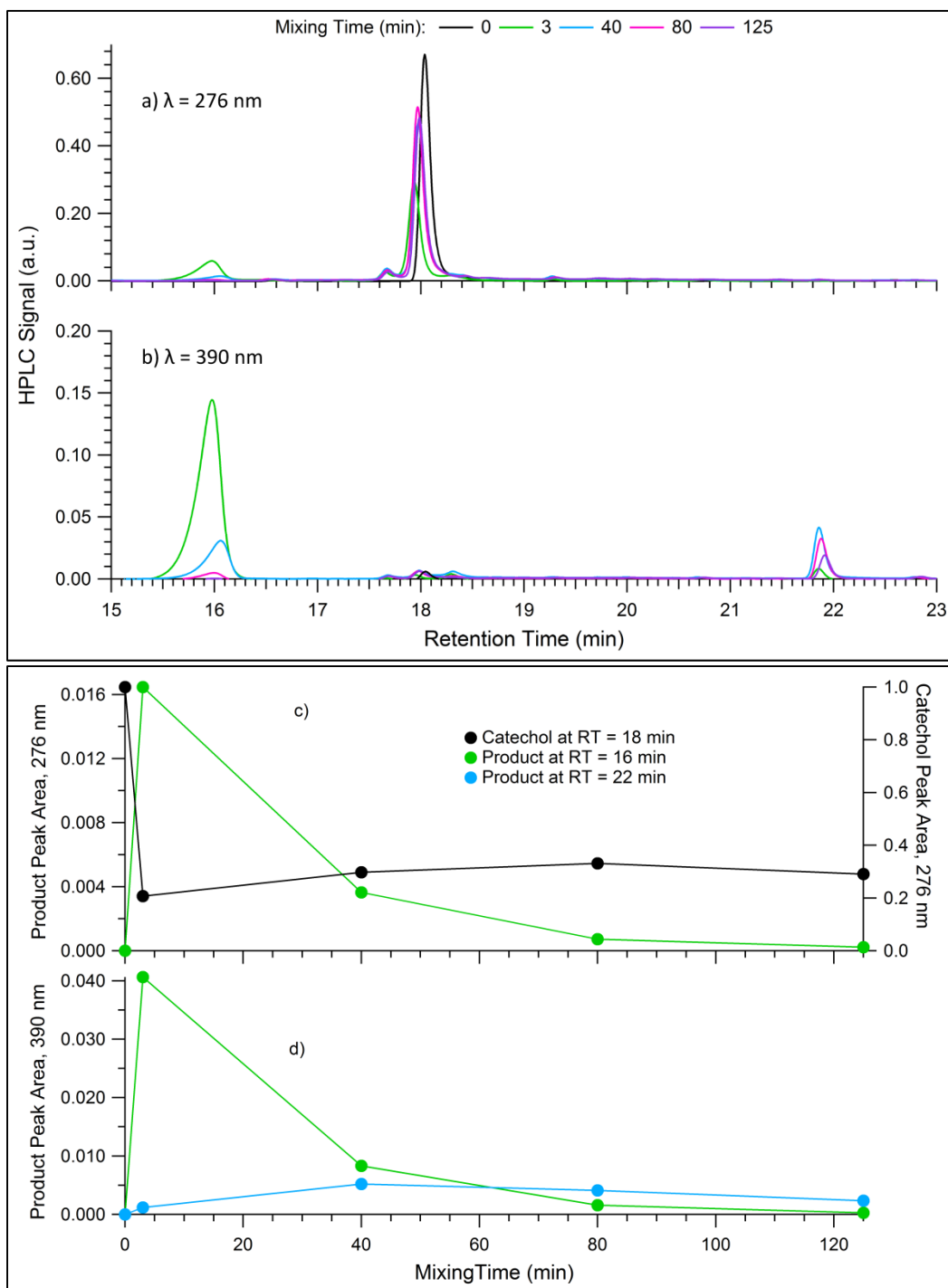
<sup>†</sup>These data were recorded by our collaborators at Wilfrid Laurier University, Waterloo, Ontario N2L 3C5, Canada.



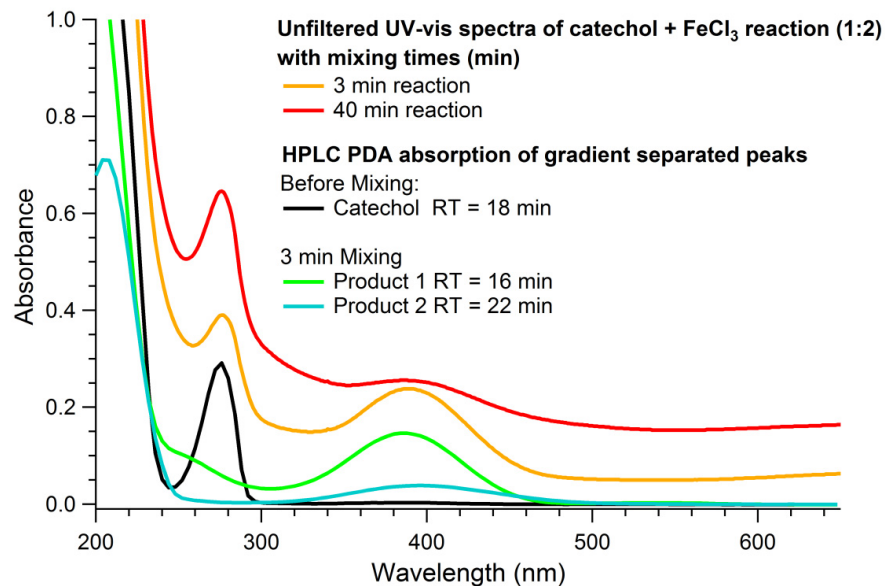
an unstable quinone species that undergoes further oxidation in the presence of dissolved O<sub>2</sub> and excess Fe(III).<sup>35</sup> It is likely that they both exist in equilibrium on the time scale of the collection time. This assignment is also similar to earlier observations of the time profile of peaks in the range 400-500 nm from guaiacol oxidation (see Figure 3.3<sup>†</sup>). For solution mixtures containing less Fe, as in the 1:1 and 2:1 molar ratios shown in Figure 3.6<sup>†</sup>, a smaller amount of this intermediate is formed, reduced by 50 and 23%, respectively, relative to that in 1:2 catechol/Fe molar ratio solutions. This result suggests that iron plays an important catalytic role in forming this oxidation product of catechol.

In addition, the kinetic curves of the RT = 17 min peak show that it reaches a minimum after 3 min of reaction (~83% decay in catechol, Figure 3.5<sup>†</sup>c), and then the signal starts to go up due to the contribution of products to the absorbance at  $\lambda = 271$  nm. These products appear to coelute at the same RT as catechol suggesting similar polarity. Gradient elution better resolved these peaks, but was still not fully successful. In these gradient HPLC experiments (Figure 3.8) catechol and the previously observed product peak eluted at 16 and 18 min, respectively. Interestingly, a second product peak was observed at a retention time of 22 min that absorbed at 390 nm, but not at 276 nm (Figure 3.9).

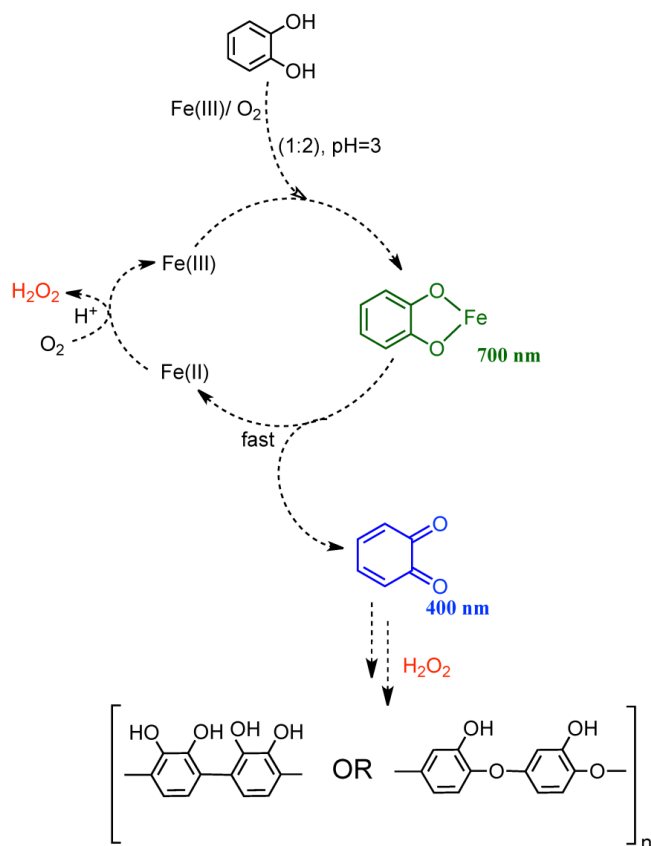
Lower amounts of Fe in the solution mixtures with 1:1 and 2:1 molar ratio catechol/Fe resulted in lower decay rates of catechol within the first 3 min (39% and 22%, respectively; Figure 3.6<sup>†</sup>c). Scheme 3.2 shows a suggested mechanism for the catechol + Fe(III) reaction based on the data presented herein. This mechanism also explains the formation of polycatechol particles that form over time, which are examined more closely in the last section. To further explore the identity of these products, we describe the results of LC-ESI-MS/MS experiments in the next section.



**Figure 3.8.** (a) and (b) HPLC chromatograms using a gradient method collected for initial catechol solutions (0.98 mM) and after reaction with  $\text{FeCl}_3$  at pH 3 as a function of reaction time with a final molar ratio of 1:2, and (b) kinetic curves for the catechol peak at 18 min and product peaks at 16 and 22 min as a function of detector wavelength.



**Figure 3.9.** Absorption spectra for unfiltered UV-vis spectra of catechol + FeCl<sub>3</sub> reaction (1:2) for 3 and 40 min mixing times and absorption of catechol and 2 products observed in gradient HPLC experiments.

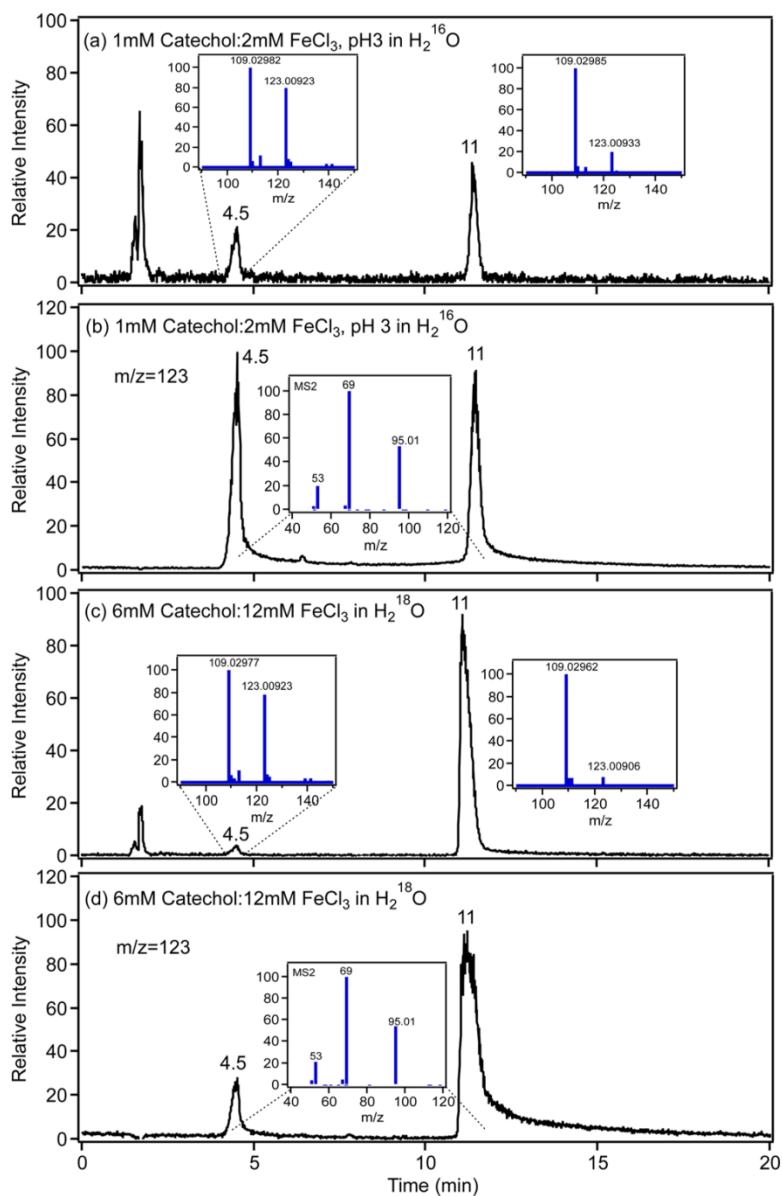


**Scheme 3.2.** Suggested mechanism for catechol oxidation and polycatechol formation in the presence of excess Fe(III) in the dark under acidic conditions.

### 3.4.2. Product Identification Using LC-ESI-MS/MS

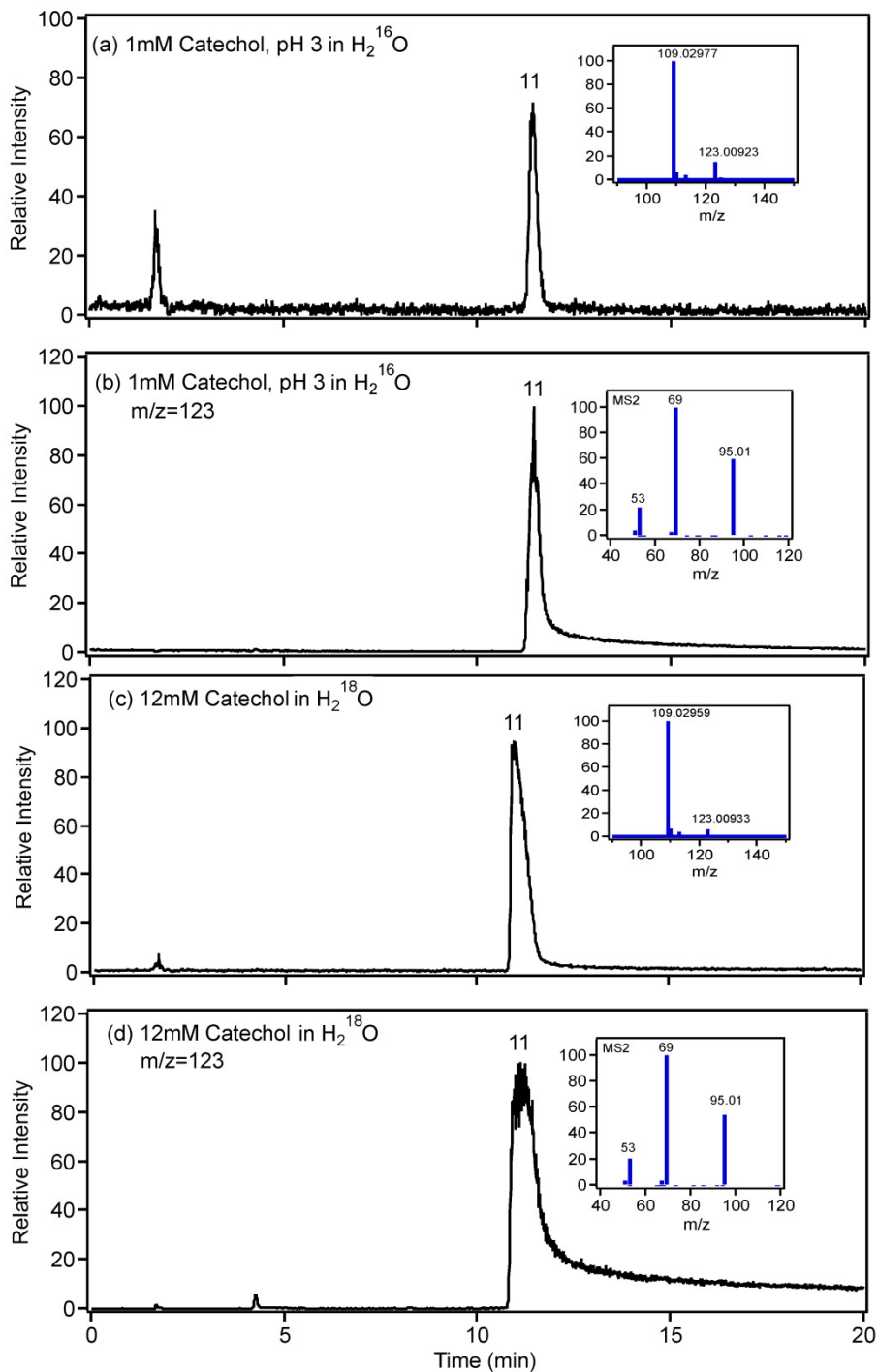
Figure 3.10<sup>†</sup> shows total ion chromatograms (TIC) of a solution mixture containing 1:2 molar ratio of catechol/Fe at pH 3 after reaction for 3 min. The reaction was carried out in normal water (H<sub>2</sub><sup>16</sup>O, Figure 3.10<sup>†</sup>a,b) and in <sup>18</sup>O-labeled water (H<sub>2</sub><sup>18</sup>O, Figure 3.10<sup>†</sup>c,d) to investigate the source of the oxygen atoms in products containing an added O atom. Similar data were collected for catechol standard solutions, as shown in Figure 3.11<sup>†</sup>. These chromatograms are similar to those collected using HPLC on a separate instrument with a UV-vis detector (Figure 3.5<sup>†</sup>) with slightly different elution times for the reactant peak (RT = 11 min) and product peak (RT = 4.5 min). The insets in Figure 3.10<sup>†</sup>a,c and Figure 3.11<sup>†</sup>a,c show the mass spectra of these major peaks. While ESI-MS/MS detection is not directly quantitative, peak ratios from spectra collected for samples under identical ionization conditions provide insight into the relative amount of a given species. In the absence of FeCl<sub>3</sub>, the MS spectra of catechol standard solutions (Figure 3.11<sup>†</sup>) show the expected [M - H]<sup>-</sup> ion peak at *m/z* 109 (C<sub>6</sub>H<sub>5</sub>O<sub>2</sub>) and a peak at *m/z* 123 ([M - H]<sup>-</sup>, C<sub>6</sub>H<sub>3</sub>O<sub>3</sub>) that coelutes with catechol with a RT of ~11 min (the RT changes slightly in the <sup>18</sup>O-labeled water, but we are going to refer to this peak as the 11 min peak regardless of the solvent). Note that the 11 min peak elutes later in <sup>18</sup>O-labeled water but the eluted compound is the same in both normal and isotopically labeled solvents. The relative ratio of the *m/z* 109 and *m/z* 123 is ~100:15 in normal water and 100:6 in <sup>18</sup>O-labeled water. As detailed below, the addition of FeCl<sub>3</sub> increases the intensity of the *m/z* 123 peak confirming that it originates from a more oxidized species than catechol. The fragmentation pattern of the *m/z* 123 from MS/MS spectra is shown in Figures 3.11<sup>†</sup>b,d and it is identical regardless of the isotopic state of water solvent. In general terms, the MS/MS of the *m/z* 123 fragmentation is identical in intensity, accuracy, ions observed, and assigned elemental composition. The absence

of mass shifts confirms that the added oxygen atom in the oxidized catechol originates from dissolved  $O_2$  and not water solvent, as suggested earlier.<sup>33</sup>



**Figure 3.10.**<sup>†</sup> Total ion and  $m/z$  123 LC-ESI-MS/MS negative ion mode chromatograms for the reaction of catechol with  $FeCl_3(aq)$  under acidic conditions after 3 min dark reaction in (a and b) normal water ( $H_2^{16}O$ ) and (c and d)  $^{18}O$ -labeled water ( $H_2^{18}O$ ). (a and c, insets) Mass spectra for the major peaks; (b and d, insets) MS/MS spectra for the  $m/z$  123 ion.

<sup>†</sup>These data were recorded by our collaborators at Wilfrid Laurier University, Waterloo, Ontario N2L 3C5, Canada.

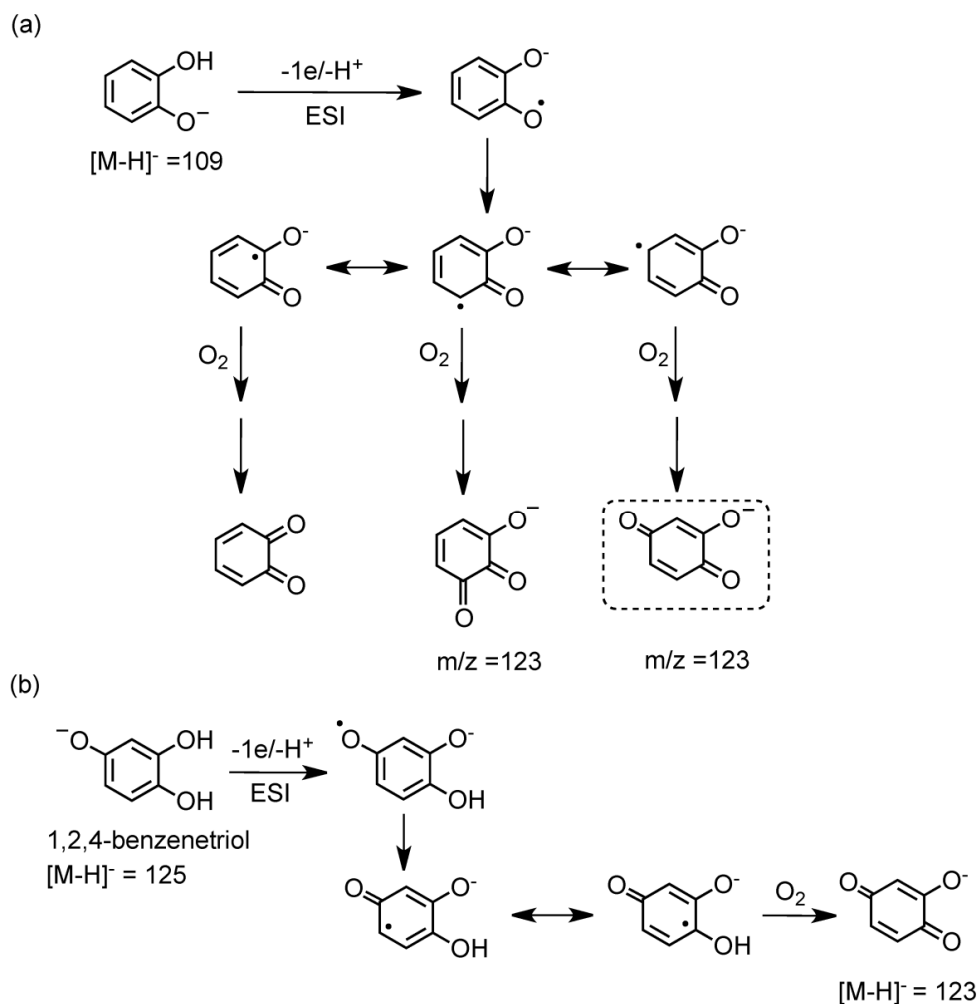


**Figure 3.11.**<sup>†</sup> Total ion and  $m/z$  123 LC-ESI-MS/MS negative ion mode chromatograms for catechol standard solutions under acidic conditions in normal water ( $H_2^{16}O$ , (a)-(b)) and in water- $^{18}O$  ( $H_2^{18}O$ , (c)-(d)). The insets in (a) and (c) show the mass spectra for the major peaks, and those in (b) and (d) show the MS/MS spectra for the  $m/z$  123 ion.

<sup>†</sup>These data were recorded by our collaborators at Wilfrid Laurier University, Waterloo, Ontario N2L 3C5, Canada.

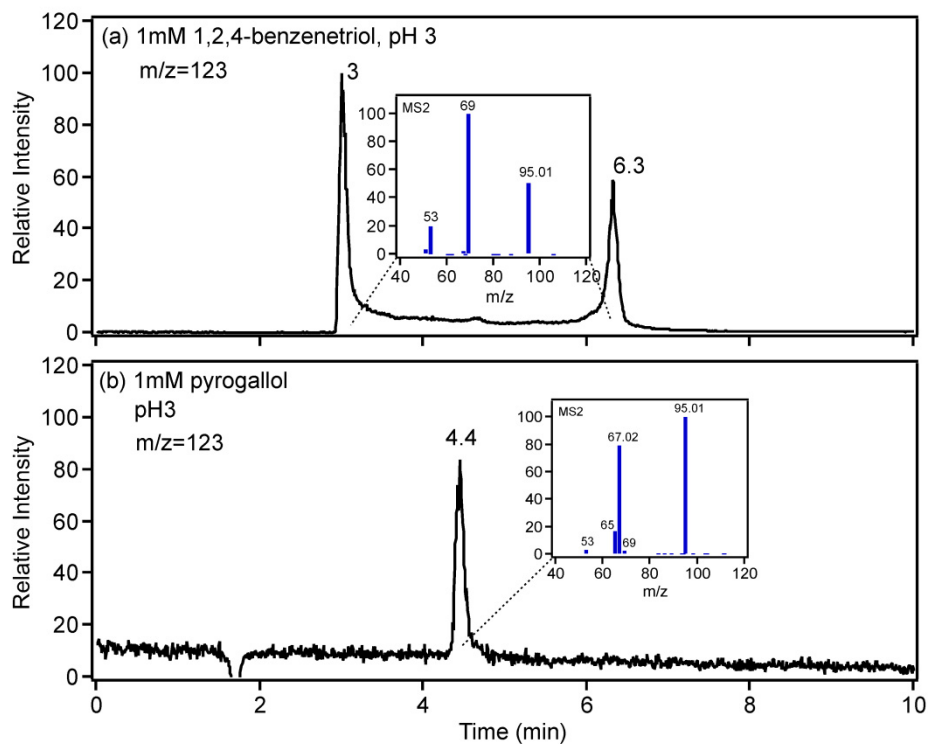
Catecholates and guaiacol are susceptible to oxidation in the presence of dissolved  $O_2$ .<sup>40</sup> Scheme 3.3 shows a likely mechanism that explains the formation of the observed species with  $m/z$  123. The relatively high voltage and ionization conditions under ambient conditions in the ESI chamber may catalyze the formation of radical anions, which, in the presence of  $O_2(aq)$ , can form hydroxylated quinone species, in the ortho- and para- positions. Artifacts associated with the oxidation and reduction of analytes in ESI sources were not sufficiently studied. Even though the source was polarized for negative ion production, both oxidation and reduction reactions could still occur on the tip of the electrospray capillary. Two reference compounds, 1,2,4-benzenetriol (VII) and pyrogallol (VIII), with the chemical formula  $C_6H_6O_3$  were tested to examine the fragmentation pattern of their oxidation products in the ESI chamber. Figure 3.12<sup>†</sup> shows the chromatograms and MS/MS spectra at pH 3 for these compounds. In Figure 3.12<sup>†</sup>a, 1,2,4-benzenetriol shows two peaks with the same fragmentation pattern because it is known to be auto-oxidizable<sup>41</sup> with interconversion between reduced and oxidized occurring over the separation time scale. The likely oxidation steps of 1,2,4-benzenetriol are presented in Scheme 3.3b. To explain the two chromatographic peaks with the same MS ion, we collected HPLC/UV-vis chromatograms for 1 mM standard solution of 1,2,4-benzenetriol at pH 3. Figure 3.13<sup>†</sup> shows these results where one chromatographic peak is observed, which is the oxidized form of this molecule. Greenlee et al.<sup>41</sup> developed a method for separation and quantification of phenolic compounds by adding antioxidants and running experiments under oxygen-free conditions using  $N_2$  gas purging. The MS/MS spectrum shown in the inset of Figure 3.12<sup>†</sup>a is identical to that in the insets of Figure 3.10<sup>†</sup>b,d and Figure 3.11<sup>†</sup>b,d. On the other hand, pyrogallol showed one peak in the TIC and in the selected ion chromatogram corresponding to  $m/z$  123 (Figure 3.12<sup>†</sup>b). The fragmentation pattern of this peak (inset) is different than that

shown in Figures 3.10<sup>†</sup>b,d and 3.11<sup>†</sup>b,d. Hence, the main conclusion is that autoxidation of catechol takes place to some extent in the ESI source, and the main product is 1,2,4-benzentriol. To the best of the authors' knowledge, the oxidation of catecholates under electrospray ionization conditions was not previously reported.



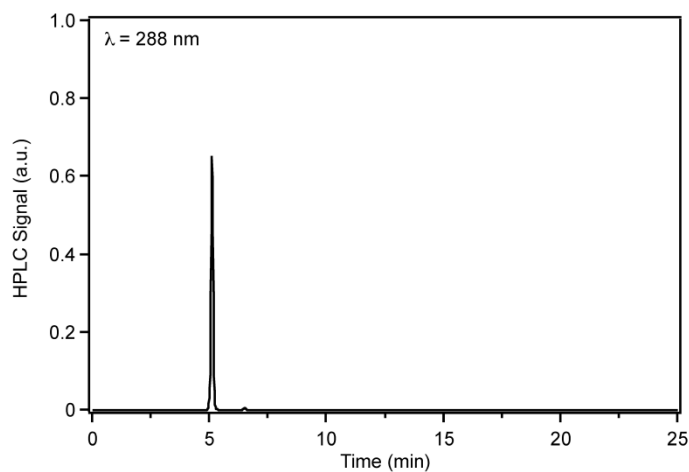
**Scheme 3.3.** Suggested mechanism for the oxidation of (a) catechol and (b) 1,2,4-benzenetriol induced in the ESI chamber by  $O_2(aq)$  explaining the origin of the  $m/z$  123 with the same fragmentation pattern for both chemicals.





**Figure 3.12.**<sup>†</sup> Chromatograms for  $m/z$  123 of reference compounds 1,2,4-benzenetriol and pyrogallol under acidic conditions in normal water ( $H_2^{16}O$ ). The insets show the MS/MS spectra for the  $m/z$  123 fragment.

<sup>†</sup>These data were recorded by our collaborators at Wilfrid Laurier University, Waterloo, Ontario N2L 3C5, Canada.



**Figure 3.13.**<sup>†</sup> HPLC chromatogram collected for 1 mM standard solution of 1,2,4-benzenetriol at pH 3.

<sup>†</sup>This data was recorded by our collaborators at Wilfrid Laurier University, Waterloo, Ontario N2L 3C5, Canada.

The addition of FeCl<sub>3</sub> to catechol solutions results in complex formation and quinone production. The total ion chromatograms (TICs) in Figures 3.10<sup>†</sup>a,c show a product peak that elutes at RT ~ 4.5 min, with mass spectra containing *m/z* 109 and 123 with 4× and 13× increase in intensity for the latter peak relative to RT ~ 11 min, respectively. Table 3.1 shows that this enhancement in intensity is consistently observed for variable amounts of Fe in solution. These results can be explained in light of the UV-vis and HPLC data presented in the previous section: the catechol-Fe complex is more polar (and therefore elutes earlier) than catechol. The complex

**Table 3.1.** Intensity ratios of major peaks observed in the mass spectra of catechol and iron chloride solution with different ratios at pH 3 at a given different retention times.

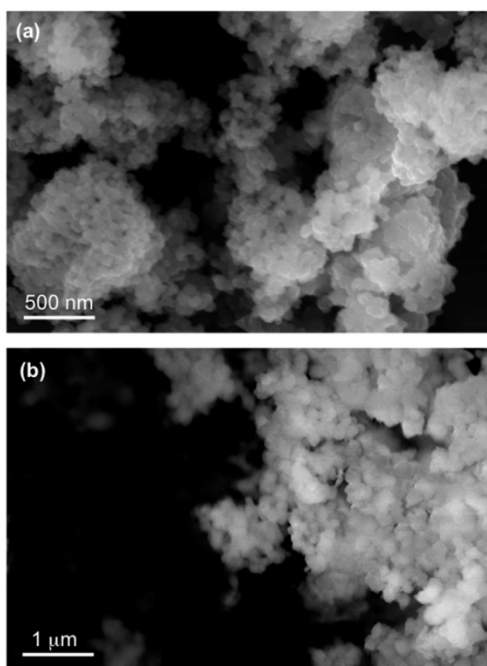
Solution	Retention time (RT)	% Intensity ratios of <i>m/z</i> 123/109 peaks
1 mM catechol standard solution in H <sub>2</sub> <sup>16</sup> O	11	14.9
12 mM catechol standard solution in H <sub>2</sub> <sup>18</sup> O	11	6.2
1 mM catechol: 2 mM FeCl <sub>3</sub> in H <sub>2</sub> <sup>16</sup> O after 3 min reaction	4.5	79.4
	11	20.2
6 mM catechol: 12 mM FeCl <sub>3</sub> in H <sub>2</sub> <sup>18</sup> O after 3 min reaction	4.5	78.3
	11	7.99
1 mM catechol: 1 mM FeCl <sub>3</sub> in H <sub>2</sub> <sup>16</sup> O after 3 min reaction	4.5	71.8
	11	16.8
1 mM catechol: 0.5 mM FeCl <sub>3</sub> in H <sub>2</sub> <sup>16</sup> O after 3 min reaction	4.5	78.2
	11	13.7
1 mM catechol: 0.33 mM FeCl <sub>3</sub> in H <sub>2</sub> <sup>16</sup> O after 3 min reaction	4.5	81.9
	11	16.1

is not observed mass spectrometrically as it is not stable in the mass spectrometric time frame. As a result, we only see the anionic portion of this complex, that is, the  $m/z$  109, which upon formation, is readily oxidized to 1,2,4-benzotriol with  $m/z$  123 (identical fragmentation pattern with product peak at RT  $\sim$  4.5 min). Moreover, HPLC/MS experiments were conducted in the positive ion mode under the same elution conditions as negative mode. The resulting spectra yielded no meaningful data because these species do not yield  $[M + H]^+$ ,  $[M + Na]^+$ , and other positive ions under these solution conditions. Also, the presence of excess Fe(III) in these solutions leads to cluster formation and ion suppression.

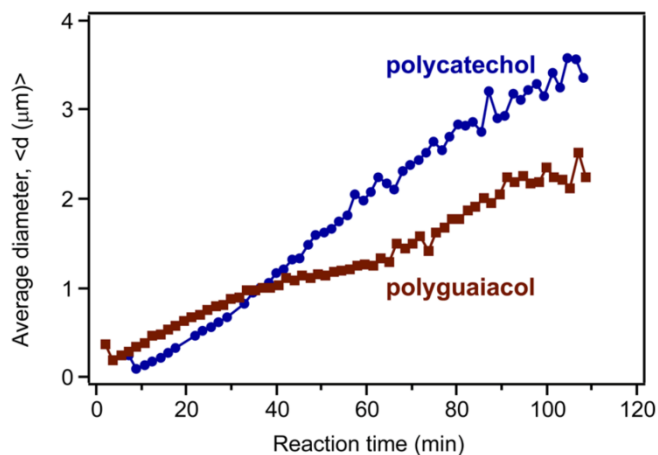
Previous studies<sup>37-39</sup> on guaiacol reaction with transition metals including iron characterized some of the soluble products of the oxidation process. Using a combination of HPLC,  $^1\text{H}$  NMR, fast atom bombardment, and chemical ionization mass spectrometry, Schmalzl et al.<sup>39</sup> studied the reaction of guaiacol with  $\text{FeCl}_3$  and reported elemental composition, retention times, characteristic chemical shifts, and masses of guaiacol oligomers ranging from dimers to pentamers at 246 (compound V), 368, 490, and 612 mass units. These oligomers formed a precipitate soluble in organic solvents and were found to be mainly organic in composition. Similar oligomers up to trimers were observed in the mass spectra of reaction products from enzymatic oxidation of guaiacol.<sup>37, 38</sup> The established mechanism that explains these results is mainly carbon-carbon coupling of guaiacoxyl radicals, with little evidence for carbon-oxygen coupling.<sup>37, 39</sup> As detailed in the last section, the formation of these polymeric species has implications on the overall optical properties and chemical reactivity of the surfaces these products coat.

### 3.4.3. Formation of Polymeric Catechol and Guaiacol Particles

Figure 3.3<sup>†c,d</sup> shows digital photographs of particles collected on a filter from the dark reaction of catechol and guaiacol with FeCl<sub>3</sub> at pH 3. Figure 3.14 shows SEM images of these particles, which clearly display their amorphous nature as micron-sized conglomerates of nanometer-sized primary particles. EDS experiments showed that polycatechol and polyguaiacol particles are organic and had less than 0.5 atomic % Fe, which was most likely due to contamination from its salt remaining after washing the particles with water. The iron content in these particles analyzed by ICP-MS was also below the detection limit, similar to the results of the control filter with no particles. Moreover, changes in particle size with reaction time was monitored using DLS experiments, which showed that particles appeared within 3 min of the



**Figure 3.14.** SEM images for (a) polycatechol and (b) polyguaiacol collected on copper grids after a 90 min dark reaction of catechol with FeCl<sub>3</sub> at pH 3 in a 1:2 molar ratio.



**Figure 3.15.** DLS measurements of the average particle size of polycatechol and polyguaiacol as a function of reaction time during the dark reaction of catechol with FeCl<sub>3</sub> at pH 3 in a 1:2 molar ratio.

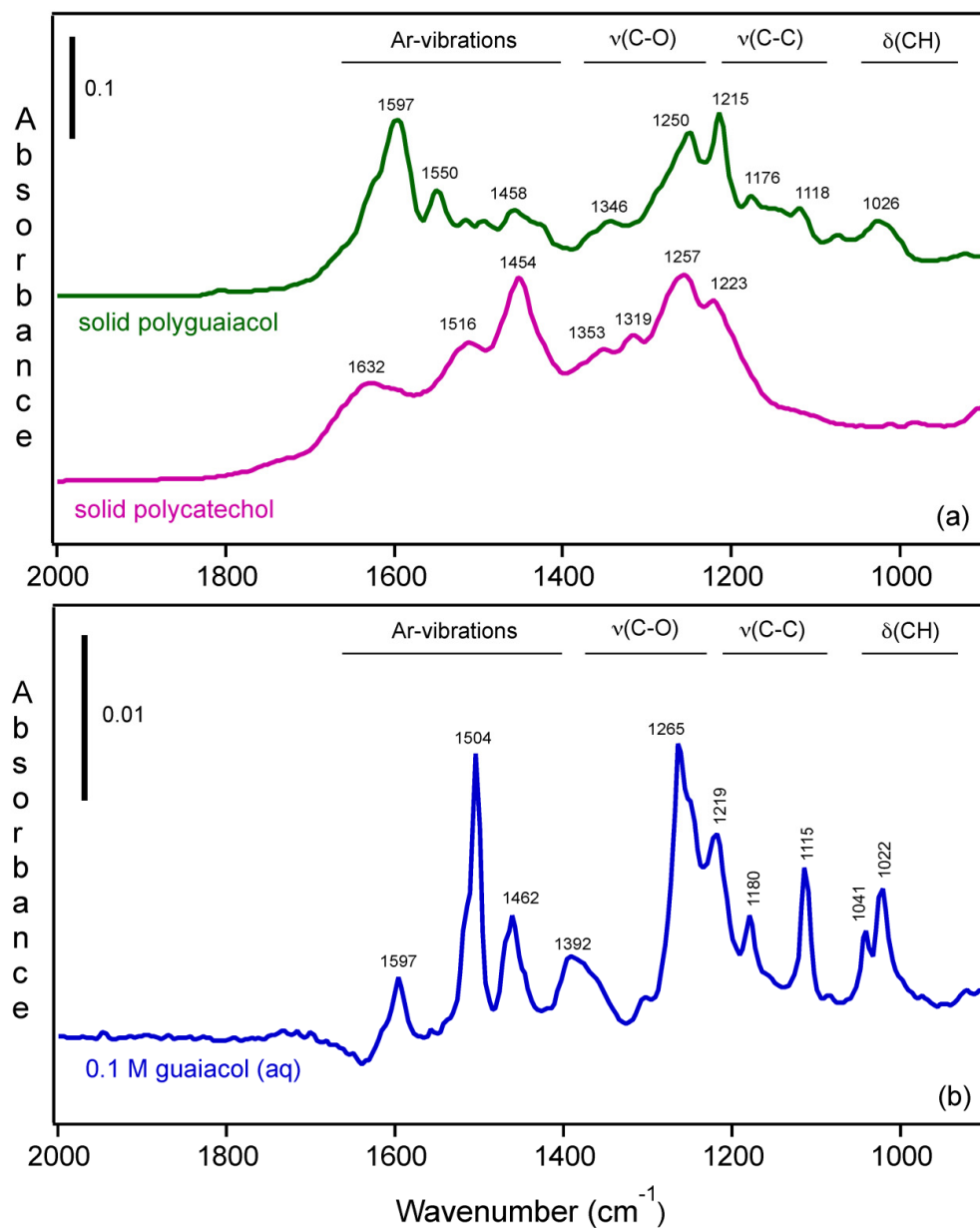
reaction of  $\text{FeCl}_3$  with either catechol or guaiacol solutions (Figure 3.15). Particles grew to average diameters on the order of a micron, which is consistent with SEM images, after 30 min of reaction time when sedimentation becomes important. Also at this time, polycatechol particles became larger in average diameter than polyguaiacol particles because of the  $1.8\times$  faster growth rate of polycatechol (36 nm/min) compared to that of polyguaiacol particles (20 nm/min). These results suggest that these particles are organic in nature and not a precipitate of iron (oxyhydr)-oxides. Mass yield experiments were also performed where particles were collected and extensively washed with Milli-Q water after 120 min reaction of  $\text{FeCl}_3$  with either catechol or guaiacol (1:2 organic reactant/Fe molar ratio) at pH 3. Polycatechol mass yield was found to be  $47 \pm 4\%$ , and that of polyguaiacol was  $49 \pm 14\%$ . This mass yield is comparable to or larger than the typical mass yields of SOA obtained by photooxidation of common volatile organic compounds, such as terpenes,<sup>42</sup> and it is larger than the yields associated with aqueous SOA (aqSOA) photochemical production.<sup>43</sup> Therefore, the iron catalyzed reactions of catecholates definitively have the potential to produce SOA with high efficiency.

Moreover, Figure 3.16<sup>†</sup>a shows ATR-FTIR spectra of solid polycatechol and polyguaiacol formed in reactions of Fe(III) with catechol and guaiacol. These spectra are compared with those recorded for aqueous phase catechol<sup>31</sup> and guaiacol (Figure 3.16<sup>†</sup>b). There are clear differences between the spectra of monomers and polymers in the 2000-1000  $\text{cm}^{-1}$  spectral range containing vibrations of aromatic (1640-1400  $\text{cm}^{-1}$ ), C-O and C-C stretching (1400-1200  $\text{cm}^{-1}$ ), and C-H bending (1200-1000  $\text{cm}^{-1}$ ) modes. This is in line with earlier reports on polycatechol using transmission FTIR using KBr pellets,<sup>44, 45</sup> where broadening and shift in peak frequencies was observed due to the rigid structure of polymers. The high intensity of features in the range of 1400-1200  $\text{cm}^{-1}$  is characteristic of phenylene (C-C) and oxyphenylene

(C-O-C) linkages. These spectra show no absorbance around  $1700\text{ cm}^{-1}$  indicative of carbonyl (C=O) groups, which were reported for catechol and guaiacol SOA due to reaction with ozone.<sup>22</sup> This clearly shows that particle formation catalyzed by iron proceeds via a different reaction pathway than SOA formation via metal-free atmospheric photo-oxidation reactions.

Oxidative enzymatic polymerization of guaiacol and catechol is well-studied in biochemical and polymer synthesis fields.<sup>17, 24, 46</sup> Brick-red colored polyguaiacol prepared from the enzymatic oxidation of monomer guaiacol using peroxidase- $\text{H}_2\text{O}_2$  as catalyst was previously characterized because of its usefulness as a model polymer for lignin biodegradation research.<sup>47</sup> In another study,<sup>39</sup> the solid material was collected from the reaction of guaiacol with Fe(III) chloride and Cr(VI) oxide, which was then solubilized for analysis using UV-vis, HPLC and mass spectrometry. In the case of polycatechol formation, enzymes free of metal centers such as peroxidase<sup>48</sup> and laccase<sup>44</sup> were shown to catalyze polymer synthesis in solutions containing hydrogen peroxide and dissolved oxygen, respectively. Mechanistically, these enzymes catalyze C-C coupling and formation of ether (C-O-C) linkages between catechol monomers (Scheme 3.2). Because of their unique thermal, structural properties, and ability to form strong charge transfer complexes with metal oxides, polycatechols are exploited in surface modifications as adhesives and coatings over a wide range of organic and inorganic materials.<sup>24, 49</sup> For example, chelating abilities of anachelin (produced by cyanobacteria)<sup>20</sup> and mussel adhesive proteins<sup>20, 49-52</sup> containing catechol moieties were exploited in modifying  $\text{TiO}_2$  surfaces via poly(ethylene glycol) to form stable, protein resistant adlayers (i.e., antifouling polymer) desirable in biomedical devices and marine technology. More related to the work presented herein is the use of the catechol derivative dopamine in anchoring functional molecules to iron oxide shell of

magnetic nanoparticles.<sup>19, 53</sup> To our knowledge, oxidative polymerization of catechol in the presence of Fe(III) and in the absence of any added oxidants has not received attention.



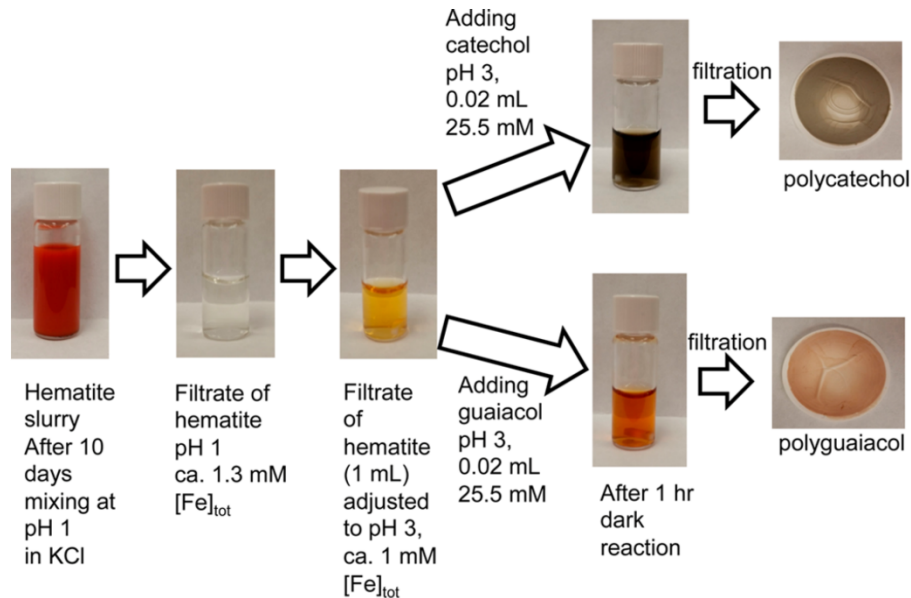
**Figure 3.16.**<sup>†</sup> ATR-FTIR absorbance spectra of (a) solid polycatechol (bottom) and polyguaiacol (top) deposited on a ZnSe ATR crystal from a water/ethanol slurry followed by drying overnight, and (b) 0.1 M aqueous solution. Similar spectra of catechol monomers were reported earlier.<sup>31</sup>

<sup>†</sup>These data were recorded by our collaborators at Wilfrid Laurier University, Waterloo, Ontario N2L 3C5, Canada.

Recently, Shi et al.<sup>54</sup> investigated the dominant mechanism that leads to iron dissolution in dust. Iron-containing dust samples were collected from two sites that represent sources of Saharan and Asian desert dust. The effect of cycling between wet aerosols (i.e., acidic conditions) and cloud droplets (i.e., more neutral pH and lower ionic strength conditions) on dissolved iron concentration was simulated over about 3 hr in the dark. The results showed that insoluble iron dissolves readily under the acidic conditions relevant to wet aerosols, whereas under more neutral pH, the dissolved iron precipitates as poorly crystalline nanoparticles. The relative amount of time mineral dust particles spend as either a wet aerosol or in cloud droplets will affect the amount of bioavailable iron upon deposition after long-range transport. Also, uptake of acids within clouds can also enhance iron dissolution in the droplets or in the residual aerosol formed after droplet evaporation. Herein, we used hematite to simulate acid-driven dissolution of iron (oxyhydr)oxides and followed the reaction of either catechol or guaiacol with the dissolved iron from these samples. Figure 3.17<sup>†</sup> shows digital images of the slurry and filtrates before and after the addition of the organics, in addition to the filters after 1 hr reaction. Clearly, the chemistry described above using FeCl<sub>3</sub> as a source of dissolved iron is similar to that from simulated aged iron-containing mineral dust particles. As emphasized in the introduction, pathways for particle formation from phenol derivatives are of increased interest to atmospheric chemists. The implications of these findings are summarized in the following section.

To help fill the gap in our understanding of the surface chemistry driven by iron on atmospherically relevant surfaces, we showed that the dark reaction of catechol and guaiacol with Fe(III) under acidic conditions and in the absence of any added oxidants results in the formation of soluble and reactive secondary organics and insoluble polymeric particles. The strong visible light absorption by the resulting soluble products and insoluble polymeric organic





**Figure 3.17.**<sup>†</sup> Formation of polycatechol and polyguaiacol from reaction with dissolved iron from acid-promoted hematite dissolution.

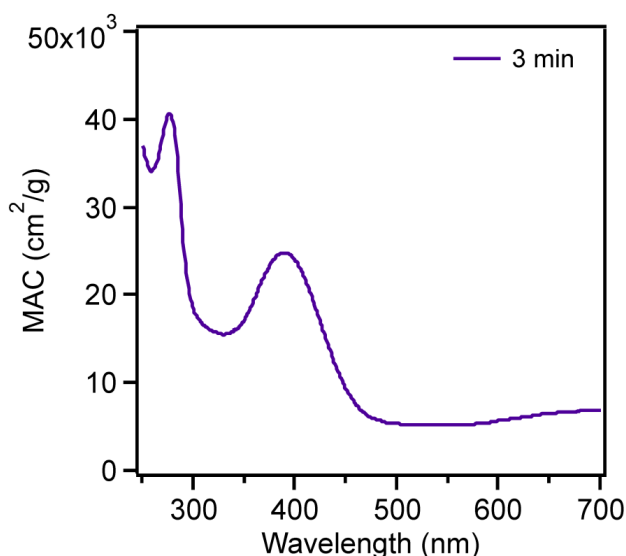
<sup>†</sup>These reactions were conducted by our collaborators at Wilfrid Laurier University, Waterloo, Ontario N2L 3C5, Canada.

material has implications for the climate. More quantitatively, the significance of these results can be assessed with the help of bulk mass absorption coefficient (MAC) of the organics, which can be calculated from the base-10 absorbance ( $A$ ), cuvette width ( $l$ ), and the initial mass concentration of dissolved catechol ( $C_{\text{mass}}$ ) as follows:<sup>26</sup>

$$\text{MAC}(\lambda) = \frac{A(\lambda) \cdot \ln(10)}{l \cdot C_{\text{mass}}} \quad (3.1)$$

Figure 3.18 shows a MAC plot for the 3 min dark reaction of 1 mM catechol with 2 mM  $\text{FeCl}_3$  at pH 3 for an unfiltered solution, that is, with both particles and soluble species contributing to the absorption. Even though we have not accounted for scattering by the particles

in the solution, which contributes to the background, it is clear that the MAC values at near-UV and visible ( $\lambda > 290$  nm) wavelengths can be as high as  $2 \cdot 10^4$   $\text{cm}^2 \text{g}^{-1}$ . These values are comparable to those from biomass burning aerosols ( $10^3$ - $10^4$   $\text{cm}^2 \text{g}^{-1}$ ).<sup>55</sup> Therefore, the efficient dark reaction between phenols and Fe has the potential to produce “brown carbon” aerosol by a secondary mechanism, as opposed to the direct production in biomass burning.



**Figure 3.18.** Mass-normalized absorption coefficient (MAC) plot for the reaction of 1 mM catechol with FeCl<sub>3</sub> after 3 min dark reaction at pH 3 (unfiltered solution). The final reaction mixture contained 1:2 molar ratio catechol:Fe. The MAC values were calculated from Eq. (3.1) and it was not corrected for the contribution from scattering by particles in solution.

Moreover, the colored polymeric particles are colloidal in solution due to their high hydrophobicity. Depending on the amount of “adsorbed water”, these polymers could partition to the surface, thus affecting the aerosols’ cloud condensation ability<sup>56,57</sup> and chemical reactivity of surfaces particularly toward reactive gas phase oxidants such as ozone,<sup>58</sup> OH,<sup>59, 60</sup> N<sub>2</sub>O<sub>5</sub>, and NO<sub>3</sub>,<sup>61</sup> in addition to light-initiated<sup>4</sup> and redox reactions.<sup>62</sup> The dark formation of these particles driven by Fe(III) under acidic conditions represents a potentially important abiotic pathway for

in situ polymer and HULIS formation in atmospheric aerosols in the presence of surface water. This secondary pathway is poorly understood relative to formation pathways of SOA,<sup>2</sup> biopolymeric component of dissolved organic carbon,<sup>63</sup> and HULIS.<sup>64, 65</sup> HULIS in particular were shown to generate reactive oxygen species such as hydrogen peroxide and superoxide radicals.<sup>66</sup> The chemistry presented herein provides molecular level details to processes that could take place in acidic multi-component systems containing organics, iron, and chloride.

## References

1. Zhang, R.; Khalizov, A.; Wang, L.; Hu, M.; Xu, W., Nucleation and Growth of Nanoparticles in the Atmosphere. *Chem. Rev.* **2012**, *112* (3), 1957-2011.
2. Ziemann, P. J.; Atkinson, R., Kinetics, products, and mechanisms of secondary organic aerosol formation. *Chem. Soc. Rev.* **2012**, *41* (19), 6582-6605.
3. Lee, S-S., Atmospheric science: Aerosols, clouds and climate. *Nat. Geosci.* **2011**, *4* (12), 826-827.
4. George, C. D. A., B.; Herrmann, H.; Weller, C.; Vaida, V.; Donaldson, D. J.; Bartels-Rausch, T.; Ammann, M., Emerging Areas in Atmospheric Photochemistry. *Atmospheric and Aerosol Chemistry*, McNeill, V. F., Ariya, P. A., Eds.; Springer: Heidelberg, **2012**; Vol. 339, pp 1-54.
5. Prather, K. A.; Hatch, C. D.; Grassian, V. H., Analysis of atmospheric aerosols. *Annu. Rev. Anal. Chem.* **2008**, *1*, 485-514.
6. Russell, L. M.; Bahadur, R.; Ziemann, P. J., Identifying organic aerosol sources by comparing functional group composition in chamber and atmospheric particles. *Proc. Natl. Acad. Sci. U. S. A.* **2011**, *108* (9), 3516-3521.
7. Rudich, Y.; Donahue, N. M.; Mentel, T. F., Aging of organic aerosol: bridging the gap between laboratory and field studies. *Annu. Rev. Phys. Chem.* **2007**, *58*, 321-352.
8. Suda, S. R.; Petters, M. D.; Yeh, G. K.; Strollo, C.; Matsunaga, A.; Faulhaber, A.; Ziemann, P. J.; Prenni, A. J.; Carrico, C. M.; Sullivan, R. C.; Kreidenweis, S. M., Influence of functional groups on organic aerosol cloud condensation nucleus activity. *Environ. Sci. Technol.* **2014**, *48* (17), 10182-10190.
9. Ault, A. P.; Guasco, T. L.; Ryder, O. S.; Baltrusaitis, J.; Cuadra-Rodriguez, L. A.; Collins, D. B.; Ruppel, M. J.; Bertram, T. H.; Prather, K. A.; Grassian, V. H., Inside versus Outside: Ion Redistribution in Nitric Acid Reacted Sea Spray Aerosol Particles as Determined by Single Particle Analysis. *J. Am. Chem. Soc.* **2013**, *135* (39), 14528-14531.

10. Guasco, T. L.; Cuadra-Rodriguez, L. A.; Pedler, B. E.; Ault, A. P.; Collins, D. B.; Zhao, D.; Kim, M. J.; Ruppel, M. J.; Wilson, S. C.; Pomeroy, R. S.; Grassian, V. H.; Azam, F.; Bertram, T. H.; Prather, K. A., Transition Metal Associations with Primary Biological Particles in Sea Spray Aerosol Generated in a Wave Channel. *Environ. Sci. Technol.* **2014**, *48* (2), 1324-1333.
11. Al-Abadleh, H. A., Review of the bulk and surface chemistry of iron in atmospherically relevant systems containing humic-like substances. *RSC Adv.* **2015**, *5* (57), 45785-45811.
12. Cwiertny, D. M.; Young, M. A.; Grassian, V. H., Chemistry and photochemistry of mineral dust aerosol. *Annu. Rev. Phys. Chem.* **2008**, *59*, 27-51.
13. Finlayson-Pitts, B. J.; Pitts, J. N. *Chemistry of the Upper and Lower Atmosphere: Theory, Experiments, and Applications*; Academic Press: 2000.
14. Nguyen, T. B.; Coggon, M. M.; Flagan, R. C.; Seinfeld, J. H., Reactive Uptake and Photo-Fenton Oxidation of Glycolaldehyde in Aerosol Liquid Water. *Environ. Sci. Technol.* **2013**, *47* (9), 4307-4316.
15. Smith, J. D.; Sio, V.; Yu, L.; Zhang, Q.; Anastasio, C., Secondary Organic Aerosol Production from Aqueous Reactions of Atmospheric Phenols with an Organic Triplet Excited State. *Environ. Sci. Technol.* **2014**, *48* (2), 1049-1057.
16. Ghorai, S.; Laskin, A.; Tivanski, A. V., Spectroscopic Evidence of Keto-Enol Tautomerism in Deliquesced Malonic Acid Particles. *J. Phys. Chem. A* **2011**, *115* (17), 4373-4380.
17. Kobayashi, S.; Makino, A., Enzymatic Polymer Synthesis: An Opportunity for Green Polymer Chemistry. *Chem. Rev.* **2009**, *109* (11), 5288-5353.
18. Statz, A. R.; Meagher, R. J.; Barron, A. E.; Messersmith, P. B., New peptidomimetic polymers for antifouling surfaces. *J. Am. Chem. Soc.* **2005**, *127* (22), 7972-7973.
19. Xu, C.; Xu, K.; Gu, H.; Zheng, R.; Liu, H.; Zhang, X.; Guo, Z.; Xu, B., Dopamine as a robust anchor to immobilize functional molecules on the iron oxide shell of magnetic nanoparticles. *J. Am. Chem. Soc.* **2004**, *126* (32), 9938-9939.

20. Zurcher, S.; Wackerlin, D.; Bethuel, Y.; Malisova, B.; Textor, M.; Tosatti, S.; Gademann, K., Biomimetic Surface Modifications Based on the Cyanobacterial Iron Chelator Anachelin. *Journal of the American Chemical Society* **2006**, *128* (4), 1064-1065.
21. NIST Chemistry WebBook (<http://webbook.nist.gov/chemistry/>), Henry's law data for catechol and guaiacol. Accessed January 2013.
22. Ofner, J.; Krueger, H. U.; Grothe, H.; Schmitt-Kopplin, P.; Whitmore, K.; Zetzsch, C., Physico-chemical characterization of SOA derived from catechol and guaiacol - a model substance for the aromatic fraction of atmospheric HULIS. *Atmos. Chem. Phys.* **2011**, *11* (1), 1-15.
23. Elhabiri, M.; Carreer, C.; Marmolle, F.; Traboulsi, H., Complexation of iron(III) by catecholate-type polyphenols. *Inorg. Chim. Acta* **2007**, *360* (1), 353-359.
24. Faure, E.; Falentin-Daudre, C.; Jerome, C.; Lyskawa, J.; Fournier, D.; Woisel, P.; Detrembleur, C., Catechols as versatile platforms in polymer chemistry. *Prog. Polym. Sci.* **2013**, *38* (1), 236-270.
25. Andreae, M. O.; Gelencser, A., Black carbon or brown carbon? The nature of light-absorbing carbonaceous aerosols. *Atmos. Chem. Phys.* **2006**, *6* (10), 3131-3148.
26. Laskin, A.; Laskin, J.; Nizkorodov, S. A., Chemistry of Atmospheric Brown Carbon. *Chem. Rev.* **2015**, *115* (10), 4335-4382.
27. Lanzl, C. A.; Baltrusaitis, J.; Cwiertny, D. M., Dissolution of Hematite Nanoparticle Aggregates: Influence of Primary Particle Size, Dissolution Mechanism, and Solution pH. *Langmuir* **2012**, *28* (45), 15797-15808.
28. Stucki, J. W., The quantitative assay of minerals for iron(2+) and iron(3+) ions using 1,10-phenanthroline: II. A photochemical method. *Soil Sci. Soc. Am. J.* **1981**, *45* (3), 638-41.
29. Stucki, J. W.; Anderson, W. L., The quantitative assay of minerals for iron(2+) and iron(3+) ions using 1,10-phenanthroline: I. Sources of variability. *Soil Sci. Soc. Am. J.* **1981**, *45* (3), 633-7.
30. Minofar, B.; Jungwirth, P.; Das, M. R.; Kunz, W.; Mahiuddin, S., Propensity of Formate, Acetate, Benzoate, and Phenolate for the Aqueous Solution/Vapor Interface: Surface Tension

- Measurements and Molecular Dynamics Simulations. *J. Phys. Chem. C* **2007**, *111* (23), 8242-8247.
31. Tofan-Lazar, J.; Situm, A.; Al-Abadleh, H. A., DRIFTS Studies on the Role of Surface Water in Stabilizing Catechol-Iron(III) Complexes at the Gas/Solid Interface. *J. Phys. Chem. A* **2013**, *117* (40), 10368-10380.
  32. Feng, W.; Nansheng, D., Photochemistry of hydrolytic iron (III) species and photoinduced degradation of organic compounds. A minireview. *Chemosphere* **2000**, *41* (8), 1137-47.
  33. Kipton, H.; Powell, J.; Taylor, M. C., Interactions of iron(II) and iron(III) with gallic acid and its homologs: a potentiometric and spectrophotometric study. *Aust. J. Chem.* **1982**, *35* (4), 739-56.
  34. Grgic, I.; Dovzan, A.; Bercic, G.; Hudnik, V., The effect of atmospheric organic compounds on the Fe-catalyzed S(IV) autoxidation in aqueous solution. *J. Atmos. Chem.* **1998**, *29* (3), 315-337.
  35. Novic, M.; Grgic, I.; Poje, M.; Hudnik, V., Iron-catalyzed oxidation of S(IV) species by oxygen in aqueous solution: influence of pH on the redox cycling of iron. *Atmos. Environ.* **1996**, *30* (24), 4191-4196.
  36. Albarran, G.; Boggess, W.; Rassolov, V.; Schuler, R. H., Absorption Spectrum, Mass Spectrometric Properties, and Electronic Structure of 1,2-Benzoquinone. *J. Phys. Chem. A* **2010**, *114* (28), 7470-7478.
  37. Hwang, S.; Lee, C.-H.; Ahn, I.-S., Product identification of guaiacol oxidation catalyzed by manganese peroxidase. *J. Ind. Eng. Chem.* **2008**, *14* (4), 487-492.
  38. Doerge, D. R.; Divi, R. L.; Churchwell, M. I., Identification of the colored guaiacol oxidation product produced by peroxidases. *Anal. Biochem.* **1997**, *250* (1), 10-17.
  39. Schmalzl, K. J.; Forsythe, C. M.; Evans, P. D., The reaction of guaiacol with iron(III) and chromium(VI) compounds as a model for wood surface modification. *Wood Sci. Technol.* **1995**, *29* (4), 307-19.
  40. Lee-Ruff, E., The organic chemistry of superoxide. *Chem. Soc. Rev.* **1977**, *6* (2), 195-214.

41. Greenlee, W. F.; Chism, J. P.; Rickert, D. E., A novel method for the separation and quantitation of benzene metabolites using high-pressure liquid chromatography. *Anal. Biochem.* **1981**, *112* (2), 367-70.
42. Lee, A.; Goldstein, A. H.; Keywood, M. D.; Gao, S.; Varutbangkul, V.; Bahreini, R.; Ng, N. L.; Flagan, R. C.; Seinfeld, J. H. C. D., Gas-phase products and secondary aerosol yields from the ozonolysis of ten different terpenes. *J. Geophys. Res.: Atmospheres* **2006**, *111* (D7).
43. Ervens, B.; Turpin, B. J.; Weber, R. J., Secondary organic aerosol formation in cloud droplets and aqueous particles (aqSOA): a review of laboratory, field and model studies. *Atmos. Chem. Phys.* **2011**, *11* (21), 11069-11102.
44. Aktas, N.; Sahiner, N.; Kantoglu, O.; Salih, B.; Tanyolac, A., Biosynthesis and Characterization of Laccase Catalyzed Poly(Catechol). *J. Polym. Environ.* **2003**, *11* (3), 123-128.
45. Sun, X.; Bai, R.; Zhang, Y.; Wang, Q.; Fan, X.; Yuan, J.; Cui, L.; Wang, P., Laccase-Catalyzed Oxidative Polymerization of Phenolic Compounds. *Appl. Biochem. Biotechnol.* **2013**, *171* (7), 1673-1680.
46. Monti, D.; Ottolina, G.; Carrea, G.; Riva, S., Redox reactions catalyzed by isolated enzymes. *Chem. Rev.* **2011**, *111* (7), 4111-4140.
47. Crawford, R. L.; Robinson, L. E.; Foster, R. D., Polyguaiacol: a useful model polymer for lignin biodegradation research. *Appl. Environ. Microbiol.* **1981**, *41* (5), 1112-16.
48. Dubey, S.; Singh, D.; Misra, R. A., Enzymic synthesis and various properties of poly(catechol). *Enzyme Microb. Technol.* **1998**, *23* (7/8), 432-437.
49. Ye, Q.; Zhou, F.; Liu, W., Bioinspired catecholic chemistry for surface modification. *Chem. Soc. Rev.* **2011**, *40* (7), 4244-4258.
50. Lee, H.; Dellatore, S. M.; Miller, W. M.; Messersmith, P. B., Mussel-inspired surface chemistry for multifunctional coatings. *Science* **2007**, *318* (5849), 426-430.
51. Dalsin, J. L.; Lin, L.; Tosatti, S.; Voeroes, J.; Textor, M.; Messersmith, P. B., Protein Resistance of Titanium Oxide Surfaces Modified by Biologically Inspired mPEG-DOPA. *Langmuir* **2005**, *21* (2), 640-646.



52. Dalsin, J. L.; Hu, B.-H.; Lee, B. P.; Messersmith, P. B., Mussel Adhesive Protein Mimetic Polymers for the Preparation of Nonfouling Surfaces. *J. Am. Chem. Soc.* **2003**, *125* (14), 4253-4258.
53. Zhou, W.-H.; Lu, C.-H.; Guo, X.-C.; Chen, F.-R.; Yang, H.-H.; Wang, X.-R., Mussel-inspired molecularly imprinted polymer coating superparamagnetic nanoparticles for protein recognition. *J. Mater. Chem.* **2010**, *20* (5), 880-883.
54. Shi, Z.; Krom, M. D.; Bonneville, S.; Benning, L. G., Atmospheric Processing Outside Clouds Increases Soluble Iron in Mineral Dust. *Environ. Sci. Technol.* **2015**, *49* (3), 1472-1477.
55. Chen, Y.; Bond, T. C., Light absorption by organic carbon from wood combustion. *Atmos. Chem. Phys.* **2010**, *10* (4), 1773-1787.
56. Taraniuk, I.; Graber, E. R.; Kostinski, A.; Rudich, Y., Surfactant properties of atmospheric and model humic-like substances (HULIS). *Geophys. Res. Lett.* **2007**, *34* (16), DOI:10.1029/2007GL029576.
57. Dinar, E.; Taraniuk, I.; Graber, E. R.; Anttila, T.; Mentel, T. F.; Rudich, Y. C. D., Hygroscopic growth of atmospheric and model humic-like substances. *J. Geophys. Res.: Atmospheres* **2007**, *112*, DOI: 10.1029/2006JD007442.
58. Nieto-Gligorovski, L. I.; Net, S.; Gligorovski, S.; Wortham, H.; Grothe, H.; Zetzsch, C., Spectroscopic study of organic coatings on fine particles, exposed to ozone and simulated sunlight. *Atmos. Environ.* **2010**, *44* (40), 5451-5459.
59. Bertram, A. K.; Ivanov, A. V.; Hunter, M.; Molina, L. T.; Molina, M. J., The reaction probability of OH on organic surfaces of tropospheric interest. *J. Phys. Chem. A* **2001**, *105* (41), 9415-9421.
60. George, I. J.; Slowik, J.; Abbatt, J. P. D., Chemical aging of ambient organic aerosol from heterogeneous reaction with hydroxyl radicals. *Geophys. Res. Lett.* **2008**, *35* (13), DOI: 10.1029/2008GL033884.

61. Gross, S.; Bertram, A. K., Reactive Uptake of NO<sub>3</sub>, N<sub>2</sub>O<sub>5</sub>, NO<sub>2</sub>, HNO<sub>3</sub>, and O<sub>3</sub> on Three Types of Polycyclic Aromatic Hydrocarbon Surfaces. *J. Phys. Chem. A* **2008**, *112* (14), 3104-3113.
62. Duesterberg, C. K.; Waite, T. D., Kinetic Modeling of the Oxidation of p-Hydroxybenzoic Acid by Fenton's Reagent: Implications of the Role of Quinones in the Redox Cycling of Iron. *Environ. Sci. Technol.* **2007**, *41* (11), 4103-4110.
63. Aluwihare, L. I.; Repeta, D. J.; Chen, R. F., A major biopolymeric component to dissolved organic carbon in surface sea water. *Nature* **1997**, *387* (6629), 166-169.
64. Graber, E. R.; Rudich, Y., Atmospheric HULIS: how humic-like are they? A comprehensive and critical review. *Atmos. Chem. Phys.* **2006**, *6* (3), 729-753.
65. Nozriere, B.; Dziedzic, P.; Cordova, A., Formation of secondary light-absorbing "fulvic-like" oligomers: a common process in aqueous and ionic atmospheric particles? *Geophys. Res. Lett.* **2007**, *34* (21), DOI: 10.1029/2007GL031300.
66. Lin, P.; Yu, J. Z., Generation of Reactive Oxygen Species Mediated by Humic-like Substances in Atmospheric Aerosols. *Environ. Sci. Technol.* **2011**, *45* (24), 10362-10368.

## **Chapter 4: Molecular Characterization and the Effects of SO<sub>2</sub> on Biodiesel and Diesel Fuel Secondary Organic Aerosol**

\*Note that statements in sections 4.1-4.5 were based on available literature at the time of the publication submission (May 2015).

## 4.1. Abstract

Secondary organic aerosol (SOA) of photooxidized diesel fuel, biodiesel fuel, and 20% biodiesel fuel/80% diesel fuel mixture was prepared under high-NO<sub>x</sub> conditions in the presence and absence of sulfur dioxide (SO<sub>2</sub>), ammonia (NH<sub>3</sub>), and relative humidity (RH). The composition of particulate organic compounds in SOA was measured using several analytical techniques including aerosol mass spectrometry (AMS), high-resolution nanospray desorption electrospray ionization mass spectrometry (nano-DESI/HRMS), and ultra-high resolution 21 Tesla Fourier Transform ion cyclotron resonance mass spectrometry (21T-FTICR/uHRMS). Results showed that sulfuric acid and condensed organosulfur species formed in photooxidation experiments with SO<sub>2</sub> were present in the particles. The high humidity (RH 90%) experiments had less organosulfur species than experiments done under dry conditions, but its most intense organosulfur peak, C<sub>6</sub>H<sub>6</sub>SO<sub>3</sub>, most likely benzene sulfonic acid, was larger than in any other sample. There was strong overlap of organosulfur species observed in this study with previous field and chamber studies of organosulfur species. Many mass spectrometry peaks of organosulfates (R-OS(O)<sub>2</sub>OH) in field studies that were previously designated as biogenic or of unknown sources might have originated from anthropogenic sources, such as photooxidation of hydrocarbons present in diesel and biodiesel fuel.

## 4.2. Introduction

Atmospheric aerosol particles contribute significantly to decreased visibility,<sup>1</sup> increased morbidity and premature mortality,<sup>2</sup> and the uncertainty in atmospheric models.<sup>3</sup> In particular, organic aerosols which contain thousands of organic compounds,<sup>4</sup> are significant and sometimes the major component of particles, providing up to 90% of the submicron particle mass.<sup>5</sup> Organic aerosols directly emitted into the atmosphere from sources such as vehicles, industrial

processing, biomass burning, and sea spray, are known as primary organic aerosols (POA). Oxidation of volatile organic compounds (VOCs) in the atmosphere form low vapor pressure multifunctional organics that condense into secondary organic aerosols (SOA) which can amount to 50-85% of the overall contribution to organic aerosols.<sup>6</sup>

Atmospheric models have improved over the last decade, but the SOA budget in urban areas is still currently underpredicted<sup>7, 8</sup> because the mechanisms of formation and growth of fine particles remain highly uncertain. Urban regions contain a complex mixture of both natural and anthropogenic primary and secondary air pollutants. The most important primary particulate matter with diameters less than or equal to 2.5  $\mu\text{m}$ , ( $\text{PM}_{2.5}$ ), emission source is traffic, accounting for up to one-third of the  $\text{PM}_{2.5}$  mass.<sup>9</sup> Emissions of diesel vehicle exhaust can contain a large contribution from unburned fuel, which can dominate vehicle emissions of reactive gas-phase carbon that can act as a source of newly formed SOA.<sup>10</sup> Similarly, biodiesel fuel exhaust can also contain unburned fuel, such as fatty acid methyl esters (FAMES).<sup>11</sup> Such products of incomplete combustion and incomplete catalytic converter oxidation may be efficient SOA precursors.<sup>12</sup> Other sources of fugitive oil and natural gas emissions of non-methane hydrocarbons (NMHCs) exist such as oil spills, refinery processing, and hydraulic fracturing.<sup>13-15</sup>

In more polluted regions, the photooxidation of VOCs may occur in the presence of sulfur dioxide ( $\text{SO}_2$ ) to form organosulfates ( $\text{R-OS(O)}_2\text{OH}$ ). Several studies have investigated the effect of photooxidation in the presence of  $\text{SO}_2$  for precursors such as isoprene, alpha-pinene, toluene, 1,3,5-trimethylbenzene, xylene, octane, and gasoline exhaust.<sup>16-21</sup> During photooxidation,  $\text{SO}_2$  can be converted to sulfuric acid by hydroxyl radicals,<sup>22</sup> and by reactive uptake onto particles involving heterogeneous oxidation of  $\text{SO}_2$  by ozone or hydrogen

peroxide.<sup>23</sup> Sulfate seed particles with varying acidity have also been used to form organosulfates in SOA where their formation is most prominent under higher acidity.<sup>24-27</sup>

The possible formation routes of organosulfates via reactions of organics with sulfur-containing oxides, acids and radicals, which will further be referred to as “sulfate nucleophiles”, include: (1) epoxide ring opening, (2) addition to protonated carbonyls, (3) substitution of organonitrates, (4) esterification of alcohols or enols, and (5) radical initiated reactions.<sup>28-30</sup> Epoxides can be protonated under acidic conditions making them more susceptible to attack from sulfate nucleophiles, forming  $\beta$ -hydroxysulfates. Similarly, protonated carbonyls can react with sulfate nucleophiles,<sup>29</sup> which could form  $\alpha$ -hydroxysulfates. Substitution of tertiary organonitrates with sulfate can rapidly occur, even over a full range of pH.<sup>31</sup>

Minerath et al.<sup>32</sup> has suggested that esterification of alcohols is kinetically infeasible for low temperatures of the upper tropospheric aerosols using methanol as the model alcohol and conducting aqueous experiments, but did note that Kane et al.<sup>33</sup> had a rate constant for sulfur esterification of 11 orders of magnitude larger than Minerath et al.’s extrapolated rate constant. The main difference between these two studies was the homogenous versus heterogeneous exposure of methanol to sulfuric acid. The discrepancy in rate constants between these two studies may be due to this difference in experimental design where Kane et al.<sup>33</sup> and Minerath et al.<sup>32</sup> investigated primarily surface and bulk chemistry, respectively. Furthermore, it was more recently observed that esterification of alcohols is more efficient in sulfuric acid aerosol than in solution.<sup>34</sup> Additionally, ketones may tautomerize to their enol form and then undergo esterification.<sup>35</sup> Sulfate radicals were proposed by Nozière et al.<sup>36</sup> to form in atmospheric aerosols from the reaction of hydroxyl radicals with bisulfate anions. The organosulfate species

found in that study were explained by the addition of sulfate radicals to double bonds and further aging by hydroxyl radicals.

Most of the previous experiments on organosulfur formation started with seed aerosols (or bulk solution) containing sulfuric acid or sulfates. Such seeded experiments may potentially miss alternative organosulfur formation pathways, such as direct SO<sub>2</sub> reactions with organic species. If ozone is present or formed during photooxidation it can react with alkenes to produce Criegee intermediates which then could react with SO<sub>2</sub>.<sup>19, 37</sup> Also, a recent paper observed the uptake of SO<sub>2</sub> on oleic acid in the absence of ozone, in the dark, described by the direct addition of SO<sub>2</sub> to double bonds.<sup>38</sup> In summary, multiple pathways for incorporation of sulfur in SOA organic compounds have been proposed and the relative role of these processes is still unknown.

In this study, SOA was generated from the photooxidation of diesel fuel and biodiesel fuel in chamber experiments to represent the possible photooxidative aging of unburned or evaporated fuel. The effects of anthropogenic pollution, such as the presence of NO<sub>x</sub>, SO<sub>2</sub>, and NH<sub>3</sub>, along with changes in relative humidity on the composition of fuel SOA were investigated. With help of high resolution nanospray desorption electrospray ionization mass spectrometry (nano-DESI/HRMS) and ultrahigh resolution and mass accuracy 21 Tesla Fourier Transform Ion Cyclotron Resonance Mass Spectrometry (21T-FTICR/uHRMS), we demonstrated that organosulfur compounds are efficiently produced in presence of SO<sub>2</sub>, without pre-existing sulfate seed aerosols. Unique organosulfur species were categorized into four subsets (compounds with an aliphatic side chain, compounds with formula C<sub>c</sub>H<sub>h</sub>SO<sub>3</sub>, compounds with formula C<sub>c</sub>H<sub>h</sub>SO<sub>4</sub>, and aromatic compounds) and compared to previous field and laboratory studies. Based on our data, some of the organosulfates in field studies that were previously designated as biogenic or of unknown origin might have originated from anthropogenic sources, such as photooxidation of

hydrocarbons present in diesel and biodiesel fuel. These results contribute to our understanding of the formation mechanisms of organosulfates in SOA.

### 4.3. Experimental

#### 4.3.1. Fuel Precursor Analysis

The compositions of diesel fuel (No 2 Fluka UST148) and biodiesel fuel (VHG labs BDBLEND-100P) were analyzed using 2D gas chromatography vacuum ultraviolet high resolution time-of-flight mass spectrometry (GC/VUV/MS).<sup>39-41</sup> Samples were diluted (100:1) in methylene chloride (HPLC grade, Sigma-Aldrich). The diluted samples were directly injected into a liquid nitrogen cooled inlet for cryo-focusing on a quartz wool inlet liner at -25°C (CIS4, Gerstel Inc.). Injection onto the gas chromatograph (GC) column was achieved by rapid heating of the CIS (10°C/sec) up to 320°C under a flow of helium. Analytes were separated using an Agilent 7890 GC equipped with a non-polar primary column (60 m × 0.25 mm × 250 μm Rxi-5Sil-MS; Restek) using a flow rate of 2 ml/min of helium. The GC temperature program was 40°C with 5 min hold, 3.5°C min<sup>-1</sup> up to 320°C, and a final hold at 320°C for 10 min. Following GC separation analytes were ionized using a vacuum-ultraviolet photon beam at 10.5 eV and then detected using a high-resolution ( $m/\Delta m \approx 4000$ ) time-of-flight mass spectrometer (HRTOF, Tofwerk). Data were collected at 100 Hz and signal averaged to 0.5 Hz. The transfer line from the GC to the TOF was maintained at 270°C. To minimize fragmentation in VUV, the ion source was operated at 170°C. The VUV photon flux of  $\sim 10^{16}$  photons/cm<sup>2</sup>·sec was generated by the Chemical Dynamics Beamline 9.0.2 of the Advanced Light Source (ALS) at Lawrence Berkeley National Laboratory.



### **4.3.2. Chamber Generation of SOA**

The photooxidation of diesel fuel (DSL) and biodiesel fuel (BDSL) was performed in a 5 m<sup>3</sup> Teflon<sup>TM</sup> chamber in the absence of seed particles with 260 ppb of NO<sub>x</sub>, and with differing levels of humidity, SO<sub>2</sub>, and NH<sub>3</sub>. Experimental conditions are summarized in Table 4.1. Hydrogen peroxide (H<sub>2</sub>O<sub>2</sub>) was used as a hydroxyl radical (OH) precursor. A measured volume of H<sub>2</sub>O<sub>2</sub> (Aldrich; 30% by volume in water) was added to the chamber by evaporation with a stream of zero air to achieve a final concentration of 2 ppm of H<sub>2</sub>O<sub>2</sub>. Then, NO and/or SO<sub>2</sub> were introduced to the chamber from pre-mixed gas cylinders. In the case that NH<sub>3</sub> was present, a 1/10 dilution of an ammonium hydroxide aqueous solution was prepared from (Fisher, 14.8 N) and was evaporated into the chamber. Dichloromethane solutions of diesel fuel and/or biodiesel fuel were added in the same manner, and the chamber content was mixed for several minutes using a Teflon<sup>TM</sup>-coated fan. The photooxidation was driven by radiation from UV-B lamps (FS40T12/UVB, Solarc Systems Inc.) with an emission centered at 310 nm. A scanning mobility particle sizer (SMPS, TSI 3080 Electrostatic Classifier and TSI 3775 Condensation Particle Counter) and an Aerodyne Time-of-Flight Aerosol Mass Spectrometer (AMS) monitored the SOA particles formed in the chamber while O<sub>3</sub> and NO/NO<sub>y</sub> data were recorded by a Thermo Scientific model 49i ozone analyzer and a Thermo Scientific model 42i-Y NO<sub>y</sub> analyzer.

### **4.3.3. Filter Collection and Analysis of SOA Particles**

SOA was sent through either a denuder train (3 m in length total) or a short denuder and collected on poly-(tetrafluoroethylene) (PTFE) filters (Millipore 0.2 μm pore size) via impaction. The longer denuder train removed more volatile species (something we intended to do for a parallel set of experiments on photolysis of SOA). Filter samples were then sealed and frozen

**Table 4.1.** Experimental conditions for chamber generated fuel SOA. Sample number, sample code name, reactant concentrations, relative humidity (RH), and SOA mass concentration are listed. The SOA mass concentrations are reported as maxima reached at the end of photooxidation (3 hr).

Sample	Sample Code	Precursor	Fuel (ppb)	SO <sub>2</sub> (ppb)	NH <sub>3</sub> (ppb)	RH (%)	[SOA] (μg/m <sup>3</sup> )
1	DSL/NO <sub>x</sub>	DSL	216	0	0	< 2	260
2	DSL/NO <sub>x</sub> /SO <sub>2</sub>	DSL	216	200	0	< 2	510
3	DSL/NO <sub>x</sub> /SO <sub>2</sub> /NH <sub>3</sub>	DSL	216	200	1000	< 2	510
4	DSL/NO <sub>x</sub> /RH	DSL	216	0	0	90	360
5	DSL/NO <sub>x</sub> /SO <sub>2</sub> /RH	DSL	216	200	0	90	470
6	BDSL/NO <sub>x</sub>	BDSL	160	0	0	< 2	45
7	BDSL/NO <sub>x</sub> /SO <sub>2</sub>	BDSL	160	200	0	< 2	85
8	MIX/NO <sub>x</sub>	20% BDSL/DSL	32/173	0	0	< 2	220
9	MIX/NO <sub>x</sub> /SO <sub>2</sub>	20% BDSL/DSL	32/173	200	0	< 2	370
10	DSL/NO <sub>x</sub> <sup>a</sup>	DSL	216	0	0	< 2	330
11	DSL/NO <sub>x</sub> /SO <sub>2</sub> <sup>a</sup>	DSL	216	200	0	< 2	630
12	DSL/NO <sub>x</sub> /SO <sub>2</sub> -high <sup>a</sup>	DSL	216	570	0	< 2	720
13	DSL/NO <sub>x</sub> /SO <sub>2</sub> /NH <sub>3</sub> <sup>a</sup>	DSL	216	200	110	< 2	530

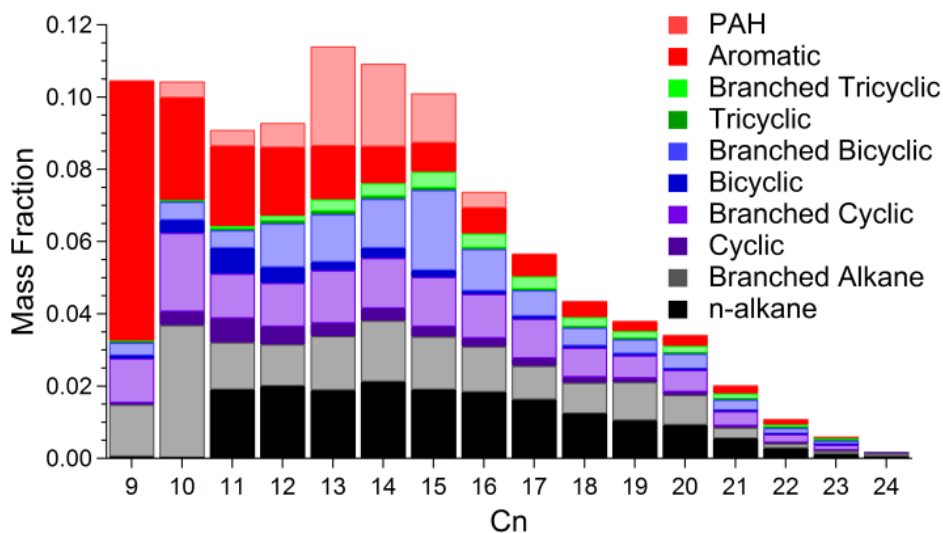
<sup>a</sup>Samples that were sent through a longer denuder train before collection.

for offline analysis nano-DESI/HRMS.<sup>42</sup> After the frozen filter samples were allowed to equilibrate to room temperature and were unsealed, they were analyzed with nano-DESI/HRMS (Thermo Fisher Scientific Inc, Waltham, MA) in negative mode using acetonitrile (Fisher) as the solvent bridge (samples 10-12 had a solvent bridge of ACN/H<sub>2</sub>O 70%). The spray voltage and heated capillary temperature were 3.5-4 kV and 250-270 °C. Several samples (labeled 2, 7, 9, and 10-13 in Table 4.1) were also recorded with 21T-FTICR/uHRMS for comparison at the Environmental Molecular Sciences Laboratory operated by the Pacific Northwest National Laboratory. 21T-FTICR/uHRMS spectra were recorded by direct infusion in negative mode with a sample flow rate, spray voltage, and capillary temperature of 0.5 μL/min, 2.4 kV, and 300°C, respectively.

## 4.4. Results and Discussion

### 4.4.1. Fuel Precursors and SOA Generation

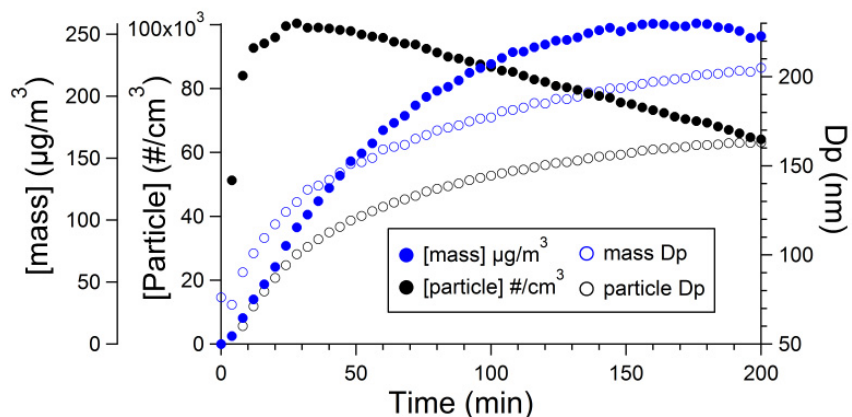
The diesel fuel composition was much more complex than the biodiesel fuel and was composed of 25% aromatics and 75% aliphatics with an average carbon number,  $C_n$ , of 14 (Figure 4.1), very similar to previous literature reports.<sup>39</sup> The polycyclic aromatic hydrocarbons (PAHs) in the diesel fuel were dominated by methylated naphthalenes, with between 1-3 methyl groups. The photooxidation SOA yield generally decreases in the order: aromatics, cycloalkanes, n-alkanes or multi-ring aromatics, and branched alkanes.<sup>43, 44</sup> All of these components, including the high SOA yielding aromatic compounds, such as naphthalene, were observed in diesel fuel, confirming that this fuel sample should produce SOA in reasonable yields.



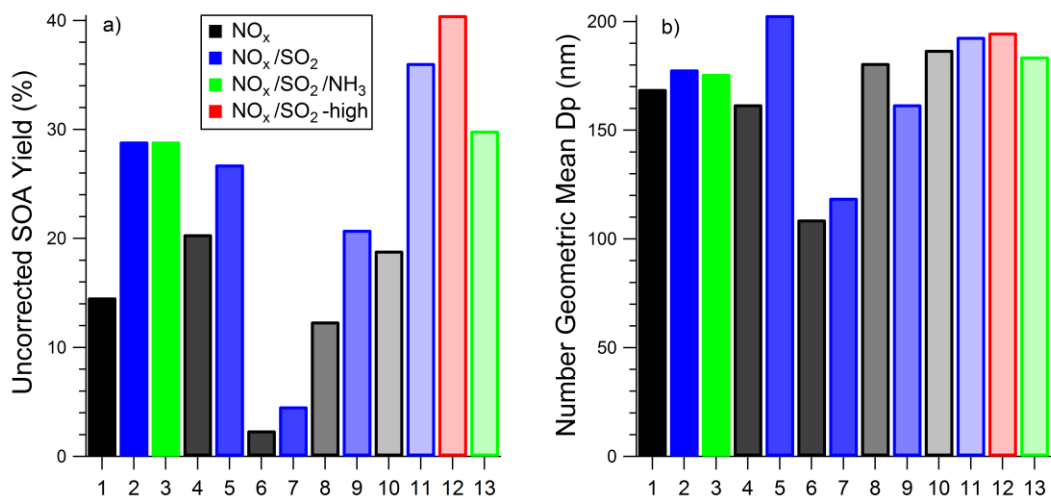
**Figure 4.1.** Mass fraction of species in diesel fuel from GC/VUV/MS analysis as a function of the carbon number ( $C_n$ ) of detected molecules. Species are stacked in the bar graph such that the height of the combined bars for a specific  $C_n$  represents the mass fraction.

The major known components of soybean oil are linoleic acid (55%), oleic acid (18%), linolenic acid (10%), palmitic acid (10%), and stearic acid (4%).<sup>45</sup> The biodiesel fuel used in this study consisted of primarily C<sub>19</sub> (~85%) and C<sub>17</sub> (~15%) FAMES of the original fatty acids found in soybean oil. Small amounts of C<sub>21</sub> and C<sub>23</sub> FAMES were also observed. The most abundant FAMES were methyl linolate and methyl oleate, which were methyl esters of the most abundant fatty acids in soybean oil. The presence of unsaturated FAMES makes biodiesel more reactive than diesel. The unsaturated FAMES in biodiesel fuel such as methyl oleate, methyl linoleate, and methyl linolenate have one, two, and three double bonds as possible sites for OH or SO<sub>2</sub> addition. However, the larger reactivity of biodiesel may be counteracted by the tendency of FAMES to fragment, which reduces the SOA yields. The photooxidation of long chain esters, such as the FAMES in biodiesel fuel, has not been well studied, but FAMES have been observed to preferentially degrade rather than just functionalize.<sup>46, 47</sup>

An example of a time profile of SOA formation from diesel is plotted in Figure 4.2. Particles formed within minutes after photooxidation started and grew to a maximum mass concentration after 3 hours, at which point the SOA collection for offline measurements started. We estimated the SOA yields for each experiment by normalizing the SMPS-measured mass concentration of SOA to the initial mass concentration of the injected fuel vapors (Figure 4.3a). None of the compounds in the fuel precursors were monitored during photooxidation, but an assumption was made that the majority of them fully reacted (based on our previous observations of chemistry in the same chamber) in order to calculate and estimate the SOA mass yields. Wall loss was not taken into account in the SOA yield calculations as well, so the SOA yields should be treated as relative. In general, the addition of SO<sub>2</sub> increased the SOA yield (Figure 4.3a) and



**Figure 4.2.** Time profile of SOA formation from sample 1, DSL/NO<sub>x</sub>. Time zero corresponds to turning on the UV lamps. The AMS sampled throughout the entire experiment; particle sampling for high-resolution offline analysis started after 200 minutes of photooxidation when the particle mass concentration reached the maximum.



**Figure 4.3.** a) Uncorrected yield and b) particle number-weighted geometric mean particle diameter of the SOA generated in the chamber. The index corresponds to the sample number in Table 1 (samples 6 and 7 are from BDSL, samples 8 and 9 are from the DSL/BDSL mixture, and the rest of the samples are from DSL). The samples are colored by the presence of SO<sub>2</sub> and NH<sub>3</sub>.

particle diameter (Figure 4.3b) whereas the addition of  $\text{NH}_3$  caused a decrease from the base case of no  $\text{SO}_2$  present. The smaller observed SOA yield from BDSL (samples 6 and 7) was most likely due to the chemistry favoring degradation of FAMES to smaller gaseous species (although we cannot rule out incomplete oxidation or unaccounted losses of biodiesel fuel in the injection lines). The 20% biodiesel experiments (samples 8 and 9) had SOA yields and particle diameters that were in between the values of the individual DSL and BDSL SOA samples of each fuel precursor. All samples had similar particle mean geometric diameters except for the BDSL samples which grew to smaller sizes.

#### 4.4.2. Average Molecular Composition

The average molecular formulas and ratios for every sample from the high-resolution mass spectrometry analysis are reported in Table 4.2. Mass spectral features with a minimum signal-to-noise ratio of 3 were extracted from the averaged mass spectra of both solvent background and sample using Decon 2LS software developed at PNNL (<http://omics.pnl.gov/software/decontools-decon2ls>). Background and sample peaks were clustered and the sample peaks that were less than 3 times larger than the background were removed. Mass spectral peaks were assigned molecular formulas as  $\text{C}_c\text{H}_h\text{O}_o\text{N}_n\text{S}_s$  species with constraints of C: 1-40, H: 2-80, O: 0-35, N: 0-1, S: 0-1, O/C or  $\text{O}^*/\text{C}$ : 0-1.2 (where  $\text{O}^*$  is the number of oxygen atoms minus 3 to focus on the degree of oxidation that is not due to sulfate or sulfonate group addition), H/C: 0.3-2.25 were performed using the Molecular Formula Calculator (<https://nationalmaglab.org/user-facilities/icr/icr-software>) for ions of the type  $[\text{M} - \text{H}]^-$  with a tolerance for Nano-DESI/HRMS and 21T-FTICR/uHRMS of  $m/z$  0.001 and 0.0005. Species absent both or either N or S will be described as CHO, CHON, or as CHOS. Some

**Table 4.2.** Average molecular formulas and ratios of SOA samples from nano-DESI/HRMS spectra. Data for samples that were also recorded with 21T-FTICR/uHRMS are provided in parentheses.

Sample #	Sample Code	<C>	<H>	<O>	<N>	<S>	<DBE>	<O/C>	<H/C>
1	DSL/NO <sub>x</sub>	10.46	12.34	6.56	0.38	-	5.48	0.66	1.13
2	DSL/NO <sub>x</sub> /SO <sub>2</sub>	11.84 (13.44)	20.57 (23.56)	7.28 (6.85)	0.67 (0.00)	0.91 (0.93)	2.88 (2.67)	0.71 (0.53)	1.82 (1.75)
3	DSL/NO <sub>x</sub> /SO <sub>2</sub> /NH <sub>3</sub>	12.26	21.99	7.00	0.42	0.92	2.47	0.63	1.83
4	DSL/NO <sub>x</sub> /RH	9.93	10.94	6.06	0.10	-	5.51	0.66	1.11
5	DSL/NO <sub>x</sub> /SO <sub>2</sub> /RH	12.15	14.91	5.66	0.16	0.23	5.77	0.55	1.25
6	BDSL/NO <sub>x</sub>	10.22	13.45	6.48	0.14	-	4.57	0.67	1.30
7	BDSL/NO <sub>x</sub> /SO <sub>2</sub>	12.96 (12.49)	15.67 (19.35)	7.70 (7.69)	0.72 (0.16)	0.87 (0.89)	6.48 (3.89)	0.77 (0.74)	1.33 (1.69)
8	MIX/NO <sub>x</sub>	9.11	11.08	5.88	0.37	-	4.76	0.67	1.20
9	MIX/NO <sub>x</sub> /SO <sub>2</sub>	15.25 (12.64)	20.46 (21.58)	7.52 (6.81)	0.75 (0.04)	0.78 (0.95)	6.40 (2.87)	0.59 (0.56)	1.52 (1.72)
10	DSL/NO <sub>x</sub> <sup>a</sup>	11.77 (15.57)	16.54 (21.03)	4.92 (7.57)	0.03 (0.03)	-	4.52 (6.08)	0.44 (0.51)	1.39 (1.35)
11	DSL/NO <sub>x</sub> /SO <sub>2</sub> <sup>a</sup>	11.64 (11.74)	17.44 (20.91)	5.02 (6.84)	0.02 (0.02)	0.18 (97)	3.94 (2.29)	0.46 (0.61)	1.48 (1.78)
12	DSL/NO <sub>x</sub> /SO <sub>2</sub> -high <sup>a</sup>	10.85 (12.35)	18.08 (21.92)	5.91 (6.86)	0.06 (0.04)	0.57 (0.87)	2.84 (2.41)	0.58 (0.59)	1.67 (1.78)
13	DSL/NO <sub>x</sub> /SO <sub>2</sub> /NH <sub>3</sub> <sup>a</sup>	10.32 (11.47)	18.88 (21.57)	5.59 (6.02)	0.10 (0.03)	0.85 (0.96)	1.93 (1.70)	0.61 (0.55)	1.85 (1.88)

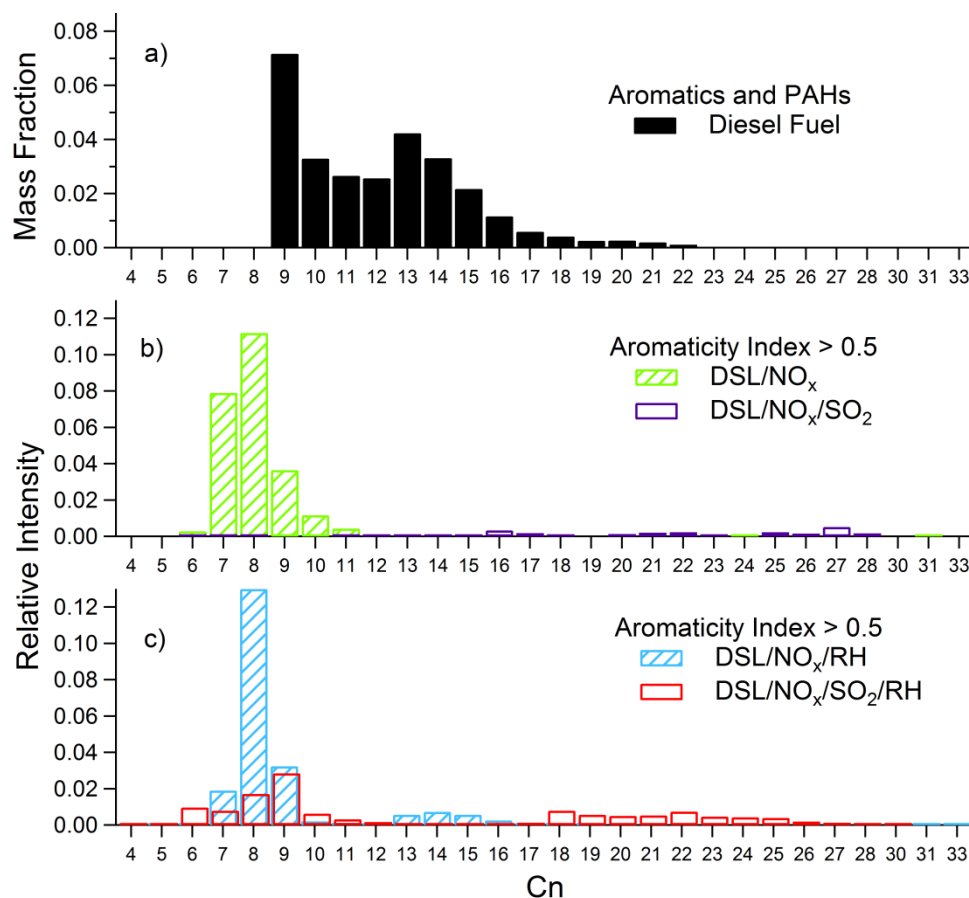
<sup>a</sup> Samples that were sent through a longer denuder train before collection.

organosulfur species were seen in 21T-FTICR/uHRMS, but not in nano-DESI/HRMS mass spectra. This was most likely caused by the different ionization methods and atmospheric pressure interfaces of the mass spectrometers. Nano-DESI may emphasize smaller, more oxidized compounds that dissolve rapidly in the working solution, whereas the ESI source in the 21T FTICR instrument relies on a direct infusion of a pre-dissolved sample. Furthermore, the ions from the nano-DESI source were injected into vacuum through a tube lens/skimmer configuration, whereas ions entered the 21T FTICR instrument through a stacked ring ion guide similar to an ion funnel that promotes more efficient ion transfer at the atmospheric pressure interface.<sup>48</sup> A steeper DC electric field gradient in the nano-DESI instrument atmospheric pressure interface yielded more energetic ion-neutral collisions in this region. Organosulfates tend to fragment easily into  $\text{HSO}_4^-$ , and more of them could be lost to fragmentation in the nano-DESI/HRMS instrument. Also, the detection of more organosulfates with 21T-FTICR/uHRMS may have been due to its higher resolution and sensitivity than nano-DESI/HRMS.

Aromatics and PAHs originally in the diesel fuel appeared to have generated DSL SOA with ring-opening reactions where the initial large structures were not conserved. We base this assertion on the fact that the carbon number distribution of the aromatics (and PAHs) in the diesel fuel shifted to smaller numbers in the SOA as seen in Figure 4.4. Aside from this specific trend in aromatics, the overall average carbon numbers (Table 4.2) in the DSL SOA were smaller than the average carbon number in the diesel fuel. The BDSL SOA also had a smaller average carbon number than the major  $\text{C}_{17}$  and  $\text{C}_{19}$  compounds in the biodiesel fuel, consistent with some degradation during the photooxidation. Overall, the photooxidation of these fuels generated smaller species on average in most of the SOA.



The average O/C and H/C ratios for the fuel samples that were photooxidized in the presence of  $\text{NO}_x$  did not show any significant difference between samples (samples containing  $\text{SO}_2$  will be discussed later). The SOA generated with biodiesel fuel showed just a small increase in H/C and, subsequently, a decrease in DBE relative to the diesel fuel samples. The biodiesel fuel did not contain a large degree of unsaturation to begin with unlike the aromatics and PAHs of the diesel fuel.



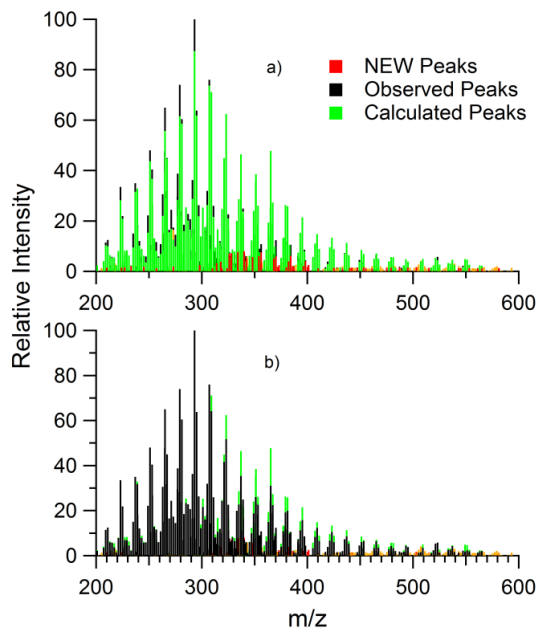
**Figure 4.4.** Comparison of aromatic species in diesel fuel and DSL SOA. Mass fraction of aromatics and PAHs of diesel fuel a) and mass spectral relative intensities of the dry b) and humid c) DSL SOA samples are overlaid in bar plots. Relative intensities of SOA samples are normalized to fractions such that the sum of relative intensities of all of the peaks in an individual sample is 1; the relative intensities of mass spectral peaks of the same Cn were added.

#### 4.4.3. Photooxidation of BDSL/DSL Mixture

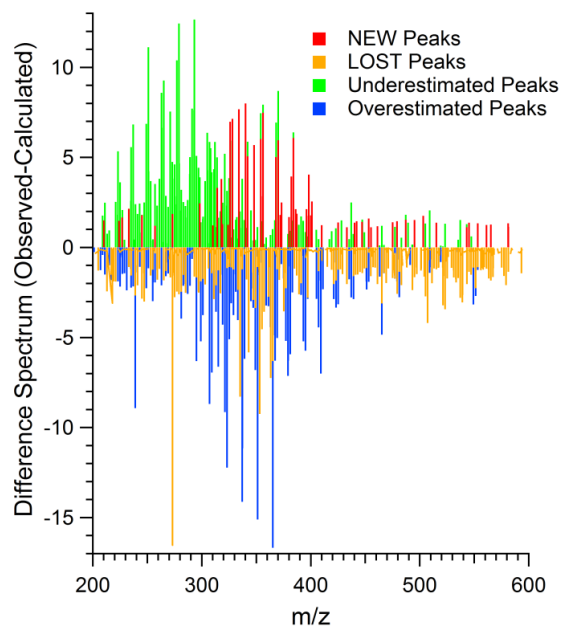
As diesel and biodiesel fuel photooxidized with different rates and with different yields (Figure 4.3a), it was not clear how they would contribute to SOA in the photooxidation as a mixture of the two fuels. To explore this question, we attempted to decompose the high-resolution mass spectra of the mixture to contributions from DSL and BDSL by their mass spectral patterns. Specifically, the MIX/NO<sub>x</sub>/SO<sub>2</sub> sample mass spectrum was compared to the DSL/NO<sub>x</sub>/SO<sub>2</sub> and BDSL/NO<sub>x</sub>/SO<sub>2</sub> mass spectra that were recorded with 21T-FTICR/uHRMS. A least squares analysis was used to solve for coefficients “a” and “b” in Equation 4.1, below. Only peaks in the individual samples that overlapped with MIX/NO<sub>x</sub>/SO<sub>2</sub> were used in the fit

$$MS_{\text{MIX/NO}_x/\text{SO}_2} = a \cdot MS_{\text{DSL/NO}_x/\text{SO}_2} + b \cdot MS_{\text{BDSL/NO}_x/\text{SO}_2} \quad (\text{Eq. 4.1})$$

analysis, but all peaks were later scaled by the coefficients and summed to represent a linear combination of mass spectra (Figure 4.5). The intensity weighted percent of the BDSL/NO<sub>x</sub>/SO<sub>2</sub> mass spectrum in the calculated linear combination was 18%, surprisingly close to its fuel precursor composition of 20% biodiesel in diesel fuel. There were some peaks lost in the mixed sample that were originally seen in the individual samples as well as some new peaks detected (Figure 4.6). Peak intensities were normalized such that the largest peak had a relative intensity (RI) of 100%. A Venn diagram of peak overlap is seen in Figure 4.7a where areas are proportional to the number of peaks; a version of the same diagram weighted by intensity is shown in Figure 4.7b. Although new peaks seen in MIX/NO<sub>x</sub>/SO<sub>2</sub> only weighted as 3% of the overall intensity of the mass spectrum, they amounted to 65 peaks. The percent CHO, CHON,

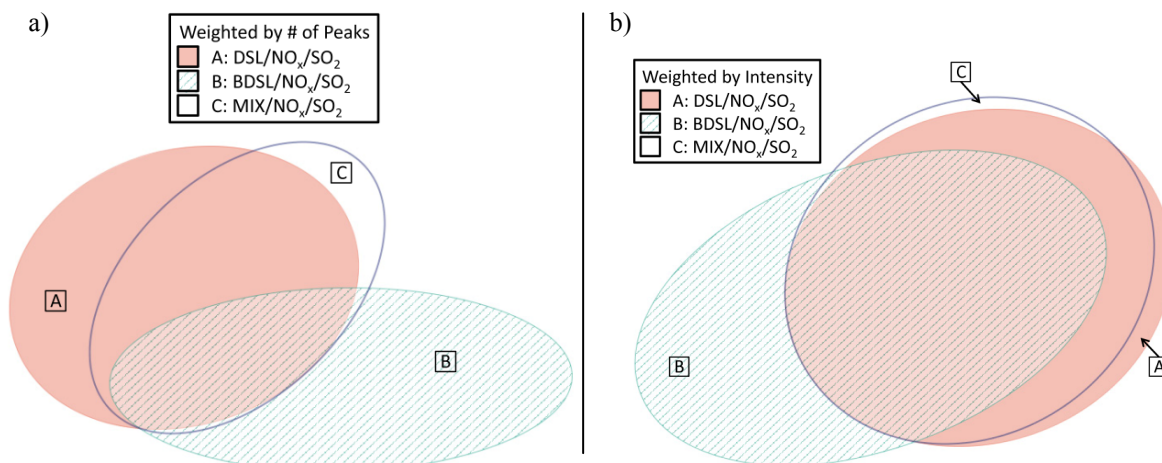


**Figure 4.5.** 21T-FTICR/uHRMS spectra of observed peaks and new peaks in MIX/NO<sub>x</sub>/SO<sub>2</sub> and a calculated spectrum of a linear combination of DSL/NO<sub>x</sub>/SO<sub>2</sub> and BDSL/NO<sub>x</sub>/SO<sub>2</sub> fit to overlapping peaks with the MIX/NO<sub>x</sub>/SO<sub>2</sub> sample.



**Figure 4.6.** The difference 21T-FTICR/uHRMS spectra between observed and calculated MIX/NO<sub>x</sub>/SO<sub>2</sub>. New and lost peaks of individual samples relative to the observed sample are also plotted. Note the change in scale relative to Figure 4.5.

sample CHOS, and CHONS of the new peaks were 5%, 3%, 20%, and 72%, respectively. The largest peak in the BDSL/NO<sub>x</sub>/SO<sub>2</sub> sample was lost in the mixed sample, C<sub>8</sub>H<sub>18</sub>O<sub>8</sub>S (100% RI), whereas the rest that were lost were less than 20% RI. The DSL/NO<sub>x</sub>/SO<sub>2</sub> peaks lost in the mixed sample were 10% RI or less. Under high NO<sub>x</sub> conditions used in this experiment, cross-reactions between alkyl peroxy radicals in diesel fuel and biodiesel fuel SOA are highly unlikely to occur in the gas-phase. The new and lost peaks in the organic composition of MIX/NO<sub>x</sub>/SO<sub>2</sub> are most likely attributed to condensed-phase or heterogeneous reactions following the particle formation.



**Figure 4.7.** Venn diagrams of the overlap of peaks between DSL/NO<sub>x</sub>/SO<sub>2</sub> (A), BDSL/NO<sub>x</sub>/SO<sub>2</sub> (B), and MIX/NO<sub>x</sub>/SO<sub>2</sub> (C) weighted by a) the *number* of peaks and b) the *intensity* of peaks.

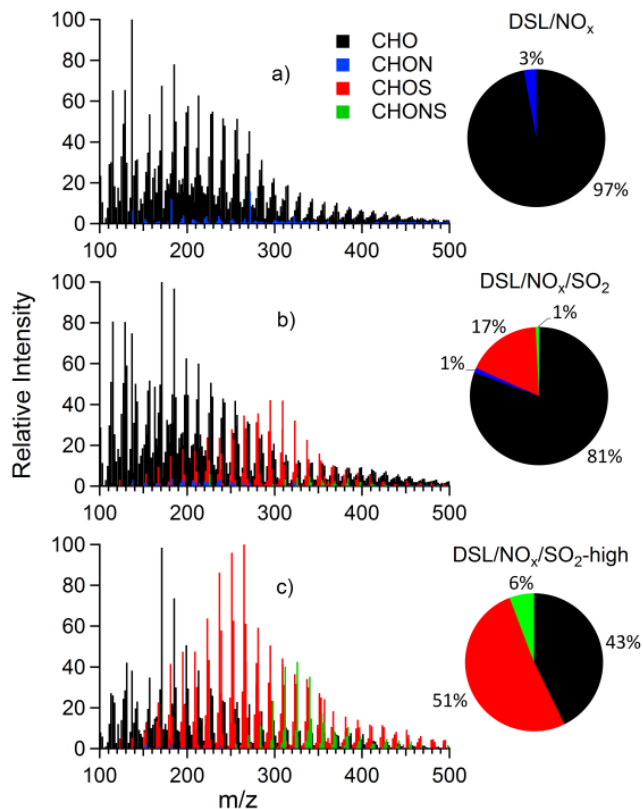
#### 4.4.4. Formation of Organosulfur Species with the Addition of SO<sub>2</sub>

There is a clear trend in Figure 4.8 of increasing organosulfur species, CHOS and CHONS, in nano-DESI/HRMS mass spectra with the addition of SO<sub>2</sub>. The intensity weighted percent CHO, CHON, CHOS, and CHONS are presented as pie charts in Figure 4.8, and the corresponding values for all SOA samples are listed in Table 4.3. With the increase in SO<sub>2</sub>, the fraction of CHOS and CHONS peaks goes from negligible to dominant. When the amount of SO<sub>2</sub> was almost tripled from DSL/NO<sub>x</sub>/SO<sub>2</sub><sup>a</sup> to DSL/NO<sub>x</sub>/SO<sub>2</sub>-high<sup>a</sup> the percent CHOS also tripled from 17% to 51%; the amount of CHONS also increased. A similar trend is also seen for other samples as well, in which the amount of SO<sub>2</sub> was increasing (Figures 4.9-4.12).

AMS data also supported the formation of condensed organosulfur species with the addition of SO<sub>2</sub>. These experiments were conducted without the presence of sulfate seed, so to better observe the formation of particulate organosulfur species in AMS data, bar plots of sulfates are reported relative to organics (Figure 4.13). The sulfates:organics ratio increased from

samples 2 to 3 and from samples 11 to 13 where  $\text{NH}_3$  was added to the DSL SOA that already contained  $\text{SO}_2$ . Although  $\text{NH}_3$  could neutralize some of the SOA acidity, it could also, at the same time, increase the amount of seed aerosol for vapors to condense on. The DSL SOA sample with the largest amount of  $\text{SO}_2$  added, sample 12, increased in sulfates:organics relative to sample 11 (as well as sample 2), which had less  $\text{SO}_2$  added. The BDSL/ $\text{NO}_x$ / $\text{SO}_2$  sample had the largest sulfates:organics ratio of all samples by far. This is most likely due to the low SOA yield of the base case, BDSL/ $\text{NO}_x$ , owing to it favoring degradative processes from photooxidation, as previously mentioned. As the SOA yield of BDSL/ $\text{NO}_x$  was smaller than the other samples to begin with, any additional SOA formed from the presence of  $\text{SO}_2$  would have had a larger effect in the sulfates:organics ratio. Although the MIX/ $\text{NO}_x$ / $\text{SO}_2$  sample only contained 20% biodiesel, it was enough to increase the sulfates:organics ratio from the DSL/ $\text{NO}_x$ / $\text{SO}_2$  sample.

The  $\text{SO}_2$  addition makes compounds with lower double bond equivalent (DBE, the combined number of double bonds and rings in the molecule; Equation 4.2) appear more prominently in the mass spectrum. Figure 4.14, which plots DBE as a function of carbon number, shows that with the increase in  $\text{SO}_2$ , the relative contribution of low DBE values clearly increases. In fact, DBE=0 compounds, with no C=C and C=O double bonds or rings, become visible in samples containing  $\text{SO}_2$  (note that sulfate  $-\text{OS}(\text{O})_2\text{OH}$  and sulfonate  $-\text{S}(\text{O})_2\text{OH}$  groups do not contribute to DBE calculated with Equation 4.2). The average DBE values listed in Table 4.2 decrease with the  $\text{SO}_2$  addition. Most likely, this is the effect of converting poorly-ionizable molecules with low oxidation states into sulfur-containing compounds that ionize readily.

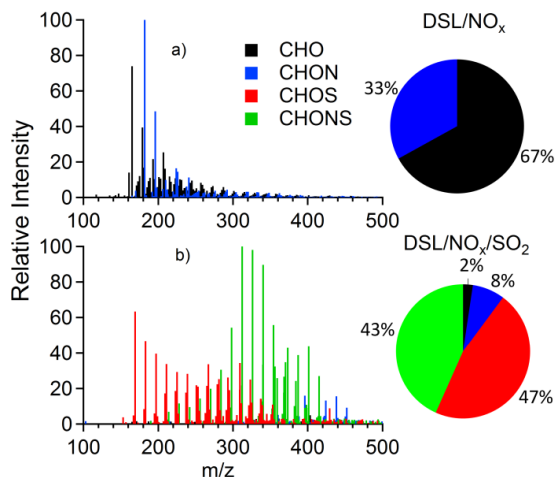


**Figure 4.8.** The effect of SO<sub>2</sub> addition on the nano-DESI/HRMS spectra of diesel fuel SOA (longer denuder samples a) 10, b) 11, and c) 12). The peaks are colored by elemental composition. Pie charts are intensity-weighted elemental composition of the peaks.

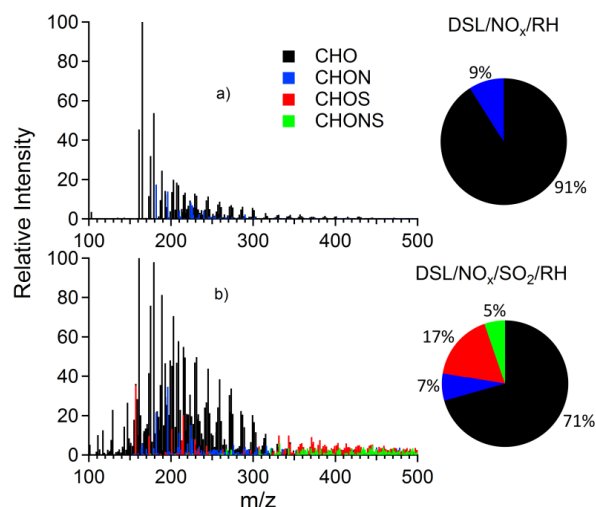
**Table 4.3.** Composition of species in SOA samples from nano-DESI/HRMS spectra. Data for samples that were also recorded with 21T-FTICR/uHRMS are provided in parentheses.

Sample #	Sample Code	% CHO	% CHON	% CHOS	% CHONS
1	DSL/NO <sub>x</sub>	67	33	-	-
2	DSL/NO <sub>x</sub> /SO <sub>2</sub>	2 (8)	8 (0)	47 (92)	43 (0)
3	DSL/NO <sub>x</sub> /SO <sub>2</sub> /NH <sub>3</sub>	5	5	59	31
4	DSL/NO <sub>x</sub> /RH	91	9	-	-
5	DSL/NO <sub>x</sub> /SO <sub>2</sub> /RH	71	7	17	5
6	BDSL/NO <sub>x</sub>	87	13	-	-
7	BDSL/NO <sub>x</sub> /SO <sub>2</sub>	17 (4)	11 (8)	44 (80)	28 (8)
8	MIX/NO <sub>x</sub>	77	23	-	-
9	MIX/NO <sub>x</sub> /SO <sub>2</sub>	10 (4)	16 (8)	34 (80)	40 (8)
10	DSL/NO <sub>x</sub> <sup>a</sup>	97 (96)	3 (4)	-	-
11	DSL/NO <sub>x</sub> /SO <sub>2</sub> <sup>a</sup>	81 (3)	1 (0)	17 (95)	1 (2)
12	DSL/NO <sub>x</sub> /SO <sub>2</sub> -high <sup>a</sup>	43 (3)	0 (0)	51 (94)	6 (3)
13	DSL/NO <sub>x</sub> /SO <sub>2</sub> /NH <sub>3</sub> <sup>a</sup>	11 (3)	5 (0)	81 (93)	3 (3)

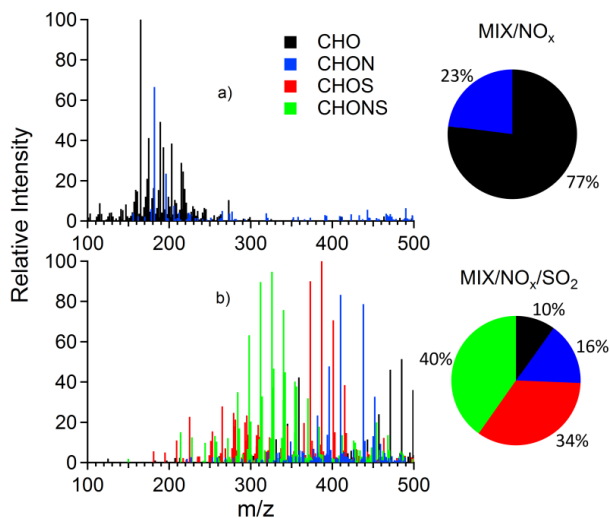
<sup>a</sup> Samples that were sent through a longer denuder train before collection.



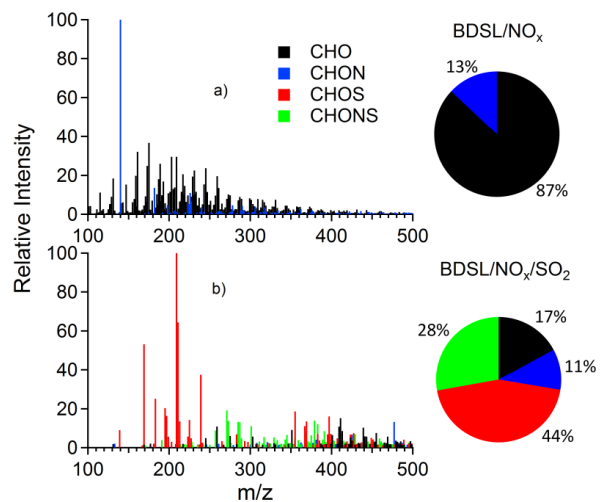
**Figure 4.9.** nano-DESI/HRMS spectra of diesel fuel SOA a) sample 1 (DSL/NO<sub>x</sub>) and b) sample 2 (DSL/NO<sub>x</sub>/SO<sub>2</sub>) colored by composition. Pie charts are intensity weighted %CHONS composition of peaks.



**Figure 4.10.** nano-DESI/HRMS spectra of diesel fuel SOA high humidity a) sample 4 (DSL/NO<sub>x</sub>/RH) and b) sample 5 (DSL/NO<sub>x</sub>/SO<sub>2</sub>/RH) colored by composition. Pie charts are intensity weighted %CHONS composition of peaks.

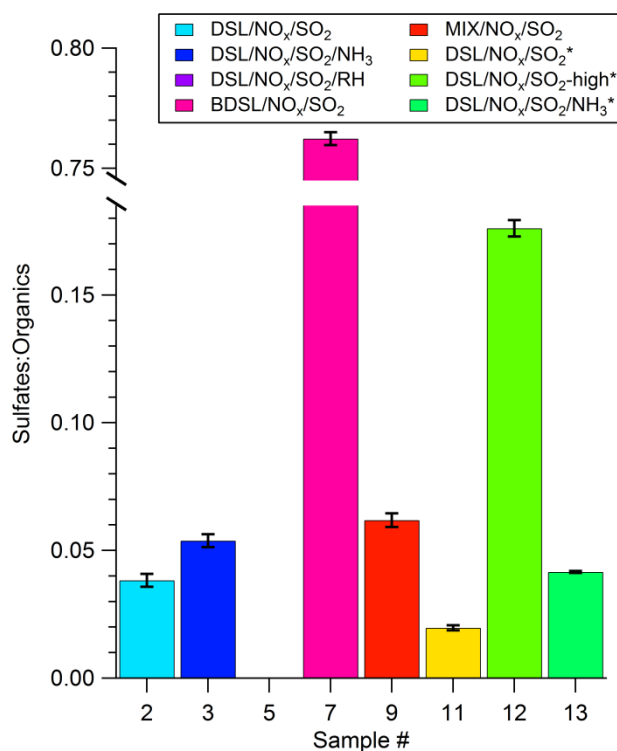


**Figure 4.11.** nano-DESI/HRMS spectra of mixed fuel SOA a) sample 8 (MIX/NO<sub>x</sub>) and b) sample 9 (MIX/NO<sub>x</sub>/SO<sub>2</sub>) colored by composition. Pie charts are intensity weighted %CHONS composition of peaks.



**Figure 4.12.** nano-DESI/HRMS spectra of biodiesel SOA samples a) 6 (BDSL/NO<sub>x</sub>) and b) 7 (BDSL/NO<sub>x</sub>/SO<sub>2</sub>) colored by composition. Pie charts are intensity weighted %CHONS composition of peak.

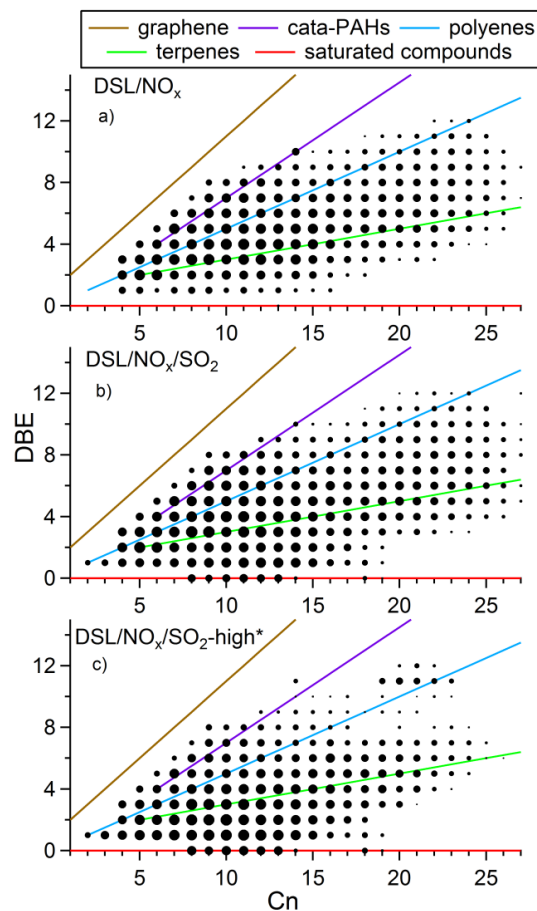
Formation of organosulfates by sulfuric acid mediated mechanisms requires some water. Although most SOA samples were prepared under dry conditions ( $RH < 2\%$ ), residual water from the chamber and also that from the addition of the aqueous hydrogen peroxide solution may have been sufficient to form sulfuric acid and sulfate nucleophiles. There is also a possibility that the organic particles dissolved some of the  $SO_2$  and  $SO_3$  formed in the chamber to further promote heterogeneous sulfuric acid and organosulfur species formation. As previously mentioned, sulfur dioxide can react directly with organics by addition to double bonds.  $SO_2$  is also highly reactive towards Criegee intermediates which may be present in the chamber once ozone is produced. The addition of  $SO_2$  may promote the formation of organosulfates by increasing the acidity of the particles, but also, in turn, increases the amount of available nucleophile.



**Figure 4.13.** Bar plot of AMS sulfate to organics data for  $SO_2$  containing fuel SOA samples.



**Figure 4.14.** Double bond equivalent (DBE) as a function of carbon number (Cn) for diesel fuel SOA samples a) 10, b) 11, and c) 12. The intensities of peaks with a specific Cn and DBE were summed and then the marker size was weighted by this. Trend lines for specific types of species with increasing Cn are plotted in color. The chemical formulas and DBE equations for these are as follows: graphene,  $C_n$ ,  $DBE = 1 + C$ ; cata-PAHs,  $C_{2n-6}H_{(c+6)/2}$ ,  $DBE = 0.75 \cdot Cn$ ; polyenes,  $C_nH_{n+2}$ ,  $DBE = 0.5 \cdot Cn$ ; terpenes,  $C_{5n}H_{8n}$ ,  $DBE = 0.2 \cdot Cn + 1$ ; saturated compounds,  $C_nH_{2n+2}$ ,  $DBE = 0$ .



$$DBE = 1 + C - \frac{H}{2} + \frac{N}{2} \quad (\text{Eq. 4.2})$$

The dry diesel SOA samples, DSL/NO<sub>x</sub> and DSL/NO<sub>x</sub>/SO<sub>2</sub>, showed that the addition of SO<sub>2</sub> changed the average molecular formula to increase in C, H, O/C, H/C, and decrease in DBE (Table 4.2). The increase in the oxidation is most likely from the addition of a sulfate or sulfonate group, which carry several oxygen atoms. The dry biodiesel SOA samples BDSL/NO<sub>x</sub> and BDSL/NO<sub>x</sub>/SO<sub>2</sub> showed a similar trend as well. In contrast, the humid diesel SOA sample, DSL/NO<sub>x</sub>/SO<sub>2</sub>/RH, showed a decrease in the average oxidation level and it did not contain as much sulfur as the other samples. Also, the DSL/NO<sub>x</sub>/SO<sub>2</sub>/RH sample did not have large *m/z* peaks of CHOS and CHONS unlike the rest of samples. There are several possible explanations

for this interesting effect of high humidity. One likely possibility is that high humidity, while promoting the conversion of SO<sub>2</sub> into sulfuric acid in the chamber, actually reduced the effective acidity in the particles by diluting them with particle-bound water. The reduction in acidity must be sufficient to prevent acid catalysis of reactions that occur in the drier samples. For example, the presence of water in wet experiments may suppress the sulfate esterification reactions of hydroxyl groups. Clearly, the effect of humidity on DSL and BDSL oxidation is complicated and deserves further study.

#### 4.4.5. Unique Subset of Organosulfur Species

The CHOS species can be separated into four unique subsets. “*Subset A*” includes aliphatic species. The definition of “aliphatic” used in this thesis was described in the recent Tao et al.<sup>49</sup> study; specifically, CHOS species with  $C > 8$ ,  $DBE < 3$ , and  $3 < O < 7$  fell in this class. “*Subset B*” includes species with the formula C<sub>c</sub>H<sub>h</sub>SO<sub>3</sub>, which do not have enough oxygen atoms in them to be organosulfates. “*Subset C*” has the formula C<sub>c</sub>H<sub>h</sub>SO<sub>4</sub>, which could be interpreted as one sulfate group attached to an oxygen-free substituent or a sulfonate group attached to a substituent containing a single oxygen atom. “*Subset D*” includes aromatic species identified by a high aromaticity index (AI).<sup>50</sup> Analysis of a large number of organic compounds showed that compounds with  $AI \geq 0.5$  are likely to be aromatic; and compounds with  $AI \geq 0.67$  are likely to be condensed aromatics.<sup>50</sup> This study used a modified version of AI, AI\* defined in Equation 4.3, such that sulfur is not included in the calculation and that oxygen atoms are replaced by O\*. The rationale for this adjustment of the AI definition is that the three O atoms directly bonded to the sulfur atom in sulfate and sulfonate groups are not reducing the number of available aromatic carbon atoms.

$$AI^* = \frac{1 + C - O^* - 0.5 \cdot H}{C - O^*} \quad (\text{Eq. 4.3})$$

The distribution of *subsets A, B, C, and D* between samples is listed in Table 4.4. Diesel fuel samples DSL/NO<sub>x</sub>/SO<sub>2</sub>, DSL/NO<sub>x</sub>/SO<sub>2</sub>/NH<sub>3</sub>, DSL/NO<sub>x</sub>/SO<sub>2</sub><sup>a</sup>, DSL/NO<sub>x</sub>/SO<sub>2</sub>-high<sup>a</sup>, and DSL/NO<sub>x</sub>/SO<sub>2</sub>/NH<sub>3</sub><sup>a</sup> were found to have an abundance of aliphatic CHOS species (*subset A*). Van Krevelen plots of DSL/NO<sub>x</sub>/SO<sub>2</sub><sup>a</sup> and DSL/NO<sub>x</sub>/SO<sub>2</sub>-high<sup>a</sup> for CHOS species are shown in Figure 4.15, with the *subset A* compounds shown by red markers. They are also obvious in the CH<sub>2</sub>-Kendrick diagram shown in Figure 4.16, which features prominent families of compounds with low DBE. These species were most likely formed via esterification of alcohols produced by the oxidation of aliphatic species in the diesel fuel. These compounds had high overlap with the compounds found in Shanghai particulate matter by Tao et al.,<sup>49</sup> who also proposed an

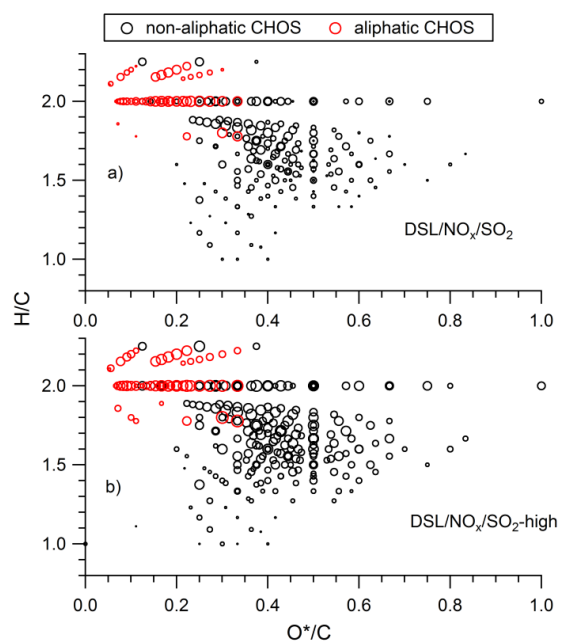
**Table 4.4.** Percent CHOS species and percent subsets of CHOS species for each sample. Percent CHOS for each sample are weighted by the sum of the intensity of *all* peaks within that sample. The subsets of CHOS species are weighted by the sum of the intensity of *only CHOS* peaks for each sample: aliphatic (A), C<sub>c</sub>H<sub>h</sub>SO<sub>3</sub> (B), C<sub>c</sub>H<sub>h</sub>SO<sub>4</sub> (C), and aromatic (D) with an average aromatic index (AI\*). An “x” denotes that peaks of that specific type were not observed.

Sample #	Sample Code	%CHOS	CHOS Subsets				
			%A	%B	%C	%D	<AI* > of D
2	DSL/NO <sub>x</sub> /SO <sub>2</sub>	47 (92)	30 (37)	1 (x)	3 (4)	3 (0.2)	0.62 (0.50)
3	DSL/NO <sub>x</sub> /SO <sub>2</sub> /NH <sub>3</sub>	59	42	x	5	0.3	0.58
5	DSL/NO <sub>x</sub> /SO <sub>2</sub> /RH	17	0.4	17	20	32	0.57
7	BDSL/NO <sub>x</sub> /SO <sub>2</sub>	44 (80)	1 (13)	x (2)	2 (3)	4 (2)	0.72 (0.74)
9	MIX/NO <sub>x</sub> /SO <sub>2</sub>	34 (80)	25 (37)	29 (x)	9 (5)	37 (0.3)	0.63 (0.51)
11	DSL/NO <sub>x</sub> /SO <sub>2</sub> <sup>a</sup>	17	42	x (0.4)	4	x (0.1)	x (0.50)
12	DSL/NO <sub>x</sub> /SO <sub>2</sub> -high <sup>a</sup>	51 (94)	32 (33)	x (2)	7 (7)	x (0.1)	0.61 (0.50)
13	DSL/NO <sub>x</sub> /SO <sub>2</sub> /NH <sub>3</sub> <sup>a</sup>	81 (93)	62 (57)	0.5 (1)	4 (3)	0.5 (0.3)	0.59 (0.53)

<sup>a</sup> Samples that were sent through a longer denuder train before collection.

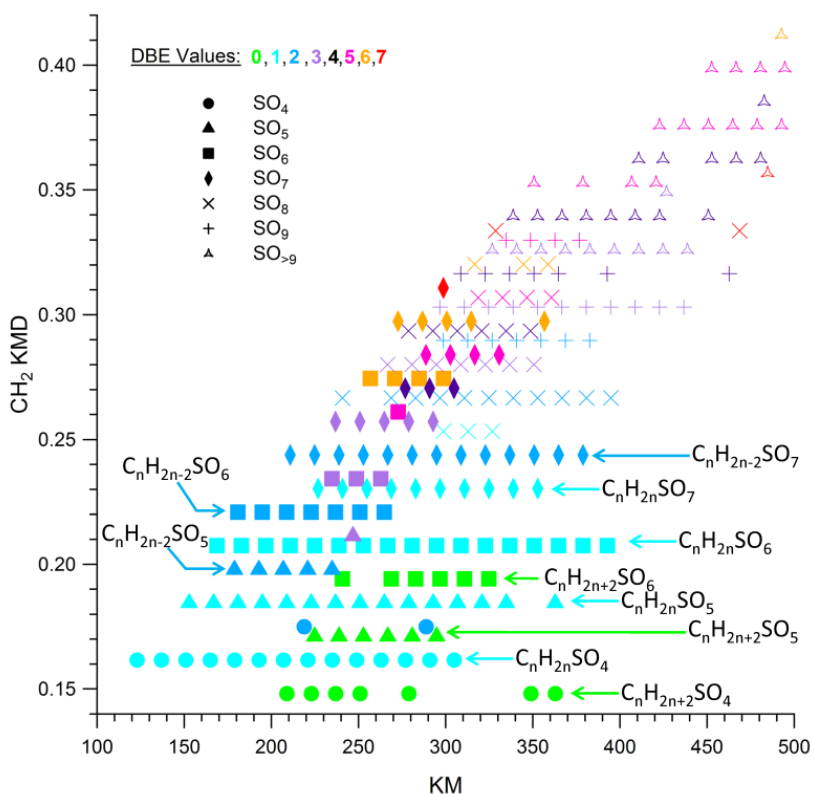
esterification mechanism for their formation as well as possible contribution from primary sources. Dry diesel SOA samples with  $\text{NH}_3$  present had the largest percentage of aliphatic CHOS species (about 60% of detected CHOS were in *subset A*), whereas the humid diesel and dry biodiesel samples had the lowest (< 2%). The effect of humidity can be attributed to the suppression of esterification by particle water, as discussed above. The effect of ammonia is counterintuitive as it is expected to reduce the particle acidity by neutralizing sulfuric acid and suppress the esterification processes; on the other hand, it increases the overall amount of sulfate nucleophiles in the particles. The reason for the low abundance of *subset A* compounds in the BDSL sample is unclear.

**Figure 4.15.** Van Krevelen diagrams of CHOS species (CHO and CHONS not shown) for a) sample 11 (DSL/ $\text{NO}_x$ / $\text{SO}_2$ , long denuder) and b) sample 12 (DSL/ $\text{NO}_x$ / $\text{SO}_2$ -high, long denuder).  $\text{O}^*$  is the number of oxygen atoms minus 3 to emphasize the degree of oxidation that is not due to the sulfate group addition. Unique aliphatic CHOS species, distinguished by  $\text{O}^* < 4$  and  $\text{DBE} < 3$ , are shown in red.



*Subset B* compounds, which have only 3 oxygen atoms in them in addition to sulfur, are most likely organosulfonates ( $\text{R-SO}_3\text{H}$ ) which were recently observed in chamber experiments.<sup>25</sup> The MIX/ $\text{NO}_x$ / $\text{SO}_2$  and DSL/ $\text{NO}_x$ / $\text{SO}_2$ /RH had the largest percent of CHO compounds falling into *subset B*, whereas the other samples had less than 2%. The high humidity diesel sample,

DSL/NO<sub>x</sub>/SO<sub>2</sub>/RH, had a large peak (35% RI) for benzene sulfonic acid. The most intense sulfonates of MIX/NO<sub>x</sub>/SO<sub>2</sub> sample were C<sub>21</sub>H<sub>14</sub>SO<sub>3</sub> (18% RI), C<sub>23</sub>H<sub>18</sub>SO<sub>3</sub> (90% RI), and C<sub>24</sub>H<sub>20</sub>SO<sub>3</sub> (100% RI, i.e., the largest peak in the spectrum), C<sub>25</sub>H<sub>22</sub>SO<sub>3</sub> (71% RI), C<sub>26</sub>H<sub>14</sub>SO<sub>3</sub> (38% RI). All of these species have the same general formula C<sub>n</sub>H<sub>2n-28</sub>SO<sub>3</sub>, all with DBE values of 15. This implies that these compounds correspond to sulfonates of substituted benzopyrene (C<sub>20</sub>H<sub>12</sub>, DBE =15).



**Figure 4.16.** Kendrick mass defect CH<sub>2</sub> plot for CHOS species of DSL/NO<sub>x</sub>/SO<sub>2</sub><sup>a</sup>, sample 11. The mass spectral peaks are colored by DBE and shaped by the total number, *x*, of oxygen atoms (as SO<sub>*x*</sub>). Prominent families are labeled with general chemical formulas.

The C<sub>c</sub>H<sub>h</sub>SO<sub>4</sub> species in *subset C*, which may be hydroxy or keto-sulfonates or organosulfates, were most abundant in the DSL/NO<sub>x</sub>/SO<sub>2</sub>/RH sample. Considering that the same sample also had a high fraction of *subset B* compounds, believed to be sulfonates, it is likely that

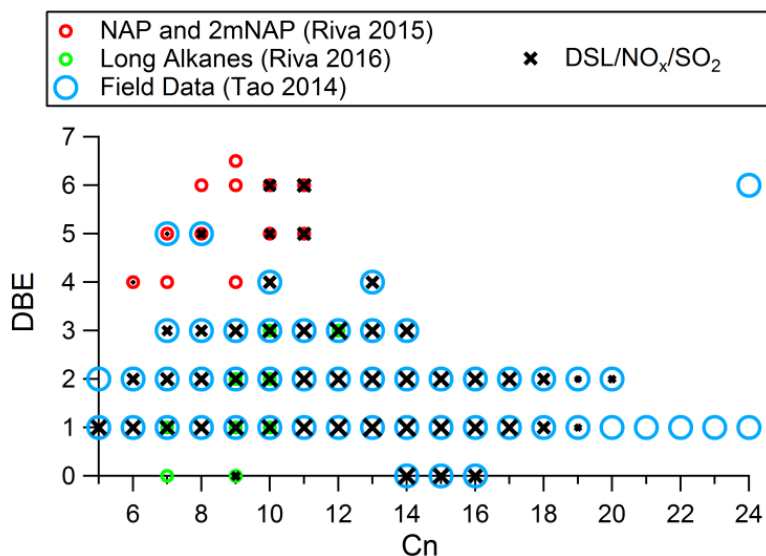
keto- and hydroxyl- sulfonates also contribute to group C. The diesel sample with the largest amount of added SO<sub>2</sub>, sample 12, had the largest intensity peaks for *subset C* and showed a clear pattern of the molecular formulas of C<sub>n</sub>H<sub>2n</sub>SO<sub>4</sub> for 2 < C < 15, which could be keto-sulfonates of saturated compounds or sulfates of unsaturated ones. Less intense mass spectral peaks of these molecular formulas were also seen in sample 11 (Figure 4.16) as well as other diesel fuel samples except for the high humidity one.

The sample with the highest fraction of aromatic CHOS (*subset D*) was MIX/NO<sub>x</sub>/SO<sub>2</sub>; the other samples had fewer than 5% of CHO species falling in this category. We mentioned above that aromatics in diesel fuel appeared to undergo ring-opening reactions that shifted the average size of the aromatic species to lower carbon numbers, and reduced the degree of aromaticity. The addition of biodiesel fuel to the mix appeared to have an inhibitory effect on these reactions, resulting in a larger fraction of aromatic products. Interestingly, the largest aromatic species of MIX/NO<sub>x</sub>/SO<sub>2</sub> were also organosulfonates, the same peaks previously emphasized for *subset C*. It could be that aromatic sulfonates undergo ring-opening reactions after being further oxidized and that the presence of reactive biodiesel components competes with this secondary oxidation of aromatic CHOS. Although this is possible, this same observation of abundant *subset B* and *D* in MIX/NO<sub>x</sub>/SO<sub>2</sub>, was not seen in FTICR data; there was less than 1% of these subsets.

#### 4.4.6. Comparison of CHOS Species to Previous Literature

There is a large overlap of organosulfur mass spectral peaks in this fuel photooxidation study with previous literature from both field and chamber measurements.<sup>24, 25, 49, 51-53</sup> To better illustrate this point, the CHOS species observed in a few selected studies are compared with the *same* species in the DSL/NO<sub>x</sub>/SO<sub>2</sub> sample on a DBE vs. carbon number plot (Figure 4.17). Most

assigned CHOS species listed in the supplementary information section of the field study by Tao et al.<sup>49</sup> are observed in the diesel fuel SOA in this study. For example, we observed the  $C_nH_{2n+2}SO_4$  family of compounds, highlighted in the Kendrick plot in Figure 4.16, that represented a dominant family of organosulfur species in Tao et al.<sup>49</sup> data. Note that we are not suggesting that *only* diesel fuel SOA is responsible for the mass spectra in Tao et al.<sup>49</sup> data, but that the data in this study has high overlap, especially with aliphatic organosulfur species. Previous literature on lab-generated SOA of long alkanes<sup>24</sup> and SOA of naphthalene (NAP) and 2-methyl-naphthalene (2mNAP)<sup>25</sup> by Riva and co-authors was also compared. The largest overlap of DSL/NO<sub>x</sub>/SO<sub>2</sub> with Riva et al.<sup>25</sup> aromatic data is for peaks from NAP, C<sub>10</sub>H<sub>10</sub>SO<sub>7</sub> and C<sub>10</sub>H<sub>10</sub>SO<sub>6</sub>, and 2mNAP, C<sub>11</sub>H<sub>12</sub>SO<sub>7</sub>, SOA of the type C<sub>n</sub>H<sub>2n-10</sub>SO<sub>6-7</sub> with DBE values of 6 suggested to be organosulfates.



**Figure 4.17.** Carbon number distribution for CHOS species observed by Tao et al. (2014), Riva et al. (2015), and Riva et al. (2016) where points are colored by source. The data from this study for the diesel SOA sample 2 (× symbols) are only included in the plot when the formula overlaps with one of the formulas previously reported in the literature. The size of the × is weighted by Log(Intensity·10).

As mentioned previously, the high humidity sample had less organosulfur species in the mass spectra. This may be due to a dilution of the sulfate nucleophile as well as a decrease in the acidity.<sup>54</sup> Interestingly, the largest intensity peaks of the humid sample, DSL/NO<sub>x</sub>/SO<sub>2</sub>/RH, that overlapped with both Tao et al.<sup>49</sup> data and Riva et al.<sup>25</sup> naphthalene data were C<sub>7</sub>H<sub>6</sub>SO<sub>5</sub> and C<sub>8</sub>H<sub>8</sub>SO<sub>5</sub>. These peaks had DBE values of 5 and were of the general chemical formula C<sub>n</sub>H<sub>2n-8</sub>SO<sub>5</sub>, which Riva found to be organosulfonates in the 2mNAP SOA. Although the Riva et al.<sup>25</sup> paper reported that RH appeared to have little effect on the formation of sulfonates and organosulfates for 2mNAP SOA in general, specifically in the case of these two organosulfates found in our high humidity samples, the concentrations increased with increasing the RH for each specific acidity (Riva et al.<sup>25</sup> samples from 10/20/2014 and 10/25/2014). The aromatic peak observed in the high humidity sample that was also seen in Riva et al.,<sup>25</sup> C<sub>6</sub>H<sub>6</sub>SO<sub>4</sub>, is most likely hydroxy benzene sulfonic acid. The largest overlap of the biodiesel fuel sample was with Tao et al.<sup>49</sup> data for peaks of C<sub>6</sub>H<sub>10</sub>SO<sub>6</sub> (also the most intense CHOS peak in general), C<sub>6</sub>H<sub>12</sub>SO<sub>6</sub>, and C<sub>8</sub>H<sub>16</sub>SO<sub>6</sub>.

#### **4.5. Atmospheric Implications**

This is the first study of organosulfates in SOA formed in the photooxidation of diesel and biodiesel fuel. It was observed that the presence of SO<sub>2</sub> increased the particle geometric mean diameter of SOA particles and formed numerous organosulfur species even under dry conditions. The suppression of organosulfur compounds under humidified conditions was not expected because most previous studies have observed higher yields of organosulfur species at elevated relative humidity. However, the previous studies relied on sulfate-containing seed particles, and could miss several important organosulfur formation pathways that are unique to SO<sub>2</sub> chemistry such as the direct addition of SO<sub>2</sub> to unsaturated species and reaction of SO<sub>2</sub> with



Criegee intermediates.<sup>19, 37, 38</sup> The high overlap of the organosulfur species observed in this study with previous field studies suggest that these alternative mechanisms of organosulfur formation could be important in the atmosphere, and they deserve additional scrutiny.

Many organosulfur species in field data that were previously appointed as biogenic in origin or labeled as species of unknown origin were also found amongst the products of photooxidation of diesel and biodiesel fuel in this study. For example, the organosulfur peak of formula  $C_5H_{10}SO_5$  was previously assigned to an unknown<sup>51</sup> or isoprene<sup>49</sup> source, and another peak,  $C_9H_{16}SO_7$ , was assigned to limonene<sup>51, 52</sup> or to a monoterpene.<sup>49</sup> Both of these formulas were prominently present in the DSL SOA mass spectra suggesting that they could also be of anthropogenic origin. A number of other examples were found of the overlap of CHOS species with those observed in previous measurements. The implication of these results is that one has to be more careful about assuming the origin of the organosulfur species based only on their formula.

This work observed that the high-resolution mass spectrum of SOA from a mixture of diesel and biodiesel fuel precursors can be reasonably represented as a combination of mass spectra of the individual precursor SOA. The peak loss and formation of unique new species in the mass spectrum of the mixture suggest that cross reactions occur between the mixed SOA compounds, presumably in the particle phase. It would be interesting to examine the prevalence of condensed-phase cross reactions between SOA compounds, and their effect on key physical properties of SOA, using similar high resolution mass spectrometry techniques.

## References

1. Wang, K.; Dickinson, R. E.; Liang, S., Clear Sky Visibility Has Decreased over Land Globally from 1973 to 2007. *Science* **2009**, *323* (5920), 1468-1470.
2. Pope, I. C.; Burnett, R. T.; Thun, M. J.; et al., Lung cancer, cardiopulmonary mortality, and long-term exposure to fine particulate air pollution. *JAMA* **2002**, *287* (9), 1132-1141.
3. Intergovernmental Panel On Climate Change: CLIMATE CHANGE 2013 The Physical Science Basis. Summary for Policymakers, **2013**. Available from: <http://www.ipcc.ch/report/ar5/wg1/>. Accessed 12/2015.
4. Goldstein, A. H.; Galbally, I. E., Known and unexplored organic constituents in the Earth's atmosphere. *Environ. Sci. Technol.* **2007**, *41* (5), 1514-1521.
5. Zhang, Q.; Jimenez, J. L.; Canagaratna, M. R.; Allan, J. D.; Coe, H.; Ulbrich, I.; Alfarra, M. R.; Takami, A.; Middlebrook, A. M.; Sun, Y. L.; Dzepina, K.; Dunlea, E.; Docherty, K.; DeCarlo, P. F.; Salcedo, D.; Onasch, T.; Jayne, J. T.; Miyoshi, T.; Shimojo, A.; Hatakeyama, S.; Takegawa, N.; Kondo, Y.; Schneider, J.; Drewnick, F.; Borrmann, S.; Weimer, S.; Demerjian, K.; Williams, P.; Bower, K.; Bahreini, R.; Cottrell, L.; Griffin, R. J.; Rautiainen, J.; Sun, J. Y.; Zhang, Y. M.; Worsnop, D. R. C. L., Ubiquity and dominance of oxygenated species in organic aerosols in anthropogenically-influenced Northern Hemisphere midlatitudes. *Geophysical Research Letters* **2007**, *34* (13), DOI: 10.1029/2007GL029979.
6. Glasius, M.; Goldstein, A. H., Recent Discoveries and Future Challenges in Atmospheric Organic Chemistry. *Environ. Sci. Technol.* **2016**, *50* (6), 2754-2764.
7. Heald, C. L.; Coe, H.; Jimenez, J. L.; Weber, R. J.; Bahreini, R.; Middlebrook, A. M.; Russell, L. M.; Jolleys, M.; Fu, T. M.; Allan, J. D.; Bower, K. N.; Capes, G.; Crosier, J.; Morgan, W. T.; Robinson, N. H.; Williams, P. I.; Cubison, M. J.; DeCarlo, P. F.; Dunlea, E. J., Exploring the vertical profile of atmospheric organic aerosol: comparing 17 aircraft field campaigns with a global model. *Atmos. Chem. Phys.* **2011**, *11* (24), 12673-12696.
8. Woody, M. C.; Baker, K. R.; Hayes, P. L.; Jimenez, J. L.; Koo, B.; Pye, H. O. T., Understanding sources of organic aerosol during CalNex-2010 using the CMAQ-VBS. *Atmos. Chem. Phys. Discuss.* **2015**, *15* (19), 26745-26793.

9. Zhang, R.; Wang, G.; Guo, S.; Zamora, M. L.; Ying, Q.; Lin, Y.; Wang, W.; Hu, M.; Wang, Y., Formation of Urban Fine Particulate Matter. *Chem. Rev.* **2015**, *115* (10), 3803-3855.
10. Gentner, D. R.; Isaacman, G.; Worton, D. R.; Chan, A. W. H.; Dallmann, T. R.; Davis, L.; Liu, S.; Day, D. A.; Russell, L. M.; Wilson, K. R.; Weber, R.; Guha, A.; Harley, R. A.; Goldstein, A. H., Elucidating secondary organic aerosol from diesel and gasoline vehicles through detailed characterization of organic carbon emissions. *Proc. Natl. Acad. Sci. U. S. A.* **2012**, *109* (45), 18318-18323.
11. Fukagawa, N. K.; Li, M.; Poynter, M. E.; Palmer, B. C.; Parker, E.; Kasumba, J.; Holmen, B. A., Soy Biodiesel and Petrodiesel Emissions Differ in Size, Chemical Composition and Stimulation of Inflammatory Responses in Cells and Animals. *Environ. Sci. Technol.* **2013**, *47* (21), 12496-12504.
12. Gordon, T. D.; Presto, A. A.; May, A. A.; Nguyen, N. T.; Lipsky, E. M.; Donahue, N. M.; Gutierrez, A.; Zhang, M.; Maddox, C.; Rieger, P.; Chattopadhyay, S.; Maldonado, H.; Maricq, M. M.; Robinson, A. L., Secondary organic aerosol formation exceeds primary particulate matter emissions for light-duty gasoline vehicles. *Atmos. Chem. Phys.* **2014**, *14* (9), 4661-4678.
13. Drozd, G. T.; Worton, D. R.; Aeppli, C.; Reddy, C. M.; Zhang, H.; Variano, E.; Goldstein, A. H., Modeling comprehensive chemical composition of weathered oil following a marine spill to predict ozone and potential secondary aerosol formation and constrain transport pathways. *J. Geophys. Res.: Oceans* **2015**, *120* (11), 7300-7315.
14. Field, R. A.; Soltis, J.; McCarthy, M. C.; Murphy, S.; Montague, D. C., Influence of oil and gas field operations on spatial and temporal distributions of atmospheric non-methane hydrocarbons and their effect on ozone formation in winter. *Atmos. Chem. Phys.* **2015**, *15* (6), 3527-3542.
15. Altieri, K. E.; Stone, A., Prospective air pollutant emissions inventory for the development and production of unconventional natural gas in the Karoo basin, South Africa. *Atmos. Environ.* **2016**, *129*, 34-42.
16. Edney, E. O.; Kleindienst, T. E.; Jaoui, M.; Lewandowski, M.; Offenberg, J. H.; Wang, W.; Claeys, M., Formation of 2-methyl tetrols and 2-methylglyceric acid in secondary organic

- aerosol from laboratory irradiated isoprene/NOX/SO<sub>2</sub>/air mixtures and their detection in ambient PM<sub>2.5</sub> samples collected in the eastern United States. *Atmos. Environ.* **2005**, *39* (29), 5281-5289.
17. Jaoui, M.; Edney, E. O.; Kleindienst, T. E.; Lewandowski, M.; Offenber, J. H.; Surratt, J. D.; Seinfeld, J. H. C. D., Formation of secondary organic aerosol from irradiated  $\alpha$ -pinene/toluene/NO<sub>x</sub> mixtures and the effect of isoprene and sulfur dioxide. *J. Geophys. Res.: Atmospheres* **2008**, *113*, DOI: 10.1029/2007JD009426.
  18. Praplan, A. P.; Hegyi-Gaeggeler, K.; Barmet, P.; Pfaffenberger, L.; Dommen, J.; Baltensperger, U., Online measurements of water-soluble organic acids in the gas and aerosol phase from the photooxidation of 1,3,5-trimethylbenzene. *Atmos. Chem. Phys.* **2014**, *14* (16), 8665-8677.
  19. Liu, T.; Wang, X.; Hu, Q.; Deng, W.; Zhang, Y.; Ding, X.; Fu, X.; Bernard, F.; Zhang, Z.; Lu, S.; He, Q.; Bi, X.; Chen, J.; Sun, Y.; Yu, J.; Peng, P.; Sheng, G.; Fu, J., Formation of secondary aerosols from gasoline vehicle exhaust when mixing with SO<sub>2</sub>. *Atmos. Chem. Phys.* **2016**, *16* (2), 675-689.
  20. Santiago, M.; Vivanco, M. G.; Stein, A. F., SO<sub>2</sub> effect on secondary organic aerosol from a mixture of anthropogenic VOCs: experimental and modeled results. *Int. J. Environ. Pollut.* **2012**, *50* (1/2/3/4), 224-233.
  21. Kleindienst, T. E.; Edney, E. O.; Lewandowski, M.; Offenber, J. H.; Jaoui, M., Secondary Organic Carbon and Aerosol Yields from the Irradiations of Isoprene and  $\alpha$ -Pinene in the Presence of NO<sub>x</sub> and SO<sub>2</sub>. *Environ. Sci. Technol.* **2006**, *40* (12), 3807-3812.
  22. Finlayson-Pitts, B. J.; Pitts, J. N., *Chemistry of the Upper and Lower Atmosphere: Theory, Experiments, and Applications*. Academic Press, San Diego, CA, USA, 2000.
  23. Li, L.; Chen, Z. M.; Zhang, Y. H.; Zhu, T.; Li, J. L.; Ding, J., Kinetics and mechanism of heterogeneous oxidation of sulfur dioxide by ozone on surface of calcium carbonate. *Atmos. Chem. Phys.* **2006**, *6* (9), 2453-2464.

24. Riva, M.; Da Silva Barbosa, T.; Lin, Y. H.; Stone, E. A.; Gold, A.; Surratt, J. D., Characterization of Organosulfates in Secondary Organic Aerosol Derived from the Photooxidation of Long-Chain Alkanes. *Atmos. Chem. Phys. Discuss.* **2016**, *2016*, 1-39.
25. Riva, M.; Tomaz, S.; Cui, T.; Lin, Y.-H.; Perraudin, E.; Gold, A.; Stone, E. A.; Villenave, E.; Surratt, J. D., Evidence for an Unrecognized Secondary Anthropogenic Source of Organosulfates and Sulfonates: Gas-Phase Oxidation of Polycyclic Aromatic Hydrocarbons in the Presence of Sulfate Aerosol. *Environ. Sci. Technol.* **2015**, *49* (11), 6654-6664.
26. Surratt, J. D.; Lewandowski, M.; Offenberg, J. H.; Jaoui, M.; Kleindienst, T. E.; Edney, E. O.; Seinfeld, J. H., Effect of Acidity on Secondary Organic Aerosol Formation from Isoprene. *Environ. Sci. Technol.* **2007**, *41* (15), 5363-5369.
27. Chan, M. N.; Surratt, J. D.; Chan, A. W. H.; Schilling, K.; Offenberg, J. H.; Lewandowski, M.; Edney, E. O.; Kleindienst, T. E.; Jaoui, M.; Edgerton, E. S.; Tanner, R. L.; Shaw, S. L.; Zheng, M.; Knipping, E. M.; Seinfeld, J. H., Influence of aerosol acidity on the chemical composition of secondary organic aerosol from  $\beta$ -caryophyllene. *Atmos. Chem. Phys.* **2011**, *11* (4), 1735-1751.
28. Kundu, S.; Quraishi, T. A.; Yu, G.; Suarez, C.; Keutsch, F. N.; Stone, E. A., Evidence and quantitation of aromatic organosulfates in ambient aerosols in Lahore, Pakistan. *Atmos. Chem. Phys.* **2013**, *13* (9), 4865-4875.
29. McNeill, V. F.; Woo, J. L.; Kim, D. D.; Schwier, A. N.; Wannell, N. J.; Sumner, A. J.; Barakat, J. M., Aqueous-Phase Secondary Organic Aerosol and Organosulfate Formation in Atmospheric Aerosols: A Modeling Study. *Environ. Sci. Technol.* **2012**, *46* (15), 8075-8081.
30. Berndt, T.; Stratmann, F.; Braesel, S.; Heintzenberg, J.; Laaksonen, A.; Kulmala, M., SO<sub>2</sub> oxidation products other than H<sub>2</sub>SO<sub>4</sub> as a trigger of new particle formation. Part 1: Laboratory investigations. *Atmos. Chem. Phys.* **2008**, *8* (21), 6365-6374.
31. Darer, A. I.; Cole-Filipiak, N. C.; O'Connor, A. E.; Elrod, M. J., Formation and Stability of Atmospherically Relevant Isoprene-Derived Organosulfates and Organonitrates. *Environ. Sci. Technol.* **2011**, *45* (5), 1895-1902.

32. Minerath, E. C.; Casale, M. T.; Elrod, M. J., Kinetics Feasibility Study of Alcohol Sulfate Esterification Reactions in Tropospheric Aerosols. *Environ. Sci. Technol.* **2008**, *42* (12), 4410-4415.
33. Kane, S. M.; Leu, M.-T., Uptake of Methanol Vapor in Sulfuric Acid Solutions. *The Journal of Physical Chemistry A* **2001**, *105* (9), 1411-1415.
34. Li, J.; Jang, M., Kinetic study of esterification of sulfuric acid with alcohols in aerosol bulk phase. *Atmos. Chem. Phys. Discuss.* **2013**, *13* (9), 23217-23250.
35. Nguyen, T. B.; Lee, P. B.; Updyke, K. M.; Bones, D. L.; Laskin, J.; Laskin, A.; Nizkorodov, S. A. C. D., Formation of nitrogen- and sulfur-containing light-absorbing compounds accelerated by evaporation of water from secondary organic aerosols. *J. Geophys. Res.: Atmospheres* **2012**, *117*, DOI: 10.1029/2011JD016944.
36. Nozière, B.; Ekström, S.; Alsberg, T.; Holmström, S. C. L., Radical-initiated formation of organosulfates and surfactants in atmospheric aerosols. *Geophys. Res. Lett.* **2010**, *37* (5).
37. Mauldin Iii, R. L.; Berndt, T.; Sipila, M.; Paasonen, P.; Petaja, T.; Kim, S.; Kurten, T.; Stratmann, F.; Kerminen, V. M.; Kulmala, M., A new atmospherically relevant oxidant of sulphur dioxide. *Nature* **2012**, *488* (7410), 193-196.
38. Shang, J.; Passananti, M.; Dupart, Y.; Ciuraru, R.; Tinel, L.; Rossignol, S. p.; Perrier, S. b.; Zhu, T.; George, C., SO<sub>2</sub> Uptake on Oleic Acid: A New Formation Pathway of Organosulfur Compounds in the Atmosphere. *Environ. Sci. Technol. Lett.* **2016**, *3* (2), 67-72.
39. Isaacman, G.; Wilson, K. R.; Chan, A. W. H.; Worton, D. R.; Kimmel, J. R.; Nah, T.; Hohaus, T.; Gonin, M.; Kroll, J. H.; Worsnop, D. R.; Goldstein, A. H., Improved Resolution of Hydrocarbon Structures and Constitutional Isomers in Complex Mixtures Using Gas Chromatography-Vacuum Ultraviolet-Mass Spectrometry. *Anal. Chem.* **2012**, *84* (5), 2335-2342.
40. Worton, D. R.; Isaacman, G.; Gentner, D. R.; Dallmann, T. R.; Chan, A. W. H.; Ruehl, C.; Kirchstetter, T. W.; Wilson, K. R.; Harley, R. A.; Goldstein, A. H., Lubricating Oil Dominates Primary Organic Aerosol Emissions from Motor Vehicles. *Environ. Sci. Technol.* **2014**, *48* (7), 3698-3706.

41. Worton, D. R.; Zhang, H.; Isaacman-VanWertz, G.; Chan, A. W. H.; Wilson, K. R.; Goldstein, A. H., Comprehensive Chemical Characterization of Hydrocarbons in NIST Standard Reference Material 2779 Gulf of Mexico Crude Oil. *Environ. Sci. Technol.* **2015**, *49* (22), 13130-13138.
42. Laskin, J.; Eckert, P. A.; Roach, P. J.; Heath, B. S.; Nizkorodov, S. A.; Laskin, A., Chemical Analysis of Complex Organic Mixtures Using Reactive Nanospray Desorption Electrospray Ionization Mass Spectrometry. *Anal. Chem.* **2012**, *84* (16), 7179-7187.
43. Jathar, S. H.; Donahue, N. M.; Adams, P. J.; Robinson, A. L., Testing secondary organic aerosol models using smog chamber data for complex precursor mixtures: influence of precursor volatility and molecular structure. *Atmos. Chem. Phys.* **2014**, *14* (11), 5771-5780.
44. Pye, H. O. T.; Pouliot, G. A., Modeling the Role of Alkanes, Polycyclic Aromatic Hydrocarbons, and Their Oligomers in Secondary Organic Aerosol Formation. *Environ. Sci. Technol.* **2012**, *46* (11), 6041-6047.
45. Milazzo, M. F.; Spina, F.; Cavallaro, S.; Bart, J. C. J., Sustainable soy biodiesel. *Renew. Sust. Energ. Rev.* **2013**, *27*, 806-852.
46. Yaakob, Z.; Narayanan, B. N.; Padikkaparambil, S.; Unni K, S.; Akbar P, M., A review on the oxidation stability of biodiesel. *Renew. Sust. Energ. Rev.* **2014**, *35*, 136-153.
47. Khoury, R. R.; Ebrahimi, D.; Hejazi, L.; Bucknall, M. P.; Pickford, R.; Brynn Hibbert, D., Degradation of fatty acid methyl esters in biodiesels exposed to sunlight and seawater. *Fuel* **2011**, *90* (8), 2677-2683.
48. Kelly, R. T.; Tolmachev, A. V.; Page, J. S.; Tang, K.; Smith, R. D., The ion funnel: theory, implementations, and applications. *Mass. Spectrom. Rev.* **2010**, *29* (2), 294-312.
49. Tao, S.; Lu, X.; Levac, N.; Bateman, A. P.; Nguyen, T. B.; Bones, D. L.; Nizkorodov, S. A.; Laskin, J.; Laskin, A.; Yang, X., Molecular Characterization of Organosulfates in Organic Aerosols from Shanghai and Los Angeles Urban Areas by Nanospray-Desorption Electrospray Ionization High-Resolution Mass Spectrometry. *Environ. Sci. Technol.* **2014**, *48* (18), 10993-11001.

50. Koch, B. P.; Dittmar, T., From mass to structure: an aromaticity index for high-resolution mass data of natural organic matter. *Rapid Commun. Mass Sp.* **2006**, *20* (5), 926-932.
51. Nguyen, Q. T.; Christensen, M. K.; Cozzi, F.; Zare, A.; Hansen, A. M. K.; Kristensen, K.; Tulinius, T. E.; Madsen, H. H.; Christensen, J. H.; Brandt, J.; Massling, A.; Nøjgaard, J. K.; Glasius, M., Understanding the anthropogenic influence on formation of biogenic secondary organic aerosols in Denmark via analysis of organosulfates and related oxidation products. *Atmos. Chem. Phys.* **2014**, *14* (17), 8961-8981.
52. Boris, A. J.; Lee, T.; Park, T.; Choi, J.; Seo, S. J.; Collett Jr, J. L., Fog composition at Baengnyeong Island in the eastern Yellow Sea: detecting markers of aqueous atmospheric oxidations. *Atmos. Chem. Phys.* **2016**, *16* (2), 437-453.
53. Kuang, B. Y.; Lin, P.; Hu, M.; Yu, J. Z., Aerosol size distribution characteristics of organosulfates in the Pearl River Delta region, China. *Atmos. Environ.* **2016**, *130*, 23-35.
54. Liggio, J.; Li, S.-M.; McLaren, R., Heterogeneous Reactions of Glyoxal on Particulate Matter: Identification of Acetals and Sulfate Esters. *Environ. Sci. Technol.* **2005**, *39* (6), 1532-1541.



## Chapter 5: Direct Photolysis of $\alpha$ -Pinene Ozonolysis SOA

Portions of this chapter were reproduced in part by permission from:

Epstein, S. A.; Blair, S. L.; Nizkorodov, S. A., Direct Photolysis of  $\alpha$ -Pinene Ozonolysis Secondary Organic Aerosol: Effect on Particle Mass and Peroxide Content. *Environmental Science & Technology* **2014**, 48 (19), 11251-11258. Copyright © 2015 American Chemical Society.

\* Note that statements made in sections 5.1-5.5 were based on available literature at the time of the publication submission (May 2014). Section 5.6 includes current literature available up to the submission date of this thesis (May 2016).

## 5.1. Abstract

Primary and secondary organic aerosols (POA and SOA) contain a complex mixture of multifunctional chemicals, many of which are photolabile. Much of the previous work that aimed to understand the aging of POA and SOA has focused on the reactive uptake of gas-phase oxidants by particles. By stripping volatile compounds and ozone from  $\alpha$ -pinene ozonolysis SOA with three 1-m-long denuders, and exposing the residual particles in a flow cell to near-ultraviolet ( $\lambda > 300$  nm) radiation, we find that condensed-phase photochemistry can induce significant changes in SOA particle size and chemical composition. The particle-bound organic peroxides, which are highly abundant in  $\alpha$ -pinene ozonolysis SOA ( $22 \pm 5\%$  by weight), have an atmospheric photolysis lifetime of about 6 days at a 24-h average solar zenith angle (SZA) of  $65^\circ$  experienced at  $34^\circ$  latitude (Los Angeles) in the summer. In addition, the particle diameter shrinks 0.56% per day under these irradiation conditions as a result of the loss of volatile photolysis products. Experiments with and without the denuders show similar results, suggesting that condensed-phase processes dominate over heterogeneous reactions of particles with organic vapors, excess ozone, and gas-phase free radicals. These condensed-phase photochemical processes occur on atmospherically relevant time scales and should be considered when modeling the evolution of organic aerosol in the atmosphere.

## 5.2. Introduction

Atmospheric particulate matter (PM) is ubiquitous, causes adverse health effects, alters climate, and degrades visibility. Depending on location, organic compounds contribute 20 to 90% of the submicron particle mass.<sup>1-4</sup> In order to understand the environmental impact of these organic aerosols (OA), we must comprehensively account for all chemical aging processes that affect the chemical composition, concentration, and physical properties of organic particles. The

majority of past OA aging studies have focused on photooxidation driven by gas-phase and heterogeneous reactions of gas-phase oxidants with OA constituents and gas-phase photochemistry.<sup>5</sup> However, UV radiation from the sun can induce photolysis and other photochemical reactions of oxygenated organic compounds directly in the condensed organic aerosol phase.<sup>6</sup> Gas-phase photolysis of volatile organic compounds (VOCs) is well studied and is accounted for in atmospheric models. On the contrary, changes in OA composition and concentration arising from condensed-phase photolysis of low volatility organic compounds have not been thoroughly quantified. OA contains peroxides,<sup>7, 8</sup> carbonyls,<sup>9</sup> organonitrates,<sup>9</sup> and other photolabile compounds that absorb light at actinic wavelengths. UV radiation is capable of reaching every molecule in a typical particle as opposed to heterogeneous photooxidation, which may be limited by mass transfer to surface reactions, especially in glassy aerosols.<sup>10</sup> (Only coarse particles that are dominated by highly absorbing species such as black carbon may absorb UV to the extent that it does not reach every molecule in the particle.)

Previous studies have found evidence of UV light modifying the composition and properties of organic aerosol. Presto et al.<sup>11</sup> found that the formation of  $\alpha$ -pinene ozonolysis secondary organic aerosol (SOA) in a smog chamber was suppressed by 20-40% when exposed to UV light. Various gas-phase photodegradation products were identified with sensitive detection techniques after irradiating d-limonene ozonolysis SOA collected on substrates.<sup>12-14</sup> Walser et al.<sup>14</sup> suggested that peroxides are the primary UV absorbers in d-limonene ozonolysis SOA based on the shape of its photodissociation action spectrum (the relative amount of gas-phase photolysis products produced as a function of the UV photolysis wavelength). Kroll et al.<sup>15</sup> observed initial SOA growth during the irradiation of a mixture of isoprene and hydrogen peroxide under low-NO<sub>x</sub> conditions, followed by a decrease in particle size as the SOA mixture

was continuously irradiated. However, low-NO<sub>x</sub> β-pinene SOA particles did not shrink upon irradiation, indicating that a rapid loss of SOA mass under UV exposure is dependent on the chemical composition of the SOA. Surratt et al.<sup>8</sup> detected similar decreases in the particle size of low-NO<sub>x</sub> isoprene SOA upon irradiation. Iodometric methods indicated that the organic peroxide content of the SOA decreased significantly during irradiation. Since the experiments of Kroll et al.<sup>15</sup> and Surratt et al.<sup>8</sup> were performed in a chamber; the authors were unable to rule out changes in particle composition and concentration due to the effects of OH radical reactions or repartitioning arising from the irradiation of gas-phase species.

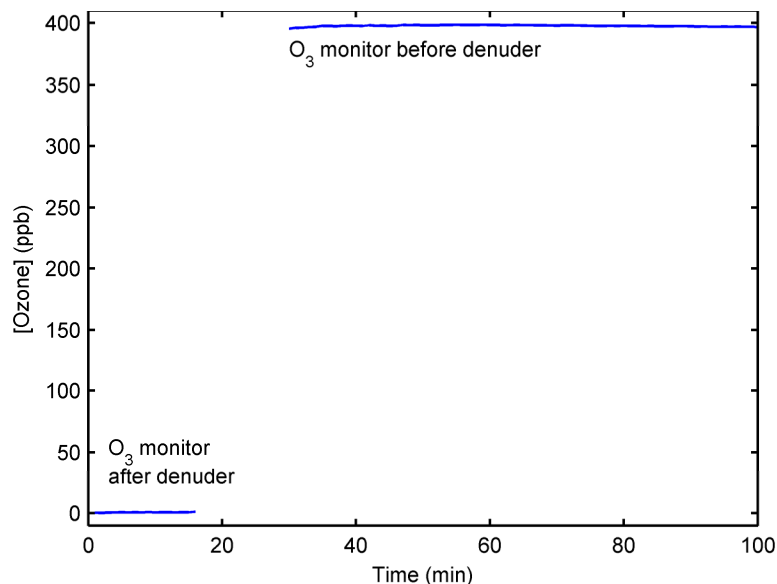
Observations of aerosol photolysis in any chamber experiment are complicated by the interaction of particles and organic vapors and by the photochemical recycling of oxidants. Irradiation of particles collected on substrates<sup>12-14</sup> or in aqueous extracts<sup>16, 17</sup> eliminates interference from gas-phase oxidants and volatiles, but may introduce additional complexities that are not applicable to the atmosphere. For example, volatile products formed during irradiation of bulk SOA materials and solutions may be inhibited from evaporation by mass transfer limitations. To overcome these limitations, we designed a coupled smog-chamber-flow tube approach in which SOA was irradiated without the presence of gas-phase oxidants and high volatility organic gases. We conducted a series of experiments with α-pinene ozonolysis SOA using this setup. Along with tracking particle size, mass concentration, and chemical composition as a function of irradiation time, we also quantified changes in the overall peroxide content of the SOA. Organic peroxides are a significant component in SOA; for example, as much as 50% by weight of α-pinene ozonolysis SOA mass was previously attributed to organic peroxides.<sup>7</sup> We similarly observed high peroxide content (22 ± 5% by weight) in α-pinene ozonolysis SOA, which was depleted by condensed-phase irradiation over atmospherically

relevant time scales. In addition, aerosol size measurements revealed slight changes in particle diameter during irradiation, which implied that condensed-phase photochemical processes resulted in a net loss of organic mass from particles.

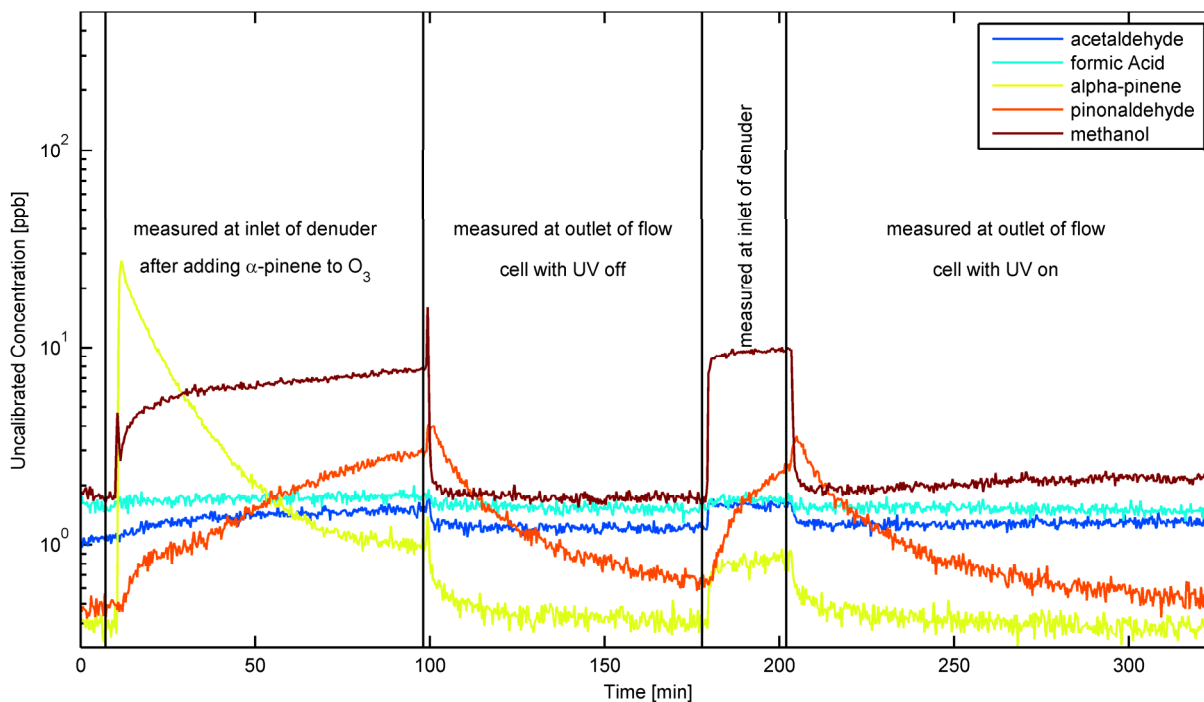
### 5.3. Experimental

#### 5.3.1. Case Studies A-C: Effect of Irradiation on Particle Composition and Size with and without High-Volatility Vapors and Oxidants

Experiments were conducted using two different setups. In the first set of experiments, we used a single quartz flow cell (as either a Photolysis Flow Tube or a Control Flow Tube of Figure 1.7), to irradiate  $\alpha$ -pinene ozonolysis SOA, which was made in a 5 m<sup>3</sup> Teflon<sup>TM</sup> smog chamber. In each experiment, 125 ppb of  $\alpha$ -pinene (Alpha-Aesar 98%) was reacted in the dark with 400 ppb of ozone produced with a commercial ozone generator. We measured the particle concentration and chemical composition with a Scanning Mobility Particle Sizer (SMPS, TSI 3080 Electrostatic Classifier and TSI 3775 or 3776 Condensation Particle Counter) and an Aerodyne Time-of-Flight Aerosol Mass Spectrometer (ToF-AMS), respectively. Concentrations of specific gas-phase compounds were measured with an Ionicon Proton Transfer Reaction Time-of-Flight Mass Spectrometer (PTR-ToF-MS). After the particle mass concentration in the chamber stabilized, the SOA was drawn at 0.39 L/min through three 1-m-long denuders that consisted of an inner and outer tube with activated charcoal in the annulus. In order to test the efficiency of denuders the ozone and VOC concentrations were recorded before and after the denuder train. The residence time in the denuders (3.5 min) was sufficient to remove all of the unreacted ozone and the majority of the gas-phase compounds. The ozone concentration was reduced by at least a factor of 400 (Figure 5.1). The effect of denuders on reducing VOCs is shown in Figure 5.2; the VOC levels were reduced by up an order of magnitude.

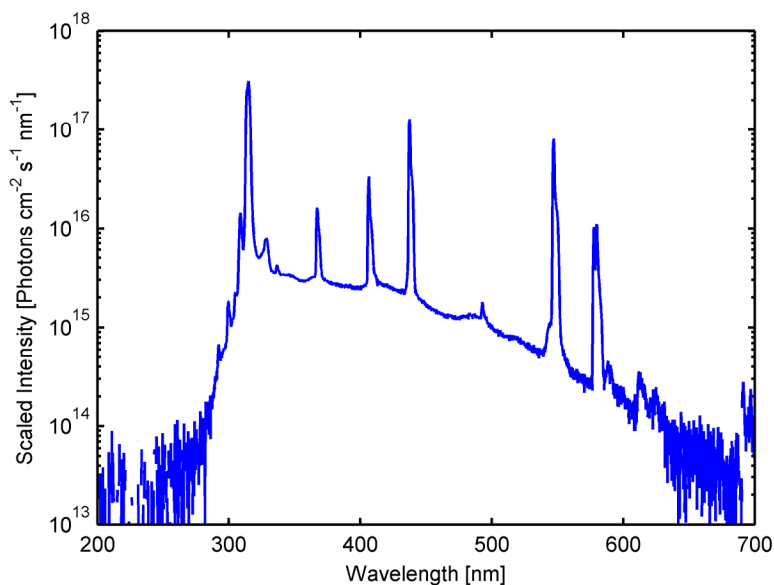


**Figure 5.1.** Ozone signal as measured before and after the denuder train. The monitor was moved between 16 and 30 minutes. The charcoal denuders remove ozone such that resulting concentrations are below detection limits. The denuder efficiency for ozone is greater than 400 ppb.



**Figure 5.2.** PTR-ToF-MS data showing the removal of VOCs after passing through the denuder and the generation of methanol upon photolysis of  $\alpha$ -pinene ozonolysis SOA. The decay of  $\alpha$ -pinene upon reaction with ozone is also evident. Pinonaldehyde is slow to respond due to its propensity to adsorb to PTR-ToF-MS transfer line tubing.

A three-way valve was used to switch between the train of denuders and a bypass line. The aerosol was then drawn into a 24 L quartz flow tube (7" outer diameter) surrounded by 16 UV lamps (Phillips 20W Ultraviolet B TL 20W/01 RS) in a vented protective enclosure. The wavelength dependence of light produced by these lamps is shown in Figure 5.3; it is dominated by a strong emission line at ~312 nm. Actinometry experiments, which are described in Appendix A, were used to determine the scaling factor ( $E = 414 \pm 30$ ) between the SOA photolysis rate inside the quartz flow tube and that in the ambient atmosphere. Isopropyl nitrite, with its known quantum yield and absorption cross section,<sup>18</sup> was used as the actinometer. The calibrated photon flux inside the flow tube was then used to calculate the effective photolysis rate experienced by SOA when exposed to 24-hr averaged sunlight in Los Angeles on the



**Figure 5.3.** Wavelength dependence of the UV-light used to photolyze the aerosol. The intensities are scaled by using the isopropyl nitrite actinometer to quantify the power of the lamps. The majority of the intensity is carried by the 312 nm line. The amount of radiation from wavelengths below 300 nm is negligible (note the logarithmic scale). Radiation above 350 nm does not significantly contribute to photolysis because of the low absorption cross sections of SOA at these wavelengths.

summer solstice. The SMPS, ToF-AMS, and PTR-ToF-MS were positioned at the outlet of the flow tube to monitor differences in gas- and particulate phase composition with and without UV exposure. The residence time of the SOA in the quartz flow tube was approximately 1 hr, set by the sample flow rate of the instruments. Particle evaporation in the flow tube likely replenished some of the semivolatile vapors, but the vapor concentrations were expected to be lower than the gas-particle equilibrium values because the measured particle evaporation times for  $\alpha$ -pinene ozonolysis SOA (several hours)<sup>19</sup> are considerably longer than the flow cell residence time (1 hr).

Table 5.1 summarizes the types of experiments conducted with this setup. In case study A, we generated SOA in the smog chamber, passed it through the denuder train, and drew it through the flow tube. The SMPS, ToF-AMS, and PTR-ToF-MS sampled the SOA with and without the presence of UV light. In case study B, SOA was generated in the smog chamber, sent through the bypass line around the denuder train, and drawn through the flow tube. The same series of perturbations in UV exposure were conducted. Case study C was conducted to investigate the effects of irradiating SOA with a higher average oxidation state.  $\alpha$ -Pinene SOA was generated in the chamber and subsequently aged with additional OH radical production from 2,3-dimethyl-2-butene (TME) ozonolysis (Sigma-Aldrich  $\geq 99\%$ ) in the dark.<sup>20</sup> TME was added to the chamber by evaporation of the headspace above a column of TME at a rate of  $50 \mu\text{g min}^{-1}$  over 90 min. The ozone concentration was reduced linearly at a rate of  $2 \text{ ppb min}^{-1}$  due to its reaction with TME. The resulting aerosol mixture was passed through the denuder train and drawn through the flow tube where we subjected it to perturbations in UV exposure.



**Table 5.1.** Summary of Experimental Conditions.

Case Study	Single or Dual Flow Cell	[ $\alpha$ -pinene] (ppb)	[O <sub>3</sub> ] (ppb)	Denuder or Bypass	Added OH?	Flow Rate (L min <sup>-1</sup> )	Residence Time
A	Single	125	400	Denuder	No	0.39	1 hr
B	Single	125	400	Bypass	No	0.39	1 hr
C	Single	125	400	Denuder	Yes	0.39	1 hr
D	Dual	60	100	Denuder	No	0.96-6	4-25 min
E	Dual	2500 + 1300	400	Denuder	No	1-8	3-22 min

### 5.3.2. Case Study D: Measurements of Aerosol Size as a Function of Irradiation Time

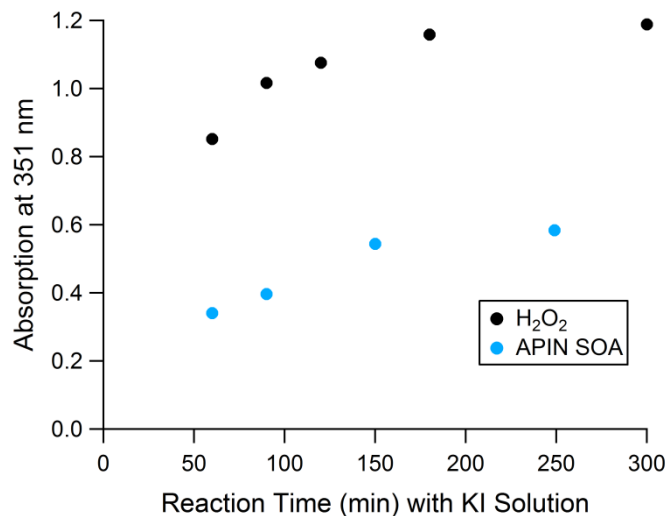
A parallel dark flow tube was added to conduct the second set of experiments at variable flow rates (Figure 1.7). With this setup, we were able to vary the flow rate and residence time through the flow tubes independently of the sampling instruments. To observe how the particle diameter changed with UV exposure, we reacted 60 ppb of  $\alpha$ -pinene with 100 ppb of ozone in the smog chamber (case study D in Table 5.1). The resulting aerosol was passed through the denuder system, split into two flows, and drawn through each of the flow cells. Mass flow controllers were used to govern the residence time of the SOA in each of the flow tubes. The UV lights remained on throughout the experiment but only penetrated the walls of the quartz flow tube (the control flow tube was protected from radiation with a layer of aluminum foil). An SMPS was used to obtain particle size data as a function of aerosol residence time in the quartz flow tube. A second SMPS was used to monitor particle size in the dark flow cell. This dual SMPS measurement allowed us to sensitively track small changes in median mobility-equivalent diameter at various UV exposure times.

### **5.3.3. Case Study E: Measurements of Aerosol Peroxide Content as a Function of Irradiation Time.**

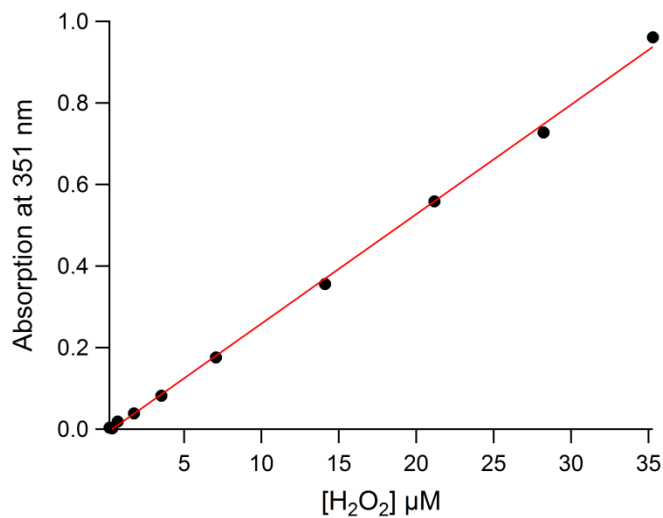
We also conducted experiments designed to measure changes in SOA peroxide content as a function of UV exposure with an iodometric peroxide test originally developed by Banerjee and Budke.<sup>21</sup> Several researchers have used versions of this test to determine peroxide content in aerosols.<sup>7, 8, 16, 22, 23</sup> Experimental details and several important considerations when using this test are summarized in Mutzel et al.<sup>24</sup> Since the iodometric test's sensitivity is limited, it was necessary to do experiments at significantly higher SOA concentrations. In these experiments, 2.5 ppm of  $\alpha$ -pinene was reacted in the dark with 400 ppb of ozone (case study E in Table 5.1). After allowing the mixture to react for 30 min, we added an additional 1.3 ppm of  $\alpha$ -pinene to consume the excess ozone and quench the reaction. One hour later, the SOA was drawn through the light and dark flow tubes at flow rates ranging from 1 to 7 L min<sup>-1</sup> and collected with two SKC Sioutas Cascade Impactors.<sup>25</sup> Stage "A" (> 2.5  $\mu$ m) of the impactors was used to retain any fugitive charcoal dust from the denuders before it reached the substrate. Stage "D" (> 0.25  $\mu$ m) was used to impact approximately 10–20% of the SOA particles on the foil substrate. The residence time in the flow cells was modified with two calibrated mass flow controllers. Two bypass lines with in-line HEPA filters were used as "make-up" air flow to maintain a constant 7 L min<sup>-1</sup> flow through the impactors at any residence time. This "makeup" flow through the HEPA filters laden with the SOA vapor-phase ensured that we did not perturb the partitioning of the collected particles while still maintaining a constant collection flow rate.

Irradiated and dark SOA was collected on aluminum foil substrates that were weighed with 1  $\mu$ g precision before and after collection. Collection times were dependent on the selected aerosol flow rate through the flow tubes but were set to collect approximately 40  $\mu$ g of SOA on

each of the foil substrates. We then dissolved each sample in a small aliquot (several mL) of a solution containing 350  $\mu\text{L}$  of glacial acetic acid (EMD 99.7%) and 25 mL of methanol (Sigma-Aldrich Absolute acetone free) in 100 mL of deionized water. The aliquot volume was selected as to generate a SOA mass concentration of  $5.7 \mu\text{g mL}^{-1}$ . Three 2 mL aliquots were withdrawn from each of the irradiated and dark solutions. We then purged each solution in a septum-cap vial with nitrogen gas (Airgas UHP-300) to eliminate the dissolved oxygen. After 5 min of purging, we added 100  $\mu\text{L}$  of 1.20 M potassium iodide (Fisher Scientific 99.7%) solution. Each solution was allowed to develop in a gastight vial for 5 h. The long reaction time was necessary because the measured  $\text{I}_3^-$  concentration continued to increase until it stabilized after approximately 5 hr of reaction time (Figure 5.4); we wanted to ensure that the reaction was at least 95% complete before each measurement was taken. A UV-vis spectrometer (Shimadzu UV-2450) was used to measure the absorbance of each sample at 351 nm as suggested by Mutzel et al.<sup>24</sup> Calibration solutions prepared by the dilution of 3.0% hydrogen peroxide (concentration verified by taking absorption spectrum) were used to validate this method yielding an  $\text{I}_3^-$  extinction coefficient of  $26,710 \text{ M}^{-1} \text{ cm}^{-1}$  at 351 nm in the reacted samples at concentrations between 0.18  $\mu\text{M}$  and 3.5  $\mu\text{M}$  peroxide (Figure 5.5). This compares well to the value of  $26,400 \text{ M}^{-1} \text{ cm}^{-1}$  published in Awtrey and Connic.<sup>26</sup>



**Figure 5.4.** The required reaction time (5 hours) for an upper limit concentration of a 44.0  $\mu\text{M}$   $\text{H}_2\text{O}_2$  standard (black) and an  $\alpha$ -pinene SOA (APIN SOA) sample concentration of 8.50  $\mu\text{g}/\text{ml}$  (blue) to finish reacting with the KI solution.



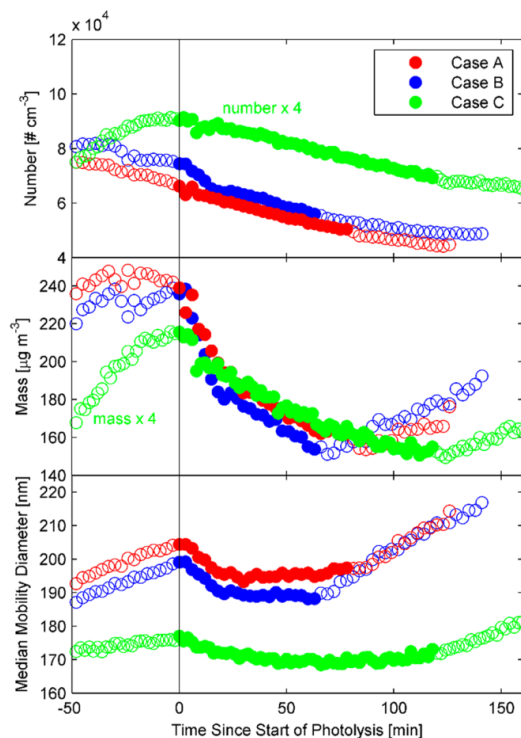
**Figure 5.5.** Calibration of  $\text{H}_2\text{O}_2$  solutions to the absorption of  $\text{I}_3^-$  at 351 nm. The extracted molar extinction coefficient is  $26,710 \text{ M}^{-1} \text{ cm}^{-1}$ .

## 5.4. Results and Discussion

### 5.4.1. Case Studies A–C: Effect of Irradiation on Particle Composition and Size with and without High-Volatility Vapors and Oxidants

SMPS measurements of particle number concentration, median mobility-equivalent diameter, and mass concentration (calculated assuming a constant particle density of  $1.2 \text{ g cm}^{-3}$ ) for case studies A (denuder), B (bypass), and C (added OH) are shown in Figure 5.6. In each of these cases, the aerosol residence time was 1 h, equivalent (Appendix A) to approximately  $17 \pm 1.2$  days of atmospheric irradiation of  $\alpha$ -pinene SOA at a 24-hr average SZA of  $65^\circ$  corresponding to  $34^\circ$  latitude (Los Angeles) at the time of the summer solstice. The number concentration exhibits a steady decline, due to particle wall losses in the smog chamber which the particles are drawn from. Turning the UV lights on or off does not noticeably change the

**Figure 5.6.** Number concentration, median mobility-equivalent diameter, and mass concentration estimated from the mobility measurements in the flow cell. The black line at time = 0 indicates when the lights were turned on. The points denoted with solid markers were acquired when the lights were on. Empty markers indicate that the lights were off during that point in the experiment. Lights were turned off after a different period in each of the three case studies.

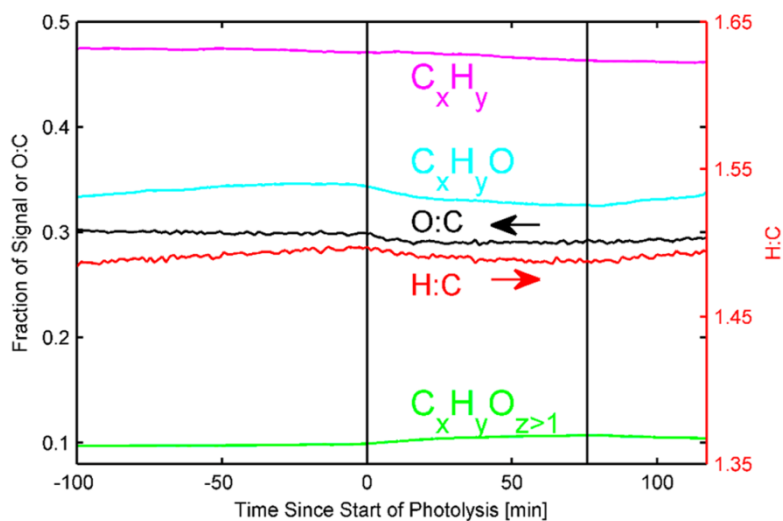


trajectory of particle number concentration. However, the particle mass concentration clearly exhibits a decline when the lights are turned on and a slow recovery toward the initial value when the lights are turned off. The apparent mass concentration does not return to its initial value after the lights are turned off due to wall losses in the smog chamber during the experiment. Irradiation also affects the average particle size. Before the lights are turned on, median mass diameter exhibits a slow steady increase due to coagulation. Upon irradiation, the particles shrink significantly. When the lights are turned off, the median mobility-equivalent diameter grows as the irradiated particles in the flow cell are replaced by dark particles from the chamber. We attribute the observed reduction in the particle diameter and mass concentration to photochemical loss of volatile products from the irradiated particles. However, these changes could also, conceivably, result from a change in the particle density upon irradiation. Since we are not measuring the particles' density directly, we cannot estimate the relative magnitude of this effect.

Monge et al.<sup>27</sup> reported that particles containing suitable photosensitizers may actually increase in size when they are irradiated in the presence of VOC compounds. If this process occurred in the  $\alpha$ -pinene ozonolysis SOA system, we would have expected to see a difference between denuded experiments (lower VOC concentrations around the particles) and undenuded experiments (higher VOC concentrations around the particles). Since we observed comparable particle shrinkage in both cases, we conclude that  $\alpha$ -pinene ozonolysis SOA does not contain molecules that could act as efficient photosensitizers.

The ToF-AMS was used to measure aerosol composition before and after irradiation. We first verified that the small temperature increase in the flow cell resulting from the irradiation did not measurably affect the particle composition (Appendix B). Therefore, all of the observed

changes in the particle ToF-AMS composition can be attributed to photochemistry. As expected, irradiation preferentially affects the oxygenated compounds, as the only photolabile functional groups in low  $\text{NO}_x$   $\alpha$ -pinene SOA are carbonyls and peroxides. This preference is illustrated in Figure 5.7 where the fraction of signal attributed to hydrocarbon fragments remains relatively constant during irradiation and the fraction of signal attributed to the oxygenated fragments evolves during irradiation.

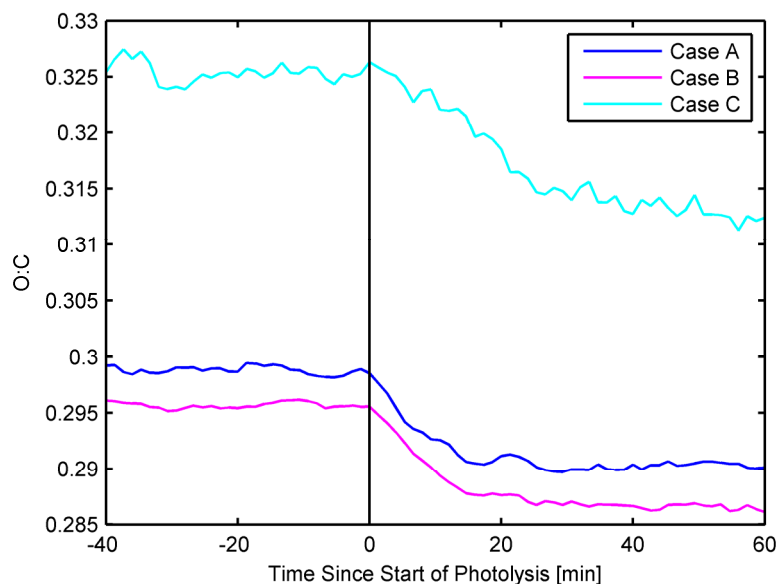


**Figure 5.7.** Fraction of signal attributed to purely hydrocarbon fragments and oxygenated hydrocarbon fragments during aerosol irradiation in case study A (the fractions do not add to 1; the remainder corresponds to fragments that do not contain carbon atoms). Average ratios of O/C corresponding to the left axis and average H/C corresponding to the right axis are also shown for the same experiment. The initial black line represents the time where the lights were turned on. The second black line indicates the time that the lights were turned off.

Fragmented ions containing one oxygen atom (O1) decrease while fragmented ions with more than one oxygen atom increase during irradiation. The decrease in the O1 ions is larger, prompting the average O/C ratio in the SOA to drop slightly during irradiation (Figure 5.8). These observations may imply that the volatile products of photolysis (e.g.,  $\text{CO}_2$ ,  $\text{H}_2\text{O}$ , formic acid, formaldehyde, and methanol) have high oxygen content and that lower O/C compounds

remaining in particles are photolyzed at a faster rate than the higher O/C compounds. However, this cannot be concluded with certainty as secondary reactions between photochemically produced free radicals and oxygen will affect the O/C in the final products.

Case studies A-C reveal similar changes in particle median mobility-equivalent diameter and mass concentration upon irradiation. In addition, changes in the average O/C ratio upon irradiation in each case were of a similar magnitude, indicating that changes in aerosol



**Figure 5.8.** Average oxygen to carbon ratio (O:C) of the SOA from the ToF-AMS before and after photolysis for all three case studies. The change in the O:C ratio is approximately the same in all cases. This observation implies that photochemistry of gas-phase compounds (which are present in case B and reduced substantially in case A) has an insignificant effect on particle composition compared to the condensed-phase photochemical processes occurring in the particles.

composition were alike (Figure 5.8). Finally, the irradiation of vapor-laden air with particles removed by a Teflon<sup>TM</sup> filter did not result in new particle formation in the flow tube. These



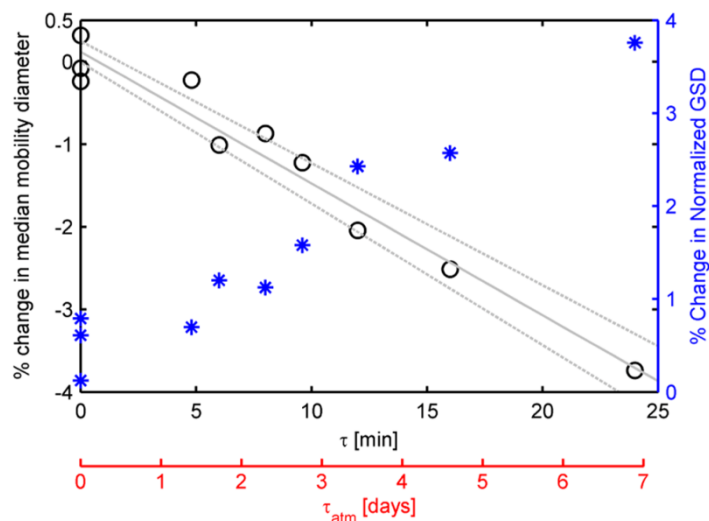
observations, in combination, suggest that while the gas-phase compounds may be photolyzed, the vapor pressures of the resulting products are not low enough to induce partitioning into the condensed phase. Furthermore, the similarity of case studies A-C implies that the rates of condensed-phase photochemical processes must be higher than the rates of heterogeneous reactions between photochemically produced gas-phase radicals and particles.

#### **5.4.2. Case Studies D and E: Dual-Flow Cell Experiments**

After modification of the experimental apparatus to include a dark flow cell along with the ability to easily vary residence time in both flow cells, we were able to more accurately measure particle median mobility-equivalent diameter as a function of irradiation time. This experimental setup provided two advantages over the single-flow cell apparatus. We were able to remove the effects of SOA particle size evolution and compositional changes due to dark aging in the smog chamber by measuring both the dark and irradiated aerosol simultaneously. This allowed us to more sensitively detect small changes in particle concentration and composition with irradiation. In addition, both flow cells expose the aerosol to the same conditions except for the presence of UV light. Most importantly, the temperatures in both irradiated and control flow cells are the same, which helps compensate for any temperature-induced mass concentration changes (temperature effects on the composition are not significant to begin with, Appendix B). Figure 5.9 illustrates the effect of UV exposure on the median particle mobility-equivalent diameter for SOA generated from the reaction of 60 ppb of  $\alpha$ -pinene with 100 ppb of ozone ( $25 \mu\text{g m}^{-3}$  of SOA).

To illustrate changes in median mobility-equivalent diameter during irradiation on an atmospherically relevant time scale, a secondary red axis illustrates the corresponding residence time at a SZA of  $65^\circ$ , which corresponds to the 24-h average SZA at  $34^\circ$  latitude (Los Angeles)

on the summer solstice. The median mobility-equivalent diameter in both the dark and UV-exposed flow cell was tracked continuously with separate SMPS instruments. Dark experiments (shown as the three values when  $\tau = 0$ ) were used to calibrate the measurements from each flow cell with each other. The median mobility-equivalent diameter shrinks measurably as the SOA is irradiated. In the absence of a complete understanding of the kinetic processes that will govern

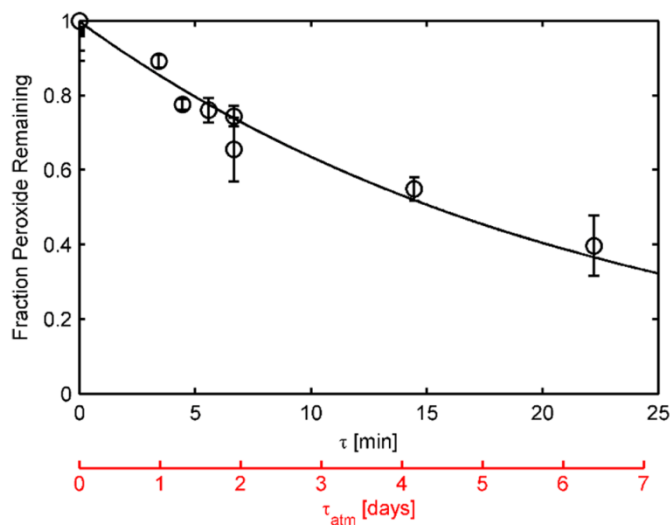


**Figure 5.9.** Change in median mobility-equivalent diameter as a function of aerosol residence time inside the flow cell (left y-axis). The percent change in the geometric standard deviation-between the dark and light flow cell-normalized by the median mobility-equivalent diameter is shown on the right y-axis. The red x-axis,  $\tau_{atm}$ , shows the corresponding atmospheric irradiation time at a solar zenith angle of  $65^\circ$ . The gray line is a linear-least-squares fit of the data. Dash gray lines indicate the bounds of the fit considering the uncertainty in the fitting constants.

a decrease in median mobility-equivalent particle size, we empirically fit the decay with a linear function. The median mobility-equivalent diameter decays at a rate of  $0.56 \pm 0.06\%$  per day at a SZA of  $65^\circ$ . The right y-axis in Figure 5.9 shows how irradiation time affects the geometric standard deviation of the particle size. At longer irradiation times, the particle distribution becomes broader and shifts to smaller sizes.

With offline iodometric peroxide tests, we were able to quantify the change in peroxide content as a function of irradiation time. The average peroxide content in the absence of irradiation was  $(7.9 \pm 1.7) \cdot 10^{-4}$  mol peroxide per gram SOA. With an assumed average molecular weight of  $273 \text{ g mol}^{-1}$ ,<sup>28</sup> this corresponds to a  $22 \pm 5\%$  weight fraction of peroxides in SOA, or equivalently to  $8.5 \pm 1.8\%$  of oxygen atoms residing in the peroxy bonds. This value is significantly smaller than the one measured by Docherty et al.<sup>7</sup> ( $\sim 47\%$  with a similar assumed molecular weight of  $300 \text{ g mol}^{-1}$ ). The disagreement may be due to differences in SOA preparation.

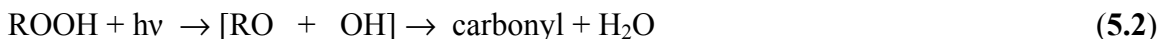
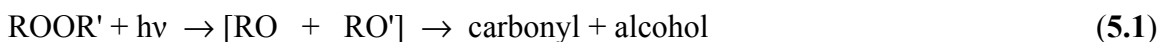
The normalized molar fraction of peroxide remaining in a sample as a function of irradiation time is presented in Figure 5.10. Each data point is the result of averaging three peroxide tests of the same SOA sample. A first-order fit of the data yields a lifetime of  $6.3 \pm 0.6$  days at  $\text{SZA} = 65^\circ$ . Note that the spontaneous decomposition of peroxides, which could occur in the absence of UV light, is explicitly accounted for in these experiments as we compare the peroxide content in the irradiated flow cell to the peroxide content in the dark flow cell. These experiments measure the net loss in peroxide content. Because peroxide photolysis may lead to the formation of secondary peroxides, the primary photochemical reactions may occur at faster rates than the measured lifetime would suggest.



**Figure 5.10.** Fraction of peroxide remaining on a molar basis [moles remaining after UV exposure/mol present before UV exposure] in SOA after exposure to UV light. Exposure to laboratory UV light is shown on the black x-axis. The red x-axis shows the corresponding atmospheric irradiation time at a solar zenith angle of  $65^\circ$ .

Measurements of chemical composition and particle size suggest that photolysis is destroying particle-bound peroxides, which is consistent with the relatively weak and highly photolabile nature of O-O peroxide bonds. Alkoxy (RO) and hydroxyl (OH) radicals formed by the photolysis of peroxides could lead to secondary reactions in the condensed phase. These reactions could further functionalize neighboring SOA molecules and result in a decrease in vapor pressure. However, the observed particle shrinkage during irradiation suggests that fragmentation, leading to the production of volatile products, wins over the functionalization. The predominance of fragmentation is consistent with a recent study by Hung et al.,<sup>29</sup> who observed an efficient photodegradation of films of  $\alpha$ -pinene ozonolysis secondary organic material upon 254 nm photolysis and suggested that aging by ultraviolet radiation was likely due to the presence of organic hydroperoxides in the film. Most likely, the two radicals formed from peroxide decomposition do not have a chance to escape the “solvent cage” of the organic matrix

(indicated by square brackets in the reactions below) and either recombine or disproportionate<sup>30</sup> within the cage:



The final stable products have smaller size and higher vapor pressures than the initial peroxides and can therefore more easily evaporate from the particle. More complicated reactions, involving RO isomerization, hydrogen atom abstraction by RO from a neighboring molecule, etc., are certainly possible,<sup>31</sup> but they are also expected to lead to products that are on average smaller in size than the original peroxides. This result is consistent with the previous observation of the fragmentation of oligomeric SOA compounds and formation of volatile products in bulk SOA irradiation experiments.<sup>12-14, 16, 17</sup>

The large change in the peroxide content resulting from the irradiation (Figure 5.10) appears to contradict the insignificant change in the measured O/C and H/C ratios (Figure 5.8). The ToF-AMS instrument relies on electron impact ionization of flash-vaporized particles, leading to extensive fragmentation, which makes the ToF-AMS results difficult to interpret in a chemical context. In particular, the O-O bonds in peroxides are relatively weak and are likely fragmented completely in the ToF-AMS. Coincidentally, this fragmentation across the O-O bond is also expected to occur during photolysis. Therefore, changes in chemical composition may be underestimated by the ToF-AMS method in situations when SOA aging is driven by condensed-phase photolysis.

## 5.5. Broader Implications

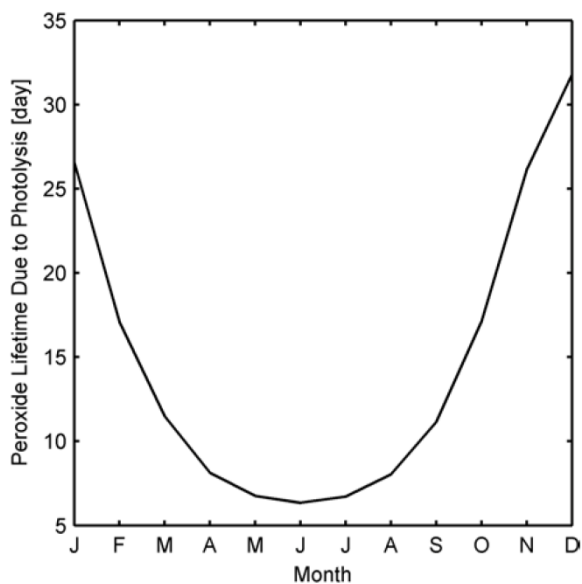
Our experiments suggest that  $\alpha$ -pinene ozonolysis SOA is photolabile on atmospherically relevant time scales. Experimental measurements of chemical composition and particle size indicate that excess ozone and high-volatility organic vapors do not appreciably participate in the photoinduced aging of  $\alpha$ -pinene ozonolysis SOA. The condensed-phase processes, in particular the irradiation of particle-bound peroxides, appear to play the dominant role in  $\alpha$ -pinene ozonolysis SOA aging. The applicability of this important result to other SOA model systems will definitively need to be verified in future experiments.

The peroxide content of SOA was found to be highly sensitive to UV exposure, which is reasonable considering the modestly high absorption cross sections and high photolysis quantum yields of peroxides.<sup>32</sup> Peroxides are abundant in all SOA produced by the ozonolysis of unsaturated organics, such as isoprene<sup>22</sup> and monoterpenes.<sup>7</sup> Therefore, condensed-phase irradiation of peroxides may induce significant changes in chemical composition and physical properties of biogenic SOA. Indeed, the primary step in the photolytic destruction of peroxides is formation of alkoxy and hydroxyl radicals (reactions 5.1 and 5.2),<sup>15</sup> which are highly reactive and could potentially start a complex chain of radical-driven condensed-phase processes. Such reactions may induce fragmentation of SOA compounds, leading to volatilization, but may also form oligomers or less-volatile products that remain in the condensed-phase.

Roughly, 50% of the initial peroxide content remains after 1 week of exposure to sunlight at 34° latitude in the summer. While specific processes may add to the particle peroxide content, the peroxide lifetime that we have measured reflects the net change in peroxide molecules during UV exposure. Within the best-estimate mean particle age of 4-7 days,<sup>33</sup> irradiation has the potential to significantly deplete the particle peroxide content. Figure 5.11 details how the

peroxide lifetime due to photolysis scales with the month of the year. The largest effects are expected in the summer; the peroxide lifetime due to irradiation during the late autumn and winter becomes too long to affect the chemical composition of SOA during its typical atmospheric lifetime.

We should point out that the destruction of peroxides by irradiation occurs on similar time scales as the aging of organic particles by OH radical, which typically serves as the main driver of atmospheric oxidation processes. Chemical lifetimes due to OH aging of aerosol are highly dependent on the species of interest and the particle size. For a 500 nm particle, the effective OH rate constant will be  $1 \cdot 10^{-12} \text{ cm}^3 \text{ molecule}^{-1} \text{ s}^{-1}$ ,<sup>34</sup> leading to an effective oxidation lifetime of 5.8 days at the globally averaged OH concentration value of  $2 \cdot 10^6 \text{ molecules cm}^{-3}$ .



**Figure 5.11.** Aerosol peroxide lifetime in the atmosphere in Los Angeles, CA (34° latitude) as a function of month. The increase in the lifetime in winter months is due to the drastic reduction in the 24-hour average solar zenith angle.

Peroxide-laden PM has been shown to induce adverse health effects in rats upon inhalation.<sup>35</sup> Venkatachari and Hopke<sup>36</sup> propose that peroxides produced in the ozonolysis of  $\alpha$ -pinene could deliver reactive oxygen species in vivo to tissue. Since particle-bound peroxides are highly photolabile, photolytic aging may act to pacify some of the adverse health effects of inhaling peroxide-laden PM.

## **5.6. Literature Update on the Photolysis of Organic Peroxides in APIN SOA**

A more recent study<sup>37</sup> found a very similar particle-bound organic peroxide content of APIN SOA, 21% compared to our study as 23%, and reported that the yield was not affected by RH or by an OH scavenger. Studies have observed that APIN SOA formed with ammonium sulfate seed decreased in SOA mass with photolysis,<sup>1,38,39</sup> and, more recently, that the effect was larger for higher RH.<sup>38</sup> However, it should be pointed out that Daumit et al.<sup>40</sup> did not see a significant photolysis effect for any RH in APIN SOA. Henry and Donahue et al.<sup>39</sup> suggested that APIN SOA mass loss was attributed to the photolytic aging of gas-phase species followed by evaporation of aerosol to maintain equilibrium.<sup>39</sup> Conversely, Wong et al.<sup>38</sup> proposed that photolabile species in particles photodegraded to more volatile components which evaporated from the particles. Condensed-phase peroxide photochemistry has been further pursued. Photolytic hydroxyl radical production rates from aqueous solutions of SOA or organic peroxide standards were reported.<sup>41</sup> These studies emphasized the importance of particle phase photolysis of peroxides, that it is a new source of hydroxyl radicals in particles, and that it contributes to the overall OH flux in SOA. In the future, it will be important to differentiate the primary photolysis of SOA compounds from secondary reactions of free radicals, like OH, produced in the initial photochemical processes in SOA.



## References

1. Donahue, N. M.; Henry, K. M.; Mentel, T. F.; Kiendler-Scharr, A.; Spindler, C.; Bohn, B.; Brauers, T.; Dorn, H. P.; Fuchs, H.; Tillmann, R.; Wahner, A.; Saathoff, H.; Naumann, K.-H.; Möhler, O.; Leisner, T.; Müller, L.; Reinnig, M.-C.; Hoffmann, T.; Salo, K.; Hallquist, M.; Frosch, M.; Bilde, M.; Tritscher, T.; Barmet, P.; Praplan, A. P.; DeCarlo, P. F.; Dommen, J.; Prévôt, A. S. H.; Baltensperger, U., Aging of biogenic secondary organic aerosol via gas-phase OH radical reactions. *Proc. Natl. Acad. Sci. U. S. A.* **2012**, *109* (34), 13503-13508.
2. Qi, L.; Nakao, S.; Cocker, D. R., Aging of secondary organic aerosol from  $\alpha$ -pinene ozonolysis: Roles of hydroxyl and nitrate radicals. *J. Air Waste Manag. Assoc.* **2012**, *62* (12), 1359-1369.
3. Amin, H. S.; Hatfield, M. L.; Huff Hartz, K. E., Characterization of secondary organic aerosol generated from ozonolysis of  $\alpha$ -pinene mixtures. *Atmos. Environ.* **2013**, *67*, 323-330.
4. Kalberer, M.; Paulsen, D.; Sax, M.; Steinbacher, M.; Dommen, J.; Prevot, A. S. H.; Fisseha, R.; Weingartner, E.; Frankevich, V.; Zenobi, R.; Baltensperger, U., Identification of Polymers as Major Components of Atmospheric Organic Aerosols. *Science* **2004**, *303* (5664), 1659-1662.
5. Hallquist, M.; Wenger, J. C.; Baltensperger, U.; Rudich, Y.; Simpson, D.; Claeys, M.; Dommen, J.; Donahue, N. M.; George, C.; Goldstein, A. H.; Hamilton, J. F.; Herrmann, H.; Hoffmann, T.; Iinuma, Y.; Jang, M.; Jenkin, M. E.; Jimenez, J. L.; Kiendler-Scharr, A.; Maenhaut, W.; McFiggans, G.; Mentel, T. F.; Monod, A.; Prévôt, A. S. H.; Seinfeld, J. H.; Surratt, J. D.; Szmigielski, R.; Wildt, J., The formation, properties and impact of secondary organic aerosol: current and emerging issues. *Atmos. Chem. Phys.* **2009**, *9* (14), 5155-5236.
6. Kroll, J. H.; Seinfeld, J. H., Chemistry of secondary organic aerosol: Formation and evolution of low-volatility organics in the atmosphere. *Atmos. Environ.* **2008**, *42* (16), 3593-3624.

7. Docherty, K. S.; Wu, W.; Lim, Y. B.; Ziemann, P. J., Contributions of Organic Peroxides to Secondary Aerosol Formed from Reactions of Monoterpenes with O<sub>3</sub>. *Environ. Sci. Technol.* **2005**, *39* (11), 4049-4059.
8. Surratt, J. D.; Murphy, S. M.; Kroll, J. H.; Ng, N. L.; Hildebrandt, L.; Sorooshian, A.; Szmigielski, R.; Vermeulen, R.; Maenhaut, W.; Claeys, M.; Flagan, R. C.; Seinfeld, J. H., Chemical Composition of Secondary Organic Aerosol Formed from the Photooxidation of Isoprene. *J. Phys. Chem. A* **2006**, *110* (31), 9665-9690.
9. Russell, L. M.; Bahadur, R.; Ziemann, P. J., Identifying organic aerosol sources by comparing functional group composition in chamber and atmospheric particles. *Proc. Natl. Acad. Sci. U. S. A.* **2011**, *108* (9), 3516-3521.
10. Koop, T.; Bookhold, J.; Shiraiwa, M.; Poeschl, U., Glass transition and phase state of organic compounds: dependency on molecular properties and implications for secondary organic aerosols in the atmosphere. *Phys. Chem. Chem. Phys.* **2011**, *13* (43), 19238-19255.
11. Presto, A. A.; Huff Hartz, K. E.; Donahue, N. M., Secondary Organic Aerosol Production from Terpene Ozonolysis. 1. Effect of UV Radiation. *Environ. Sci. Technol.* **2005**, *39* (18), 7036-7045.
12. Mang, S. A.; Henricksen, D. K.; Bateman, A. P.; Andersen, M. P. S.; Blake, D. R.; Nizkorodov, S. A., Contribution of Carbonyl Photochemistry to Aging of Atmospheric Secondary Organic Aerosol. *J. Phys. Chem. A* **2008**, *112* (36), 8337-8344.
13. Pan, X.; Underwood, J. S.; Xing, J. H.; Mang, S. A.; Nizkorodov, S. A., Photodegradation of secondary organic aerosol generated from limonene oxidation by ozone studied with chemical ionization mass spectrometry. *Atmos. Chem. Phys.* **2009**, *9* (12), 3851-3865.
14. Walser, M. L.; Park, J.; Gomez, A. L.; Russell, A. R.; Nizkorodov, S. A., Photochemical Aging of Secondary Organic Aerosol Particles Generated from the Oxidation of d-Limonene. *J. Phys. Chem. A* **2007**, *111* (10), 1907-1913.
15. Kroll, J. H.; Ng, N. L.; Murphy, S. M.; Flagan, R. C.; Seinfeld, J. H., Secondary Organic Aerosol Formation from Isoprene Photooxidation. *Environ. Sci. Technol.* **2006**, *40* (6), 1869-1877.

16. Bateman, A. P.; Nizkorodov, S. A.; Laskin, J.; Laskin, A., Photolytic processing of secondary organic aerosols dissolved in cloud droplets. *Phys. Chem. Chem. Phys.* **2011**, *13* (26), 12199-12212.
17. Nguyen, T. B.; Laskin, A.; Laskin, J.; Nizkorodov, S. A., Direct aqueous photochemistry of isoprene high-NO<sub>x</sub> secondary organic aerosol. *Phys. Chem. Chem. Phys.* **2012**, *14* (27), 9702-9714.
18. Ludwig, B. E.; McMillan, G. R., Primary quantum yields in photodissociation of isopropyl nitrite. *J. Amer. Chem. Soc.* **1969**, *91* (5), 1085-8.
19. Vaden, T. D.; Imre, D.; Beranek, J.; Shrivastava, M.; Zelenyuk, A., Evaporation kinetics and phase of laboratory and ambient secondary organic aerosol. *Proc. Natl. Acad. Sci. U. S. A.* **2011**, *108* (6), 2190-2195.
20. Lambe, A. T.; Zhang, J.; Sage, A. M.; Donahue, N. M., Controlled OH Radical Production via Ozone-Alkene Reactions for Use in Aerosol Aging Studies. *Environ. Sci. Technol.* **2007**, *41* (7), 2357-2363.
21. Banerjee, D. K.; Budke, C. C., Spectrophotometric determination of traces of peroxides in organic solvents. *Anal. Chem.* **1964**, *36* (4), 792-6.
22. Nguyen, T. B.; Bateman, A. P.; Bones, D. L.; Nizkorodov, S. A.; Laskin, J.; Laskin, A., High-resolution mass spectrometry analysis of secondary organic aerosol generated by ozonolysis of isoprene. *Atmos. Environ.* **2010**, *44* (8), 1032-1042.
23. Ziemann, P. J., Aerosol products, mechanisms, and kinetics of heterogeneous reactions of ozone with oleic acid in pure and mixed particles. *Faraday Discuss.* **2005**, *130* (Atmospheric Chemistry), 469-490.
24. Mutzel, A.; Rodigast, M.; Inuma, Y.; Boege, O.; Herrmann, H., An improved method for the quantification of SOA [secondary organic aerosol]-bound peroxides. *Atmos. Environ.* **2013**, *67*, 365-369.
25. Misra, C.; Singh, M.; Shen, S.; Sioutas, C.; Hall, P. M., Development and evaluation of a personal cascade impactor sampler (PCIS). *J. Aerosol Sci.* **2002**, *33* (7), 1027-1047.

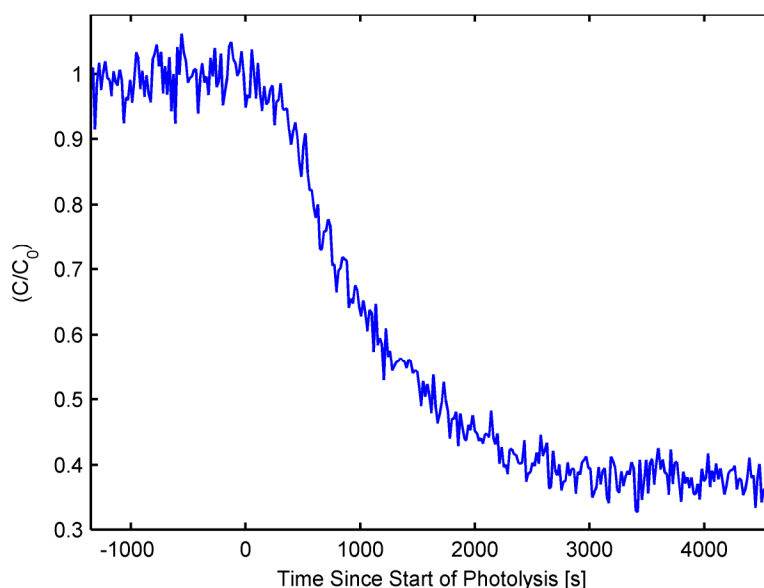
26. Awtrey, A. D.; Connick, R. E., The Absorption Spectra of  $I_2$ ,  $I_3^-$ ,  $I$ ,  $IO_3^-$ ,  $S_4O_6^{2-}$  and  $S_2O_3^{2-}$ . Heat of the Reaction  $I_3^- = I_2 + I$ . *Journal of the American Chemical Society* **1951**, *73* (4), 1842-1843.
27. Monge, M. E.; Rosenorn, T.; Favez, O.; Muller, M.; Adler, G.; Riziq, A. A.; Rudich, Y.; Herrmann, H.; George, C.; D'Anna, B., Alternative pathway for atmospheric particles growth. *Proc. Natl. Acad. Sci. U. S. A.* **2012**, *109* (18), 6840-6844.
28. Romonosky, D. E.; Laskin, A.; Laskin, J.; Nizkorodov, S. A., High-Resolution Mass Spectrometry and Molecular Characterization of Aqueous Photochemistry Products of Common Types of Secondary Organic Aerosols. *J. Phys. Chem. A* **2015**, *119* (11), 2594-2606.
29. Hung, H.-M.; Chen, Y.-Q.; Martin, S. T., Reactive Aging of Films of Secondary Organic Material Studied by Infrared Spectroscopy. *J. Phys. Chem. A* **2013**, *117* (1), 108-116.
30. Kamboures, M. A.; Nizkorodov, S. A.; Gerber, R. B., Ultrafast photochemistry of methyl hydroperoxide on ice particles. *Proc. Natl. Acad. Sci. U. S. A.* **2010**, *107* (15), 6600-6604.
31. Finlayson-Pitts, B. J.; Pitts, J. N. *Chemistry of the Upper and Lower Atmosphere: Theory, Experiments, and Applications*; Academic Press: 2000.
32. Epstein, S. A.; Shemesh, D.; Tran, V. T.; Nizkorodov, S. A.; Gerber, R. B., Absorption Spectra and Photolysis of Methyl Peroxide in Liquid and Frozen Water. *J. Phys. Chem. A* **2012**, *116* (24), 6068-6077.
33. Rudich, Y.; Donahue, N. M.; Mentel, T. F., Aging of Organic Aerosol: Bridging the Gap Between Laboratory and Field Studies. *Annu. Rev. Phys. Chem.* **2007**, *58* (1), 321-352.
34. Donahue, N. M.; Chuang, W.; Epstein, S. A.; Kroll, J. H.; Worsnop, D. R.; Robinson, A. L.; Adams, P. J.; Pandis, S. N., Why do organic aerosols exist? Understanding aerosol lifetimes using the two-dimensional volatility basis set. *Environ. Chem.* **2013**, *10* (3), 151-157.
35. Morio, L. A.; Hooper, K. A.; Brittingham, J.; Li, T.-H.; Gordon, R. E.; Turpin, B. J.; Laskin, D. L., Tissue Injury Following Inhalation of Fine Particulate Matter and Hydrogen Peroxide Is Associated with Altered Production of Inflammatory Mediators and Antioxidants by Alveolar Macrophages. *Toxicol. Appl. Pharmacol.* **2001**, *177* (3), 188-199.

36. Venkatachari, P.; Hopke, P. K., Characterization of products formed in the reaction of ozone with  $\alpha$ -pinene: case for organic peroxides. *J. Environ. Monit.* **2008**, *10* (8), 966-974.
37. Li, H.; Chen, Z.; Huang, L.; Huang, D., Organic peroxides' gas-particle partitioning and rapid heterogeneous decomposition on secondary organic aerosol. *Atmos. Chem. Phys.* **2016**, *16* (3), 1837-1848.
38. Wong, J. P. S.; Zhou, S.; Abbatt, J. P. D., Changes in Secondary Organic Aerosol Composition and Mass due to Photolysis: Relative Humidity Dependence. *J. Phys. Chem. A* **2015**, *119* (19), 4309-4316.
39. Henry, K. M.; Donahue, N. M., Photochemical Aging of  $\alpha$ -Pinene Secondary Organic Aerosol: Effects of OH Radical Sources and Photolysis. *J. Phys. Chem. A* **2012**, *116* (24), 5932-5940.
40. Daumit, K. E.; Carrasquillo, A. J.; Sugrue, R. A.; Kroll, J. H., Effects of Condensed-Phase Oxidants on Secondary Organic Aerosol Formation. *J. Phys. Chem. A* **2016**, *120* (9), 1386-1394.
41. Badali, K. M.; Zhou, S.; Aljawhary, D.; Antinolo, M.; Chen, W. J.; Lok, A.; Mungall, E.; Wong, J. P. S.; Zhao, R.; Abbatt, J. P. D., Formation of hydroxyl radicals from photolysis of secondary organic aerosol material. *Atmos. Chem. Phys.* **2015**, *15* (14), 7831-7840.
42. McVay, R. C.; Zhang, X.; Aumont, B.; Valorso, R.; Camredon, M.; La, Y. S.; Wennberg, P. O.; Seinfeld, J. H., SOA formation from the photooxidation of  $\alpha$ -pinene: systematic exploration of the simulation of chamber data. *Atmos. Chem. Phys.* **2016**, *16* (5), 2785-2802.

## Appendices

## Appendix A: Quantification of UV-light Intensity in the Flow Cell

In order to determine the intensity of the UV-lamps, we photolyzed isopropyl nitrite (IPN), a compound with a known photolysis quantum yield.<sup>1</sup> We mixed 14 ppm of IPN with 227 ppm of cyclohexane to serve as a hydroxyl radical scavenger in the smog chamber. We then pumped this mixture through the quartz flow cell and measured the relative concentration of isopropyl nitrite with the PTR-ToF-MS (Figure A.1). UV lamps were turned on until a steady-



**Figure A.1.** Change in relative concentration of isopropyl nitrite after the UV-lamps were turned on measured with the PTR-ToF-MS. For this experiment, the residence time in the flow cell was one hour. The flux is determined from comparison of the steady-state values of IPN before and after photolysis, as described below.

state concentration of IPN was established. A mass balance on IPN concentration at steady state yields the following relationship for the loss of IPN along the length of the flow cell in a plug-flow limit:

$$\frac{dC_{IPN}}{dV} = -\frac{J_{IPN}C_{IPN}}{Q} \quad (\text{Eq. A.1})$$

$C_{IPN}$  is the molar concentration of IPN,  $V$  is the incremental reaction volume,  $J_{IPN}$  is the first-order photolysis rate constant, and  $Q$  is the flow rate of IPN through the flow cell. Integration yields the following equation relating the ratio of the initial and final IPN concentration to the residence time,  $\tau$ , and the photolysis rate constant:

$$\ln\left(\frac{C_{IPN}^0}{C_{IPN}^F}\right) = J_{IPN}\tau \quad (\text{Eq. A.2})$$

It is also possible to derive a different equation that treats the flow cell as a continuously-stirred-tank-reactor. However, the plug-flow working equation appears to better capture the behavior of the flow cell as it leads to more reproducible UV-light intensities measured at different residence times. With the average quantum yield of IPN ( $\langle\Phi\rangle$  [*molecule/photon*]), the absorption cross section of IPN ( $\sigma(\lambda)$  [*distance<sup>2</sup> molecule<sup>-1</sup>*]), and the unscaled dimensionless wavelength dependence of UV-light inside the flow cell,  $U(\lambda)$  (measured with a spectrometer), we could calculate the effective spectral flux density of photons inside the flow cell as a function of wavelength,  $F_{lamp}(\lambda)$  [photons s<sup>-1</sup> volume<sup>-1</sup>]:

$$F_{lamp}(\lambda) = \frac{U(\lambda) \cdot J_{IPN}}{\langle\Phi\rangle \int U(\lambda) \cdot \sigma(\lambda) \cdot d\lambda} \quad (\text{Eq. A.3})$$

$F_{lamp}(\lambda)$  represents the number of photons crossing a unit area per time per wavelength interval. Ideally, the quantum yield of IPN photolysis would also be a function of wavelength. However, wavelength-dependent measurements of quantum yield require several different monochromatic

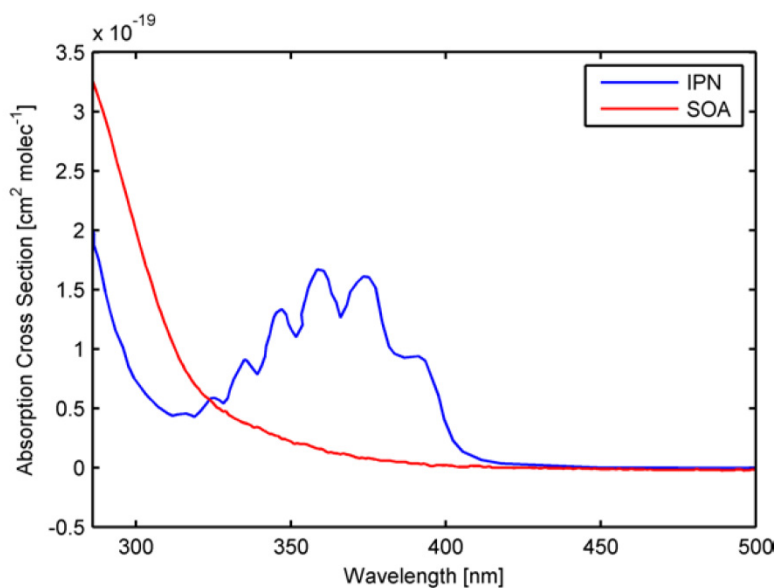


light sources and were not available in the literature. Assuming that the quantum yield of IPN is independent of wavelength within the UV region may lead to a slight bias in the estimated atmospheric photolysis lifetime. We define the unitless ratio of lamp intensity to the intensity of solar radiation,  $E$ , as:

$$E = \frac{\int F_{lamp}(\lambda) \cdot \sigma_{SOA}(\lambda) \cdot d\lambda}{\int F_A(\lambda) \cdot \sigma_{SOA}(\lambda) \cdot d\lambda} \quad (\text{Eq. A.4})$$

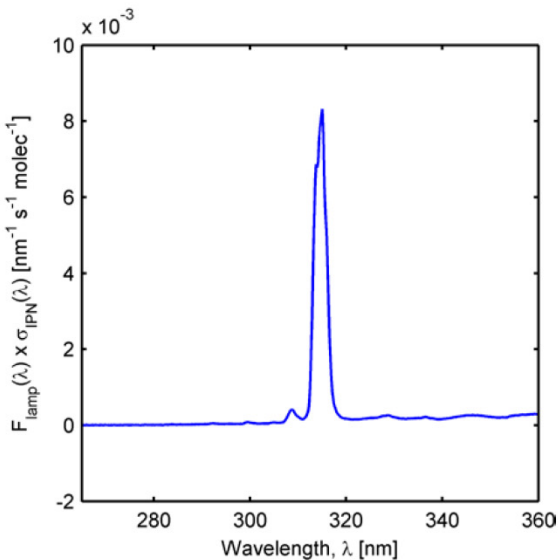
where  $F_A(\lambda)$  [*photons s<sup>-1</sup> volume<sup>-1</sup>*] is the actinic flux at the 24-hour-averaged solar zenith angle in Los Angeles on the summer solstice predicted by the NCAR/ACD Tropospheric Ultraviolet and Visible Radiation Model<sup>2</sup> with a surface albedo of 0.15. The unitless ratio,  $E$ , is used to convert laboratory-determined photolysis lifetimes to tropospheric lifetimes. A typical value for our experiments was  $E = 414 \pm 30$  when calculated for the 24-hour average solar flux in Los Angeles. The absorption spectrum of  $\alpha$ -pinene ozonolysis SOA was obtained from UV-vis absorption measurements of SOA from Romonosky et al.<sup>3</sup> The absorption cross section of IPN, digitized from Ludwig and McMillan,<sup>1</sup> and the molar extinction coefficients of  $\alpha$ -pinene ozonolysis SOA are shown in Figure A.2. Since absorption cross sections appear as a ratio as in Equation A.4, and its units cancel out, molar extinction coefficients  $\epsilon(\lambda)$  [*volume mole<sup>-1</sup> distance<sup>-1</sup>*] or even measured SOA absorbance can be used in this equation. However, for the sake of consistency, we converted all units to those of base-e absorption cross sections, typically used in gas-phase measurements. We used an effective molecular weight of 300 g mol<sup>-1</sup> for the SOA molecules in this conversion.

The product of the absorption cross section of IPN and the effective spectral flux density of light entering the flow tube as a function of wavelength is shown graphically in Figure A.3. This “action spectrum” shows which wavelengths contribute the most to photochemistry (these values

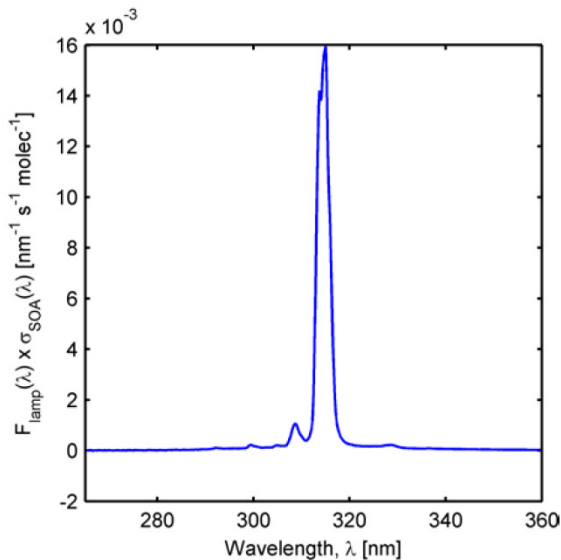


**Figure A.2.** Absorption cross section of IPN and the molar extinction coefficient of  $\alpha$ -pinene ozonolysis SOA.

appear in the numerator and denominator of Equation A.4). The major wavelength contributing to photochemistry in our measurements is 312 nm. Figure A.4 shows a similar action spectrum for the SOA photolysis, which is also dominated by the 312 nm wavelength.

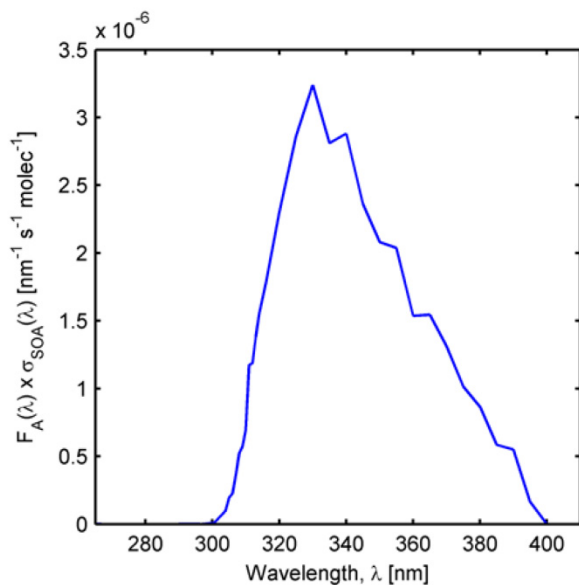


**Figure A.3.** Action spectrum for IPN light absorption from the UV-lamp.



**Figure A.4.** Action spectrum for SOA light absorption from the UV-lamp.

The action spectrum for the SOA light absorption from sunlight is shown in Figure A.5. Because the solar spectrum is more uniform than that of the UV lamp, a broader range of wavelengths, from 300 nm to 380 nm contribute to SOA photolysis.



**Figure A.5.** Action spectrum for SOA light absorption from sunlight at a solar zenith angle of 65°C.

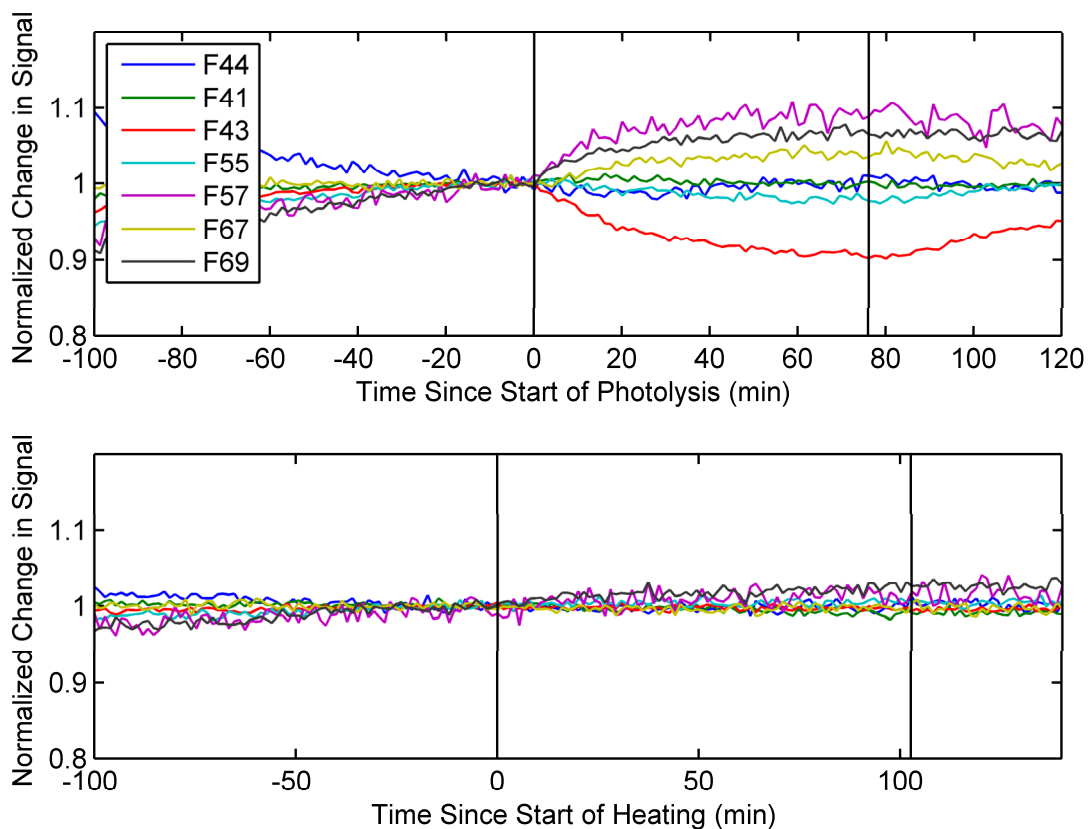
## Appendix B: Negligible Overheating of Aerosol Particles in Flow Cell

To confirm that SOA photolysis, and not particle heating, was responsible for changes in particle size and chemical composition, we measured the temperature of air leaving the quartz UV-transparent flow cell and the foil-wrapped borosilicate flow cell at the lowest experimental flow rate. The temperature of the air in both the dark and light flow cell each rose slightly ( $\sim 3^\circ\text{C}$  over an hour) at the same rate, confirming that temperature effects were properly accounted for with the “dark” flow cell. To ensure that heating was not changing particle composition, we intentionally heated the quartz flow cell by  $4.4^\circ\text{C}$  and tracked particle composition with the ToF-AMS. We did not observe significant changes in chemical composition upon heating (See Figure B.1.). In addition, heat-transfer calculations of particle heating by the UV-lamp confirm that the UV-light intensity is not strong enough to heat the particles beyond the temperature of the bulk gas (see below).

At steady-state the heat supplied to the particles from the UV lamps is removed by convection and conduction to the bath gas. We assume that the particle temperature is uniform and conduction is negligible. Assuming that conduction does not affect the particle temperature provides an upper estimate of the particle temperature at equilibrium. Therefore,

$$P_{hv}V_p \left( \frac{N_A \rho}{M_w} \right) = hA(T_p - T_{bath}) \quad (\text{Eq. B.1})$$

where  $P_{hv}$  is the power per molecule of the lamp,  $V_p$  is the volume of the particle,  $NA$  is Avogadro’s number,  $\rho$  is the particle density,  $M_w$  is the average molecular weight of the particle,  $h$  is the heat transfer coefficient,  $A$  is the particle surface area,  $T_p$  is the temperature of the



**Figure B.1.** The normalized change in signal for seven key unit-masses as measured by the ToF-AMS. The upper pane details changes in these key masses when the SOA is photolyzed (time = 0) and the lamps are turned off (indicated by the second vertical black line). The lower pane details changes when the SOA is heated by 4.4°C inside the flow cell. The second vertical black line indicates when the heat source was removed.

particle, and  $T_{bath}$  is the temperature of the “bath” gas carrying the aerosol. The power of the lamp is derived from the isopropyl nitrite actinometer data and the absorption cross section of  $\alpha$ -pinene SOA.

$$P_{hv} = \int \frac{h_p c}{\lambda} \sigma(\lambda) F_{lamp}(\lambda) d\lambda \quad (\text{Eq. B.2})$$

$h_p$  is Planck's constant,  $c$  is the speed of light,  $\lambda$  represents wavelength,  $\sigma(\lambda)$  is the absorption cross section of  $\alpha$ -pinene SOA, and  $F_{lamp}(\lambda)$  is the flux of photons entering the flow cell as a function of wavelength. Equation B.1 can be re-arranged to the following form:

$$T_p = \frac{1}{6} \frac{P_{hv} D}{h} \left( \frac{N_A \rho}{M_w} \right) + T_{bath} \quad (\text{Eq. B.3})$$

where  $D$  is the particle diameter. The temperature enhancement resulting from the absorption of UV and the resulting convection to the bath gas,  $\Delta T$ , can be written as:

$$\Delta T = \frac{1}{6} \frac{P_{hv} D}{h} \left( \frac{N_A \rho}{M_w} \right) \quad (\text{Eq. B.4})$$

For a spherical particle, the heat transfer coefficient  $h$  can be obtained from the following empirical relationships:

$$Nu = 2 + \frac{0.589 \cdot Ra^{1/4}}{\left[ 1 + \left( \frac{0.469}{Pr} \right)^{9/16} \right]^{4/9}} \quad (\text{Eq. B.5})$$

$$Gr = \frac{D^3 \rho^3 g \Delta T \beta}{\mu^2} \quad (\text{Eq. B.6})$$

$$Nu = \frac{hD}{k} \quad (\text{Eq. B.7})$$

$$Pr = \frac{\mu C_p}{k} \quad (\text{Eq. B.8})$$

$$Ra = Gr \cdot Pr \quad (\text{Eq. B.9})$$

where  $Nu$ ,  $Gr$ ,  $Pr$ , and  $Ra$  are dimensionless numbers,  $g$  is the gravitational constant,  $k$  is the thermal conductivity of air,  $C_p$  is the heat capacity of air,  $\beta$  is the coefficient of volume

expansion of air, and  $\mu$  is the viscosity of air. For a 100 nm particle with a density of  $1.5 \text{ g cm}^{-3}$ , the temperature enhancement is less than  $2 \cdot 10^{-6} \text{ K}$  indicating that evaporation resulting from particle heating is negligible.

## Appendix References

1. Ludwig, B. E.; McMillan, G. R., Primary quantum yields in photodissociation of isopropyl nitrite. *J. Amer. Chem. Soc.* **1969**, *91* (5), 1085-8.
2. Novic, M.; Grgic, I.; Poje, M.; Hudnik, V., Iron-catalyzed oxidation of S(IV) species by oxygen in aqueous solution: influence of pH on the redox cycling of iron. *Atmos. Environ.* **1996**, *30* (24), 4191-4196.
3. Romonosky, D. E.; Ali, N. N.; Saiduddin, M. N.; Wu, M.; Lee, H. J.; Aiona, P. K.; Nizkorodov, S. A., Effective absorption cross sections and photolysis rates of anthropogenic and biogenic secondary organic aerosols. *Atmosp. Environ.* **2016**, *130*, 172-179.